Electrical Resistivity Structure of the Altiplano-Puna Magma Body and Volcan Uturuncu from Magnetotelluric Data

by

Matthew Joseph Comeau

A thesis submitted in partial fulfillment of the requirements for the degree of

Doctor of Philosophy

in

Geophysics

Department of Physics
University of Alberta

Abstract

An intense episode of silicic volcanism in the Southern Altiplano over the past ten million years has created a major volcanic province in the Central Andes known as the Altiplano-Puna Volcanic Complex (APVC). Geophysical evidence indicates that magma is still present in a large mid-crustal reservoir known as the Altiplano-Puna Magma Body (APMB). An analysis of the geodetic data shows that the magma in the APMB is moving, causing observed surface deformation. Broadband magnetotelluric (MT) data collected as part of this thesis were used to generate two-dimensional and three-dimensional electrical resistivity models of the crust below the APVC with the goal of imaging the melt distribution within and above the APMB. The two-dimensional resistivity model gives new constraints on the east-west extent of the APMB, whereas the three-dimensional resistivity model focuses on a spatially broad (~150 km) and temporally continuous (decades) zone of deformation around Volcan Uturuncu in southern Bolivia. Low electrical resistivities (< 3 Ωm) at a depth of ~14 km below sea level are interpreted as being due to the andesitic melts of the APMB and require a minimum melt fraction of 15%. The upper surface of the APMB shallows beneath Volcan Uturuncu, where the inflation is the fastest, and the geometry is consistent with geodynamic models that propose upward movement of melt, in agreement with viscosity calculations derived from the MT data. The shallower resistivity structure is characterized by several discrete electrically conductive bodies, oriented approximately east-west and located close to sea level. These are interpreted as a combination of dacitic partial melt and fluids, and are related to melt movement through the crust and may be a pre-eruptive magma storage location. A quantitative comparison of the resistivity models with seismic velocity models shows that a deep magma body with a silica-rich upper layer can explain both datasets.

Acknowledgements

I would like to take this opportunity to thank my supervisor, Professor Martyn Unsworth. He was always available for help throughout my time at the University of Alberta and his guidance and advice have been invaluable to me. I would also like to thank the members of my committee for our conversations on this research project and comments on my thesis. I have benefited from discussions with many colleagues at the University of Alberta, including: Darcy Cordell, Benjamin Lee, Mitch Liddell, Greg Nieuwenhuis, Robert Ferner, Allan Gray, Enci Wang, Juliane Huebert, and Dennis Rippe.

This research project involved the collection of a large magnetotelluric dataset in the Altiplano-Puna plateau, a remote and rugged area that had its difficulties. Therefore, it would have been impossible without the help and enthusiasm of those who participated and assisted me in each field campaign: Faustino Ticona, Eusebio "Tico" Ticona, Enrique Calvo, Dauth Porcil, Djamil Al Halbouni, Matthew Drew, Grover Arismendi, Pablo Vargas Vargas, Santiago Ramos, Marcos Zeballos, Dr. Daniel Diaz, Fernando Zamudio, Sergio Leon, Monica Doorenbos, Victor Cuezzo, Dante Scatolon, Hermann Binder, Hernan Barcelona, Gisele Veronica Peri, and Dr. Ben Heit. I would also like to thank Dra. Cristina Pomposiello, Dra. Alicia Favetto, and Pablo "Pichi" Maciel for their support in Argentina, and the support from Mayel Sunagua in Bolivia. A big thank you to Daniel Berera and the village of Quetena Chico for hosting us while we collected data. Thanks is also given to SERNAP in the Plurinational State of Bolivia for allowing us to deploy stations in the Area Protegido Eduardo Avaroa of Sur Lipez Province. This project would not have been possible without the magnetotelluric instruments and technical support from Phoenix Geophysics, as well as the magnetotelluric instruments loaned from the Canadian Polaris Consortium.

Alan Jones and Gary McNeice are thanked for providing their tensor decomposition program, Randi Mackie for the use of his 2-D MT inversion algorithm, and Weerachai Siripunvaraporn for providing the 3-D MT inversion algorithm. Numerical and Statistical Servers at the University of Alberta as well as WestGrid Canada were used to run the 3-D MT inversions. This research was financially supported by NSERC and NSF grants to Martyn Unsworth.

Table of Contents

List of Tables

List of Figures

Figure 2.4: Timeline of significant events in the formation of the present-day Andes, see text for details.

Figure 2.5: A graphical illustration of the Volcano Explosivity Index (Newhall and Self, 1982), with some examples of volcanic eruptions. (*Figure from http://plutons.science.oregonstate.edu/ supervolcano).*

Figure 2.6: A schematic cross-section through the continental crust across a subduction zone showing a volcanic system. Basaltic magmas pool at the base of the crust where they differentiate and melt crustal rocks. More evolved andesitic magmas then rise to the middle crust forming batholiths complexes. Magmatic fluids continue to ascend through the crust and may form a shallow pre-eruptive chamber. *(From Richards, 2011).*

Figure 2.7: The Altiplano-Puna *Volcanic Complex* (APVC; de Silva, 1989) is a large ignimbrite province which covers an area of more than 50,000 km^2. Black triangles mark major volcanoes along the modern volcanic arc. White triangle marks the location of Volcan Uturuncu.

Figure 2.8: Ignimbrite units from the Altiplano-Puna Volcanic Complex (APVC) and their associated ages. Coloured areas show the ignimbrite distributions while darker areas show the inferred locations of their source calderas. The black lines represent the international borders, separating Bolivia (north), Chile (south-west), and Argentina (south-east). *(Adapted from Salisbury et al., 2010; Uturuncu lava deposits from Muir et al., 2015).*

Figure 2.9: Panel A shows the cumulative erupted volume over the past 11 million years for the Altiplano-Puna Volcanic Complex (APVC). Three pulses of activity are visible, but during the last few million years the APVC has entered a waning stage. Panel B shows the eruptive volumes and duration of individual events. Colours match Figure 2.8, which shows the location of each event. *(Modified from Salisbury et al., 2010; Uturuncu data from Muir et al., 2015).*

Figure 2.10: Ignimbrite deposits of the Altiplano-Puna Volcanic Complex in Southern Bolivia. Photo taken November 12, 2011, from the village of Quetena Grande, looking south.

Figure 2.11: Volcan Uturuncu, located in Southern Bolivia, Sud Lipez Province, has an elevation of 6008 m and a relief over the surrounding area of 1500-1800 m. Photo taken October 31, 2010, 4 km north of the village of Quetena Chico, looking south-east.

Figure 2.12: The cumulative erupted volume and eruptive history for Volcan Uturuncu. Six discrete pulses of activity are visible (grey bars), with lulls of 50-180 thousand years. *(Modified from Muir et al., 2015).*

Figure 3.1: The ANCORP profile (bold black line) extended across the Altiplano, at 21°S. Red diamonds mark the seismometer locations and white circles mark the earthquake epicenters used in the tomography analysis. Magnetotelluric stations are marked as black circles. Volcanoes are marked with white triangles; Volcan Uturuncu is marked with a gold star. Blue line shows the Altiplano-Puna Volcanic Complex (de Silva, 1989). (*Adapted from Haberland et al., 2003*).

Figure 3.2: Attenuation tomography image along the ANCORP profile, latitude 21ºS. Low seismic quality factors (Q_p) indicate high attenuation. Earthquakes (black dots) mark the location of the subducting Nazca plate (Wadati-Benioff seismic zone). The dashed line indicates the Moho boundary, from Yuan et al. (2002). (*Adapted from Haberland et al., 2003*).

Figure 3.3: The spatial extent of the Altiplano-Puna Magma Body (APMB; bold black line) inferred from seismic receiver functions. Coloured squares mark the location of seismic stations used by Zandt et al. (2003); diamonds are the stations used in the study of Chmielowski et al. (1999). The colour corresponds to whether the APMB was detected below the station (red), was not detected (blue), or was indeterminate (yellow). Inset figure shows example P-wave arrivals, plotted as amplitude against time, used to determine the APMB location, see text for more details. Green circles and squares mark the location of major ignimbrite or volcanic complexes, which young towards the west. A dashed black line shows the Altiplano-Puna Volcanic Complex (de Silva, 1989), which overlaps with the APMB. Volcan Uturuncu is marked with a black star, near the centre of the APMB; Volcan Lazufre is marked with a black circle. Inset map shows the location in South America. (*Adapted from Zandt et al., 2003*).

Figure 3.4: A receiver function analysis from a local network of seismic stations around Volcan Uturuncu reveal a low-velocity layer at approximately 15 km depth below sea-level. (*Modified from McFarlin et al., 2014*).

Figure 3.5: A shear-wave velocity model across the Altiplano-Puna Volcanic Complex and Volcan Uturuncu from the joint inversion of ambient noise tomography and receiver functions from Ward et al. (2014). Panel A shows a vertical cross-section through the model. The 2.9 km/s contour defines a large low-velocity zone, attributed to the Altiplano-Puna Magma Body, below Volcan Uturuncu. Locations referred to in the text are identified for reference (see Chapter 5 for more information): LC - Laguna Colorado; Q - Volcan Quetena; U - Volcan Uturuncu; V - Laguna Vilama; P - Mina Pirquitas; M - Mungayoc. The location of the cross-section is marked with a red line on Panel C. Panel B shows the model at one station (Laguna Colorado; LCOL), marked with a black star on Panel C. A low velocity zone (LVZ) is marked by the 2.9 km/s contour. Panel C shows a horizontal slice through the model at a depth of 15 km below sea-level. Black dashed line is the APVC, dotted lines mark large ignimbrite calderas. The observed surface deformation pattern (see Section 3.6) of uplift (inner white dashed circle) and subsidence (outer white dashed circle) are shown. (*Adapted from Ward et al., 2014*).

Figure 3.6: Earthquake locations recorded from 2009 to 2010 (Jay et al., 2012), with depth below sea-level colour coded. Most earthquakes occurred within the upper 7 km, and are located below Volcan Uturuncu (marked with white triangle). Green triangles indicate location of seismic receivers used.

Figure 3.7: A depth slice through the seismic tomography model of Jay et al. (2012) derived from ambient noise in the area around Volcan Uturuncu (at centre). The model shows a small low-velocity zone (LVZ; red colours) directly beneath Volcan Uturuncu. This LVZ is spatially correlated with earthquake epicenter locations. Black squares are seismometers locations. Black lines mark the 5000 m and 5500 m topography contours and identify the location of Volcan Uturuncu. *(Modified from Jay et al., 2012).*

Figure 3.8: A map showing the location of magnetotelluric sites collected by Schwarz and Kruger (1997; black dots) along the ARC profile and by Brasse et al. (2002; green dots) along the ANCORP profile. The location of the APVC is marked for reference (blue line; de Silva, 1989). Volcan Uturuncu is marked with a gold star.

Figure 3.9: Two-dimensional electrical model of Schwarz and Kruger (1997) across the Altiplano along the ARC profile (see Figure 3.7 for map of sites). A high-conductivity zone (resistivity < 2 Ωm) is detected at a depth of ~20 km, with a total conductance of 23,000 S (Schwarz and Kruger, 1997). (*Adapted from Schwarz and Kruger, 1997*).

Figure 3.10: Magnetotelluric 2-D inversion model of Brasse et al. (2002) across the Altiplano along the ANCORP profile (latitude 21ºS, see Figure 3.1 and 3.7 for map). Earthquake locations (black dots) mark the downgoing Nazca plate, and the Andean Low-Velocity Zone (ALVZ) derived from the receiver function analysis of Yuan et al. (2002). (*Adapted from Brasse et al., 2002*).

Figure 3.11: Residual gravity field obtained from subtracting the effect of the modelled subducting Nazca slab and the Moho from the Bouguer anomaly data. Central Andean gravity high is identified with a dashed line. (*Modified from Prezzi et al., 2009*).

Figure 3.12: High-resolution gravity measurements around Volcan Uturuncu (Ut) reveal a large gravity low (blue colour). Select calderas from Salisbury et al. (2011) are shown as white lines: Gc - Guacha; Vm- Vilama; LC - Laguna Colorada. (*Figure adapted from del Potro et al., 2013*).

Figure 3.13: A density model around Volcan Uturuncu (U) shows numerous low density 3-D features reaching from the Altiplano-Puna Magma Body (APMB) to the surface. These low density pathways and are interpreted to be ascending fluid or magma (del Potro et al., 2013). The model uses a density contrast of 150 kg/m^3, equivalent to a melt fraction of 25%. (*Figure modified from del Potro et al., 2013*).

Figure 3.14: Heat flow map of the Central Andes. Circles indicate measurement locations. In the vicinity of Volcan Uturuncu heat flow values of 100-300 mW/m^2 are seen. Note the data has been interpolated between measurements positions. (*Adapted from Hamza et al., 2005*).

Figure 3.15: Both map-view and profile-view images of InSAR data shows the circular deformation pattern around Volcan Uturuncu. The uplift is symmetric, has a diameter of ~75 km, and a nearly constant rate of 1 cm/yr over the time period of 1992-2011. Cross sections of the data reveal a moat of subsidence around the inflation pattern. (*Adapted from Henderson and Pritchard, 2013*).

Figure 3.16: A summary of proposed geodynamic and seismic models. APMB-RF — location of the Altiplano-Puna magma body (APMB) as defined by seismic receiver functions (RF; Zandt et al., 2003). APMB-ANT+RF — the low-velocity layer determined from the joint ambient noise tomography (ANT) and receiver function model of Ward et al. (2014). U — relative location of Volcan Uturuncu. InSAR data reveals the inflation centre is located ~3 km west of the summit (Pritchard and Simons, 2004). 1 — Spherical inflation source 17 km below sea level (BSL) (Pritchard and Simons, 2004). 2 — Horizontal oblate source 19 km BSL (Pritchard and Simons, 2004). 3 — Prolate ellipsoid 16 km BSL (Hickey et al., 2013). 4 — Diapir extending vertically 5 km from APMB (Fialko and Pearse, 2012). 5 — Flat topped body rising 7 km from the APMB (Walter and Motagh, 2014). BDT — The brittle to ductile transition depth is estimated to be 0.8-2.2 km BSL (Jay et al., 2012). Black dots are earthquake hypocenters projected onto a west-east plane below Uturuncu (Jay et al., 2012). S1 — Pre-eruptive magma storage location (depth of -2.1 to 0.7 km BSL) predicted by Muir et al. (2014). S2 — Shallow low-velocity zone identified with ANT by Jay et al. (2012).

Figure 3.17: A compilation of geophysical evidence around Volcan Uturuncu (red star) and across the Altiplano-Puna Volcanic Complex (APVC, dashed blue line; de Silva, 1989). Receiver function analysis reveals a large low-velocity zone, interpreted as the Altiplano-Puna Magma Body (APMB, dotted yellow line; Zandt et al., 2003). Joint inversion of ambient noise tomography data and receiver function data also show a low-velocity zone (red line, 2.9 km/s velocity contour; Ward et al., 2014). Geodetic data shows a pattern of inflation and subsidence

around Volcan Uturuncu (pink and purple circles; Henderson and Pritchard, 2013). A density model derived from gravity data shows low-density conduits rising from the APMB to the surface (green circles; del Potro et al., 2013). Large calderas and prominent ignimbrite eruption centres are shown as orange ellipses (Salisbury et al., 2010). Geothermal areas are shown as grey ellipses. The modern-day volcanic arc follows the eastern border of Chile.

Figure 4.1: The electrical resistivity and conductivity values for various Earth materials. Values were taken from Simpson and Bahr (2005), and references therein. Electrical conductivity varies over many orders of magnitude and is therefore a useful parameter to define different Earth materials. Ranges of values are shown as bars and are coloured blue for high resistivity, and red for low resistivity (conductive).

Figure 4.2: Effective resistivities computed by various mixing laws for the case of a medium with two phases (ρ_1=100 Ωm and ρ_2=1 Ωm; for example, conductive pore fluid in a resistive rock matrix). Archie's Law (AL; blue dashed line) and Modified Archie's Law (MAL; red line) are shown for cementation factors of m=1.0 (interconnected) and m=2.0 (isolated). The Hashin-Shtrikman upper bound (HS+; black dotted line) and lower bound (HS-; black line) are also shown. At low porosities Archie's Law gives values outside the range of either of the two phases (i.e., ρ > 100 Ωm; shown with a grey box), an unphysical result.

Figure 4.3: An illustration of Snell's Law. Electromagnetic energy incident on the Earth's surface is transmitted vertically downwards ($\theta_2 = 0$), because the wavenumber of the air is much smaller than the wavenumber of the Earth's surface ($k_1 << k_2$).

Figure 4.4: Apparent resistivity (A) and phase angle (B) are plotted against period, which acts as a proxy for depth. Shallow structure is seen at lower periods, and deeper structure at longer periods. The phase is below 45° when the apparent resistivity increases, and is above 45° when the apparent resistivity decreases. Note the log scales for both apparent resistivity and period. The MT data shown were collected near Volcan Uturuncu in Southern Bolivia; see Chapter 5 for details.

Figure 4.5: A 2-D Earth scenario with a conductor extending along a strike direction that is not aligned with the coordinate system. We can rotate our magnetotelluric station coordinate measurement system (X_0, Y_0) to that defined by the geo-electric strike direction (X, Y). The electric fields are then defined to flow either along strike (TE mode) or across strike (TM mode), simplifying our 2-D analysis.

Figure 4.6. A schematic of a magnetotelluric field setup. Long (~100 m) electrical dipoles are used to measure both E_x and E_y field components. Induction coil magnetometers are used to measure H_x, H_y, and H_z field components. A data logger is placed at the centre, representing the station location.

Figure 4.7: The phase tensor represented as an ellipse. The magnitudes of the minor and major axes are given by $\phi_{\min}$ and $\phi_{\max}$. If the magnetotelluric data are 1-D these are equal and the phase tensor will be a circle. The skew angle β is non-zero if the data are 3-D, and acts as a measure of the deviation from two dimensionality. The angle $\alpha - \beta$ gives the orientation of the major axis, equivalent to a 2-D geo-electric strike direction. (*Figure adapted from Caldwell et al., 2004*).

Figure 4.8: Static shifts can be caused by topography. Adjacent MT stations (3 km separation) show similarly shaped apparent resistivity and phase curves. However, the apparent resistivity values for Panel B, which sits on a ridge top, are shifted two orders of magnitude lower.

Figure 5.1: (A) Components of the Phoenix V5-2000 MT system. Shown from left to right are: porous-pot electrodes, connection cables, magnetic induction coils (for x, y, and z components), a laptop to process and store data, the MTU data acquisition unit, and a GPS antenna for time synchronization. (*Photo from http://www.phoenix-geophysics.com).* (B) Installing a magnetotelluric site (1495O31-11). Photo was taken October 31, 2011, looking east towards Volcan Uturuncu.

Figure 5.2: A topographic map showing the locations of all 225 magnetotelluric stations (red circles). The thin black line marks the international border. Pink circle shows the approximate

limits of inflation deformation for both Uturuncu and Lazufre; purple circle shows the subsidence observed at Uturuncu (Henderson and Pritchard, 2013). Green broken line marks the extent of the Altiplano-Volcanic Complex (APVC; de Silva, 1989). Dotted grey line marks the limit of the seismically-inferred Altiplano-Puna Magma Body (APMB; Zandt et al., 2003). Black triangles mark major volcanoes along the modern volcanic arc. Places of interest are marked with black squares.

Figure 5.3: A topographic map showing the locations of 187 magnetotelluric stations (circles) collected in 2011 (yellow), 2012 (red), and 2013 (purple) in Bolivia and NW Argentina. Thin black line marks the international borders. Green letters A, B, and C mark the location of Profile 1, a long transect from the western-most station to the eastern-most station over Volcan Uturuncu. Volcan Uturuncu is marked by a white triangle and the letter U. Places of interest are marked by blue stars and identified with a number. 1 - Laguna Colorado; 2 - Volcan Quetena; 3 - Quetena Chico; 4 - Soniquera; 5 - Cerro Gordo; 6 - Sol de Manana; 7 - Salar de Chalviri; 8 - Laguna Hedionda; 9 - Laguna Verde; 10 - Laguna Coruto; 11 - Rio Chilenas; 12 - Laguna Vilama; 13 - Volcan Granada; 14 - Mina Pirquitas; 15 - Mungayoc; 16 - Cochinoca; 17 - Abra Pampa.

Figure 5.4: Magnetic activity shown as Ap indices during each field season when magnetotelluric data was recorded. Magnetic activity was generally quiet, with a median Ap value of 4.0. (Historical geo-magnetic data is from The Space Weather Prediction Centre, *ftp://ftp.swpc.noaa.gov/pub/indices/old_indices/*).

Figure 5.5: Time series for 5 channels of magnetotelluric data from station 1495N06-11. E_x and E_y are the two orthogonal horizontal components of the electric field. B_x, B_y, and B_z, are the three components of the magnetic field. Note the correlation between B_x and E_y, and between B_y and E_x. The sampling rate is 15 Hz, the lowest the instrument can record. Time is measured from 11:25:24 UTC, on November 7, 2011.

Figure 5.6: Typical magnetotelluric data collected in the study area displayed as apparent resistivity and phase curves. Period acts as a proxy for depth, with short period sensing shallow

structures and long periods sensing deeper structures. Low-resistivity zones (conductors) in a volcanic environment can be caused by aqueous fluids, partial melt, or hydrothermal alteration. The data have been rotated to the strike direction. The transverse electric (TE) mode apparent resistivity is derived from electric currents flowing along strike and the transverse magnetic (TM) mode from currents flowing across strike. Panel A, from a station east of Volcan Uturuncu, shows a multi-layered structure with two resistivity minima. The second minimum (C2) is identified as the APMB. Panel B, from a station near Volcan Quetena, shows a third resistivity minimum (C4), indicating an upper-crustal conductor identified as a shallow magma body. Panel C, from a station near the end of the study area in NW Argentina, shows minor resistivity and phase variations. No deep conductor is observed here. See text for further interpretations.

Figure 5.7: Apparent resistivity and phase curves from 187 MT stations plotted atop each other. The bold curve is the Type 1 curve (shown in Figure 5.6 Panel A; station 1495N06-11). The consistent shape of all the curves is striking. However, the different starting resistivity values imply that large static shifts are present.

Figure 5.8: Histograms of Bahr skew for a broad period range of (A) 1-1000 s, as well as selected period bands, (B) 0.1-1 s, (C) 1-10 s, (D) 10-100 s, and (E) 100-1000 s. Skew values are mostly less than 0.1 for shorter periods (<10 s), an indication of 1-D or 2-D structure. However, at the longest periods (>100 s), several stations show skew values higher than 0.3, indicating 3-D structure.

Figure 5.9: A Bahr skew pseudosection along Profile 1 allows the location of the high skew value stations ($\eta > 0.3$, yellow and red colours) to be determined. Q - Volcan Quetena; U - Volcan Uturuncu.

Figure 5.10: Results of tensor decomposition of the MT impedance data around Volcan Uturuncu. Bins of periods from 1-10 s (A), 10-100 s (B), and 100-1000 s (C) are shown. There is no well defined strike direction for short periods (< 10 s). At longer periods (10-1000 s) a clear strike direction of N30°E is observed. The strike is closer to N0°E in Argentina, however the rose diagram is dominated by the more numerous stations in Bolivia.

Figure 5.11: Rose diagram plots for 1 - 3,000 s showing the long period trend for the whole data set (A), as well as two subsections, the western portion (B) and the eastern portion (C).

Figure 5.12: Fit of the measured impedance to the values predicted by a multi-site / multi-period tensor decomposition in the period band 1-1000 s for fixed strike angles. Panel A shows the results using the MT data in Bolivia, and Panel B uses the data in Argentina (B). The minima shows the preferred strike direction for all sites and all periods included in the calculation. An error floor of 3% was used.

Figure 5.13: Pseudosection showing the fit of the tensor decomposition to the measured impedance data on Profile 1. Profile 1 has two distinct segments: AB and BC, see Figure 5.3. A strike direction of N30°E was used for segment AB and N0°E for segment BC. The generally low misfit values (< 2) indicate that a 2-D approach can be considered valid. Q = Volcan Quetena; U= Volcan Uturuncu. White triangles indicate the position of MT sites.

Figure 5.14: Real induction vectors at periods of 55 s (A) and 294 s (B) plotted using the Weise convention (i.e., pointing away from conductors). A scale arrow of magnitude 0.3 is shown for reference. At long periods (i.e., 294s) the induction vectors point away from a large conductor, thought to be the APMB, and define its edges near Laguna Colorado (LC) and Mungayoc (M).

Figure 5.15: Phase tensors calculated for periods of 3 s (A), 31 s (B), and 294 s (C). The ellipse axes indicate the direction of maximum induction, equivalent to a 2-D geo-electric strike direction, also shown on the rose diagram. At longer periods the phase tensors show a preferred direction of N30°E. Ellipses are coloured with skew value. Skew is generally low, but is locally very high west of Volcan Uturuncu near Volcan Quetena (black triangle) and near the profile end in NW Argentina.

Figure 5.16: Histograms of the phase tensor ellipse axis ratio for selected periods (A, C, E, G). Histograms of phase tensor skew angle for selected periods (B, D, F, H). Dashed red lines show the median values. The last bins show all values equal to or larger than that value. Skew values

are mostly small (<2), except at long periods (e.g., 294 s). At short periods (e.g., 0.3 s) the phase tensor ellipse are nearly circular, implying 1-D structure.

Figure 6.1: Regional profile (Profile 1) with two segments, AB and BC. The magnetotelluric (MT) data were rotated to the determined geo-electric strike directions (AB = N30°E; BC = N0°E, see Section 5.5), and projected onto profile segments oriented perpendicular to the strike direction (N120°E for segment AB and N90°E for segment BC). Circles mark the location of MT sites. MT data from the sites marked by black circles were used for the 2-D inversion model. Volcan Uturuncu is marked with an orange triangle.

Figure 6.2: The preferred 2-D resistivity model obtained from the joint inversion of transverse electric (TE) and transverse magnetic (TM) mode magnetotelluric (MT) data, along Profile 1 (segment AB and BC are joined), see Figure 6.1 for a location map. A combined r.m.s. misfit of 1.49 was achieved after 200 iterations, indicating an acceptable fit to the measured MT data. The approximate limits of uplift and subsidence are shown as pink and purple bars above the resistivity model (Henderson and Pritchard, 2013). The limits of the Altiplano-Puna Volcanic Complex is shown as a grey bar above the resistivity model, note it extends westward beyond the figure (de Silva, 1989). The red triangle at the western edge of the profile marks the modern-day volcanic arc. Note that the depths are referenced to sea-level. Hatched pattern shows approximate limit of penetration for EM signals with a period of 1000 s, and there is minimal resolution in this region. Black triangles indicate MT sites locations used in the inversion. The white box shows the limits of the 3-D inversion discussed below in Section 6.3 (see Figure 6.19). Labelled conductors and resistors (e.g., C1, R1) are discussed in the text. The large deep conductor has an east-west extent of ~170 km, extending from Laguna Colorado, Bolivia, to Mungayoc, Argentina. LC - Laguna Colorado; Q - Volcan Quetena; U - Volcan Uturuncu; VC - Vilama Caldera; G - Volcan Granada; P - Pirquitas; M - Mungayoc; Co - Cochinoca.

Figure 6.3: Pseudosections of both the measured magnetotelluric data and the modeled data for Profile 1 (segments AB and BC) for both TM mode (Panels A and B) and TE mode (Panels C and D). U - Volcan Uturuncu. Profile location as indicated in Figure 6.1. Segment AB is rotated to N30°E; segment BC is rotated to N0°E).

Figure 6.4: Pseudosection residuals showing fit of the MT observed data to the response of the inversion model for Profile 1 (segments AB and BC). The residuals are scaled by the data error. Black triangles mark the location of the MT stations. U - Volcan Uturuncu.

Figure 6.5: Profile 1 used a mesh which included topography. The starting model used for the preferred inversion was a 10 Ωm halfspace. Panel A shows the mesh design with topography for segment AB, and panel B shows the mesh for segment BC. Black triangles are MT sites.

Figure 6.6: The L-curve represents the compromise between fitting the measured magnetotelluric data (r.m.s. misfit) and producing a spatially smooth resistivity model (roughness), by varying the regularization parameter, τ, identified with blue dots. A value of τ = 10 was chosen for segment AB, and a value of τ = 3 was chosen for segment BC.

Figure 6.7: A convergence curve for the preferred 2-D inversion shows both segments of Profile 1 (AB and BC) smoothly converged to an r.m.s. misfit of 1.49 within the first 50 iterations, although the inversion algorithm was run for 200 iterations, see text for details.

Figure 6.8:. The r.m.s. misfit for each MT site in the preferred 2-D inversion along Profile 1 for both the TE mode (red dots) and the TM mode (blue dots). The average misfit of 1.49 is shown as a dashed grey line.

Figure 6.9: Data fit for the preferred 2-D MT inversion model at three sites, one for each identified curve type (see Chapter 5). The line shows the model response and the points are the measured data with error bars. The model generally fits the data well.

Figure 6.10: Static shift coefficients estimated by the 2-D inversion for the preferred model. A value of 1 corresponds to no shift of the apparent resistivity. Damping parameter = 10,000; variance constraint = 10%.

Figure 6.11: Resistivity models produced by varying the tau parameter, which controls model roughness. Panel C shows the preferred 2-D model with a tau value of τ=10. The main resistivity features are seen in each model.

Figure 6.12: Resistivity models produced with various strategies for correcting static shifts, see text for details. Panel A shows the preferred 2-D resistivity model. The main features are observed in each model, indicating they are required by the MT data.

Figure 6.13: Varying the starting model halfspace resistivity of the 2-D inversion has only a small effect on the r.m.s. misfit of the model (blue line; right-hand y-axis) or the roughness (red line; left-hand y-axis).

Figure 6.14: Varying the strike angle used in the inversion has minimal change on the model. The r.m.s. misfit for a strike angle of 20° (Panel A) is 1.49; for a strike angle of 20° (Panel B; preferred model) is 1.49; a strike angle of 40° (Panel C) is 1.51.

Figure 6.15: A test for the requirement of the intermediate depth resistivity features in the preferred 2-D model. Panel A shows the first inversion model (similar to the preferred model, but with no topography). Note the depths are measured from surface, not sea-level as in Figure 6.2. Panel B shows the inversion model edited to eliminate the intermediate depth features. This model is then used as the starting model for a second inversion run (Panel C). The intermediate depth features are recovered completely, showing that they are required by the inversion in order to fit the MT data.

Figure 6.16: Apparent resistivity and phase curves for the MT data at station 1463N16-11, south of Volcan Uturuncu. The fit to the data from the inversion model (Panel A in Figure 6.14) is shown, and the forward response when the intermediate features are removed (as in Panel B, Figure 6.14). The MT response with and without the intermediate features is very different, and they are required by the model in order to fit the measured MT data.

Figure 6.17: Profile 2 (red line, AB) runs along the southern line roughly parallel to Profile 1, but offset southwards by about ~30 km. Panel A shows the location of the magnetotelluric sites used in the 2-D model (grey circles). Volcan Uturuncu is marked with an orange triangle. SM - Sol de Manana geothermal field; C - Salar de Chalviri. Panel B shows the 2-D inversion model. Data were rotated to the geo-electric strike direction of N30°E and projected onto the 2-D profile (line AB). Note the differences in the western edge of the conductive body, and the lack of a bulge below Volcan Uturuncu.

Figure 6.18: A set of 73 magnetotelluric sites around Volcan Uturuncu (red circles, S73), and an extended set of 96 sites (blue and red circles, S96), are used in the 3-D MT inversion. Black circles are MT stations which are not used in the 3-D inversion. The grey box marks the area (approximately 40 x 40 km) shown in the preferred 3-D resistivity model. Volcan Uturuncu (U) is located at near the middle of this grid of stations and Volcan Quetena (Q) is to the west. Inset map shows the location of the study are within South America.

Figure 6.19: The preferred 3-D resistivity model (S73), as shown by Comeau et al. (2015). The upper panels show vertical slices through the inversion model, both West-East (Panel A) and South-North (Panel B). The lower panels show depth slices 1700 m above sea-level (Panel C) and 900 m below sea-level (Panel D). The 73 MT sites used in the inversion are shown as grey circles. Black dots are earthquake hypocenters from Jay et al. (2012). A r.m.s misfit error of 0.95 was achieved, indicating an acceptable fit to the measured MT data. The locations of each slice are indicated by grey lines on the other slices. Depths are measured from sea-level, assuming a mean surface elevation of 5000 m. U = Volcan Uturuncu. The hatched pattern shows the skin depth limit for EM signals, below this limit there is no resolution.

Figure 6.20: The 3-D inversion of the preferred model shows convergence with a 2-stage approach. The left panel shows the first stage, with 4 iterations. The right panel shows the second stage, when the inversion is run a second time, starting with the final model from the first stage as the prior model. After 6 iterations, the r.m.s. misfit converges to 0.95.

Figure 6.21: The preferred 3-D inversion used a 2-stage approach, using the final model from the first stage as the prior model for the second stage, see text for details. The left side shows the first stage model; the right side shows the second stage model. The second stage acts to refine and accentuate the resistivity features. Panels A and B compare a vertical south-north slice; Panels C and D compare a horizontal slice at a depth of -1700 m below sea-level.

Figure 6.22: Data fit for the preferred 3-D inversion at four representative MT sites. The map shows their location on the S73 grid of MT sites. The line shows the model response and the points are the measured data with error bars. The model generally fits the data well.

Figure 6.23: The 3-D inversion model including tipper data. The main resistivity features are similar to the preferred model (Figure 6.19). Panels A and B are west-east and south-north vertical slices through the 3-D model. Panels C and D are horizontal slices at -1700 m below sea-level and 900 m below sea-level. The location of magnetotelluric sites used in the inversion are shown as black circles.

Figure 6.24: The fit of the induction vectors for a period of 9.35 s (Panel A), 149 s (Panel B), and 595 s (Panel C). An induction vector of length 0.3 is shown for scale. The response and the data are generally close. Note that tipper data was not recorded at every MT site.

Figure 6.25: Resistivity models produced by varying the smoothing parameters in the inversion algorithm. The models are made smoother in the vertical direction (panels A and B) by decreasing the ratio of the horizontal (x and y) to vertical (z) smoothing parameters. Default smoothing with all directions given equal weight is shown in panels C and D. Making the model smoother in the horizontal directions is shown in panels E and F. These models used a modified approach with emphasis on fitting longer period data. Panels A, C, and E are west-east vertical slices through the 3-D model along latitude 22.267°S. Panels B, D, and F are horizontal slices at 900 m below sea-level. The location of magnetotelluric sites used are shown as black circles.

Figure 6.26: Resistivity models produced by varying the error floor applied to the magnetotelluric (MT) data used in the inversion algorithm. The main features were recovered in

each case. Panels A, C, and E are west-east vertical slices through the 3-D model along latitude 22.267 °S. Panels B, D, and F are horizontal slices at 900 m below sea-level. The location of MT sites used in the inversion are shown as black circles.

Figure 6.27: The extended S96 3-D resistivity model. The upper panels show vertical slices through the inversion model, while the lower panels show depth slices. The location of the 96 magnetotelluric sites used in the inversion are shown as grey circles. Black dots are earthquake hypocenters from Jay et al., (2012). The locations of each section or slice are indicated by grey lines on the other slices. The hatched pattern shows the skin depth limit for EM signals, below this limit there is no resolution. The grey dashed boxed outlines the area of preferred inversion (S73) for comparison.

Figure 6.28: Apparent resistivity and phase curves for the MT data (points) at station 1463N09-11 (#1 in Figure 6.22), north of Volcan Uturuncu. The fit to the data from the forward response (solid lines) when the intermediate features are removed, and the inversion response (dashed lines) are shown. The MT response with and without the intermediate features is different, and they are required by the model in order to fit the measured MT data.

Figure 6.29: A test for the requirement of the intermediate depth features in the 3-D resistivity model. The inversion prior model used was the preferred 3-D model edited to eliminate the intermediate depth features from 2-12 km below surface. The intermediate depth features are recovered in this model, showing that they are required in order to fit the MT data.

Figure 6.30: Resistivity model with topography produced by the MODEM inversion algorithm of Kelbert el al. (2014).

Figure 6.31: Map showing the inferred extents of the APMB from different methods. The magnetotelluric (MT; black line) data show smaller horizontal extents for the APMB then either the receiver functions analysis (RF; orange line) of Zandt et al. (2003) or the joint ambient noise tomography and receiver function analysis (ANT+RF; red line, 2.7 km/s velocity contour) of Ward et al. (2014). The MT data can constrain the east and west extents, where there is station

coverage (solid black lines), but not the north and south boundaries (dashed black line). MT stations are shown as black dots. The Altiplano-Puna volcanic complex (APVC; de Silva, 1989) is shown as a blue line. Approximate limits of the inflation pattern are shown (Henderson and Pritchard, 2013).

Figure 6.32: Results of a synthetic inversion study. Column A shows the synthetic resistivity model, with intermediate conductors positioned at a depth of -3 km BSL to 3 km BSL, and with a deeper conductor at a depth of 15 km BSL. Column B shows the recovered inversion model. The expected geometry of the intermediate and deep conductors are outlined in gray. Column C shows the recovered inversion model when the deeper conductor is raised to a depth of 10 km BSL. Rows, from top to bottom, show West-East vertical slices, South-North vertical slices, and a horizontal slice at a depth of -1.7 km BSL. The resistivity values and the geometry of the structure is fairly well resolved.

Figure 6.33: Results of a synthetic inversion as in Figure 6.32 but with the site distribution of S96 and three intermediate depth dyke-like conductors. Column A shows the synthetic resistivity model and column B shows the recovered 3-D inversion model. The expected geometry of the conductors are outlined in gray. The resistivity values and the geometry of the structure is fairly well resolved.

Figure 6.34: Results of a synthetic inversion study. Column A shows the synthetic model, with intermediate conductors positioned at a depth of -3 km BSL to 3 km BSL, and with a deeper conductor at a depth of 15 km BSL. The intermediate conductors extend East-West beyond the edges of the model. Column B shows the recovered 3-D inversion model. The expected geometry of the intermediate and deep conductors are outlined in gray. Rows, from top to bottom, show West-East vertical slices, South-North vertical slices, and a horizontal slice at a depth of -1.7 km BSL. The resistivity values and the geometry of the structure is fairly well resolved.

Figure 6.35: Results of a synthetic inversion study as in Figure 6.34 but with a single continuous intermediate depth conductor which extends North-South beyond the model. Panel A shows the

synthetic model and Panel B shows a horizontal depth slice through the recovered 3-D inversion model. The expected geometry of the conductor is outlined in gray. The resistivity values and the geometry of the structure is fairly well resolved.

Figure 7.1: Resistivity-depth profiles for each MT station from the MT response of the inversion resistivity model is shown in Panel A. The depth to the top of the prominent deep conductor (i.e., C2, the APMB) is given by the inflection point of the resistivity curve, shown as a grey box at a depth of 13-14 km below sea-level. Panels B and C show simple 1-D synthetic models with a halfspace (Panel B, orange line) and a layer (Panel C, purple line) with the inversion model resistivity-depth profile shown as a black line, both with 5% Gaussian noise added (solid line) and without (dashed line). The top of the conductive layer is identified with the inflection point of the resistivity-depth curve. Panels D and E show the synthetic 1-D resistivity models (with noise added) with the same colour-scale used throughout this thesis, with dashed lines indicated the sharp boundaries in the true model.

Figure 7.2: Ambient noise and receiver function joint inversion (ANT+RF) velocity model (Ward et al., 2014). Panel A shows a horizontal slice at 15 km BSL. Panel B shows a vertical section along latitude 22.3°, with a vertical exaggeration of 3. The 2.9 km/s contour (green colour) encompasses a large low-velocity zone attributed to the Altiplano-Puna Magma Body. Black dots indicate MT sites, for reference purposes. Volcan Uturuncu is marked with a white triangle and labelled U. The velocity model does not extend east of longitude 66° W.

Figure 7.3: Comparing the shear-wave velocity model of Ward et al. (2014) (Panel A) and the S96 3-D MT resistivity model (Panel B), on a common grid. A general trend of increasing resistivity with increasing velocity can be seen. Note that the depth is defined with reference to the ground surface, not sea-level, as in other figures.

Figure 7.4: Quantitative resistivity-velocity correlation for the S96 3-D MT resistivity model and the velocity model of Ward et al. (2014). Panel A shows the resistivity-velocity correlation histogram. A general trend of increasing resistivity with increasing velocity can be seen. Zones of correlation are colour coded. Panel B shows the spatial location of the outlined zones. Zone 1

(red) maps to the APMB; zone 2 (blue) maps to the lid above the APMB; zone 3 (green) coincides with the small scale features above the APMB.

Figure 7.5: The low velocity zone identified as the 2.9 km/s velocity contour in the ambient noise tomography (ANT) model of Jay et al. (2012) at a depth of 4 km below surface is spatially correlated with the conductive dyke-like features seen in the preferred 3D magnetotelluric resistivity model (depth of 6 km below surface). Black circles are magnetotelluric site locations (S73). Volcan Uturuncu is marked with a white star. Shaded area on the figure indicates region outside the bounds of the ANT velocity model.

Figure 7.6: Panel A: the preferred 3-D electrical resistivity plotted as depth-resistivity profiles for all MT stations. The inflection point of the resistivity-depth profile is at 13-14 km BSL (gray box). Panel B: the S-wave velocity model of Ward et al. (2014) for 2 stations, LCOL near Laguna Colorado and PTLP north of Volcan Uturuncu. The slowest velocities for both stations (dashed lines, minimum) occur at a depth of ~14 km BSL, but the low-velocity zone (LVZ) of Ward et al. (2014) defined by the 2.9 km/s contour (solid lines) encompasses a large region, as the ANT results are smeared vertically. Panel C: published depths to the APMB from seismic receiver functions analysis show depths of 10-17 km BSL.

Figure 7.7: Variation of melt resistivity as a function of temperature for dacite and andesite melt with a range of water and sodium contents. The resistivity data were calculated using the SIGMELTS database of Pommier and Le Trong (2011). The lava composition was taken from Muir et al. (2014) and Sparks et al. (2008). Temperatures measurements are from Sparks et al. (2008). Depths are below surface (rather than sea-level), as this controls the pressure. Minimum resistivity values possible for the compositions and temperatures tested are shown.

Figure 7.8: Conductivity values from the model of Laumonier et al. (2014) for dacite samples from Volcan Uturuncu with varying water content, measured as weight percent (H_2O wt%). Temperature is fixed at 870°C, and pressure is based on the depth to both a shallow magma body (~4 km depth; 130 MPa) and a deep magma body (~30 km depth; 1000 MPa). The red and blue lines show the pure melt conductivity (and resistivity) values for the shallow body and deep

magma body, respectively. Thin grey lines represent the conductivity of a melt and crystal (Cx) mixture, as identified in the legend. Gray bands represent values which are compatible with MT measurements, according to Laumonier et al. (2014). These values are consistent with the SIGMELTS model of Pommier and Le Trong (2011), as shown in Figure 7.7. *(Figure adapted from Laumonier et al., 2014).*

Figure 7.9: Bulk resistivity of a partially molten rock as a function of melt percentage. Panel A shows pure dacite melt with a resistivity of 5 Ωm. Panel B shows pure andesitic melt with resistivity of 0.1 Ωm. Red lines show the bulk resistivity computed using Modified Archie's Law (MAL; Glover et al., 2000), for various degrees of melt interconnection (cementation factor m=1.0, 1.5, 2.0). The solid black line shows the Hashin-Shtrikman lower bound (HS-L), and the dashed line shows the upper bound (HS-U). HS-L is the preferred value, see text for details. Depths are below surface, as this controls the pressure (~5 km below surface = sea-level). The minimum melt percentage for dacite is 80%, implying that a second conducting phase may be required to explain the data. The minimum melt percentage for the andesite is 15%.

Figure 7.10: Panel A shows the solubility of water for varying pressures for both basaltic and rhyolitic melts, from the model of Newman and Lowenstern (2002). Panel B shows an isobaric (constant pressure) solubility plot for both water and carbon dioxide (CO_2).

Figure 7.11: Panel A shows shear wave velocity (Vs) as a function of melt fraction. The relations of Dvorkin (2008) and Takei (2000) give similar results. Panels B and C show that the shear-wave velocity is sensitive to the fluid content and will be constant in a layer of melt, despite the melt's composition or inhomogeneities within the melt.

Figure 7.12: Bulk resistivity forward model for varying silica contents. Input parameters of temperature, melt fraction, silica content, and water content are shown in Panels A-D. The predicted bulk resistivity of a magma chamber is shown in Panel E for three models. Each model has the same temperature profile, a melt fraction of 25 %, water content of 6 wt%, and sodium content of 3 wt%. Model 1 (red) is uniform with 60 % silica; Model 2 (blue) is a layered magma

chamber with 65 % silica in the upper portion; Model 3 (green) is a layered chamber with 70 % silica in the upper portion.

Figure 7.13: Bulk resistivity forward model for varying water contents. Input parameters of temperature, melt fraction, silica content, and water content are shown in Panels A-D. The predicted bulk resistivity of a magma chamber is shown in Panel E, as in Figure 7.12.

Figure 7.14: Melt resistivity values for the whole model space computed from SIGMELTS are shown. Panel A shows how the resistivity varies as a function of silica content, for different water contents (W). A connectivity of m=1 and a melt fraction of 25% is assumed. Panel B shows how the resistivity varies as a function of water content, for different silica contents (S). Panel C assumes a silica content of 60% and a water content of 6% and shows how the resistivity varies with melt fraction, for different connectivity values (M). Panel D shows how the resistivity varies as a function of the connectivity parameter m from Archie's law, for different melt fractions (F). The black dot represents the values used in Model 1. Resistivity values cover a large range: from ~0.5 to 20 Ωm.

Figure 7.15: Forward model MT curves for various models shown as apparent resistivity and phases curves, see text for details. Panels show variations in silica content (A), variations in water content (B), and variations in melt fraction and melt geometry (C). The models are very similar but the differences are large enough to distinguish between models with MT data.

Figure 7.16: Panel A: synthetic models for a uniform magma chamber (Model 1, red line) and a layered magma chamber (Model 7, green line), with the addition of a conductive surface layer. Panel B: resistivity-depth profile for the 1-D synthetic inversion resistivity model. The depth to the top of the prominent deep conductor (i.e., the APMB) is given by the inflection point of the resistivity curve. Random Gaussian noise (5%) was added to the data in order to create a more realistic model. True synthetic models are shown in Panels C and E as colour plots, whereas inversion resistivity models are shown in Panels D and F. Dashed lines indicated sharp boundaries in the true model of magma chamber location and its upper and lower portions for the layered case. The surface conductor acts to mask the signal, reducing the resolution in the

magma chamber. The models show that MT data can reliably show a layered magma chamber at a greater depth than a uniform one, when the lower layer is more conductive.

Figure 7.17: Variation of melt viscosity with temperature for various melt compositions, using the model of Giordano et al. (2008). Note that there are multiple ways to lower the viscosity: a higher temperature leads to a lower viscosity; a higher water content (weight percent, wt%) leads to a lower viscosity; a lower silica fraction (% SiO_2) leads to a lower viscosity.

Figure 7.18: Variation of melt viscosity and electrical resistivity for a deep andesite body (blue lines) and shallow dacite body (red lines) for fixed temperatures, water content (CW, in weight percent, wt%), and composition (the OB parameter) using the relation of Pommier et al. (2013), see text for details. Note the resistivity also depends on the temperature, water content, and composition. A resistivity value of 0.2 Ωm for the deep andesite body with 6 wt% water gives a viscosity value of 10^6 Pa·s; a resistivity value of 1.0 Ωm for the shallow dacite body with 4 wt% water gives a viscosity value of 10^8 Pa·s.

Figure 7.19: The relative viscosity (ratio of viscosity to melt viscosity) as a function of melt fraction and crystal fraction. The experimental values of Caricchi et al. (2007) are shown with black lines for a high strain rate ($8x10^{-4}$ s^{-1}; solid line) and a low strain rate ($0.005x10^{-4}$ s^{-1}; dashed line). Experimental values from Costa (2005) (strain rate of $0.01x10^{-4}$ s^{-1}) are shown as blue circles, while the empirical relation of Costa (2005) is shown as a blue line.

Figure 7.20: Several proposed geodynamic models overlain with the preferred 3-D resistivity model. C2 — The deep conductor interpreted as the APMB. C4 — The shallow conductor interpreted as a pre-eruptive magma body. 1 — Spherical inflation source (Pritchard and Simons, 2004). 2 — Horizontal ellipsoid source (Pritchard and Simons, 2004). 3 — Vertical ellipsoid source (Hickey et al., 2013). 4 — Diapir extending above APMB (Fialko and Pearse, 2012). 5 — Flat topped body above the APMB (Walter and Motagh, 2014). Depths to the Altiplano-Puna magma body from seismic receiver functions (APMB-RF; Zandt et al., 2003) correlate well with the depth inferred from the MT data. Ambient noise tomography (APMB-ANT; Ward et al., 2014) shows a broader range for the APMB, likely encompassing the small scale features above

the APMB and smearing the results. U — relative location of Volcan Uturuncu. InSAR data reveals the inflation centre is located ~3 km West of the summit (Pritchard and Simons, 2004). Black dots are earthquake hypocenters from Jay et al., (2012). Earthquake locations correlate with the shallow conductor (C4) interpreted to be a pre-eruptive magma storage location, as predicted by Muir et al. (2014) from the geo-barometry of erupted dacites (S1) and Jay et al. (2012) from a low-velocity zone identified with ANT (S2).

Figure A.1: Preferred 3-D resistivity model (S73). A vertical slice through the inversion model along latitude 22.267°S. Black dots are earthquake hypocenters from Jay et al. (2012). The symbol U marks the location of Volcan Uturuncu.

Figure A.2: Preferred 3-D resistivity model (S73). A vertical slice through the inversion model along longitude 67.192°W. Black dots are earthquake hypocenters from Jay et al. (2012). The symbol U marks the location of Volcan Uturuncu.

Figure A.3: An alternative view of the preferred 3-D MT resistivity inversion model (S73). The view is looking south-east, along two vertical slices which intersect at the location of Volcan Uturuncu.

Figure A.4: Resistivity as a function of silica content (Panel A) and water content (Panel B) using the SIGMELTS model of Pommier and LeTrong (2011). Black line in Panel B shows the relation of Laumonier et al. (2014) for dacite (silica content of 63% - 68%).

Figure A.5: Vertical sections of the 3-D resistivity model S96, shown looking northwards.

Figure A.6: Vertical sections of the 3-D resistivity model S96, shown looking westwards.

CHAPTER 1: INTRODUCTION

The Andean subduction zone is a convergent plate boundary, where the oceanic Nazca plate subducts beneath the continental South American plate (Cahill and Isacks, 1992). This region encompasses the Altiplano-Puna high plateau (average elevation of 4000 m), which is one of the largest and most extensive high plateaux on Earth (Isacks, 1988; Allmendinger et al., 1997). A major ignimbrite flare-up during the last 10 m.y. caused a series of large caldera-forming eruptions that formed the Altiplano-Puna volcanic complex (APVC) (de Silva, 1989) on the Altiplano-Puna plateau in Southern Bolivia and Northern Argentina (South America), as shown in Figure 1.1.

Geophysical studies have shown that the APVC is underlain by anomalously low seismic velocities (eg., ANCORP, 1996; Chmielowski et al., 1999; Beck and Zandt, 2002; Zandt et al., 2003), high seismic attenuation (Haberland et al., 2003; Schurr et al., 2003), low electrical resistivities (e.g., Schwarz and Kruger, 1997; Brasse et al., 2002; Schilling et al., 2006), anomalously high heat flow values (Henry and Pollock, 1988; Springer and Forster, 1998; Hamza et al., 2005), and is associated with a negative Bouguer anomaly (del Potro et al., 2013). Together, these geophysical anomalies give evidence for the presence of a major mid-crustal magma body, the Altiplano-Puna Magma Body (APMB), and make this region a key location for understanding silicic magmatism in continental crust.

Furthermore, satellite-based geodetic data shows a spatially broad (~75 km) and temporally continuous (decades long) deformation pattern coincident with the APMB and centered on Volcan Uturuncu, which includes a central ring of uplift (10-15 mm/year) and an outer ring of subsidence (Fialko and Pearse, 2012; Henderson and Pritchard, 2013). The geometry of the inflation source is not well constrained, and multiple geodynamic models have been proposed which are consistent with the currently available data. Geodetic models with inflation source depths in the range of 15-20 km below sea-level (BSL) (e.g., Pritchard and Simons, 2004) correlate well with depths to the APMB determined from seismic data (e.g., Chmielowski et al.,

1999; Zandt et al., 2003). However, currently available geophysical data above the APMB are not able to image small-scale features and therefore cannot image conduits or pathways of ascending melt between the APMB and the surface nor shallow magma storage locations. The question of the distribution of melt within the APMB and above it remains unconstrained, and more geophysical data are required.

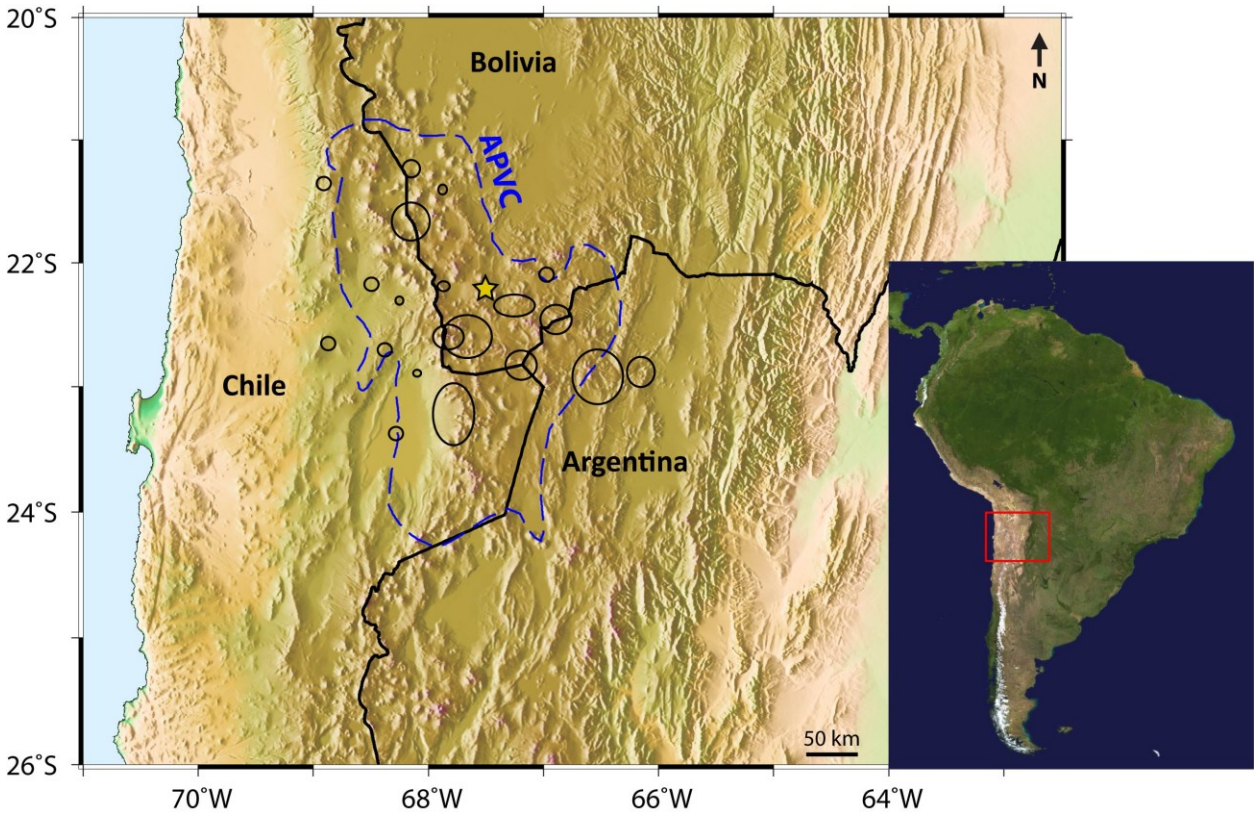

Figure 1.1: A topographic map of the study area in the Central Andes. The inset map shows the location within South America. The Altiplano-Puna volcanic complex (APVC; de Silva, 1989) is outlined in blue. A gold star marks the position of Volcan Uturuncu. Large calderas and prominent ignimbrite eruption centres are indicated with black ellipses (Salisbury et al., 2010). All topographic base maps in this thesis were created with the Generic Mapping Tools package of Wessel and Smith (1991).

The electrical resistivity of a rock is sensitive to its composition, particularly its fluid content (e.g., partial melts, aqueous fluids). Therefore magnetotelluric (MT) data are useful for the investigation of subsurface magma distribution because they can map subsurface electrical resistivity to depths of ~100 km (Chave and Jones, 2012). As part of this thesis, data were collected from an array of 187 broadband MT stations from 2011 to 2013 in Southern Bolivia, around Volcan Uturuncu, and in North-Western Argentina to investigate the crustal magma distribution both regionally below the APVC and locally below Volcan Uturuncu. Extensive sensitivity studies have been undertaken to show that a MT survey with dense station spacing (< 5 km) can resolve conductive bodies (e.g., magma bodies) on the scale of kilometres both near the surface (depth of a few kilometres) and in the mid-crust (~20 km).

The research presented in this thesis is part of an international collaborative project known as PLUTONS, which used a multi-disciplinary approach to study the regional structure of the APVC in addition to a detailed investigation of Volcan Uturuncu, located at the center of the APVC. Volcan Uturuncu represents a location where pluton formation from magma cooling and crystallizing in the Earth may be occurring in real time (Sparks et al., 2008; Pritchard and Simons, 2004; Brown, 2013).

The focus of this thesis is the collection, analysis, and interpretation of data from a high-resolution MT survey around Volcan Uturuncu and across the APVC. The goal was to image the APMB and the magmatic system beneath Volcan Uturuncu, providing constraints on magma body depth, volume, and composition. These parameters have implications for the deformation of the continental crust in this region. Additional information from other datasets collected by other PLUTONS researchers are also be used to constrain the interpretation of the electrical resistivity model derived from MT data. This includes seismic velocity models, gravity-derived density models, and petrological data. This is the first large-scale, high-resolution, broadband magnetotelluric study of the Altiplano and of Volcan Uturuncu, consisting of several 2-D profiles and a 3-D network of MT stations, and will give a better understanding of the resistivity structure of this area.

The geological and tectonic history of the study area is introduced in **Chapter 2**. Emphasis is placed on the Altiplano-Puna plateau and the APVC, above which Volcan Uturuncu is located. Super-volcanoes and super-eruptions are discussed as well as magma dynamics. The petrological and geochemical signatures of ignimbrites erupted from the APVC are discussed, as are their variations with time.

In **Chapter 3** previous geophysical studies of the APVC are reviewed. Evidence for the existence of a large magma body from seismic studies is reviewed, including receiver function analysis, attenuation tomography, ambient noise tomography, and local seismicity. Previous MT studies in the Central Andes detected a high conductivity zone, providing further support for a pervasive region of partial melt below the Altiplano. Evidence from geodetic methods that detect ground deformation around Volcan Uturuncu and anomalously high regional heat flow measurements in the area give further support to this idea.

Chapter 4 introduces the magnetotelluric (MT) method, the main geophysical exploration method used in this thesis, and explains how it measures the resistivity structure of the subsurface from the Earth's surface. The electrical properties of typical Earth materials are discussed and equations to calculate bulk resistivity are compared. The MT impedance tensor is explained and examples of MT data from the study area of the APVC are shown as apparent resistivity and phase curves. The concepts of dimensionality, directionality, geoelectric strike, data distortion, and MT data inversion are introduced, and will be applied in later chapters.

The magnetotelluric data acquired in the APVC are analyzed in **Chapter 5**. A brief description of the MT data collection is given, along with an introduction to magnetotelluric instrumentation. Tensor decomposition is first performed to determine an appropriate geoelectric strike direction for the data where a 2-D approach is used, and then distortion parameters and phase tensors are employed to show where 3-D effects are present and which areas require a 3-D approach.

Both 2-D and 3-D inversions of the MT data are presented in **Chapter 6** with a discussion of the various inversion parameters used and their effects on the resistivity model, along with a description of the main robust resistivity features of the models. The misfit of the predicted

(modeled) MT data and measured MT data is shown to be acceptable for the final resistivity models. Synthetic modeling and inversion studies are used to investigate the reliability of the main resistivity features.

Chapter 7 describes in detail the interpretation of the resistivity models derived from the MT data. A melt fraction is estimated from both the partial melt layer believed to be the APMB and a shallow (~5 km depth) magma storage region below Volcan Uturuncu. A synthesis with previous geophysical studies is important, and the interpretation of the resistivity models is constrained by comparison with the seismic velocity models and geodetic models. In particular, comparison with seismic velocity models leads to the question of whether the APMB is a layered magma body, with a silica-rich top layer, whereas viscosity calculations are used to compare several proposed geodynamic models.

In **Chapter 8** a summary of the thesis is presented and a consistent model is developed. A number of final conclusions are presented, followed by a discussion of future and unfinished work.

CHAPTER 2: TECTONICS AND VOLCANISM OF THE CENTRAL ANDES

2.1 Introduction

The Andes mountain chain is located above a convergent plate boundary, and is one of the longest mountain chains on Earth, extending for 9,000 km along the western edge of the South American continent (see Cahill and Isacks, 1992). In this chapter the tectonic setting and geological history of the Andes are discussed, with a particular focus on the study area in the Central Andes: the Altiplano-Puna Volcanic Complex (APVC). Volcano eruption magnitudes and frequencies are discussed as well as magma dynamics within the crust. The APVC is described and petrological and geochemical signatures of the ignimbrites erupted within the APVC are discussed.

2.2 Tectonics of the Andes

2.2.1 Tectonic Setting

The Andean subduction zone is a convergent plate boundary, where the oceanic Nazca plate subducts beneath the continental South American plate (Cahill and Isacks, 1992). The current plate convergence rate in the Andes is approximately 9 cm/year, although some variation occurs along the length of the Andes (Ramos, 1999). The convergence rate has changed over time, ranging from ~5 cm/year to ~20 cm/year from 35-10 million years ago (Ma) and dropping to ~10 cm/year over the past 10 million years (m.y.) (e.g., De Celles et al., 2015). The Andes are the classic example of a strongly coupled subduction zone (Cahill and Isacks, 1992), where subducting plate motion causes compression and deformation of the overriding plate (i.e., in the Andes and sub-Andean ranges). This situation is in contrast to a weakly coupled subduction zones, where trench roll-back creates extension and back-arc spreading (e.g., the Japan Sea). The Andes are located above the subduction zone and have been built and uplifted by a range of

processes that include crustal thickening, magmatic addition, and lithospheric delamination (e.g., Isacks, 1988; Francis and Hawkesworth, 1994; Beck et al., 2014) (see Section 2.3.3 for details).

2.2.2 Main Geological Subdivisions of the Andes

The surface geology of the Andes can be separated into a number of major across-strike divisions (i.e., west-east) (Allmendinger et al., 1997) as shown in Figure 2.1. The fore-arc region consists of the area between the oceanic trench, which is sediment-poor in the Central Andes (e.g., von Huene et al., 1997), and the volcanic arc. The Western Cordillera (WC) corresponds to the location of the present day volcanic arc, while the Eastern Cordillera (EC) lies farther east and is a deformation zone characterized by large thrust faults (Allmendinger et al., 1997). The Sub-Andean ranges are a fold and thrust belt, where Andean deformation occurs today. Further east is the undeformed craton of the South American continent, which consists of a number of joined cratonic blocks (such as the Amazonian craton, the Sao Francisco craton, the Paranapanema craton, the Rio de La Plata craton, etc.), which were joined throughout the Proterozoic (Peri et al., 2015; Cordani et al., 2003).

The Andes show along-strike variations (i.e., north-south); see Section 2.2.3 for further details. The Central Andes, which is approximately between 15ºS and 30ºS (e.g., de Silva and Francis, 1991), contain the Altiplano-Puna high plateau between the WC and the EC, see Figure 2.1. The center of this flat, high altitude plateau is covered by several large salars (salt flats or evaporated lakes), evidence of past and present internal drainage within the plateau (Allmendinger et al., 1997). The southern end of this region is characterized by very large silicic eruptions east of the modern volcanic arc over the past 10 m.y. that have formed extensive ignimbrite sheets (Allmendinger et al., 1997). More detail on the Altiplano-Puna plateau, the main study area in this thesis, is given in Section 2.2.5.

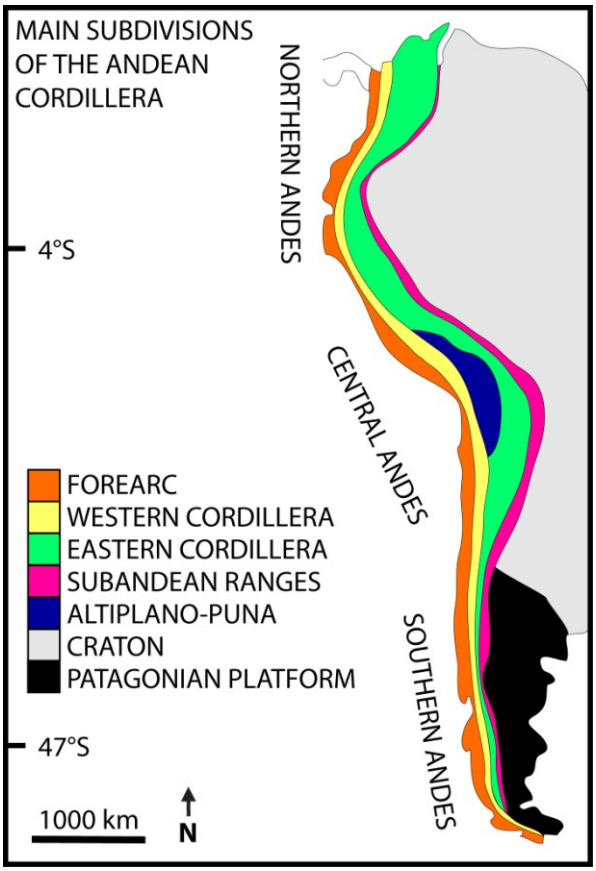

Figure 2.1: Simplified schematic of the main subdivisions of the Andean Cordillera. *(Figure adapted from Ramos, 1988).*

2.2.3 Volcano Distribution and Slab Subduction Angle

The present-day volcanic arc of the Andes shows significant along-strike variations. Active volcanism in the Andes occurs in three distinct zones at the present, separated by gaps of no volcanic activity. The areas of active volcanism are the Northern Volcanic Zone, the Central Volcanic Zone, and the Southern Volcanic Zone. Gaps of volcanic activity are caused by variations in the dip angle of the downgoing Nazca plate. In areas where volcanic activity occurs, the plate subducts at angles of about 30º in the upper 100 km, whereas in areas where volcanism is absent flat-slab subduction occurs, with dip angles of less than 5º (e.g., Cahill and Isacks, 1992). Figure 2.2 shows the distribution of present-day volcanoes in the Andes and the depth

contours to the subducting slab. Cross-sections show the slab geometry for flat slabs (Panels 1 and 3) and for a dipping slab (Panel 2). In the areas with flat-slab subduction the plate descends to a depth of ~100 km, then flattens (dip angle 0º-5º) (Cahill and Isacks, 1992). After continuing eastward for 200-300 km, the slab steepens to an angle of 30º and continues to descend (see Figure 2.2). These volcanic gaps in flat-slab regions occur because subduction zone volcanism requires the downgoing slab to sink to a depth of approximately 100 km, where metamorphic dewatering of minerals (prograde reactions) in the oceanic slab causes partial melting in the overlying mantle wedge by lowering the melting temperature of the mantle rocks (e.g., Gill, 1981; Stern, 2002; Lowrie, 2004). The resulting magma then rises buoyantly, differentiating along the way, to form the volcanic arc at the surface. This process does not occur when the slab subducts at low angles because a high enough temperature is not attained in the mantle wedge for metamorphism, halting fluid ascent through the mantle (e.g., Ramos and Folguera, 2009).

Current estimates suggest that 10% of modern subduction zones exhibit flat subduction (Gutscher et al., 2000; Skinner and Clayton, 2013). The geological record shows evidence of past flat subduction episodes in North America, where flat slab subduction occurred ~70 Ma during the Laramide orogeny (Humphreys et al., 2003), followed by the steepening of the slab in the middle Cenozoic (~40 Ma), which caused ignimbrite eruptions in the western United States (De Celles et al., 2009). Thus flat flab subduction is not unusual, and a cyclical model of subduction zone dynamics is plausible, where crustal shortening, high-flux magmatic events, gravitational foundering of arc roots, and small slab angle changes occur cyclically on times scales of 20-40 m.y. (De Celles et al., 2009; De Celles et al., 2015). The cause of flat-slab subduction is not fully understood, but several mechanisms have been proposed, such as mantle wedge dynamics, the age of the subducting plate, and the thickness of the subducting plate (e.g., Skinner and Clayton, 2013). For example the subduction of ridges on the oceanic plate can force the slab upwards (Skinner and Clayton, 2013). Similarly, the subduction of a younger, more buoyant slab may shallow the subduction angle (e.g., Capitanio et al., 2011).

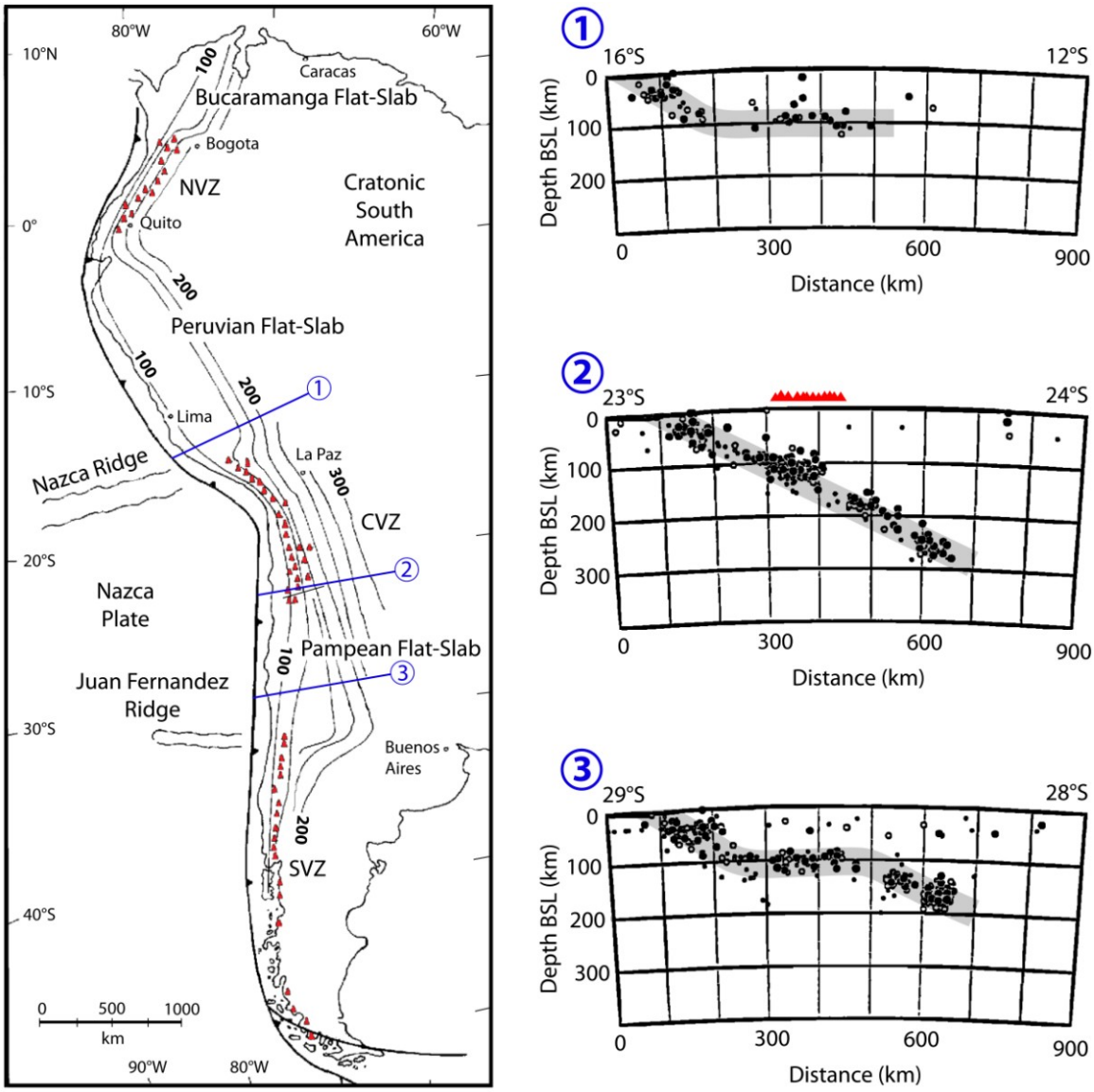

Figure 2.2: The present-day volcanoes of the Andes (red triangles) are distributed in several zones: NVZ - Northern Volcanic Zone; CVZ - Central Volcanic Zone; SVZ - Southern Volcanic Zone. The depth to the subducting slab is shown in 25 km contours (black lines). Flat-slab regions, as evidenced by the large spacing of the slab-depth contour lines, are found between the volcanic zones. Three cross-sections (Panels 1, 2, and 3) show the slab geometry at depth (grey band) from earthquake locations (black circles). Approximate positions of the cross-sections are drawn on the map for reference (blue lines). The location of the volcanic arc on Panel 2 is indicated with red triangles. *(Map adapted from Ramos, 1999; cross-sections adapted from Cahill and Isacks, 1992).*

2.2.4 The Bolivian Orocline

The Central Andes, located between latitudes of approximately 10°S and 30°S, shows a unique feature which is the concave bending of the Andean orogen, known as the Bolivian Orocline (e.g., Isacks, 1988). This is one of the few concave convergent margins on Earth (Capitanio et al., 2011), as most subduction zones show a convex margin, caused by the intersection of a flat plane into a spherical Earth. The bending of the orogen at this location may be related to the age of the subducting Nazca plate (Capitanio et al., 2011), because the extent to which the downgoing plate sinks into the mantle depends on its age and thickness. Capitanio et al. (2011) proposed that the older, denser (negatively buoyant), and thicker crust at the centre of the subducted plate (approximately latitude 18°S) causes trench rollback to be slowest there, leading to bending of the orogen. The plate's age at the trench also causes variations in the overriding plate thickness, which could help produce the cordillera's topography (Capitanio et al., 2011). In Figure 2.3, Panel A shows the correlation between the age of the subducting Nazca plate at the trench and the concave bending of the Bolivian Orocline, while Panel B compares the plate age with the plateau topography. Panel C shows a west-east section across the Central Andes, revealing the topography of the Altiplano-Puna plateau. Panel D shows the variation in crustal thickness across the Andes, and implies that the crust beneath the Altiplano is isostatically balanced (Beck et al., 1996; see Chapter 3 for more details).

Using GPS data from the Central Andes, Allmendinger et al. (2005) observed counter-clockwise rotation north of the Bolivian Orocline and clockwise rotation south of the Orocline at rates of ~0.4°-1.6°/m.y. These results matched values determined by paleomagnetic analyses of rocks 25 m.y. old and younger (Allmendinger et al., 2005). McQuarrie (2002) emphasised that the evolution of the Bolivian orocline is linked to the along-margin changes in crustal shortening observed, with ~500 km of crustal shortening observed north of latitude 23°S and only ~150 km of shortening south of 23°S. This difference in shortening rates is attributed to the oblique angle of plate convergence south of 23°S which inhibited deformation there, enhancing the Bolivian orocline over the past 50 m.y.

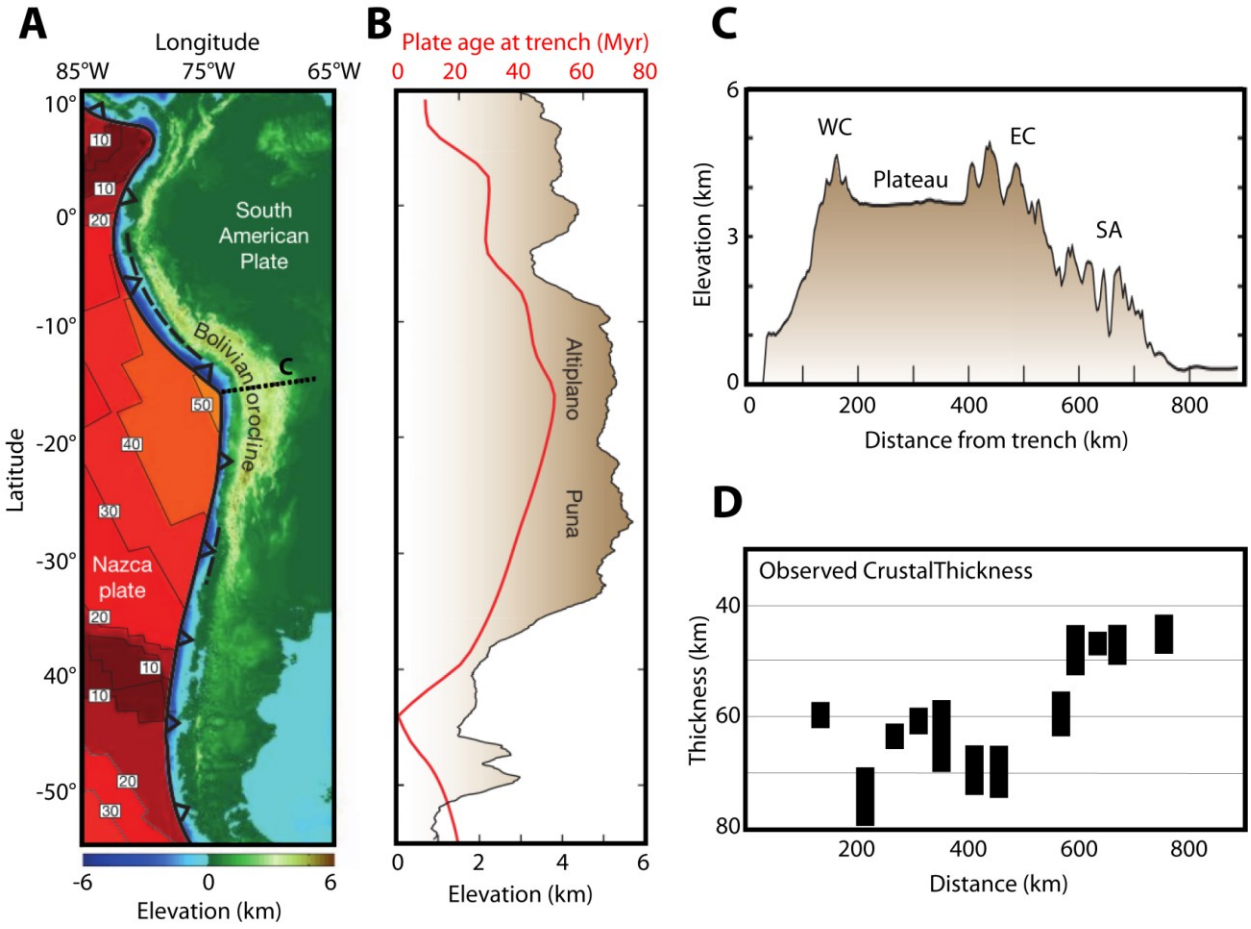

Figure 2.3: Panel A shows the topography of the Andes and the age of the subducting Nazca plate (in millions of years). Panel B shows that the age of the plate at the trench is correlated with the along-margin topography of the Andes. Panel C shows a cross-section across the Central Andes, the location of which is illustrated by the dashed line in panel A. WC - Western Cordillera; EC - Eastern Cordillera; SA - Sub-Andean Ranges. Panel D shows the variation in crustal thickness across the Andes. The thickest crust occurs below the Altiplano-Puna plateau, where it is 65 km thick on average. (*Panels A, B, and C adapted from Capitanio et al., 2011; Panel D adapted from Beck et al., 1996*).

2.2.5 The Altiplano-Puna Plateau

One obvious topographic feature of the Central Andes is the widening of the orogen between ~17º S and ~27º S. This region encompasses the Altiplano-Puna high plateau, which is one of the largest and most extensive high plateau on Earth, second only to the Tibetan plateau (Isacks, 1988; Allmendinger et al., 1997). High plateaux more commonly form in continent-continent collision zones, such as the Tibetan plateau or the East Anatolian plateau (e.g., Royden et al., 2008; Unsworth, 2010). A high plateau forming above a subduction zone is very unusual. In fact, this situation is found nowhere else on Earth today - surprising considering the 55,000 km of subduction zones on Earth (Stern, 2002). The Altiplano-Puna is a relatively flat plateau with an average elevation of over 4000 m. The crustal thickness below the plateau ranges from 50 km to a maximum of 75 km, with an average of 65 km (e.g., Beck et al., 1996; Beck and Zandt, 2002; Heit et al., 2008). A cross-section through the Altiplano-Puna plateau, the main study area in this thesis, can be seen in Panel C of Figure 2.3, highlighting the topography of the region.

This region of thickened crust and high elevation can be divided into two distinct sub-regions: the Altiplano in Bolivia and the Puna in northern Argentina and Chile. The exact location of the transition from the Altiplano to the Puna is debated, but is generally located between a latitude of 22°S and 23°S (e.g., Allmendinger et al., 1997; Coira et al., 1993). Several fundamental changes occur in the southward transition from the Altiplano to the Puna, the most significant being changes in lithospheric thickness and in crustal thickness (Allmendinger et al., 1997). The lithosphere thickness below the Altiplano is variable but is measured to be ~150 km thick on average, whereas below the Puna it is less than 100 km thick (McGlashan et al., 2008). The crustal thickness decreases southward, going from 60-75 km below the Altiplano to 50-60 km below the Puna (e.g., Yuan et al., 2002; McGlashan et al., 2008). On average, the elevation of the Puna plateau is ~500 m higher than the Altiplano, and has a more arid climate (Allmendinger et al., 1997). The Puna is also more mountainous, as it is deformed into a series of basins and ranges, giving it a rougher topography than the Altiplano (Allmendinger et al., 1997).

2.3 Temporal Evolution of the Andes

2.3.1 Early History

The supercontinent Pangea began to break up in the early Jurassic Period (~180 Ma) forming Laurasia and Gondwana. At that time, along the western margin of the Gondwana craton, terrane accretion was the dominant tectonic process (Ramos, 1988). In the early Cretaceous Period (~140 Ma) Gondwana separated into multiple continents, including the present day South American continent (along with Africa, Antarctica, India, and Australia) (White et al., 2013, and references therein). During the Cretaceous period (~100 Ma) the oceanic Farallon plate began to subduct below continental South America (Mai, 2006; Capitanio et al, 2011). By ~30 Ma the Farallon plate had fully fragmented into the Nazca plate to the south and the Cocos plate to the north (Lonsdale, 2005). Over the past ~100 m.y. the volcanic arc has experienced an eastward migration of up to 200 km, caused by tectonic erosion at the convergent margin (Mai, 2006, and references therein). Tectonic erosion removes material from the overriding plate in a subduction zone causing landward migration of the trench, and also of the magmatic arc (e.g., von Huene and Scholl, 1991; Currie et al., 2007). The eastward migration of the volcanic arc has allowed erosion to expose extinct volcanoes, some of which are associated with the large porphyry copper deposits found in Northern Chile (see Richards, 2011). Some of the world's largest and best producing porphyry copper mines are found in this region (Richards, 2011). Similar systems may be forming today below the volcanic arc and APVC.

2.3.2 Initiation of Subduction and Slab Geometry

The present plate configuration of the oceanic Nazca plate subducting below the continental South American Plate developed from the Eocene Epoch to the Oligocene Epoch (~45-27 Ma) (Mai, 2006; Capitanio et al., 2011), causing the development of the present day Andean mountain belt during the past 42 m.y. (Andes orogeny) (Ramos, 1988). The widening of the Eastern Cordillera and Bolivian orocline formation started around this time as well (Eocene, ~45 Ma) (e.g., Arriagada et al., 2008; McQuarrie, 2002). Uplift of the Altiplano-Puna plateau and

crustal thickening due to crustal shortening began in the late Oligocene Epoch (~25 Ma) (Allmendinger et al., 1997), although it may have begun as early as 40 Ma (McQuarrie, 2002).

One proposed scenario is that a rapid shallowing of the subducting Nazca slab occurred ~20 Ma below the Central Andes, which led to arc migration eastward and then to a cessation of magmatism altogether (e.g., Ramos and Folguera, 2009; Kay et al., 1994; Ramos et al., 2002). The sudden shallowing of the slab may have been caused by a rebound after slab breakoff due to eclogitization (Haschke et al., 2002), or by the subduction of an oceanic ridge beneath the continent, as occurred approximately 11-14 Ma as the Juan Fernandez ridge subducted near a latitude of 30°S, which is speculated to have caused the Chilean flat slab (e.g., Ramos and Folguera, 2009; Kay et al., 1994; Ramos et al., 2002). The downgoing slab began to steepen again 12 Ma, eventually achieving the angle of 30° we see today (Allmendinger et al., 1997; Ramos and Folguera). Intense volcanism commenced on the Altiplano 10 Ma and subsequent volcanism was progressively shifted towards the west (Allmendinger et al., 1997), to the Western Cordillera which now marks the present-day magmatic arc. This shift can be observed in the ages of volcanic deposits throughout the Altiplano-Puna plateau (such as the ignimbrite deposits of the APVC shown in Section 2.5). Figure 2.4 shows the significant events in the formation of the present-day Andes.

2.3.3 Plateau Uplift and Crustal Thickening

Allmendinger et al. (1997) suggested that the uplift of the Altiplano began approximately 25 Ma. This is temporally coincident with an increase in plate convergence rate and a shallowing of the subduction angle of the Nazca plate (Ramos, 1988). The Puna plateau uplift is thought to be younger than the Altiplano uplift, commencing 15 Ma (Allmendinger et al., 1997), although new isotopic evidence from Canavan et al. (2014) and Quade et al. (2015) shows that Puna uplift may have started as early as 36 Ma. The Altiplano plateau is believed to have attained about one quarter of its modern elevation by 20 Ma and one half of its modern elevation by 10 Ma (Gregory-Wodzicki, 2000), which implies about ~2000 m of uplift have occurred since 10 Ma. How was the Altiplano-Puna plateau uplifted? Possible mechanisms include contributions from

crustal shortening, magmatic addition to the crust, underplating of tectonically eroded forearc material, or lithospheric foundering (e.g., Allmendinger et al., 1997; Garzione et al., 2008).

The Altiplano-Puna plateau uplift correlates temporally and spatially with intense episodes of magmatism, showing that uplift was likely caused by the horizontal shortening of a thermally softened crust (Allmendinger et al., 1997). Isacks (1988) suggested that crustal shortening was the most important mechanism for crustal thickening of the central Andes plateau. However estimates of crustal shortening vary greatly and can be difficult to constrain (Allmendinger et al., 1997). Estimates place the total amount of crustal shortening in Bolivia (i.e., the Altiplano) at 190-320 km, which can account for only 65% - 80% of the observed crustal thickening (Allmendinger et al., 1997; Sheffels, 1990; Schmitz, 1994). Since 10 Ma crustal deformation occurred almost exclusively in the Sub-Andean ranges (Allmendinger and Gubbels, 1996), with two thirds of the total shortening coming from that area (Allmendinger et al., 1997). Crustal shortening in Northern Argentina (i.e., the Puna) is estimated to be much less, possibly only 75 km (Allmendinger et al., 1997). Therefore, one fifth to one third of the crustal thickness needs to be accounted for by processes other than crustal shortening, such as magmatic addition. Crustal flow may also be a viable mechanism for crustal thickening, as seen in Tibet (Rippe and Unsworth, 2010).

An intrusive to extrusive ratio (or plutonic to volcanic ratio) can be used to estimate the volume of a crustal magma chamber from its erupted material observed at the surface (de Silva and Gosnold, 2007). Using a typical intrusive to extrusive ratio of 1.5:1 Francis and Hawkesworth (1994) showed that magmatic addition since 15 Ma could only account for ~1.5% of the crustal thickness observed on the Altiplano. Other authors prefer a ratio of up to 5:1 for this region, given its high magmatic activity (de Silva and Gosnold, 2007; Bachmann et al., 2007). Recent seismic studies (Ward et al., 2014) find an intrusive to extrusive ratio as high as 35:1 for this area, showing previous estimates of the proportion of magmatic addition may have been drastic under-estimates. Using this new intrusive to extrusive ratio, magmatic addition could be responsible for one third of the crustal thickness required to explain the Altiplano.

Lithospheric thinning from delamination processes may also be responsible for the plateau uplift (Allmendinger et al., 1997). Heavier, thickened mantle lithosphere delaminates and sinks through the asthenosphere, thinning the lithosphere and causing crustal uplift due to the more buoyant (less dense) crustal lithosphere (Gregory-Wodzicki, 2000). Convective removal of continental lithosphere from gravitational instabilities and dripping of small high density anomalies have been proposed in the Central Andes (e.g., Ducea et al., 2013) and modelling results from Wang et al. (2015) support these ideas.

An alternate view for the rise of the Altiplano proposed by Lamb and Davis (2003) shows how climate change may be a possible cause. The Peru-Chile trench, located off the western coast of South America, is noticeably empty of sediments in the Central region (latitudes 12-28ºS), and this lack of sediments can be attributed to a lack of erosion in the region due to the arid climate. Lamb and Davis (2003) suggested this lack of sediments causes less lubrication on the subducting plate and creates stresses that can support and lift the Altiplano. Numerical experiments by Pysklywec (2006) showed that climate-controlled surface erosion and trench sedimentation in plate collision settings have an effect on lithosphere deformation.

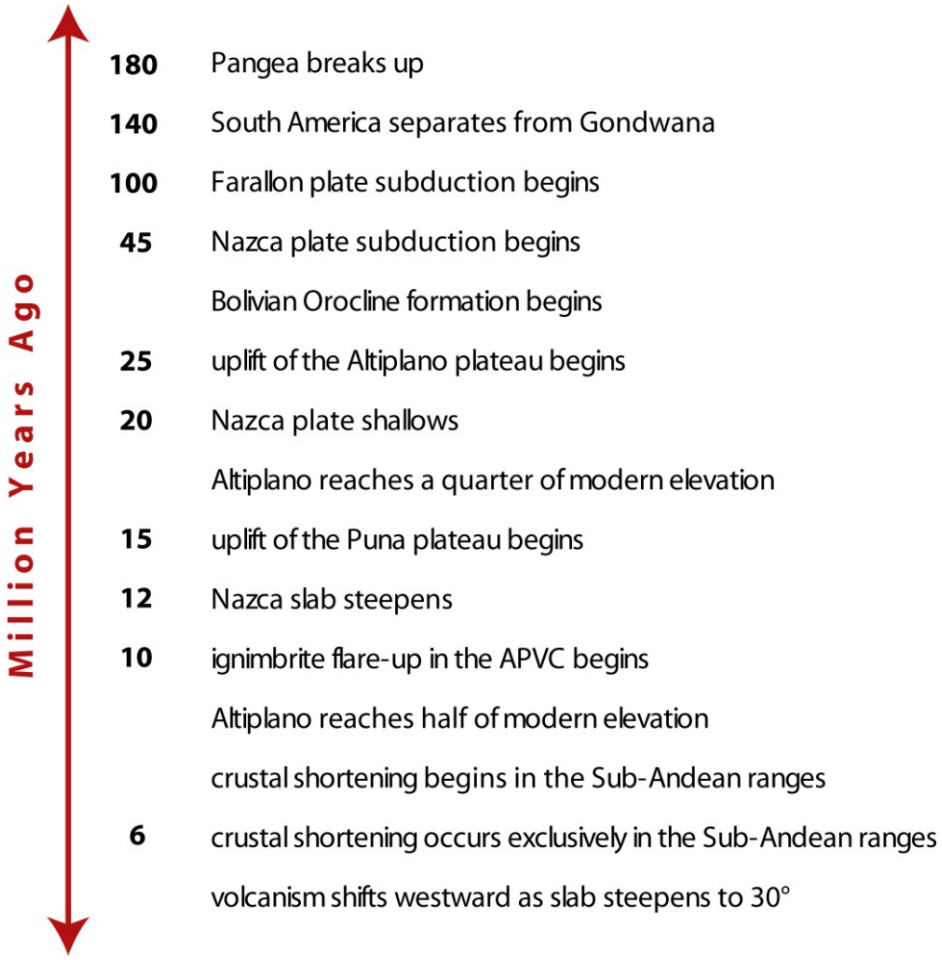

Figure 2.4: Timeline of significant events in the formation of the present-day Andes, see text for details.

2.4 Andean Magmatism

Over the last 10 m.y., in addition to volcanic arc magmatism, an intense episode of volcanism has occurred in the Southern Altiplano (de Silva, 1989; de Silva et al., 2006). This episode included many large caldera-forming eruptions, a number of which were super-volcanoes (a volcanic eruption that ejected a volume greater than 1000 km^3; see Section 2.4.1 for more details), that created large ignimbrite deposits (pyroclastic ash-flow; welded tuff), and which together define a large ignimbrite province known as the Altiplano-Puna Volcanic Complex

(APVC; de Silva, 1989). This section describes the Volcano Explosivity Index by which the magnitudes of volcanic eruptions are measured, and compares the super-volcano eruptions in the Central Andes since 10 Ma with others around the globe. In order to better understand the structure and evolution of the APVC and its calderas the processes of magma storage in the crust and the ascent mechanisms through the crust are discussed.

2.4.1 Eruption Size and Frequency

The Volcano Explosivity Index (VEI) (Newhall and Self, 1982) is a quantitative tool to compare eruption magnitudes based on multiple parameters (e.g., volume of ejecta, column height, qualitative description, duration, power, etc). The volume of ejecta erupted is the most important metric and is measured on a logarithmic scale as a dense-rock equivalent (DRE), for ease of comparison between different eruption styles. The scale ranges from 0 to 8, with VEI of 5 equal to 1 km^3 of DRE ejecta or more, a VEI of 6 equal to 10 km^3 of DRE ejecta, etc. The largest known volcanic eruptions, from volcanoes known as super-volcanoes, have a VEI of 8, quantified as an ejected volume greater than 1000 km^3 in a single eruption. To put this in perspective, the 1980 Mt. St. Helens eruption had a VEI of 5, and the Krakatoa eruption in 1883 had a VEI of 6 (Newhall and Self, 1982). Figure 2.5 shows a graphical illustration of the VEI scale and gives some examples of known eruption magnitudes.

It is normally assumed that eruption size is inversely correlated with eruption frequency, and this is generally true. However Caricchi et al. (2014) have shown that the distinction between super-volcanoes and smaller eruptions is more complex than just the difference in ejecta volume - the eruption mechanisms are distinct. Caricchi et al. (2014) showed that smaller eruptions can be triggered by an injection of new magma into a magma chamber, while super-eruptions are triggered only by the magma buoyancy once the chamber grows too large. In fact these chambers may accumulate magma for a million years without erupting (Caricchi et al., 2014).

Mason et al. (2004) compiled a list of 42 known super-eruption events (VEI = 8) over the past 45 m.y. Of these, 19 occurred within the last 14 m.y, giving a rate of ~1.4 super-eruptions per

million years (over that time period). The list includes the large volcanic complexes of Taupo (27,000 years ago), Toba (74 ka and 790 ka), Yellowstone (5 events, 0.6-7 Ma), the California/Nevada region (5 events, 0.7-13 Ma), and the Central Andes (6 events, 2-9 Ma). Older events (25-45 Ma) include those in the southwestern United States (22 events), the Sierra Madre Occidental, and the Ethiopian plateau.

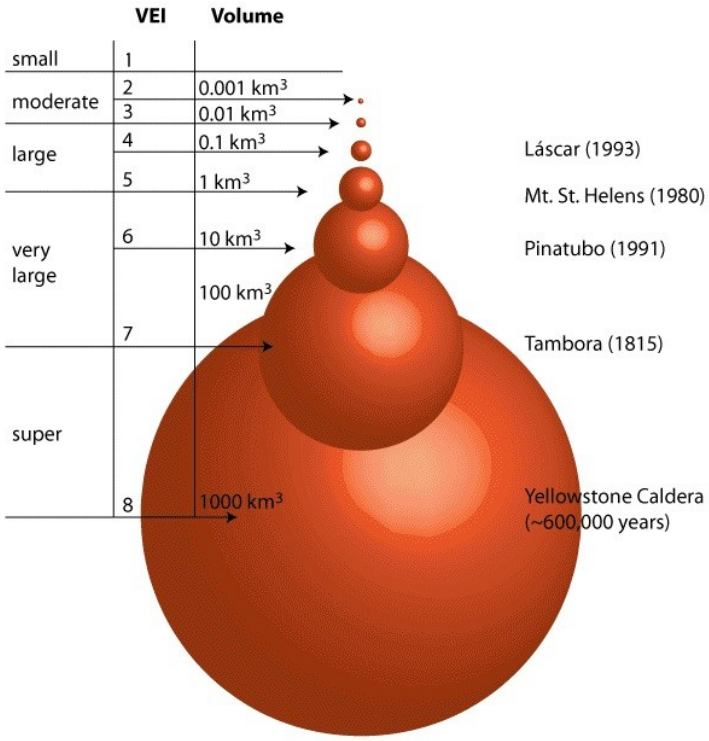

Figure 2.5: A graphical illustration of the Volcano Explosivity Index (Newhall and Self, 1982), with some examples of volcanic eruptions. (*Figure from http://plutons.science.oregonstate.edu/supervolcano).*

2.4.2 Magma Evolution and Distribution

In subduction settings, water released by the subducting oceanic plate lowers the melting point of the mantle wedge and creates melt (Annen et al., 2006). Basaltic magmas rise from the mantle

wedge and pool at the base of the crust where they have neutral buoyancy due to their density being equal to the density of crustal rock (see Zellmer and Annen, 2008). Here they may undergo differentiation to melts with a range of compositions from mafic to felsic, and melting of crustal rocks may also occur (Annen et al., 2006). Hildreth and Moorbath (1988) introduced the idea of a MASH zone in the lower crust, where melting, assimilation, storage, and homogenization occur, giving mantle-derived magmas a crustal signature. After differentiation at the base of the crust, more evolved, silica-rich magmas (e.g., andesitic) rise through the crust and can form magma reservoirs in the middle crust (Hildreth and Moorbath, 1988).

As the magma cools in the crust, certain minerals will crystallize at certain temperatures according to Bowen's reaction series (Bachmann and Bergantz, 2008). Within a magma reservoir compaction or gravitational separation by crystal settling can work to separate the higher density crystals from the melt, leading to successive enrichment of silica (SiO_2) in a magma as it ascends through the crust (Bachmann and Bergantz, 2008). Crystal separation within a magma reservoir is particularly efficient for a range of crystal fractions from ~45-65% per volume (Bachmann and Bergantz, 2008). Below this range convection currents stir the crystals, leaving them in suspension and creating homogenous magmas, while above this range only separation by compaction is possible (Bachmann and Bergantz, 2008; Bachmann and Bergantz, 2004). A magma reservoir may contain both eruptible magma, which has a crystal fraction of < 50% and is able to flow, as well as magma mush, which is a more rigid framework of linked crystals (Bachmann and Bergantz, 2008). Erupted volcanic rocks are therefore the liquid melt component from the magma reservoir, while the crystal-rich mush often stays within the reservoir and later crystallizes into a pluton (Bachmann et al., 2007).

Further evolution and separation in mid-crustal reservoirs cause evolved magmas to continue their ascent through the crust, often forming shallow pre-eruptive chambers below what will become a volcano or caldera. Bachmann and Bergantz (2008) found that most volcanic eruptions come from shallow chambers at depths of 4-10 km (pressures of 100-300 MPa). These shallow chambers commonly occur at the brittle-ductile transition zone (BDTZ), as it is an important strength transition within the crust (Sparks et al., 2008). The BDTZ marks the point where crustal rocks are warm enough to deform in a ductile manner, rather than break apart in a brittle

manner. Its depth varies based on the temperature of the crust and the composition of the crustal rocks (e.g., a depth of ~15 km for continental crust). Figure 2.6 shows a cross-section through the continental crust at a subduction zone illustrating how magma ascends from the mantle to the surface in a typical volcanic system.

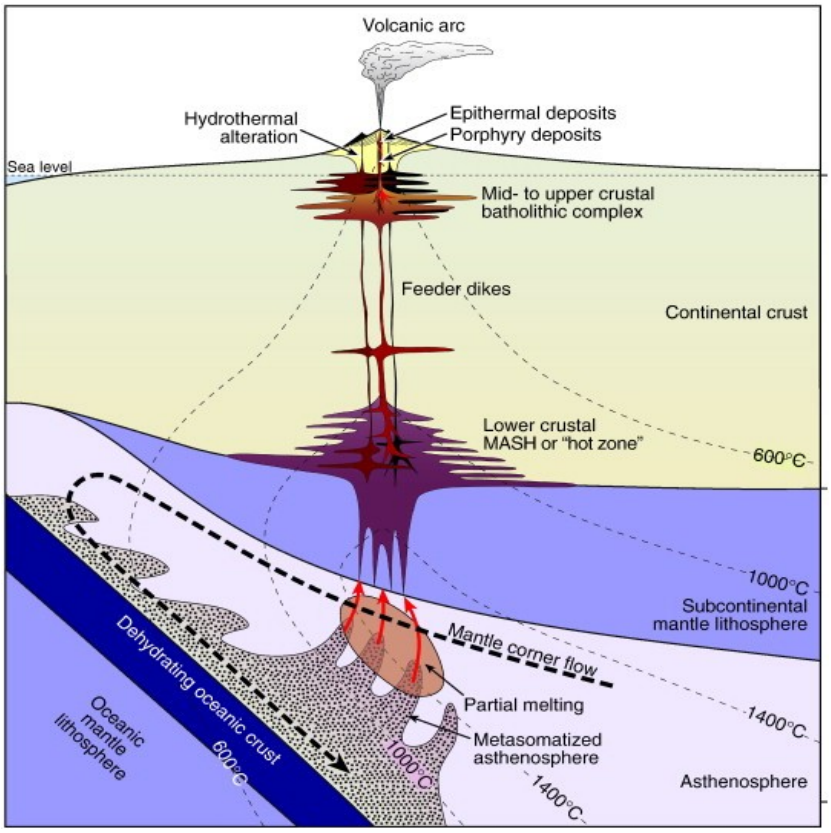

Figure 2.6: A schematic cross-section through the continental crust across a subduction zone showing a volcanic system. Basaltic magmas pool at the base of the crust where they differentiate and melt crustal rocks. More evolved andesitic magmas then rise to the middle crust forming batholiths complexes. Magmatic fluids continue to ascend through the crust and may form a shallow pre-eruptive chamber. *(From Richards, 2011).*

2.5 The Altiplano-Puna Volcanic Complex

The intense episode of silicic volcanism in the Southern Altiplano since 10 Ma, referred to as an ignimbrite flare-up, is responsible for creating a major volcanic province in the Central Volcanic Zone known as the Altiplano-Puna Volcanic Complex, or APVC (de Silva, 1989). The APVC, as defined by de Silva (1989), covers an area of more than 50,000 km^2 between the Bolivian Altiplano and the Atacama basin in Northern Chile (from latitudes of ~21ºS to ~24ºS), as shown in Figure 2.7. This is the one of the youngest and one of the largest ignimbrite provinces on Earth, with Taupo and Yellowstone being the only other known ignimbrite provinces with more than 10,000 km^3 of deposits within the past 10 m.y. (Mason et al., 2004).

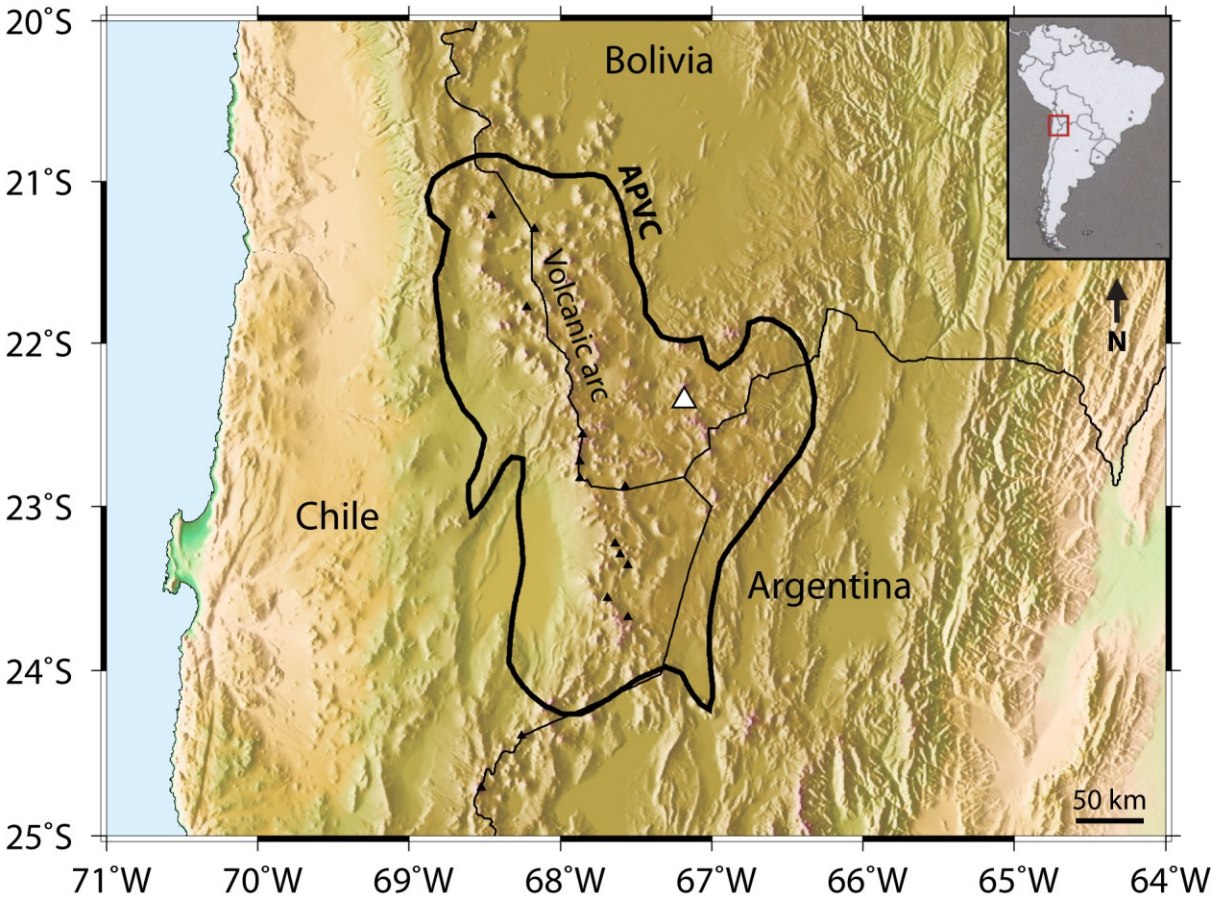

Figure 2.7: The Altiplano-Puna Volcanic Complex (APVC; de Silva, 1989) is a large ignimbrite province which covers an area of more than 50,000 km^2. Black triangles mark major volcanoes along the modern volcanic arc. White triangle marks the location of Volcan Uturuncu.

The timing and location of magmatism within the APVC is consistent with a subducting slab that steepened rapidly (e.g., Allmendinger et al, 1997) (see Section 2.3.2), although another possible cause may be a delamination event (Kay et al., 2010). The steepening of the subducting slab is thought to have increased the volume of the asthenospheric wedge and caused melting of the overlying mantle and crust (Kay, 2001). Ignimbrite flare-ups are transient events caused by a change in mantle magma productivity rates, as compared to background rates, and are often believed to be linked to changes in the slab angle (e.g., de Silva and Gosnold, 2007; De Celles et al., 2009; Ducea, 2001). The average magma extrusion rate of the APVC has been calculated to be 3,000 km^3/m.y. to 5,000 km^3/m.y., which appears to be consistent with typical supply rates for continental volcanic systems (de Silva and Gosnold, 2007). However, intrusion rates during active pulse episodes may be 5-10 times higher, and extrusion rates may be as high as 60,000 km^3/m.y. (2 m^3/s) (de Silva and Gosnold, 2007).

Large volcanic complexes, such as the APVC, contain an assemblage of caldera structures and volcanoes located close together, and are often nested or overlapping, representing multiple eruptions in both time and space. The location and dimensions of calderas at the surface can give us information about the plutonic structure below (de Silva and Gosnold, 2007). Careful geological mapping and sampling have revealed the distribution of many separate ignimbrite units spread across the APVC. The large caldera complexes dominating this region are thought to be the sources for these huge ignimbrite sheets, which have a minimum estimate of 10,000-15,000 km^3 (de Silva and Gosnold, 2007). Figure 2.8 shows a map of ignimbrite distributions throughout the APVC and their associated ages. A compilation of ignimbrite ages and volumes reveals that eruptions in the APVC began 10 Ma and occurred mostly in major pulses 8.4 Ma, 5.5 Ma, and 4.0 Ma, which may have each lasted 0.1-0.6 m.y. (Salisbury et al., 2010). A small and final fourth pulse is evident at 3.0 Ma. Four major events have occurred in the past 3 m.y. but have had minor contributions to the total volume ejected, as activity diminished. This implies the APVC has entered a waning stage (Salisbury et al., 2010). Previous temporal gaps in volcanism at the APVC have not been longer than 1.5 m.y. Figure 2.9 shows the cumulative erupted volume since 11 Ma for the APVC, as well as the eruptive volume and duration of each separate event shown in Figure 2.8. Figure 2.10 shows an example of the ignimbrite deposits of the APVC.

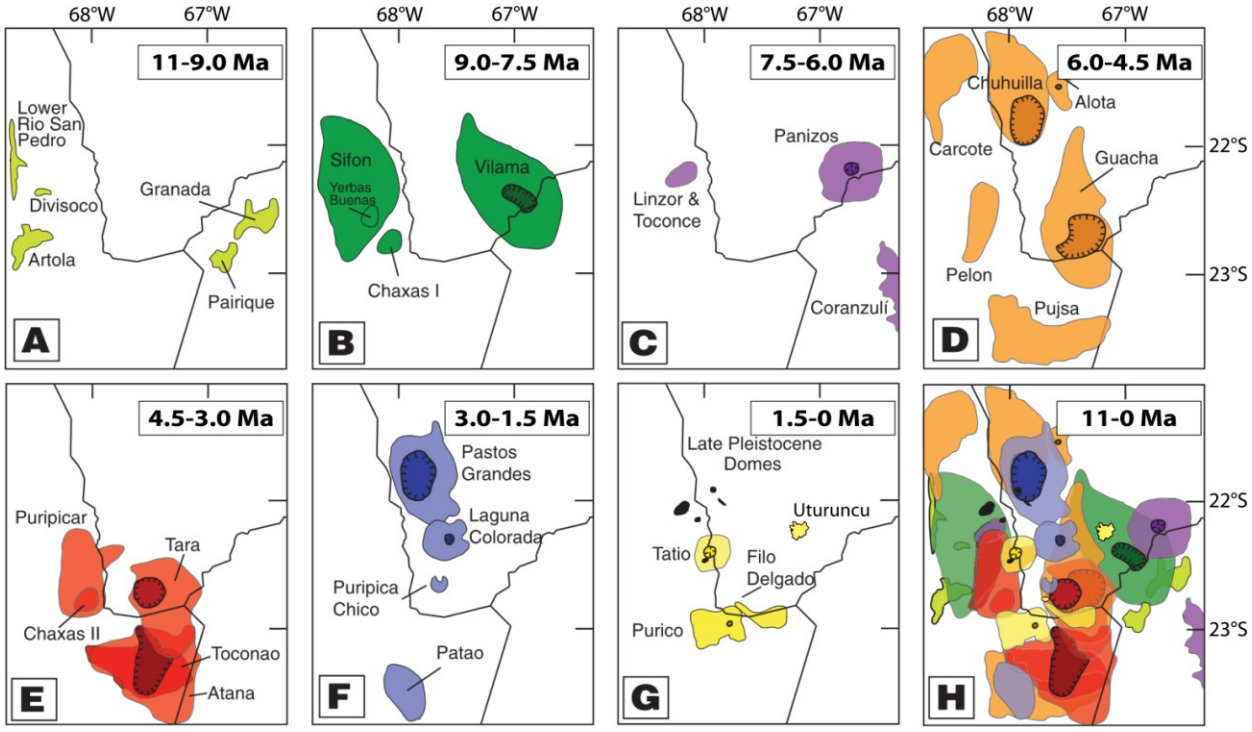

Figure 2.8: Ignimbrite units from the Altiplano-Puna Volcanic Complex (APVC) and their associated ages. Coloured areas show the ignimbrite distributions while darker areas show the inferred locations of their source calderas. The black lines represent the international borders, separating Bolivia (north), Chile (south-west), and Argentina (south-east). *(Adapted from Salisbury et al., 2010; Uturuncu lava deposits from Muir et al., 2015).*

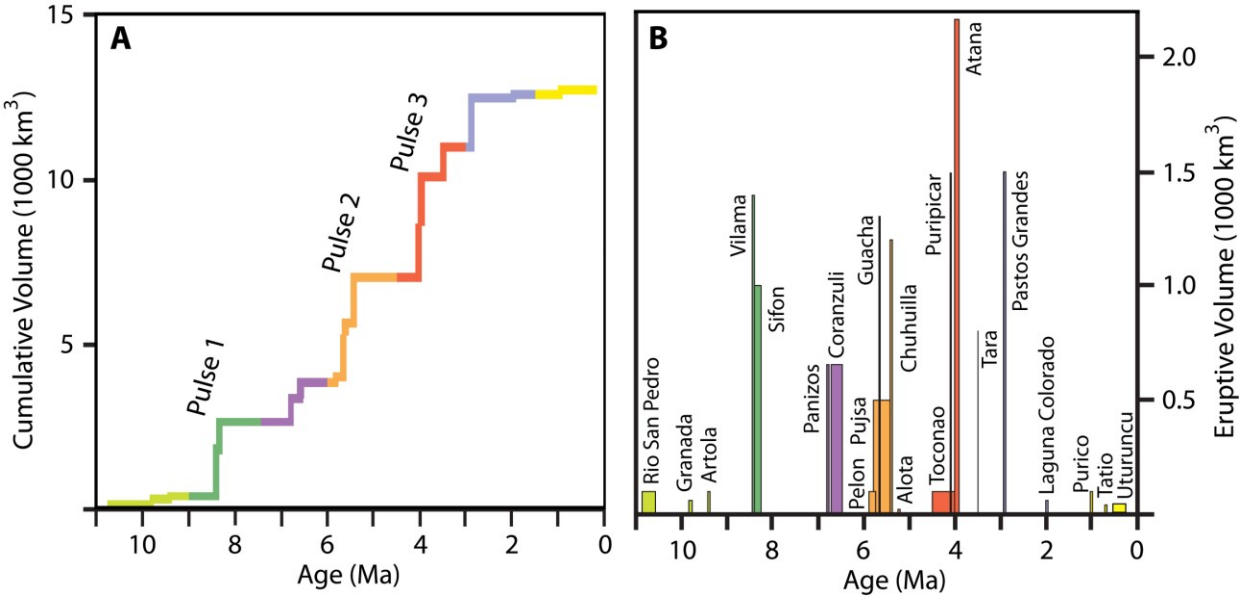

Figure 2.9: Panel A shows the cumulative erupted volume over the past 11 million years for the Altiplano-Puna Volcanic Complex (APVC). Three pulses of activity are visible, but during the last few million years the APVC has entered a waning stage. Panel B shows the eruptive volumes and duration of individual events. Colours match Figure 2.8, which shows the location of each event. *(Modified from Salisbury et al., 2010; Uturuncu data from Muir et al., 2015).*

Figure 2.10: Ignimbrite deposits of the Altiplano-Puna Volcanic Complex in Southern Bolivia. Photo taken November 12, 2011, from the village of Quetena Grande, looking south.

2.5.1 Ignimbrite Geochemical Signatures of the APVC

The ignimbrite deposits of the APVC show similar petrological and geochemical signatures, despite being formed by temporally and spatially separated eruptions. About 90% of the erupted magma from the APVC ignimbrite flare-up event is dacite (63-68% SiO_2), with 6% rhyodacite (68-72% SiO_2), 4% rhyolite (72%+ SiO_2), and < 0.5% andesite (57-63% SiO_2) (de Silva and Gosnold, 2007). Evidence from isotopes and trace element analysis shows that the ignimbrites require a minimum of 30% mantle-derived magma mixed with crustal melt from depths of 15-30 km (de Silva, 1989). The relatively homogenous composition implies that the ignimbrites were produced from the same large homogenous magma reservoir, which is presumed to underlie the APVC at a depth of ~20 km (e.g., Sparks et al, 2008; see Chapter 3).

Spatially separated ignimbrites likely erupted from different shallow pre-eruptive magma chambers below each caldera (de Silva and Gosnold, 2007). This explains the small variations in composition that are likely related to the evolution of the magma during its ascent through the crust to separate shallow magma chambers. At Volcan Uturuncu, dacite magmas appear to have erupted from depths of 4-8 km (110-220 MPa) (de Silva and Gosnold, 2007; Muir et al., 2014). The evidence suggests a multi-level model where mafic (45-52% SiO_2) mantle magmas pond and mix with crustal melts in a lower crustal MASH zone, then migrate as intermediate magmas (i.e., andesite, ~60% SiO_2) to the main magma reservoir (~20 km deep), evolving further to more silicic dacite melts (i.e., ~65% SiO_2) that accumulate pre-eruptively in shallow magma chambers (~5 km deep) below the volcanoes of the APVC (de Silva and Gosnold, 2007).

2.5.2 Volcan Uturuncu

Volcan Uturuncu (meaning Jaguar in the local indigenous language of Quechua) is a stratovolcano located near the middle of the APVC in Southern Bolivia, Sud Lipez Province, in the back-arc region, approximately 70 km from the current volcanic arc. Volcan Uturuncu has an elevation of 6008 m and a relief over the surrounding area of 1500-1800 m (Sparks et al., 2008), see Figure 2.11. The volcanic edifice sits on older erupted ignimbrites, mostly Vilama (8.4 Ma)

and Guacha (5.7 Ma) ignimbrites, from the APVC (Salisbury et al., 2011; Muir et al., 2015). Volcan Uturuncu has had six discrete periods of eruptive activity from 1.05 Ma to 0.25 Ma with lulls of 50,000-180,000 years (Muir et al., 2015). The long lull of 250,000 years since the last eruption remains unexplained. An eruptive timeline and cumulative erupted volume is shown in Figure 2.12.

Muir et al. (2015) noticed that, overall, erupted magmas from Volcan Uturuncu have consistent mineralogy over its entire 0.80 m.y. eruptive history, and comparable as well to the APVC. However, they found that both magnesium-rich and magnesium-poor andesitic magmas were erupted in parallel, implying that any magma mixing in the magma reservoir must have been localized such that discrete magma batches could co-exist. Muir et al. (2015) envision a model where several small magma reservoirs are repeatedly formed in the shallow crust (~4 km depth) beneath Volcan Uturuncu and successive eruptions from the same vent are tapping different parts of the magmatic system below. The authors propose that the magmatic system below Volcan Uturuncu is connected to the APMB via a vertical conduit of magma mush.

Figure 2.11: Volcan Uturuncu, located in Southern Bolivia, Sud Lipez Province, has an elevation of 6008 m and a relief over the surrounding area of 1500-1800 m. Photo taken October 31, 2010, 4 km north of the village of Quetena Chico, looking south-east.

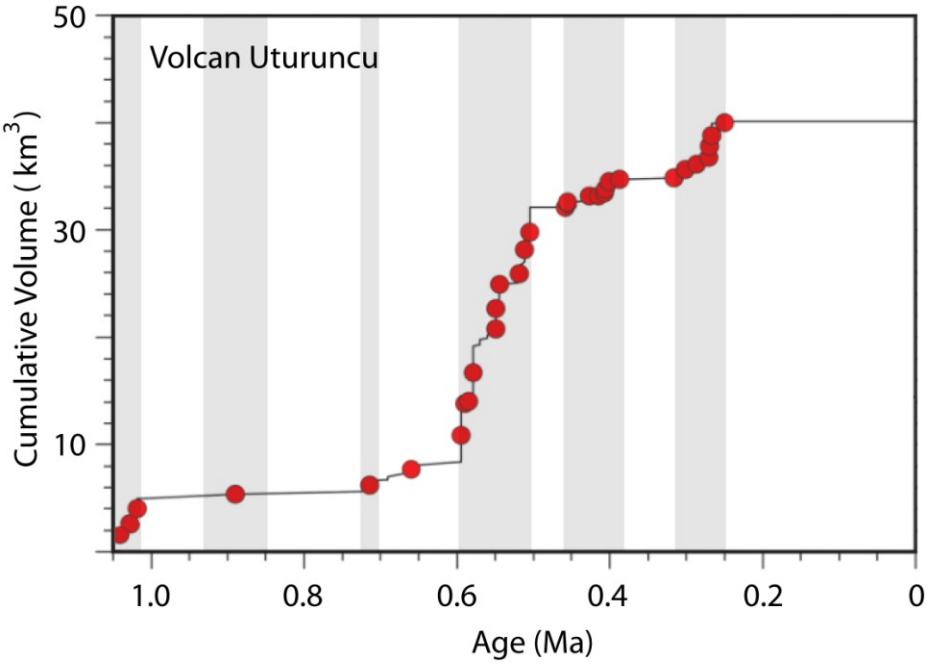

Figure 2.12: The cumulative erupted volume and eruptive history for Volcan Uturuncu. Six discrete pulses of activity are visible (grey bars), with lulls of 50-180 thousand years. *(Modified from Muir et al., 2015).*

2.6 Summary

The present-day Andean subduction zone, where the Nazca plate subducts beneath the South American plate, developed over the past 45 m.y. or more (Cahill and Isacks, 1992; Capitanio et al., 2011). Uplift of the Altiplano-Puna high plateau began later, about 25 Ma, temporally coincident with a shallowing of the subduction angle (Allmendinger et al., 1997; Ramos, 1988). The high elevation of the plateau (average of 4000 m) and the very thick crust (average of 65 km) can both be explained by crustal shortening and magmatic addition (e.g., Isacks, 1988; Allmendinger et al., 1997; Beck et al., 1996).

A steepening of the subducting slab at 10 Ma may have caused an ignimbrite flare-up, creating the large ignimbrite complex of the APVC (today located in the back-arc) (Allmendinger et al.,

1997). Intense volcanism continued for 8 m.y. and migrated westward as the downgoing slab continued to steepened to the angle of 30° observed today (de Silva and Gosnold, 2007; Allmendinger et al., 1997). This migration can be seen in the ages of the ignimbrite deposits of the APVC (Salisbury et al., 2010). Several of the eruptions caused by the ignimbrite flare-up had ejecta volumes of more than 1,000 km^3 and so are classified as VEI=8, or super-volcanoes. The large calderas observed at the surface and the geochemical analysis of the erupted ignimbrites give evidence for a large homogenous magma reservoir below the APVC at a depth of ~20 km, with multiple shallow magma chambers located beneath individual calderas or volcanoes which contain eruptible, evolved magma (e.g., de Silva and Gosnold, 2007; Sparks et al., 2008).

CHAPTER 3: PREVIOUS GEOPHYSICAL STUDIES

3.1 Introduction

This chapter describes previous geophysical studies of the Altiplano-Puna region and summarizes evidence for the existence of a large crustal magma body located below the Altiplano-Puna Volcanic Complex. The shapes, sizes, and depths of magma bodies are of interest to researchers studying both local volcanic systems and large-scale tectonic processes.

Both geological and geophysical studies can be used to study magma bodies and the processes that occur within them. Geological studies can be used to study ancient magma bodies once they are exposed at the surface by erosion, and geochemical analysis can be used to estimate temperatures and pressures at which the rocks were differentiated and crystallized (de Silva and Gosnold, 2007; Muir et al., 2014). In contrast, geophysical studies can give real-time constraints on current magmatic processes (Iyer, 1984). Seismic methods, electromagnetic methods, and gravity methods have all been shown to be able to image magma bodies (e.g., Schutt et al., 2008; Zhdanov et al., 2011; Kauahikaua et al., 2000). These geophysical methods generally use surface measurements to obtain information on the physical parameters of the subsurface, an often difficult task in volcanic environments, due to the complex terrain and hazardous environment. Geodetic techniques measure deformation at the surface of the Earth to infer what is occurring in the subsurface (e.g., Wicks et al., 2006; Pritchard, 2006). This can be done with remote sensing from a satellite (i.e., InSAR imaging) or with ground based GPS surveys. Using these techniques it is possible to measure how a magma body grows in size (or shrinks), and how it moves beneath the surface (Pritchard, 2006).

3.2 Seismic Studies of the Altiplano

Seismic waves propagate differently in regions of solid rock and in regions containing fluid or partial melt (i.e., slower velocity and higher attenuation in fluids; see sections below for more details) (Shearer, 2009), and can therefore be used to delineate crustal magma bodies. Seismic imaging of magma bodies has been successful in many cases, such as: the Socorro midcrustal magma body near Rio Grande, New Mexico (e.g., Sanford et al., 1977; Balch, 1997; Schlue et al., 1996), the magma body below the Long Valley Caldera in California (e.g., Steeples and Iyer, 1976), as well as the large magma body below Yellowstone (e.g., Evans, 1982; Chu et al., 2010; Farrell et al., 2014; Huang et al., 2015). In this section the physical principles of the seismic method are briefly reviewed and several seismic studies across the Altiplano are described.

Seismic energy produced from either natural sources, such as earthquakes, or from man-made controlled sources, such as explosions, travels through the Earth as seismic waves. The velocity of the wave depends on the density and rigidity of the medium through which it is traveling. Body waves (i.e., Primary waves and Secondary waves) travel through the Earth and are non-dispersive (i.e., the velocity is independent of the frequency of the wave), while surface waves (e.g., Rayleigh waves, Love waves) travel along the surface of the Earth and are dispersive (i.e., the velocity depends on the frequency of the wave) (Shearer, 2009). Primary waves (P-waves, travelling with velocity V_p) are compressional waves and travel the fastest, hence they are detected by a seismometer at the surface of the Earth as the first arrival. Secondary waves (S-waves, velocity V_s) are shear or transverse waves and travel slower through the Earth, arriving at the detector at a later time. The seismic technique measures the travel times and amplitudes of the waves as they arrive at the detector. From these times the seismic velocities can be inferred, and velocity anomalies can be determined (Shearer, 2009). The reflection coefficient can also be calculated based on the difference in seismic impedance (defined as the product of velocity and density) between two materials, helping to identify the location of anomalies in the subsurface (Shearer, 2009).

The velocity of a seismic body wave is related to the rock density, p, and to the Lamé parameters, μ and λ, which describe the elastic properties of the rock medium (i.e., stress-strain relation within a material) (Lowrie, 2004; Shearer, 2009), and can be written as,

$$V_p = \sqrt{\frac{\mu + \lambda}{p}} \text{ , and} \quad \text{(Eq. 3.1)}$$

$$V_s = \sqrt{\frac{\mu}{p}} \ . \quad \text{(Eq. 3.2)}$$

Therefore the ratio of compressional wave velocity to shear wave velocity, V_p/V_s, can give information about the elastic properties of the rock independent of density, and can help to interpret the rock type. Poisson's ratio, defined as the ratio of lateral contraction to longitudinal extension of a rock, can be computed from the V_p/V_s ratio, and is a good tool in identifying fluid type (Lowrie, 2004; Pickett, 1963). Poisson's ratio (ν), in terms of V_p and V_s, can be written as,

$$\nu = \frac{(V_p/V_s)^2 - 2}{2 \cdot (V_p/V_s)^2 - 2} \ . \quad \text{(Eq. 3.3)}$$

Poisson' s ratio ranges from 0 to 0.5, with the maximum value reached as V_s approaches zero. Shear waves cannot propagate in a fluid (Shearer, 2009), and so a high V_p/V_s ratio (above ~1.73) and high Poisson's ratio indicates fluid content. Average values for Poisson's ratio in continental crust range from 0.23 to 0.29 (Zandt and Ammon, 1995).

3.2.1 First Seismic Studies of the Altiplano

Early seismic refraction profiles across the western Altiplano found that the middle crust was characterized by a low-velocity zone (LVZ) at depth of 10-20 km below the surface (Wigger et al., 1994). However these early studies used a broad station spacing (~16 km) and could not

resolve small scale lateral variations in the velocity structure. Other seismic networks showed that a crustal thicknesses of up to 75 km existed below the Altiplano (e.g., Beck et al., 1996; Yuan et al., 2002; Beck and Zandt, 2002). The first seismic study to produce high-resolution images across the extent of the Altiplano and the convergent continental margin was the Andean Continental Research Project (ANCORP; ANCORP Group, 2003). In 1996, ANCORP recorded a 400 km long seismic profile at a latitude of 21°S, across the Bolivian Altiplano and Northern Chile to the Pacific Ocean. This profile had reflection and refraction components with shots located every 6 km, and a passive component with earthquakes measured for several months. The aim was to image the subduction zone, as well as to provide insights into crustal thickening and plateau formation.

Figure 3.1 shows the location of the ANCORP study. Seismometer locations, MT station locations (see Section 3.3), and epicenters of earthquake used as sources are shown. The spatial limits of the APVC are also shown (de Silva, 1989). The ANCORP project found an increased reflectivity and a low-velocity zone beneath the Altiplano at depths of 15-35 km BSL. P-wave velocities ranged from 3.6-6.5 km/s, and V_p/V_s ratios (a good indicator of fluid content) above 1.85 were found (implying a high Poisson's ratio of ~0.3) (Schurr, 2000; Yuan et al., 2002). The results were interpreted as evidence for widespread partial melting of the plateau crust (ANCORP Group, 2003).

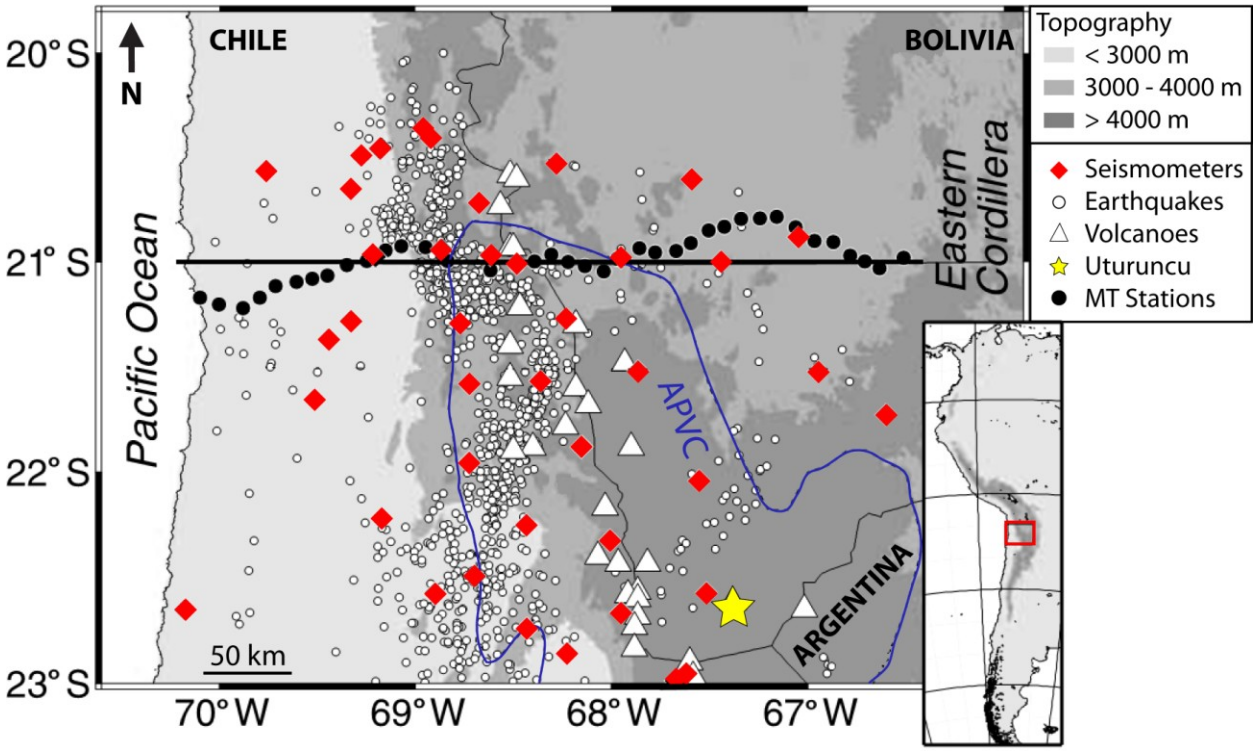

Figure 3.1: The ANCORP profile (bold black line) extended across the Altiplano, at 21°S. Red diamonds mark the seismometer locations and white circles mark the earthquake epicenters used in the tomography analysis. Magnetotelluric stations are marked as black circles. Volcanoes are marked with white triangles; Volcan Uturuncu is marked with a gold star. Blue line shows the Altiplano-Puna Volcanic Complex (de Silva, 1989). (*Adapted from Haberland et al., 2003*).

3.2.2 Seismic Attenuation Tomography

It is possible to measure the intrinsic attenuation (or energy intensity loss) of a seismic wave as it propagates through a medium (Thurber, 1993). The seismic quality factor Q, which is inversely proportional to the amount of attenuation, quantifies the attenuation of the wave and can be expressed for both P-waves (Q_p) and S-waves (Q_s). Haberland et al. (2003) created attenuation tomographic images of the crust and upper mantle below the Bolivian Altiplano (along latitude 21ºS), as shown in Figure 3.2, using local earthquake data from the ANCORP seismological

network (see Figure 3.1 for location map). The results of this study showed that the midcrust beneath the Altiplano was characterized by very high attenuation, with Q_p values in some areas as low as 100. Other areas, such as the crustal forearc and descending Nazca plate had low attenuation, with Q_p values >500. Fluids are known to enhance seismic attenuation (e.g., Mavko, 1980; Rietbrock, 2011); therefore Haberland et al. (2003) concluded that the most likely cause of the low Q_p values observed in the Altiplano crust was partial melts. The area of high attenuation correlates directly with the low-velocity zone seen by other studies (e.g., ANCORP, 2003).

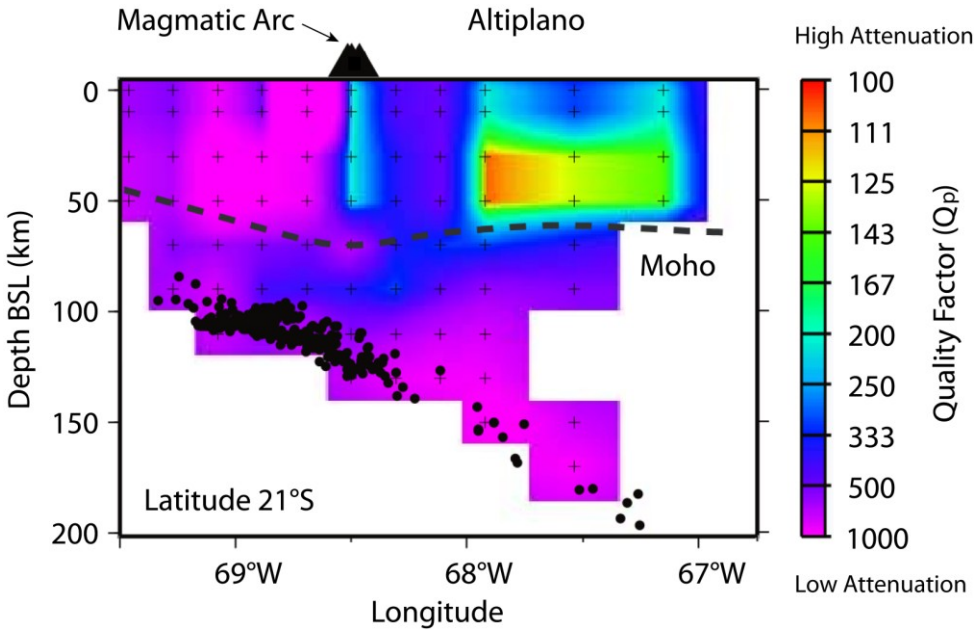

Figure 3.2: Attenuation tomography image along the ANCORP profile, latitude 21ºS. Low seismic quality factors (Q_p) indicate high attenuation. Earthquakes (black dots) mark the location of the subducting Nazca plate (Wadati-Benioff seismic zone). The dashed line indicates the Moho boundary, from Yuan et al. (2002). (*Adapted from Haberland et al., 2003*).

3.2.3 Receiver Function Analysis

The seismic receiver function method (RF) can be used to study crustal discontinuities in V_p and V_s (Langston, 1977). Seismic P-waves from distant earthquakes undergo a P-to-S conversion (Ps) at discontinuities below the seismometer, revealing information about what is directly below the station and not along the entire ray path. The travel-time difference between the direct P-wave and the converted S-wave (Ps), which travels slower and therefore arrives later, will give information about the Earth structure beneath the station, such as the distance to the discontinuity (Owens, 1987). The polarity of the Ps-wave arrival will be the same as the direct P-wave arrival when the conversion occurs as the wave passes from a higher velocity layer to a lower velocity layer (e.g., bottom of a LVZ), and a negative polarity will be observed when the conversion occurs as the wave passes from a lower velocity layer to a higher velocity layer (e.g., top of a LVZ) (Owens, 1987).

A receiver function study by Chmielowski et al. (1999) revealed a negative-polarity arrival ~2 s after the direct P-wave arrival for seismometer sites located in the southern Altiplano (from 22°S to 23°S; see Figure 3.3 for site locations). This was interpreted as a converted Ps-wave from the top of a low-velocity layer, at a depth of approximately 19 km below the surface (~14 km BSL). A positive-polarity Ps-wave was observed at 4-5 s, and was interpreted as the bottom of the low-velocity layer. Constraining both the top and bottom of the low-velocity layer allows its thickness to be calculated as ~0.81 km (assuming V_p = 3.0 km/s for the low-velocity layer) (Chmielowski et al., 1999). Modeling the resulting simple three-layer model as a thin low-velocity layer produced synthetic results that fit the observed receiver function data, both in arrival time and in amplitude (Chmielowski et al., 1999). The results were interpreted as a sill-like magma body located below the Altiplano, and it became known as the Altiplano-Puna Magma Body (APMB) (Chmielowski et al., 1999). The APMB was estimated to have a minimum area of 12,500 km^2 and possibly much more (Chmielowski et al., 1999). Realizing the significant spatial extent of the APMB, which likely underlies most of the APVC, this feature was identified as one of the largest known active continental crustal magma bodies. In comparison, the magma chamber detected below Yellowstone (~8 km depth) and the chamber

below Socorro (~19 km depth) have areas of less than 2,000 km^2 (Sheetz and Schlue, 1992; Farrell et al., 2014). New results from Huang et al. (2015) show that a deeper chamber exists below Yellowstone (~35 km depth) with an area of ~5,000 km^2.

Similar evidence for a midcrustal low-velocity layer was obtained by Beck and Zandt (2002) who carried out a receiver function study across the Central Andes with seismometers deployed approximately along latitude ~19.5°S (from approximately 60°W to 70°W longitude). The low-velocity layer was observed at multiple stations and could be traced across the entire west-east width of the Altiplano (from approximately 68°W to 65.75°W) at an estimated depth of 14-20 km below surface. No constraint on the thickness of the low-velocity layer was given; however the data show varying thicknesses of 6-15 km (Beck and Zandt, 2002). Beck and Zandt (2002) concluded that this may be a region of partial melt. Leidig and Zandt (2003) reached similar conclusions from their analysis but went a step further and modelled the upper crust as highly anisotropic. Their models show 10% - 20% anisotropy in the upper 15 km of the crust, with a dip angle of 45° from vertical and a strike direction of 30° - 60° for the slow direction (300° - 330° for the fast direction). Leidig and Zandt (2003) fit the receiver function data with a low velocity layer (Vs=1.0 km/s) at a depth of 14-17 km and a thickness of 1-2 km.

Zandt et al. (2003) significantly expanded the coverage of previous receiver function studies by compiling seismic data from multiple projects, including more than 100 seismometer locations. With such broad coverage (longitudes 70°W to 65°W, latitudes 20°S to 26°S; see Figure 3.3) it is possible to determine the lateral extent of the APMB. To distinguish between seismic sites that had detected the APMB and those that had not, Zandt et al. (2003) considered both the amplitude of the signal and its arrival time. If a negative-polarity conversion (top of the low-velocity layer) arrived ~2 s after the direct P-wave with an amplitude comparable to the direct P-wave, then this was taken as evidence for the presence of the APMB. If the amplitude was low (30% to 50% of the direct P-wave amplitude), then the presence of the APMB was considered ambiguous, or it was suggested that the seismic station was located on the edge of the APMB. For sites where either the amplitude was very low or where the signal did not arrive near ~2 s, the APMB was considered absent.

Figure 3.3 shows the inferred boundaries of the APMB from Zandt et al. (2003). The resulting map of the lateral extent of the APMB shows it covers ~60,000 km^2. An important observation is that the area of the APMB is closely correlated with the distribution of ignimbrite complexes of the APVC, rather than with the line of Quaternary arc volcanoes. This spatial correlation gives evidence that the APMB is associated with the magmatic plumbing of the APVC, rather than with that of the active arc volcanoes (Zandt et al., 2003).

As part of the PLUTONS project West et al. (2013) used a local network of seismic stations around Volcan Uturuncu (the network is within longitudes 68°W to 66.5°W, latitudes 21.5°S to 22.75°S) to carry out a receiver function study, and found a low-velocity layer at approximately 15 km depth BSL, with a thickness of ~20 km, as shown in Figure 3.4. Low P velocities but high Vp/Vs ratios led to the conclusion that the shear wave velocities were so low because of the presence of partial melt (West et al., 2013; McFarlin et al., 2014). A second low-velocity zone at a depth of 50-60 km was also observed, and may be a deeper magma source (McFarlin et al., 2014).

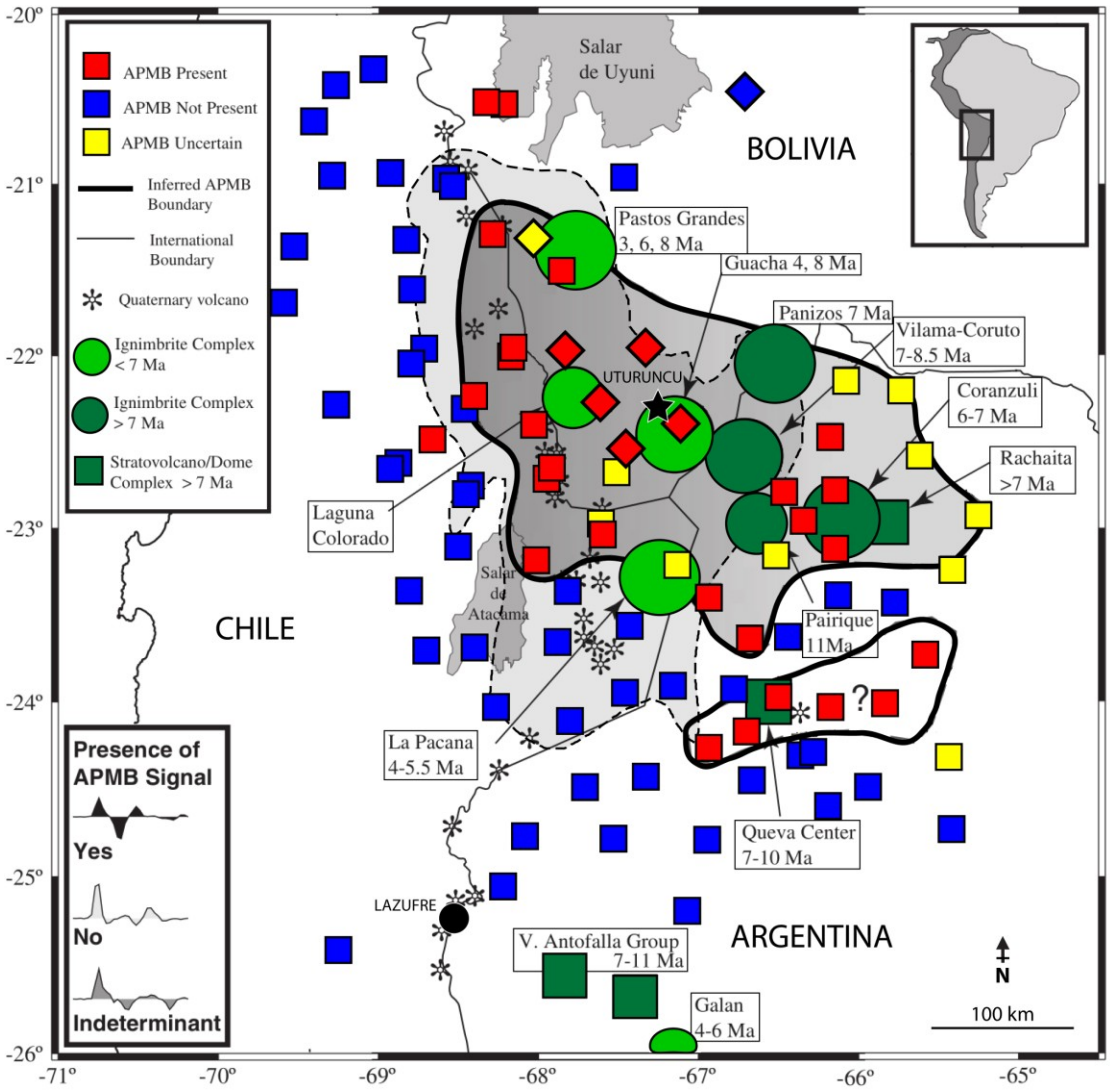

Figure 3.3: The spatial extent of the Altiplano-Puna Magma Body (APMB; bold black line) inferred from seismic receiver functions. Coloured squares mark the location of seismic stations used by Zandt et al. (2003); diamonds are the stations used in the study of Chmielowski et al. (1999). The colour corresponds to whether the APMB was detected below the station (red), was not detected (blue), or was indeterminate (yellow). Inset figure shows example P-wave arrivals, plotted as amplitude against time, used to determine the APMB location, see text for more details. Green circles and squares mark the location of major ignimbrite or volcanic complexes, which young towards the west. A dashed black line shows the Altiplano-Puna Volcanic Complex (de Silva, 1989), which overlaps with the APMB. Volcan Uturuncu is marked with a black star, near the centre of the APMB; Volcan Lazufre is marked with a black circle. Inset map shows the location in South America. (*Adapted from Zandt et al., 2003*).

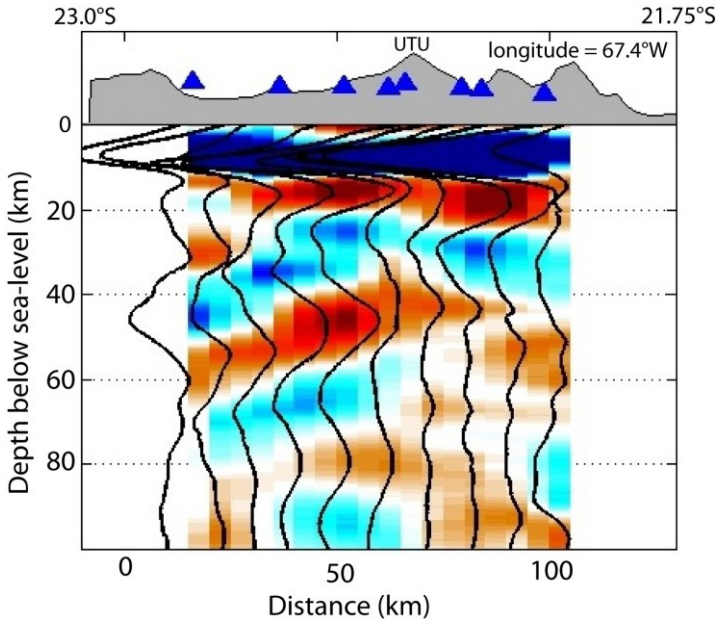

Figure 3.4: A receiver function analysis from a local network of seismic stations around Volcan Uturuncu reveal a low-velocity layer at approximately 15 km depth below sea-level. (*Modified from McFarlin et al., 2014*).

3.2.4 Ambient Noise Tomography

Ambient noise tomography (ANT) uses the correlation of seismic signals measured at two separate points to extract surface wave dispersion data (typically Rayleigh waves) along the path between them (Sabra et al., 2005; Shapiro et al., 2005). The surface wave velocities can then be inverted to give models of shear wave velocity (V_s). Because the surface waves are dispersive, both the wave velocity and the depth of penetration is dependent on the frequency of the wave, with lower frequencies having higher velocities and greater depth of penetration (Shearer, 2009).

Seismic data from various networks deployed from 1994 to 2012 have been combined to image the shear wave velocity structure of the Central Andes using the ANT method (Ward et al., 2013). A major mid-crustal low-velocity body was observed, with $V_s < 2$ km/s and background

velocities of ~3.5 km/s. At a depth of 15 km BSL the results show a regionally extensive low-velocity body (V_s < 2.75 km/s) coincident with the APMB. This was interpreted as a magma mush zone (Ward et al., 2013). Velocity model cross-sections show a broad region of low velocities (2.5 - 3.0 km/s) below the APVC, stretching from the surface down to 25 km BSL. Ward et al. (2014) expanded on this study by using a joint inversion of both Rayleigh wave dispersion from ANT and P-wave receiver functions from regional seismic stations (ANT+RF). Such a joint inversion of two complementary methods helps to overcome the limitations of each method. P-wave receiver functions are sensitive to velocity contrasts but less so to absolute velocity structure, while surface-wave dispersion is sensitive to the absolute velocity structure (Ward et al., 2014). However, surface-wave dispersion has a period-dependent sensitivity to structures which causes averaging over layered structures and produces smooth S-wave velocity models (Ward et al., 2014). This can be a problem where the vertical velocity varies rapidly over a short distance (e.g., in a sill-like magma body), causing a smooth vertically smeared region rather than a sharp interface.

Figure 3.5 shows the ANT and RF joint inversion velocity model of Ward et al. (2014). They observed a LVZ at depth of 5-25 km BSL (V_s < 3.0 km/s), with the lowest velocities located at a depth of ~15 km BSL, where velocities as low as 1.5 - 2.0 km/s were imaged. The LVZ is located at the centre of the APVC and coincides with the observed surface deformation pattern around Volcan Uturuncu (see Section 3.4; see Chapter 2). The top surface of the LVZ is undulating, with a slight upward bulge below Volcan Uturuncu, where the LVZ is thickest and shallowest (Ward et al., 2014). The LVZ bottom, defined as the 2.9 km/s velocity contour, is observed at a depth of ~20 km BSL, and the LVZ is no longer imaged at 25 km BSL and lower. Uncertainties in the depth to the LVZ are estimated as ± 2 km to the top, and +4/-1 km to the bottom. The bottom of the LVZ has greater uncertainty because it appears as a diffuse boundary, in comparison to the sharper boundary observed at the top of the LVZ (Ward et al., 2014). Ward et al. (2014) interpret the LVZ as a crystallized mush zone, because the non-zero shear wave velocity suggests that the anomaly is not fully fluid. The percentage of fluids and melts were interpreted to range from 10% for the area encompassed by the 2.9 km/s velocity contour to 25% for the area with the lowest velocities, < 2 km/s (Ward et al., 2014).

A problem with ANT is that this method is not sensitive to small-scale (< 10 km) vertical structures, and therefore shows one smooth and continuous LVZ. The velocity model images the long-wavelength structure of the APMB only, and smears the small scale features (e.g., a few kilometres). The smaller eruptions of the APVC were likely fed from regions of accumulated magma in the shallow crust derived from the deeper APMB storage region (see Hildreth, 1981), and this implies vertical melt transport and small scale vertical features, which the ANT method may not resolve.

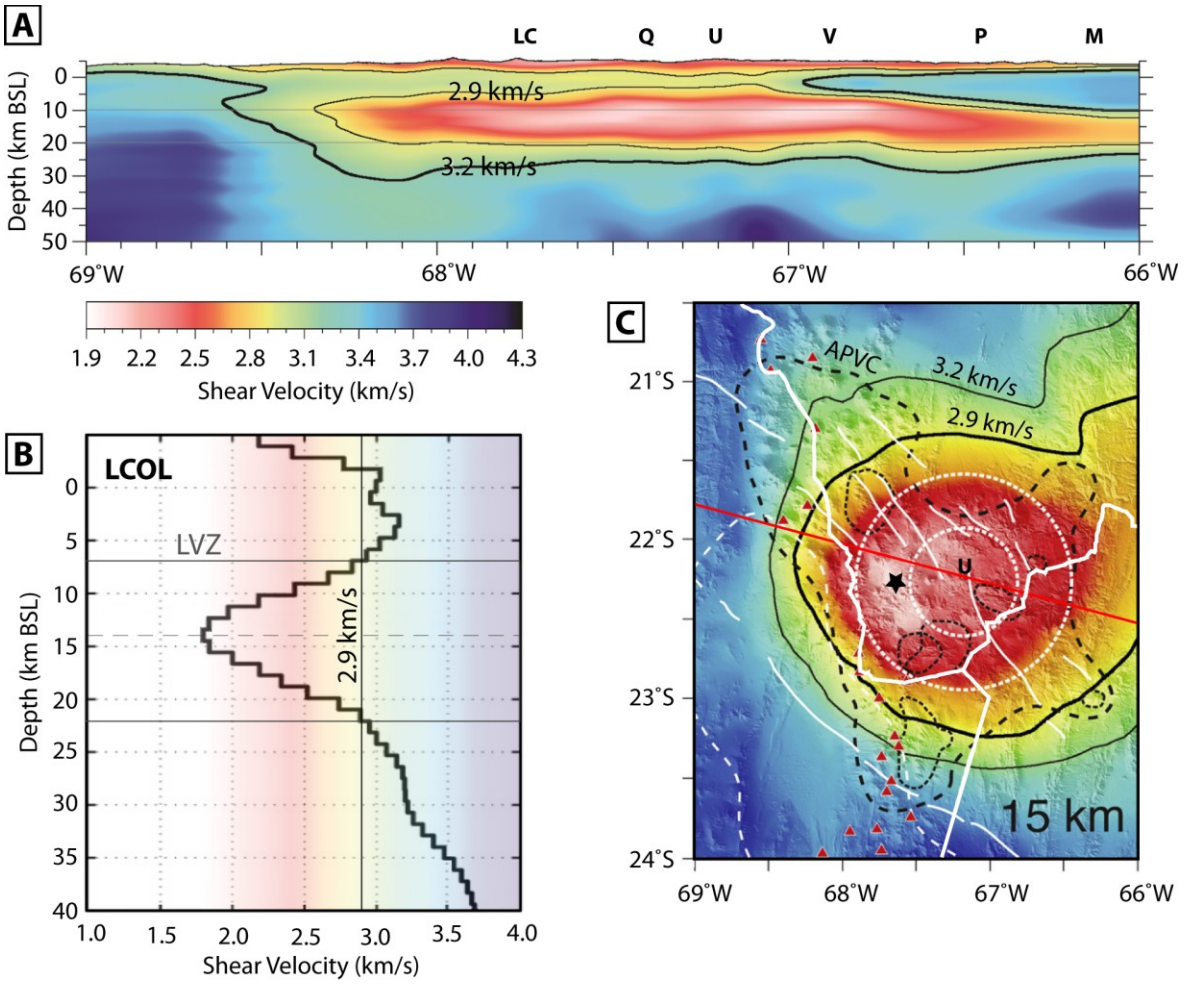

Figure 3.5: A shear-wave velocity model across the Altiplano-Puna Volcanic Complex and Volcan Uturuncu from the joint inversion of ambient noise tomography and receiver functions from Ward et al. (2014). Panel A shows a vertical cross-section through the model. The 2.9 km/s contour defines a large low-velocity zone, attributed to the Altiplano-Puna Magma Body, below Volcan Uturuncu. Locations referred to in the text are identified for reference (see Chapter 5 for more information): LC - Laguna Colorado; Q - Volcan Quetena; U - Volcan Uturuncu; V - Laguna Vilama; P - Mina Pirquitas; M - Mungayoc. The location of the cross-section is marked with a red line on Panel C. Panel B shows the model at one station (Laguna Colorado; LCOL), marked with a black star on Panel C. A low velocity zone (LVZ) is marked by the 2.9 km/s contour. Panel C shows a horizontal slice through the model at a depth of 15 km below sea-level. Black dashed line is the APVC, dotted lines mark large ignimbrite calderas. The observed surface deformation pattern (see Section 3.6) of uplift (inner white dashed circle) and subsidence (outer white dashed circle) are shown. (*Adapted from Ward et al., 2014*).

3.2.5 Magma Body Volume Constraints

Volcanic calderas at the surface of the Altiplano can give us information about the magmatic system below (de Silva and Gosnold, 2007). An intrusive to extrusive ratio (or plutonic to volcanic ratio) can be estimated, which compares the volume of magma in a reservoir to the volume erupted. Most researchers working in the Central Andes have proposed an intrusive to extrusive ratio of 1.5:1 or 3:1 (e.g., Francis and Hawkesworth, 1994; de Silva and Gosnold, 2007; see Section 2.3) for the APVC region. Ward et al. (2014) found a plutonic to volcanic ratio of 35:1, which, if correct, shows that previous magma volume estimates may have been under-estimated. A higher plutonic to volcanic ratio implies that a smaller fraction of magma is erupted, meaning large quantities of melt remain in the crust, where it solidifies to form intrusive rocks.

New constraints on the thickness and spatial extent of the APMB from seismic modeling give its volume as 500,000 km^3 ± 30% (Ward et al., 2014). This estimate is an order of magnitude larger than previous estimates, which gave a maximum volume of 60,000 km^3 for the plutonic zone beneath the APVC (de Silva and Gosnold, 2007). In comparison, at Yellowstone, which is generally considered to be one of the largest active volcanic complexes in the world, the lower crustal magma body, which is presumed to link a mantle plume with an upper-crustal reservoir, has been found to contain a volume of 46,000 km^3 (Huang et al., 2015). The Socorro magma body in New Mexico is presumed to have a volume of less than 1,000 km^3 (Sheetz and Schlue, 1992). The APMB has a truly enormous volume and cannot be a single molten magma body, as overpressure from magma buoyancy would cause the chamber to be emptied in an eruption (Malfait et al., 2014). Ward et al. (2014) suggest instead it may be a collection of smaller partial melt zones that were created sequentially over the 10 m.y. history of the APVC.

3.2.6 Shallow Seismicity Below Volcan Uturuncu

The Wadati–Benioff seismic zone is a region of deep seismicity associated with the down-going plate in a subduction zone (see Figure 3.2). The differential motion above and within the plate causes frequent earthquakes. Seismic methods that use passive earthquakes sources (such as those mentioned in the previous sections) often rely on deep earthquakes occurring in the downgoing Nazca plate. Another source of seismic activity is volcano-tectonic earthquakes that occur below volcanoes (Lahr et al., 1994). These earthquakes may occur due to stresses from the injection of magma into the crust and magma migration through the crust (e.g., dike propagation) (Roman and Cashman, 2006).

Jay et al. (2012) installed a local network of 15 seismometers around Volcan Uturuncu from 2009-2010 to study the shallow, volcano related seismicity. Figure 3.6 shows earthquake epicenter locations with their depths categorized by colour (Jay et al., 2012). The majority of earthquakes recorded occurred at depths at or above sea level (~5 km depth below surface). An average of 3 earthquakes per day (April 2009 to April 2010) were detected by Jay et al. (2012). The majority of the earthquake events recorded were in swarms; clusters of earthquakes with a small temporal separation (< 1 hour) and a small spatial separation (few kilometres). Swarms of up to 60 earthquakes occurred several times per month. Earthquake swarms are often seen in volcanic and hydrothermal areas (Stankova et al. 2008; Hill and Prejean 2005). Sparks et al. (2008) recorded an average of 62 earthquakes per day below Volcan Uturuncu at depths of 3-4 km below surface; however they only recorded for 6 days (April 1-6 2003), and this may have been during a swarm episode. The earthquake magnitude scale is a logarithmic scale that quantifies the amplitude of ground motion and energy released from earthquakes (see Ritcher, 1935). Most earthquakes events recorded by Jay et al. (2012) had magnitudes ranging from −1 to 1.5. The swarm events normally had higher magnitudes of up to 4.

Jay et al. (2012) compared the earthquake activity at Aleutian arc volcanoes to that found at Volcan Uturuncu. The authors found that although Uturuncu had ~200 events/year above a

magnitude of 0.9 from 2009-2010 (see Section 3.2.6), Okmok Volcano (last eruption 2008) had only ~85 events/year, Peulik (last eruption 1814) had only 30 events/year, and Westdahl (last eruption 1992) had less than 10 events/year. These Alaskan volcanoes also show ground deformation, but it varies with the eruption cycle, and inflation is not long-lived (~ a year) (Jay et al., 2012, and references therein). The authors concluded that although Uturuncu is dormant, and the Aleutian arc volcanoes examined are actively erupting, Uturuncu shows much more seismic activity than the others.

The APMB is similar to the Socorro Magma Body in New Mexico, because they are both defined seismically by receiver function studies as thin sills (< 1 km thick) and located at depths of 19 km below surface (e.g., Sheetz and Schlue, 1992; Chmielowski et al., 1999). Nine earthquake swarms have occurred at the Socorro Magma Body from 1980 to 2012, lasting from days to months, consisting of up to 500 earthquakes (Jay et al., 2012, and references therein). In comparison, at Uturuncu, above the APMB, swarms occur several times per month, but last for only hours, and may contain up to 60 earthquakes (Jay et al., 2012). Most earthquakes below Uturuncu occur above a depth of ~5 km below surface (Jay et al., 2012; see Section 3.2.6), about 10-15 km above the surface of the APMB; similarly at the Socorro most earthquakes are detected at a depth of 6-7 km below surface, about 12 km above the surface of the Socorro Magma Body (Stankova et al., 2008). The Yellowstone caldera shows significantly more seismicity than Uturuncu (an average of 1591 events/year above magnitude 1.1 from 1994 - 2011), but has comparable swarm activity, with swarms of 20 to 300 events occurring up to several times a month (Yellowstone Volcano Observatory online database, http://volcanoes.usgs.gov/volcanoes/yellowstone).

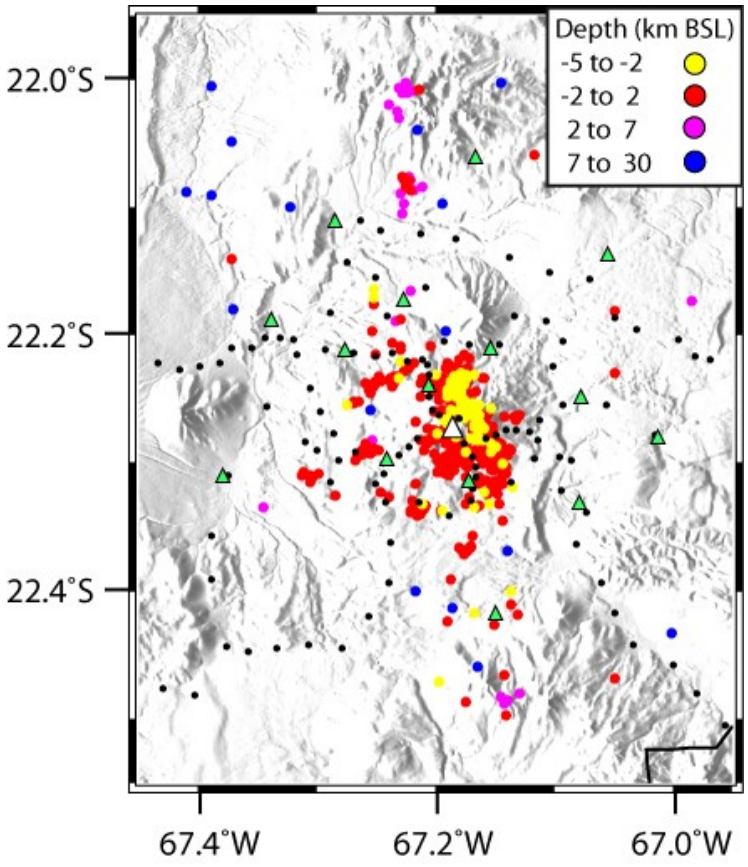

Figure 3.6: Earthquake locations recorded from 2009 to 2010 (Jay et al., 2012), with depth below sea-level colour coded. Most earthquakes occurred within the upper 7 km, and are located below Volcan Uturuncu (marked with white triangle). Green triangles indicate location of seismic receivers used.

3.2.7 Local Ambient Noise Tomography Study Below Volcan Uturuncu

A small scale ANT survey from the local seismometer network imaged a small low-velocity zone at a depth of -1 to -3 km BSL (2-4 km depth below surface) directly beneath Volcan Uturuncu (Jay et al., 2012), shown in Figure 3.7. The small low-velocity zone was spatially correlated with the observed earthquake locations. This small low-velocity zone was interpreted to be due to a shallow hydrothermal system beneath the volcano, and fumarolic activity observed

at the surface supports this hypothesis (Jay et al., 2012). Alternatively, petrological data from erupted dacites have inferred the existence a pre-eruptive magma storage location below Volcan Uturuncu at a similar depth (1.9-5.7 km below surface, 50-150 MPa) (Muir et al., 2014; de Silva and Gosnold, 2007).

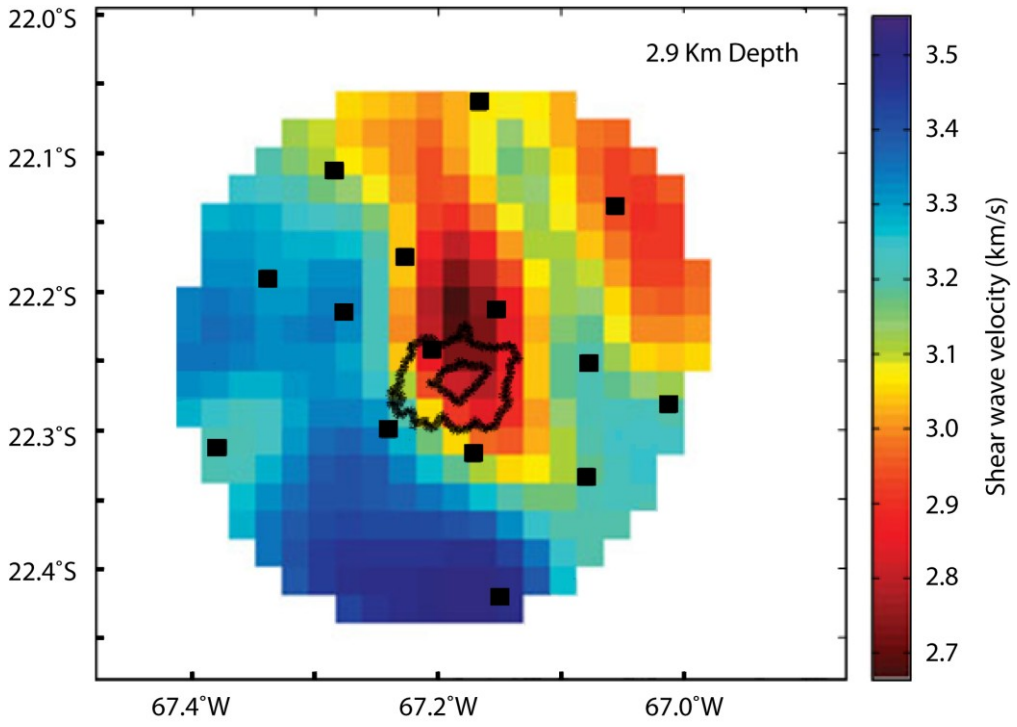

Figure 3.7: A depth slice through the seismic tomography model of Jay et al. (2012) derived from ambient noise in the area around Volcan Uturuncu (at centre). The model shows a small low-velocity zone (LVZ; red colours) directly beneath Volcan Uturuncu. This LVZ is spatially correlated with earthquake epicenter locations. Black squares are seismometers locations. Black lines mark the 5000 m and 5500 m topography contours and identify the location of Volcan Uturuncu. *(Modified from Jay et al., 2012).*

3.3 Magnetotelluric Studies of the Altiplano

The magnetotelluric (MT) method is a passive source technique that uses natural electromagnetic signals to define the electrical conductivity (Simpson and Bahr, 2005); see Chapter 4 for more details. Electrical conductivity is an important property because it is highly sensitive to the presence of fluids and partial melts, making MT a useful tool to map magma distribution within the crust (Chave and Jones, 2012). Several different materials besides partial melts can produce a low resistivity, such as aqueous fluids or clay from hydrothermal alteration (see Chapter 4).

Magnetotelluric imaging of crustal magma bodies has had success in revealing magma bodies below both ancient calderas and present day volcanoes (Newman et al., 1985), such as: the Socorro midcrustal magma body in New Mexico (e.g., Jiracek et al., 1987; Hermance and Neumann, 1990), the magma body below the Long Valley Caldera in California (e.g., Park and Torres-Verdin, 1988; Wannamaker et al., 1991), the large magma body below Yellowstone (Zhdanov et al., 2011), and a zone of partial melt below Mt. St. Helens (Hill et al., 2009). MT studies have also been used to focuse on the shallower aspects of volcanoes and geothermal fields, such as: Mt. Ruapehu (Ingham et al., 2009), Taupo geothermal field (Bertrand et al., 2012), Mt. Etna (Siniscalchi, 2012), and Iwate volcano (Aizawa, 2009).

3.3.1 Early MT Studies of the Altiplano

Throughout the 1980s a number of MT profiles were recorded in the Central Andes (Schwarz and Kruger, 1997; Schilling et al., 1997; Schwarz, 1994). Long-period MT data (100 - 10,000 s) were recorded at 9 sites in Bolivia's Lipez Province (22°S to 21°S, mostly North of Volcan Uturuncu); 15 other sites were collected farther east in Bolivia's Tarija region; 24 sites were collected in northwestern Argentina (24°S to 25°S); and 67 sites were collected in Chile (22°S to 24 °S). In general, the data was of poor quality, primarily due to noise. Figure 3.8 shows a map of the MT sites collected, as discussed by Schwarz and Kruger (1997). A 2-D electrical resistivity cross section through the Central Andes was created by joining several west-east

profiles together (ARC profile; Schwarz and Kruger, 1997); ARC-A along latitude 22.2°S in Chile and ARC-B and ARC-C along 21.3°S and 21.5°S in Bolivia. Figure 3.9 shows the 2-D resistivity model of the ARC profile from Schwarz and Kruger (1997). An extensive high conductivity zone (HCZ; resistivities < 2 Ωm) was detected below the Altiplano at a depth of ~20 km. The total conductance, the product of a layer's conductivity and its thickness, was found to be 23,000 S (Schwarz and Kruger, 1997). Schilling et al. (1997) noted that the thickness of the HCZ was not resolved well, but assumed a thickness of 40 km; their resistivity models show the HCZ below the Altiplano has a minimum of 10 km thickness. The HCZ anomaly was interpreted as being due to partially molten rocks, magmatic dykes, and magma chambers, and the melt fraction required to give the low resistivity values observed in the HCZ (0.5-1 Ωm) was estimated to be 14-27% melt by volume (Schilling et al., 1997).

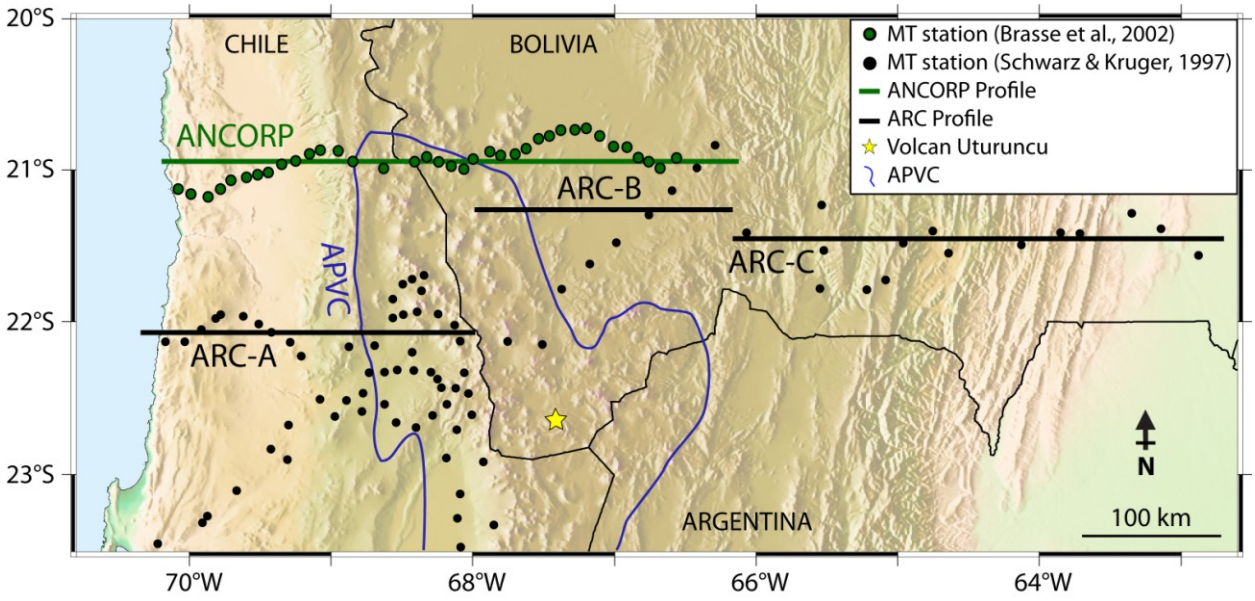

Figure 3.8: A map showing the location of magnetotelluric sites collected by Schwarz and Kruger (1997; black dots) along the ARC profile and by Brasse et al. (2002; green dots) along the ANCORP profile. The location of the APVC is marked for reference (blue line; de Silva, 1989). Volcan Uturuncu is marked with a gold star.

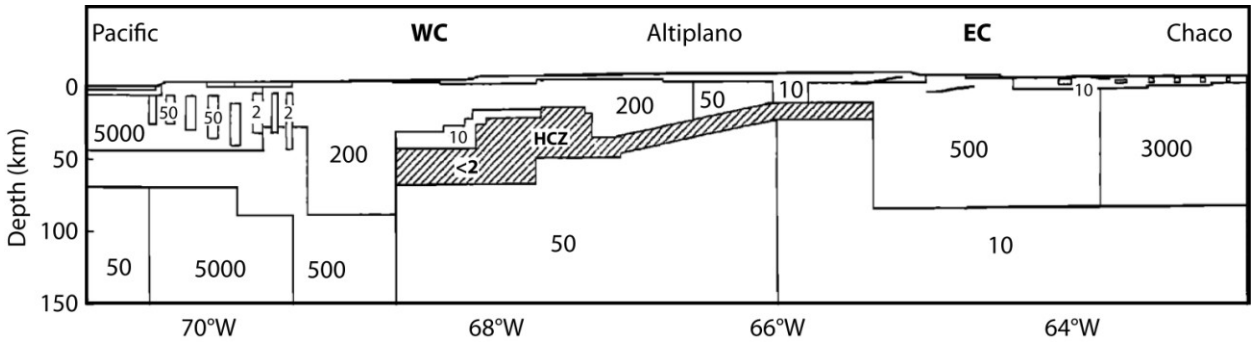

Figure 3.9: Two-dimensional electrical model of Schwarz and Kruger (1997) across the Altiplano along the ARC profile (see Figure 3.7 for map of sites). A high-conductivity zone (resistivity < 2 Ωm) is detected at a depth of ~20 km, with a total conductance of 23,000 S (Schwarz and Kruger, 1997). (*Adapted from Schwarz and Kruger, 1997*).

3.3.2 The Bolivian Altiplano Conductivity Anomaly

A long-period MT study was carried out to the north of the Schwarz and Kruger (1997) study, at a latitude of 21ºS along the ANCORP seismic line (see Figure 3.1 and 3.7 for location) (Brasse et al., 2002; ANCORP, 2003). Figure 3.10 shows the 2-D inversion model of the ANCORP MT profile from Brasse et al. (2002). A highly conductive zone (resistivity of < 2 Ωm) was detected below the Altiplano in the mid-crust. The top of the HCZ undulated between 10 and 30 km depth (Brasse et al., 2002). Interestingly, a resistor (resistivity of 100-1000 Ωm) is seen below the modern-day volcanic arc. Tipper data (from the vertical and horizontal magnetic fields; see Section 4.6) along the same line were fit using a model with a conductive zone at a depth of 15 to 20 km below surface, although the depth was not well resolved (Soyer and Brasse, 2001). Widespread partial melting of the crust beneath the Altiplano was proposed as an interpretation (Schilling et al., 2006; Brasse et al., 2002). Magnetotelluric results north of 19ºS do not show a mid-crustal HCZ (Schilling et al. 2006; Brasse and Eydam, 2008), it is only detected in the vicinity of the APVC.

Brasse et al. (2002) noted that nowhere else on Earth has a comparable conductive anomaly been observed, both in terms of its size and its high conductance (~23,000 S). In fact, the crustal conductance values detected in the Bolivian Altiplano may be some of the highest anywhere in the world, evidence that this is a region of high magmatic activity. In comparison, a conductance of 20,000 S is equivalent to 5,000 m of sea-water, assuming a conductivity of 4 S/m for sea-water. In stable continental regions the average conductance is 100 S and no more than 1,000 S (Wei et al., 2001). The Tibetan crust is another area with very high conductance, as seen in the INDEPTH project results, ranging from 3,000 to 20,000 S (Wei et al., 2001).

The MT study of Brasse et al. (2002) lies along the ANCORP line where seismic data exists. A seismic reflection study (see Section 3.2.1) along the same profile revealed highly reflective zones correlating in depth with the upper boundary of the Altiplano conductor. The correlated depth to the LVZ and the HCZ acts as a confirmation that both methods are seeing the same anomalous structure, and is significant because it limits the possible mechanisms responsible for this anomaly.

The area of high conductivity also closely coincides with the area of very high attenuation seen by Haberland et al. (2003), as described in Section 3.2.2. High temperatures alone can explain the attenuation results, but cannot explain the low resistivity values observed, while electrical conductors such as graphite can explain the low resistivity values, but would not affect the attenuation. Therefore, these correlated results (high conductivity, low velocity, high attenuation) support the interpretation of interconnected partial melts, which would significantly increase the conductivity, lower the velocity, and increase the attenuation, giving cohesive evidence of a large crustal magma body (Haberland et al.,2003; Pommier, 2014b).

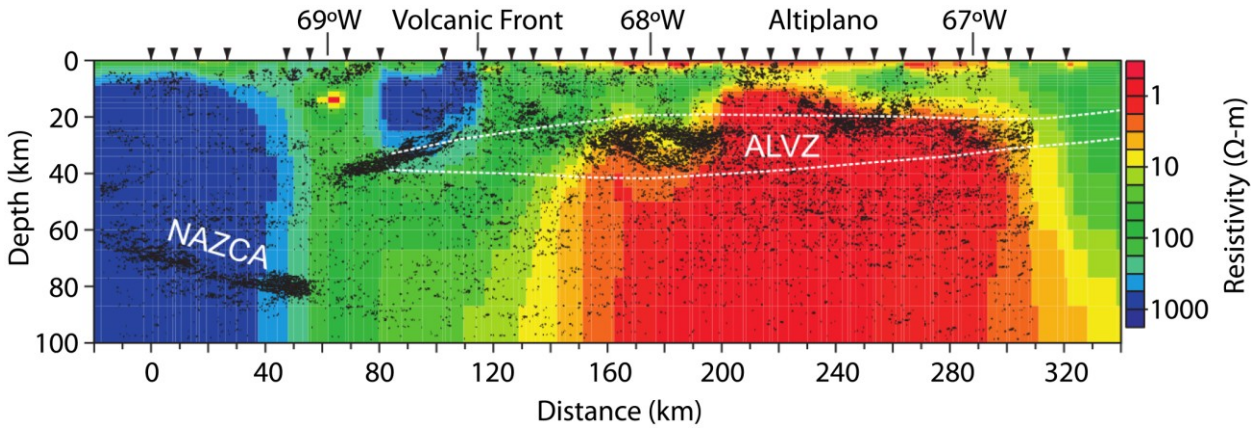

Figure 3.10: Magnetotelluric 2-D inversion model of Brasse et al. (2002) across the Altiplano along the ANCORP profile (latitude 21ºS, see Figure 3.1 and 3.7 for map). Earthquake locations (black dots) mark the downgoing Nazca plate, and the Andean Low-Velocity Zone (ALVZ) derived from the receiver function analysis of Yuan et al. (2002). (*Adapted from Brasse et al., 2002*).

3.4 Gravity Measurements of the Central Andes

The acceleration due to gravity at the surface of the Earth is on average 980,665 mGal (1 Gal = 0.01 m/s^2), although it varies by ~5000 mGal from the equator (978,000 mGal) to the poles (983,200 mGal) (see Lowrie, 2004). Accurate gravity measurements can show density variations within the Earth and can be used to infer the locations of different tectonic structures and rock types (Lowrie, 2004). For example, a zone of partial melt, being of lower density than the surrounding crustal host rock, will cause a negative gravity anomaly, because less mass than was expected is observed (Iyer, 1984). Examples where gravity imaging has been successful in delineating magma bodies include: the magma body below the Long Valley Caldera in California (e.g., Battaglia et al., 1999; Tizzani et al., 2012), the large magma body below Yellowstone (e.g., Savino, 1979; Lehman, 1982), and the magma body below the Geysers-Clear Lake, California (e.g., Isherwood, 1976).

Regional gravity surveys of the Central Andes have reported a strong negative Bouguer anomaly (up to -50 mGal residual) in southern Bolivia, which correlates with the location of the APVC and the present-day magmatic arc (Gotze and Kirchner, 1997; Prezzi et al., 2009), as shown in Figure 3.11. These low values give evidence for partial melting and low-density volcanic rocks (Prezzi et al., 2009). Furthermore, the extremely thick crust in this region can account for the mass deficit, because the crustal rock has lower density than the underlying mantle. The southern Puna area also has a strong negative Bouguer anomaly (up to -100 mGal) (Prezzi et al., 2009). Positive residual anomalies (larger than 50 mGal) are seen in the forearc, the Salar de Atacama basin, and in the Bolivian Eastern Cordillera. The regional gravity high observed below the Salar de Atacama basin is due to the dense, cold, and strong Atacama block (Prezzi et al., 2009). The Central Andean gravity high (CAGH) identified by Gotze and Krause (2002) is a positive anomaly previously identified in the isostatic residual gravity signal along the magmatic arc (long wavelength anomalies from isostatic compensation are removed from the Bouguer anomaly revealing anomalous density variations). This high-density structure has been interpreted to be the relic of a pre-Andean subduction zone (Gotze and Krause, 2002).

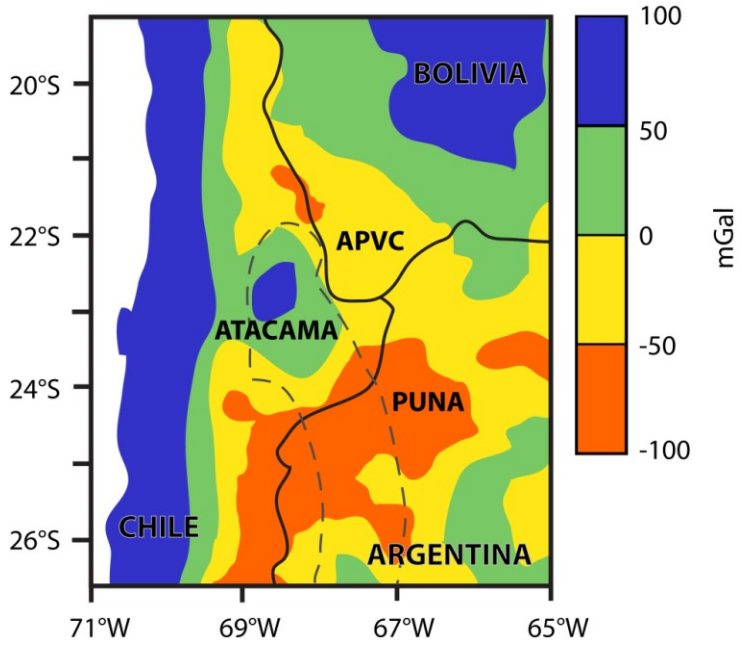

Figure 3.11: Residual gravity field obtained from subtracting the effect of the modelled subducting Nazca slab and the Moho from the Bouguer anomaly data. Central Andean gravity high is identified with a dashed line. (*Modified from Prezzi et al., 2009*).

3.4.1 Gravity Measurements Around Volcan Uturuncu

New results from high-resolution gravity measurements around Volcan Uturuncu reveal a large negative Bouguer anomaly (del Potro et al., 2013), as shown in Figure 3.12. Del Potro et al. (2013) created a 3-D density model, shown in Figure 3.13, which shows numerous low density features. These density features are generally narrow (~15 km wide), vertically elongated structures reaching from the surface down to the APMB (modeled at a depth of 20 km below surface). According to del Potro et al. (2013), the low density anomalies have no direct correlation with the surface location of ancient calderas. However, by comparing the caldera locations of Salisbury et al. (2011) it appears that 5 out of 9 low density anomalies are spatially correlated with nearby caldera complexes. In particular, one anomalous low-density structure below Volcan Uturuncu correlates spatially with observed ground deformation (see Section 3.6) (del Potro et al., 2013; Pritchard and Simons, 2004).

These low density pathways were modeled with a density difference of 150 kg/m^3 (compared to the surrounding rock), which is equivalent to a melt fraction of ~25%, and these pathways were interpreted to be fluid or magma (del Potro et al., 2013). One possible ascent mechanism, proposed by del Potro et al. (2013), is that buoyant magma accumulates at the top of the APMB and partially molten granitic bodies ascend diapirically through the crust due to gravitational instability. They dismissed dyking as a plausible ascent mechanism for vertical transport of magma from the APMB, due to its depth. The numerous 3-D structures above the APMB were not detected with seismic methods (discussed in Section 3.2). The high-resolution density model of del Potro et al. (2013) is able to image short wavelength (kilometre-scale) features above the APMB, while seismic methods can only image longer wavelength features (i.e., the APMB), and are not sensitive to such small variations.

If it is assumed that magma buoyancy over the entire crustal column, from the APMB to the surface, is neutral, as in Caricchi et al. (2014), then the density contrast required when the APMB is located at a given depth can be calculated, following the example given by Muir et al. (2015) (which assumes the volcano and the magma column within it have an elevation of 1500 m above

the surface). using the density model of del Potro et al. (2013) a density contrast can be converted to a melt fraction. Therefore the depth of the crustal magma mush column (depth to the APMB) can give constraints on the melt fraction possible in the density model of del Potro et al. (2013). For example, if the APMB is located at a depth of 25 km below the surface the melt fraction required is 22%; a depth of 20 km gives a melt fraction of 35%; and a depth of 15 km gives a melt fraction of 49%.

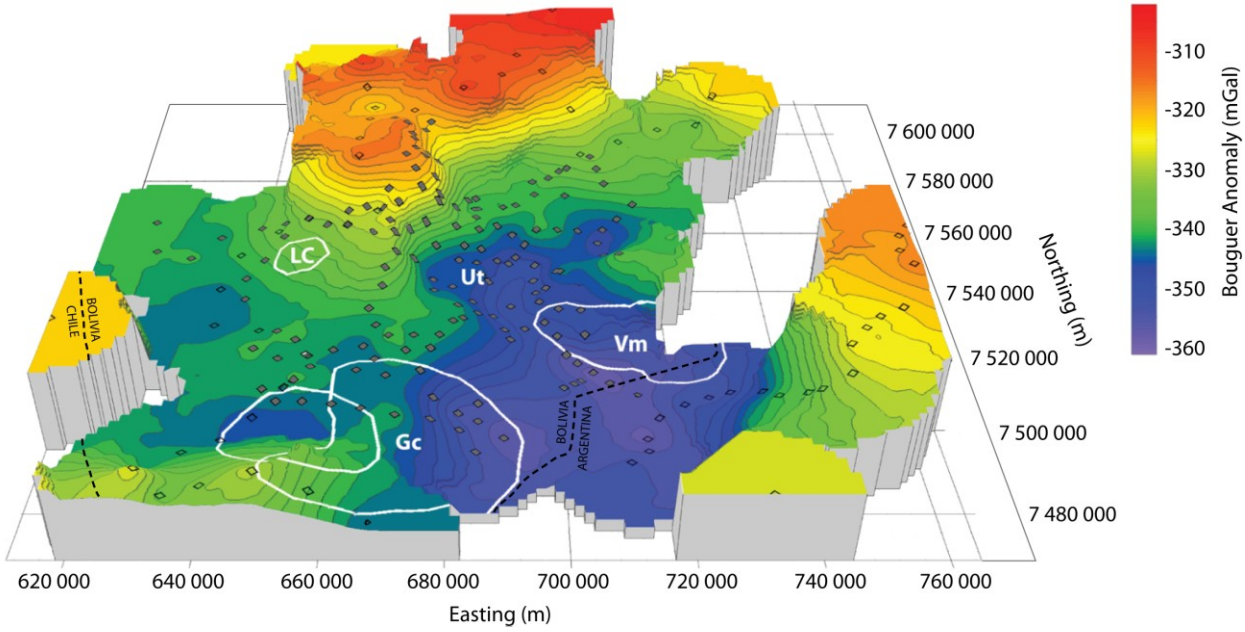

Figure 3.12: High-resolution gravity measurements around Volcan Uturuncu (Ut) reveal a large gravity low (blue colour). Select calderas from Salisbury et al. (2011) are shown as white lines: Gc - Guacha; Vm- Vilama; LC - Laguna Colorada. (*Figure adapted from del Potro et al., 2013*).

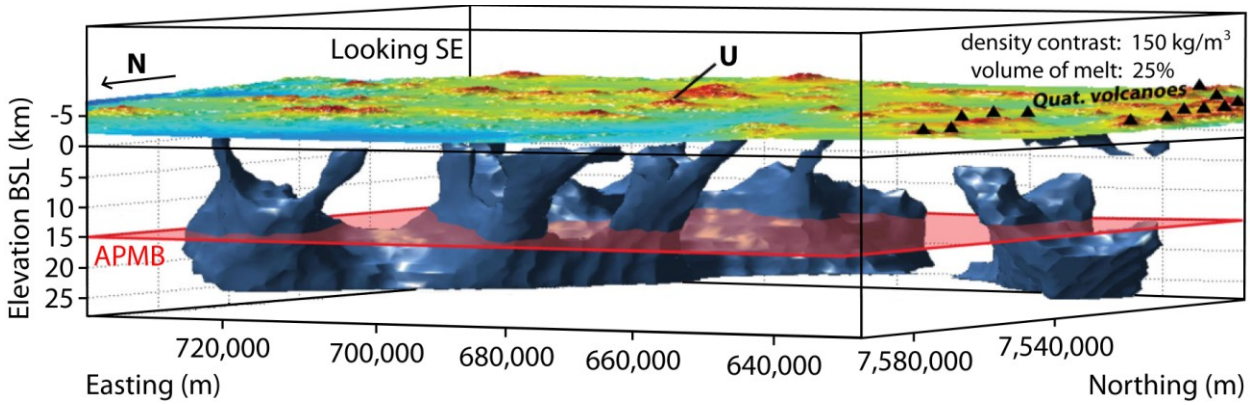

Figure 3.13: A density model around Volcan Uturuncu (U) shows numerous low density 3-D features reaching from the Altiplano-Puna Magma Body (APMB) to the surface. These low density pathways and are interpreted to be ascending fluid or magma (del Potro et al., 2013). The model uses a density contrast of 150 kg/m^3, equivalent to a melt fraction of 25%. (*Figure modified from del Potro et al., 2013*).

3.5 Heat Flow Measurements

Heat flows from sources within the Earth to its surface, giving a global average on the continents of 65±2 mW/m^2, and of 101±2 mW/m^2 for the oceans where the lithosphere is generally thinner (Pollack et al., 1993). The two main sources of this heat are residual heat from Earth's formation and radiogenic heat from the radioactive decay of elements in the Earth (see Lowrie, 2004). The heat is not released uniformly from the Earth but is concentrated in areas where heat is more easily transported from the Earth's interior by convection, such as at mid-ocean ridges and mantle plumes. If a local heat source exists in the crust, such as a magma chamber located below the surface, the measured surface heat flow is expected to be higher. Therefore, identifying areas of anomalous heat flow can give evidence for magma bodies.

There are no heat flow measurements on Volcan Uturuncu, but sparse measurements do exist in the surrounding region. The closest heat flow measurements in Southern Bolivia (Kolpani, 21.3°S, 66.7°W; 121 km NNE of Uturuncu) are ~100 mW/m^2 (Henry and Pollack, 1988).

Anomalously high heat-flow values of 150 mW/m^2 have also been measured west of Uturuncu in Northern Chile (El Loa; 138 km west of Uturuncu) (Springer and Forster, 1998). Heat flow maps of South America show the Altiplano-Puna region as having a very high heat flow of more than 140 mW/m^2 (Hamza et al., 2005; Hamza et al., 1996). Caution is required because the data are sparse and heavily interpolated (Springer, 1999). Figure 3.14 shows the heat flow map of the Central Andes from Hamza et al. (2005), with the position of Volcan Uturuncu indicated. The heat flow values around Uturuncu are shown to be 100-300 mW/m^2.

Thermal gradient (K/km) is related to heat flow (q, mW/m^2) through the thermal conductivity of the material (κ, W/mK), which can be assumed to be 2-3 for most rocks (Lowrie, 2004), written as,

$$q = \kappa \left(\frac{\partial T}{\partial z}\right) . \qquad \text{(Eq. 3.4)}$$

These anomalously high heat flow values create a temperature-heat paradox (Giese and Schilling, 2000; Schilling et al., 2006), since thermal models show that conductive heat transfer from intruded magmas and radiogenic heat production can only account for two thirds of the observed heat flow (Schilling et al., 2006; Babeyko et al., 2002). Furthermore, these models predict that the solidus temperatures of typical crustal rocks would be reached at a depth of only 25 km below surface (Schilling et al., 2006, and references therein). Advective heat transfer is required to explain the high heat flow values, with crustal melting and mass transfer the most likely scenario (Schilling et al., 2006; Babeyko et al., 2002), which would lead to high local variability.

Using heat flow values of 150-200 mW/m^2, which are extremely high, and thermal parameters for granite rock, Jay et al. (2012) calculated the brittle–ductile transition zone depth to be 2.2-0.8 km BSL. This explains why most earthquake depths observed below Volcan Uturuncu are above sea level (see Figure 3.6), because sea-level represents the approximate depth of the brittle-ductile transition zone (BDT).

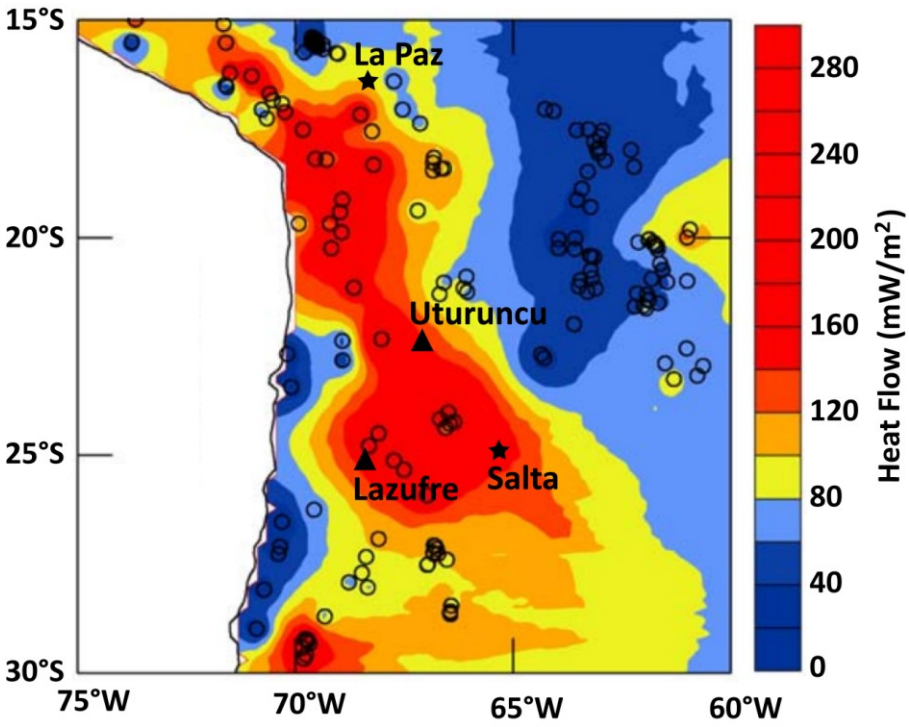

Figure 3.14: Heat flow map of the Central Andes. Circles indicate measurement locations. In the vicinity of Volcan Uturuncu heat flow values of 100-300 mW/m^2 are seen. Note the data has been interpolated between measurements positions. (*Adapted from Hamza et al., 2005*).

3.6 Geodetic Measurements at Volcan Uturuncu

Interferometric synthetic aperture radar (InSAR) is a powerful geodetic technique which uses remote sensing to map surface deformation (Pritchard, 2006; Pritchard and Simons, 2004; Pritchard and Simons, 2004b). Continuous GPS monitoring or campaign-style GPS surveys can also map surface displacements, often with more spatial accuracy, but with considerably less spatial coverage than InSAR (Dzurisin, 2003). InSAR lacks the temporal resolution of a continuous GPS monitoring station, which can capture rapid variations and deformation events in near real-time, but has the advantage of observing remote or hard to access locations. InSAR measurements have uncertainties of about 4 mm/year (Pritchard and Simons, 2004) while GPS

surveys typically have uncertainties of 2-3 mm/year horizontally and 10 mm/year vertically (Dzurisin, 2003). The use of these geodetic techniques to measure centimetre-scale changes over time-spans of years makes these the methods of choice for monitoring natural hazards, such as volcanoes and earthquakes (e.g., Dvorak and Dzurisin, 1997). Based on both the spatial distribution and the rate of surface deformation, the location and size of the deformation source can be inferred (Pritchard, 2006).

3.6.1 Ground Deformation around Volcan Uturuncu

A satellite-based geodetic (InSAR) survey of the approximately 1000 catalogued volcanoes in the Central Andes Volcanic Zone (de Silva and Francis, 1991) detected ground deformation at four volcanoes (Pritchard and Simons, 2004). At Volcan Uturuncu, data collected from 1992-2011 showed a broad (~75 km), circularly symmetric area of surface uplift with a nearly constant uplift rate of 1 cm/year (e.g., Henderson and Pritchard, 2013). This uplift pattern is also surrounded by a ring of subsidence (Fialko and Pearse, 2012; Henderson and Pritchard, 2013), with a diameter of ~150 km. Figure 3.15 shows both a profile and a map view of the InSAR data, revealing the deformation pattern around Volcan Uturuncu. The surface deformation pattern observed is spatially smooth, and basic geodetic models (see Section 3.6.2 below) were used to infer a source depth of ~18 km BSL (Pritchard and Simons, 2004). There is no consensus on the mechanisms responsible for the observed uplift, although given the depth of the inferred source it is likely to be of magmatic origin, rather than hydrothermal (Fialko and Pearse, 2012).

It is common for volcanoes to cyclically inflate and deflate on time scales of several years, (Riddick and Schmidt, 2011; Vasco et al., 2007), in many cases at much higher rates than those observed at Uturuncu. For example, at Laguna del Maule in Chile InSAR data revealed an inflation rate of ~25 cm/year from 2007 to 2014, with a diameter of ~15 km (Feigl et al., 2014). The large diameter of the inflation pattern at Uturuncu (~75 km) is both impressive and uncommon. Only two other volcanic centres in the Central Andes show broad surface inflation patterns (Pritchard and Simons, 2002). These are Lazufre, on the Chile-Argentina border, which

has an inflation diameter of 30-45 km (Ruch et al., 2008; Ruch et al., 2009), and Hualca Hualca, in Peru (near Sabancaya Volcano), which has an inflation diameter of 60 km (Pritchard and Simons, 2004).

What makes Uturuncu unusual, besides the large diameter of the deformation pattern (~150 km diameter for inflation and subsidence), is that steady inflation has been observed for several decades, without deflation (Henderson and Pritchard, 2013). A study by del Potro et al. (2013b) analysed levelling data collected in 1965 by the Instituto Geográfico Militar of Bolivia and concluded that 65 cm of uplift occurred from 1965 to 2011 (45 years; average of 1.4 cm/yr), implying continuous uplift has been occurring for ~50 years. In comparison, the nearby volcanic complex of Lazufre shows a similar inflation rate of about 3 cm/year beginning abruptly in 1998 and lasting until 2010, with no deformation measured prior to 1998 (e.g., Pearse and Lundgren, 2013; Pritchard and Simons, 2004). InSAR data analysis over the Socorro Magma Body in New Mexico (which has several similarities with the APMB, such as its depth and tectonic history) indicates a steady uplift rate of approximately 0.2 cm/year measured from 1992-2007 (e.g., Pearse and Fialko, 2010; Fialko and Simons, 2001). Levelling data from Larsen et al. (1986) from the period of 1912-1951 show similar uplift magnitudes, implying that the uplift observed at the Socorro Magma Body may be long-lived, similar to the situation observed at Volcan Uturuncu, above the APMB.

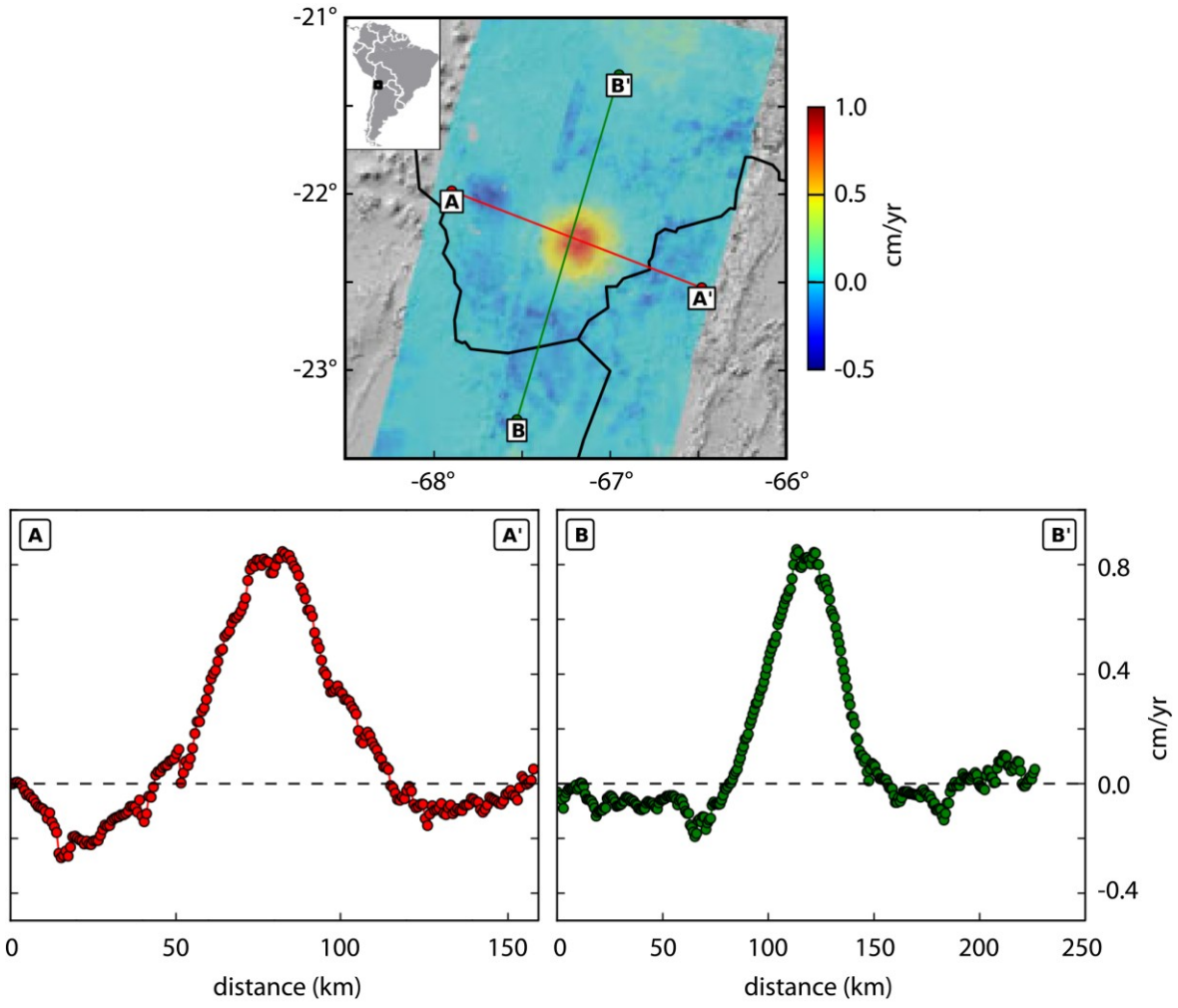

Figure 3.15: Both map-view and profile-view images of InSAR data shows the circular deformation pattern around Volcan Uturuncu. The uplift is symmetric, has a diameter of ~75 km, and a nearly constant rate of 1 cm/yr over the time period of 1992-2011. Cross sections of the data reveal a moat of subsidence around the inflation pattern. (*Adapted from Henderson and Pritchard, 2013*).

3.6.2 Geodetic Models to Explain Deformation

Modelling the deformation source position and evolution from InSAR data, which gives only surface velocities, requires assumptions of the material properties of the Earth, and is a non-unique process (Dzurisin, 2003). A summary of the proposed inflation source geometries from geodetic modeling of the deformation pattern around Volcan Uturuncu is shown in Figure 3.16, and details are discussed below. Depths to the APMB from seismic RF and from ANT are also shown (Zandt et al. 2003; Ward et al., 2014), along with estimates of the depth to the brittle to ductile transition zone (Jay et al., 2012), earthquake hypocenters below Volcan Uturuncu (Jay et al., 2012), the shallow low-velocity zone below Uturuncu identified by Jay et al. (2012), and the pre-eruptive magma storage location predicted by Muir et al. (2014).

Pritchard and Simons (2004) used a simple elastic halfspace model for various source geometries to find the depth required by the observed deformation data. Their results show the following: for a vertical ellipsoid shaped source, a depth of ~18 km BSL to the centre of the source fit the data; for a horizontal ellipsoid a depth of ~19 km BSL; for a spherical source a depth of ~17 km BSL. A Mogi (point) source fits the inflation pattern when located at a depth of 25 km BSL (Henderson and Pritchard, 2013).

Hickey et al. (2013) used a more realistic visco-elastic layered model to determine the depth of the inflation source. Their results show that a vertical ellipsoid centered at a depth of ~16 km BSL and with a size of 9 km by 3 km fit the deformation data; a horizontal ellipsoid required a greater depth of ~28 km BSL and a size of 2 km by 11 km; a spherical source fits at a depth of ~25 km BSL with a radius of 6 km. Hickey et al. (2012) proposed the broad surface deformation pattern observed could best be fit with a vertically elongated source (prolate ellipsoid shape) driven by lateral motion of magma within the APMB.

A closer examination of the InSAR data by Fialko and Pearse (2012) revealed a moat of subsidence surrounding the central inflation pattern, a deformation pattern they called "sombrero uplift". They proposed that this deformation is the result of a large ballooning diapir fed by the

APMB. A Rayleigh-Taylor gravitational instability within the magma body could cause the formation of a buoyant diapir above it, and the inflation of such a diapir could cause the observed surface uplift. The subsidence can be explained by the same model: as material migrates laterally towards the diapir it is being withdrawn from the surrounding areas and causes the observed subsidence (Fialko and Pearse, 2012). The fact that the diapir appears to be located spatially in the middle of the APMB, and almost directly below Volcan Uturuncu, gives credibility to this model. In order to fit the deformation data, the buoyant region is viscoelastically modeled with a semi-ellipsoid dome shape, a height of 6.5 km and a width of 10 km, which rises out of a thin (1.5 km) horizontal APMB (Fialko and Pearse, 2012).

Walter and Motagh (2014) found that the strength and the pattern of the deformation can be better fit with a flat-topped source, whether diapir-like or prolate in shape. Modeling the observed surface stress fractures around Volcan Uturuncu and local lineaments, they propose that a flat-topped magma body at a depth of 11 - 15 km BSL fit the data best.

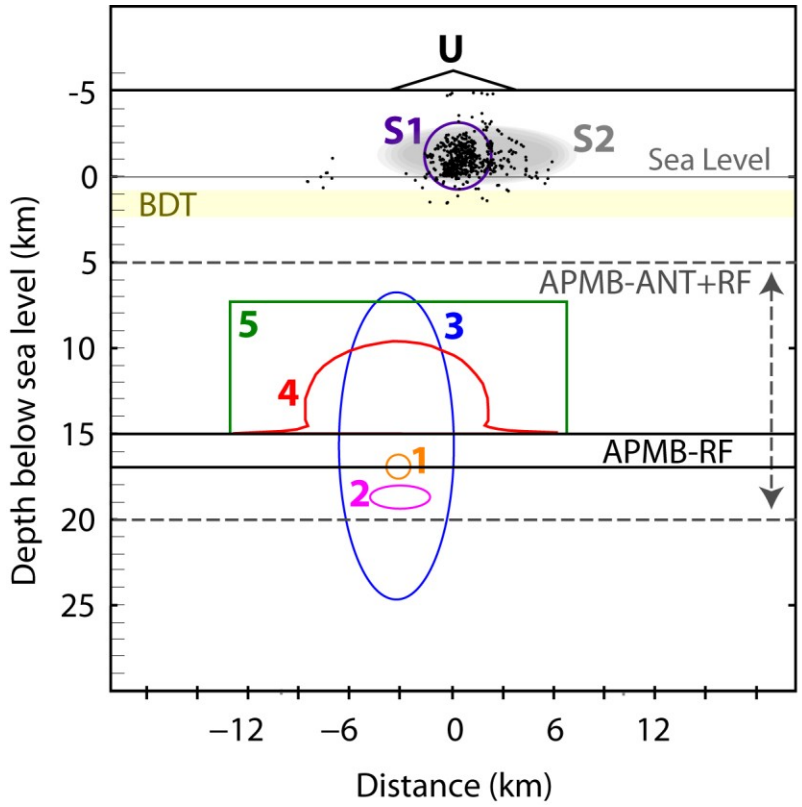

Figure 3.16: A summary of proposed geodynamic and seismic models. APMB-RF — location of the Altiplano-Puna magma body (APMB) as defined by seismic receiver functions (RF; Zandt et al., 2003). APMB-ANT+RF — the low-velocity layer determined from the joint ambient noise tomography (ANT) and receiver function model of Ward et al. (2014). U — relative location of Volcan Uturuncu. InSAR data reveals the inflation centre is located ~3 km west of the summit (Pritchard and Simons, 2004). 1 — Spherical inflation source 17 km below sea level (BSL) (Pritchard and Simons, 2004). 2 — Horizontal oblate source 19 km BSL (Pritchard and Simons, 2004). 3 — Prolate ellipsoid 16 km BSL (Hickey et al., 2013). 4 — Diapir extending vertically 5 km from APMB (Fialko and Pearse, 2012). 5 — Flat topped body rising 7 km from the APMB (Walter and Motagh, 2014). BDT — The brittle to ductile transition depth is estimated to be 0.8-2.2 km BSL (Jay et al., 2012). Black dots are earthquake hypocenters projected onto a west-east plane below Uturuncu (Jay et al., 2012). S1 — Pre-eruptive magma storage location (depth of -2.1 to 0.7 km BSL) predicted by Muir et al. (2014). S2 — Shallow low-velocity zone identified with ANT by Jay et al. (2012).

3.7 Compilation of Evidence for the APMB

As discussed throughout this chapter, various geophysical methods have given evidence for the existence of the APMB: seismic methods detected a LVZ below the Altiplano, interpreted as a layer of partial melt; a HCZ was detected with MT, and interpreted as a zone of partial melt; geodetic data shows a ground deformation pattern around Volcan Uturuncu which can be modeled with source depths and geometries which match other evidence, gravity studies reveal several low-density structure, interpreted to be magma conduits connecting the APMB to the surface. Figure 3.17 shows a compilation of this evidence. Large calderas and prominent ignimbrite eruption centres of the APV, as discussed in Section 2.5, are shown (Salisbury et al., 2010). Known, active geothermal areas (El Tatio, Chile; Sol de Manana, Bolivia; Aguas Termales de Polques, Chalviri, Bolivia) are also shown.

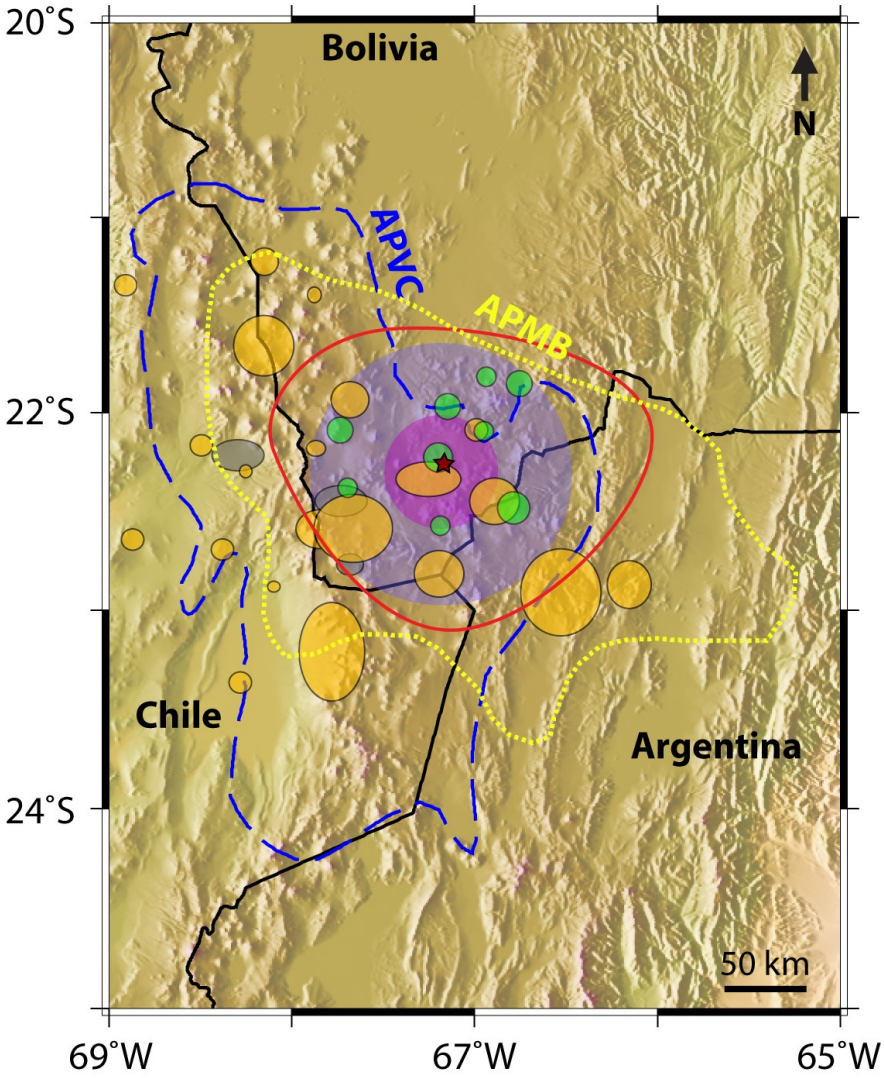

Figure 3.17: A compilation of geophysical evidence around Volcan Uturuncu (red star) and across the Altiplano-Puna Volcanic Complex (APVC, dashed blue line; de Silva, 1989). Receiver function analysis reveals a large low-velocity zone, interpreted as the Altiplano-Puna Magma Body (APMB, dotted yellow line; Zandt et al., 2003). Joint inversion of ambient noise tomography data and receiver function data also show a low-velocity zone (red line, 2.9 km/s velocity contour; Ward et al., 2014). Geodetic data shows a pattern of inflation and subsidence around Volcan Uturuncu (pink and purple circles; Henderson and Pritchard, 2013). A density model derived from gravity data shows low-density conduits rising from the APMB to the surface (green circles; del Potro et al., 2013). Large calderas and prominent ignimbrite eruption centres are shown as orange ellipses (Salisbury et al., 2010). Geothermal areas are shown as grey ellipses. The modern-day volcanic arc follows the eastern border of Chile.

3.7.1 Compilation of Depths to the APMB

Various geophysical methods discussed throughout this chapter have detected the APMB. Table 3.1 provides a summary of the published depth estimates to the APMB. Receiver function analysis images the top of a thin (<2 km) low-velocity zone as a sharp boundary at a depth of ~15 km BSL (e.g., Chmielowksi et al., 1999; Beck and Zandt, 2002; Zandt et al., 2003). Ambient noise tomography methods, which are not sensitive to narrow vertical structures, image a diffuse low velocity zone from just below sea-level to depths of ~25 km BSL (Ward et al., 2013; Ward et al., 2014). Previous magnetotelluric studies detected the top of a high-conductivity zone at depths of 10-15 km BSL (e.g., Brasse et al., 2002; Schwarz and Kruger, 1997). Geodetic data has been modeled with a variety of inflation source depths and geometries at depths of approximately 15-20 km BSL (e.g., Pritchard and Simons, 2004; Henderson and Pritchard, 2013; Hickey et al., 2012; Walter and Motagh, 2014).

Table 3.2 provides a summary of the depths to a shallow magma reservoir. Seismic ANT results, earthquake hypocentres, and petrology all agree a shallow magma reservoir is located below Volcan Uturuncu at a depth near sea-level, or just above it (e.g., Jay et al., 2012; Muir et al., 2014; Sparks et al., 2008). These methods are remarkably consistent in the predicted depth to the shallow magma reservoir, which is located 2 - 6 km below surface (-3 - 1 km BSL). Geodetic methods (such as InSAR) have not detected this chamber, because any deformation signal would likely be dominated by the larger signal of the APMB, thereby hiding the smaller signal of a shallow chamber (Sparks et al., 2008).

Table 3.3 shows a compilation of thickness estimates for the APMB. Several seismic receiver function studies (e.g., Chmielowski et al., 1999; Zandt et al., 2003; Leidig and Zandt, 2003) imaged the APMB as a thin sill with a thickness of ~1 km, while others detected a broader low-velocity zone of 10-20 km thickness (e.g., McFarlin et al., 2014; Beck and Zandt, 2002). The joint ambient-noise tomography and receiver function study of Ward et al. (2014) also shows a broader low-velocity zone 10-20 km thick. Previous magnetotelluric results detected a very thick high conductivity zone, 10-40 km thick, interpreted to be the APMB.

METHOD	DEPTH TO	DEPTH BSL (KM)	CITATION
Elastic modeling (center of inflation source)	Vertical Ellipsoid source Horizontal Ellipsoid source Spherical source	18 19 17	Pritchard and Simons (2004)
	Mogi point source	20	Henderson and Pritchard (2013)
Visco-elastic modelling (center of inflation source)	Vertical Ellipsoid source Horizontal Ellipsoid source Spherical source	16 28 25	Hickey et al. (2012)
	Sill-shaped intrusion Mogi point source	17 16	Walter and Motagh (2014)
Lineament Stress Models	Top of a flat-topped source	13	Walter and Motagh (2014)
Seismic Reflection	Top of Low Velocity zone (latitude 21°S)	15-20	ANCORP (1996)
Seismic Receiver Functions (RF)	Top of Low Velocity zone (latitude 22-22.5°S)	14	Chmielowski et al. (1999)
	Top of Low Velocity zone (latitude 19.5°S)	15	Beck and Zandt (2002)
	Top of Low Velocity zone (~1 km/s)	15	Zandt et al. (2003)
	Low-Velocity zone (~1 km/s)	14-17	Leidig and Zandt (2003)
Ambient Noise Tomography (ANT)	Low Velocity zone	0-25	Ward et al. (2013)
Joint ANT + RF	Low Velocity zone (< 2.9 km/s)	6-23	Ward et al. (2014)
	Slowest Velocities	13-15	Ward et al. (2014)
Magnetotellurics	Top of a High Conductivity Zone	15	Schwarz and Kruger (1997)
Magnetotellurics	Top of a High Conductivity Zone	10-30	Brasse et al. (2002)

Table 3.1: A summary of the published depths to the Altiplano-Puna Magma Body, as detected by various geophysical methods. Geodetic methods model source depth and geometry to fit the InSAR ground deformation signal observed; seismic methods detect a low-velocity zone; electrical methods detect a high conductivity zone. The surface is assumed to be at an elevation of 5000 m above sea-level.

METHOD	DEPTH TO	DEPTH BSL (KM)	CITATION
Ambient Noise Tomography (ANT)	Low Velocity Zone	-3 to -1	Jay et al. (2012)
Earthquake Hypocentres	Earthquake Cluster	-3 to 1	Jay et al. (2012)
Geochemistry	Pre-Eruptive Body	-3.1 to 0.7	Muir et al. (2014)

Table 3.2: A summary of depths to a shallow pre-eruptive magma chamber, as detected by various methods. The surface is assumed to be at an elevation of 5000 m above sea-level. Geodetic methods have not detected this small, shallow chamber, because it may be hidden by the much larger deformation signal of the APMB.

METHOD	THICKNESS OF FEATURE	THICKNESS (KM)	CITATION
Seismic Receiver Functions (RF)	Low Velocity zone (latitude 22-22.5°S)	< 1	Chmielowski et al. (1999)
	Low Velocity zone (latitude 19.5°S)	6-15	Beck and Zandt (2002)
	Low Velocity zone	1	Zandt et al. (2003)
	Low-Velocity zone	1-2	Leidig and Zandt (2003)
	Low-Velocity zone (near Uturuncu)	20	McFarlin et al. (2014)
Joint Ambient Noise Tomography and RF	Low Velocity zone (< 2.9 km/s)	10-20	Ward et al. (2014)
Magnetotellurics	High Conductivity Zone	10-40	Schilling et al. (1997)

Table 3.3: Summary of thickness estimates for the Altiplano-Puna Magma Body.

3.8 Summary

Geophysical studies have shown that the APVC is underlain by anomalously low seismic velocities (e.g., ANCORP, 1996; Chmielowski et al., 1999; Beck and Zandt, 2002; Zandt et al., 2003), high seismic attenuation (Haberland et al., 2003; Schurr et al., 2003), low electrical resistivities (e.g., Schwarz and Kruger, 1997; Brasse et al., 2002; Schilling et al., 2006), anomalously high heat flow values (Henry and Pollack, 1988; Springer and Forster, 1998;

Hamza et al., 2005), and associated with a negative Bouguer anomaly (del Potro et al., 2013). Together, these anomalies give evidence for a major mid-crustal magma body, the Altiplano-Puna Magma Body (APMB), and make this region a key location for understanding silicic magmatism in continental crust. Furthermore, InSAR data shows a broad (~70 km) and continuous (decades long) deformation pattern coincident with the APMB and centered on Volcan Uturuncu, which includes a central ring of uplift and an outer ring of subsidence. Geodetic models of inflation source depths (~15 to 20 km BSL) correlate well with depths to the APMB determined from seismic and magnetotelluric data. The geometry of the inflation source is not well constrained, but multiple models exist which are coherent with the available data. Only the density model derived from gravity data (del Potro et al., 2013) is able to show small-scale features above the APMB and shows the existence of pathways of melt ascending from the APMB. The question of the distribution of melt within the APMB and above it remains unconstrained, and more geophysical data are necessary to answer this question.

CHAPTER 4: THE MAGNETOTELLURIC METHOD

4.1 Introduction

The magnetotelluric (MT) method is a geophysical technique that uses temporal fluctuations of the naturally occurring electric and magnetic fields of the Earth to determine spatial variations in the electrical resistivity of the Earth's subsurface. As will be shown below, the MT method works because measurements of both the amplitude and phase of these fields at the surface are dependent on the electrical resistivity beneath the Earth's surface. The electrical resistivity is sensitive to the presence of fluids and magma (e.g., Unsworth and Rondenay, 2012), and therefore the MT method is useful to identify magma bodies in the Earth (as seen in Chapter 3), which is the goal of this thesis.

In this chapter, the basics of the MT exploration method are explained. This includes a review of the physics of the propagation of electromagnetic fields, and a discussion of the electrical resistivity properties of Earth materials. The impedance tensor for a 1-D, 2-D, and 3-D Earth is then introduced. Following this, an example of MT data is presented as apparent resistivity and phase curves plotted against period (used as a proxy for depth). Dimensionality, directionality, and geo-electric strike concepts are explained, as well as data distortion and static shifts. MT data modeling and inversion is briefly introduced in the final section.

4.1.1 A History of the Magnetotelluric Method

The magnetotelluric (MT) exploration method was first proposed by Tikhonov (1950), but remained virtually unknown until Cagniard (1953) independently proposed the method and developed the theoretical aspects of the MT method in detail. Cagniard (1953) established that the electrical properties of the subsurface can be determined as a function of depth from the frequency-dependent impedance, which is the ratio of orthogonal electric and magnetic field

components measured at the surface of the Earth. High-frequency signals provide information about the near surface, and low-frequency (long period) signals are sensitive to the lower layers of the Earth. Thus by using a wide frequency range it is possible to determine the variation of electrical resistivity with depth. Horizontal resistivity variations (along a profile or a grid) can be determined by measuring at multiple stations.

Wait (1954) challenged the validity of the MT technique by criticizing an important assumption of MT: that incident electromagnetic (EM) fields can be considered plane waves at the surface of the Earth. It was later shown that the plane wave assumption is valid for the resistivity values typically found in the crust and upper mantle, which are relatively low resistivities (Madden and Nelson, 1964). This established MT as a new geophysical exploration technique and ushered in a new era of deep EM exploration.

4.1.2 Sources of Electromagnetic Energy Used in Magnetotellurics

The passive source EM signals used in the MT method originate in two distinct processes and each has a unique frequency content (Heise et al., 2006). EM signals with frequencies above 1 Hz originate from worldwide lightning activity. Lightning discharges produce EM signals, known as sferics, which travel around the Earth within a resistive waveguide that is bounded by the Earth's relatively conductive surface below, and the ionosphere's conductive plasma region above (see Simpson and Bahr, 2005).

EM signals with frequencies below 1 Hz originate in the interaction between the Earth's magnetosphere and the solar wind. The solar wind, as described by Parker (1958), is a stream of plasma, mostly ions, electrons, and protons, radiating continually from the Sun. At the magnetopause, the boundary where the solar wind interacts with the Earth's magnetic field, positively charged ions and negatively charged ions are deflected in opposite directions, setting up electrical currents. The solar wind varies in both intensity and velocity and can cause distortions of the Earth's magnetosphere, creating continuous magnetic field variations which are detectable at the surface of the Earth. An increase in solar wind pressure will cause compression

of the Earth's magnetic field lines, starting sinusoidal-type harmonic oscillations of the magnetosphere, known as geomagnetic pulsations (Simpson and Bahr, 2005, and references therein). For example, a magnetospheric oscillation known as a Pc3 signal is often seen in MT data at a period of 10 - 45 s. Other continuous pulsation are also observed, known as Pc5 (150 - 600 s), Pc4 (45 - 150 s), Pc2 (5 - 10 s), and Pc1 (0.2 - 5 s) signals (Vozoff, 1990). A sudden increase in the rate of plasma radiation from the Sun can cause magnetic storms, which provide the largest variations in the magnetic field. These magnetic storms are also responsible for the aurora borealis, and can last for several days (see Simpson and Bahr, 2005).

The Earth itself has a strong internal magnetic field which is established by dynamo action in the outer core via magnetohydrodynamic processes (Lowrie, 2004). However, the internal magnetic field has variations on the timescales of years, and so is of limited use for geophysical exploration techniques. Therefore it is the external magnetic field that provides the main source of EM signals for MT exploration.

4.2 Electrical Properties of the Earth

4.2.1 Electromagnetic Constants and Constitutive Equations

The electromagnetic behaviour in a given medium can be expressed in terms of three material constants: magnetic permeability, electric permittivity, and electrical conductivity. Constitutive equations can be written that define these parameters and their relationship with electromagnetic fields:

$$\mathbf{B} = \mu\mathbf{H} \,, \qquad \text{(Eq. 4.1)}$$

$$\mathbf{D} = \varepsilon\mathbf{E} \,, \qquad \text{(Eq. 4.2)}$$

$$\mathbf{J} = \sigma\mathbf{E} \,, \qquad \text{(Eq. 4.3)}$$

where **B** is the magnetic flux (units of T), **H** is the magnetic field strength (units of A/m), μ is the magnetic permeability (units of H/m), **D** is the electric flux (units of C/m^2), **E** is the electric field strength (units of V/m), ε is the electric permittivity (units of farads/meter), **J** is the electric current density (A/m^2), and σ is the conductivity (units of S/m).

Magnetic permeability is the ability of a material to become magnetized (by supporting a magnetic field within it) in the presence of an applied magnetic field (Griffiths, 1999). The magnetic permeability free-space (vacuum) value, $\mu_0 = 4\pi \times 10^{-7}$ H/m, is commonly used, because variations from the free-space value for Earth materials are small (Zhdanov and Keller, 1994). Therefore, when μ is constant, **H** and **B** can be used interchangeably. A related concept is the dimensionless proportionality constant of magnetic susceptibility (χ) which indicates how magnetized a material becomes in an applied magnetic field. If χ is positive then the material is called paramagnetic, and the magnetic field in the material becomes strengthened. If χ is negative the material is diamagnetic, and the magnetic field in the material is weakened. Ferromagnetic materials have a permanent magnetization with no need for an external applied field and have positive magnetic susceptibility.

The electric permittivity is the ability of a material to resist the formation of an electric field within it. Relative electric permittivity (ε_r), also known as the dielectric constant of a material (also K), is defined as the ratio of the electric permittivity of a given medium as compared to the free space value, ε_o. This can be written as $\varepsilon_r = \varepsilon_m/\varepsilon_o$, where ε_m is the electric permittivity of a specific substance or medium. At the low frequencies used in MT (kHz to μHz) any variations in the electric permittivity can be neglected and the free-space value, $\varepsilon_0 = 8.85 \times 10^{-12}$ F/m, can be used (Simpson and Bahr, 2005). The conductivity (σ) is the material's ability to allow electric current flow, and is the inverse of resistivity (ρ, units of Ωm). Therefore, resistivity is a measure of the opposition to electric current flow through a material, with the mechanical analog being friction (Griffiths, 1999). All materials show electrical resistivity (except for special superconducting materials).

4.2.2 Electrical Conductivity of Earth Materials

The electrical conductivity (inverse of resistivity) of typical Earth materials can vary over many orders of magnitude, as shown in Figure 4.1. This makes conductivity a useful parameter to define different Earth materials. The electrical conductivity is very sensitive to the presence of fluids within the crust and upper mantle, because the resistivity contrast with the surrounding rocks can be large (e.g., Unsworth and Rondenay, 2012). By gaining information on the electrical properties of the subsurface, we can interpret the underlying structure.

The electrical resistivity of a material depends on the mobility and density of charge carriers. The charge carriers move in an electric field and the mobility is defined as the average drift velocity per unit electric field. Electronic conduction occurs in pure metals where electrons (the charges carriers) are abundant and can move easily through the metal (high mobility) (e.g., copper). Ionic (electrolytic) conduction occurs when a material contains free ions which act as charge carriers. In magmas and partial melts, ions can move easily through the molten rock and these ions act as charge carriers, creating electric current. For silicic melts the sodium (Na) ions are the most important charge carriers, due to their smaller size and greater mobility, compared to other ions (e.g., potassium) (Pommier and Le Trong, 2011).

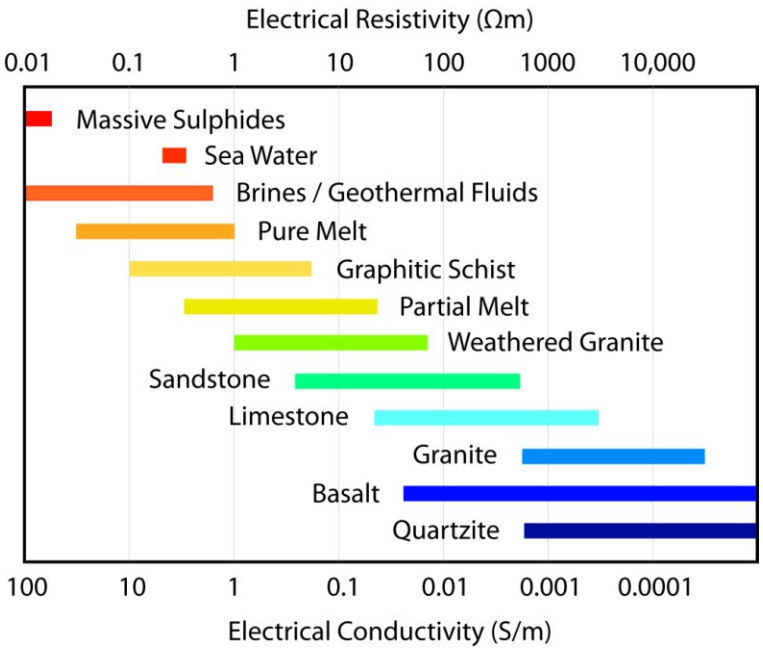

Figure 4.1: The electrical resistivity and conductivity values for various Earth materials. Values were taken from Simpson and Bahr (2005), and references therein. Electrical conductivity varies over many orders of magnitude and is therefore a useful parameter to define different Earth materials. Ranges of values are shown as bars and are coloured blue for high resistivity, and red for low resistivity (conductive).

4.2.3 Archie's Law and Other Mixing Models

Pure materials in the Earth are uncommon, as most rocks are formed from an assemblage of several minerals. Thus to determine the resistivity of an aggregate rock a calculation is required which considers the combination of several materials with different resistivities. Several mixing models have been used to calculate the effective resistivity (or bulk resistivity) for a combination of different materials with different resistivities. The resistivities of each material, their volume fractions, and their geometries (i.e., isolated or inter-connected) can be used to calculate the effective resistivity.

In a rock with significant pore space that is saturated with fluid (e.g., with brines or partial melts), both the rock porosity and the pore fluid resistivity will control the bulk resistivity of the rock, while the resistivity of the rock matrix doesn't contribute and can be considered neglible. This relation was first quantified by Archie (1942) who showed that for a fluid-saturated rock the bulk resistivity can be written as

$$\rho = \rho_f \Phi^{-m} , \qquad \text{(Archie's Law)} \qquad \text{(Eq. 4.4)}$$

where ρ_f is the pore fluid resistivity, Φ is the porosity, and m is the cementation factor. The cementation factor relates to the permeability and is equal to 1 for crack-shaped interconnected pores and 2 or higher for spherical-shaped isolated pores. Resistivity is the inverse of conductivity, so this relation can be written in terms of conductivity, as

$$\sigma = \sigma_f \Phi^{m} . \qquad \text{(Archie's Law)} \qquad \text{(Eq. 4.5)}$$

Archie's Law is a simplification that assumes that the host rock resistivity is much higher than the fluid resistivity and that the only conducting pathway is through the pore fluid. This relation only works for media with one conducting phase. Although originally proposed for a system of rock grains and saline fluids, this equation has also been used for the situation where partial melt fills the pore spaces (e.g., Hermance, 1979; Watanabe and Kurita, 1993). Note this relation will not work when clay minerals are present, as these provide an extra conduction pathway through an electrical double layer (EDL) of cations that forms between the clay-fluid interface (Waxman and Smits, 1968).

A Modified Archie's Law proposed by Glover et al. (2000) allows two conducting phases to be considered, removing the assumption that the mineral grains of the host rock do not allow conduction. Modified Archie's Law can be written in terms of effective conductivity as

$$\sigma = \sigma_r (1 - \Phi)^p + \sigma_f (\Phi)^m, \qquad \text{(Modified Archie's Law)} \qquad \text{(Eq. 4.6)}$$

$$\text{with } p = \frac{\log(1-\Phi^m)}{\log(1-\Phi)}, \qquad \text{(Eq. 4.7)}$$

where σ_r is the rock conductivity and σ_f is the pore fluid conductivity.

The Hashin-Shtrikman bounds are another commonly used two-phase mixing model. The Hashin-Shtrikman upper and lower bounds represent the maximum and minimum bulk resistivity possible if the host rock and the pore fluid are connected in a series or a parallel fashion (Hashin and Shtrikman, 1962). This method allows the calculation of the minimum porosity required to cause the observed bulk resistivity values, and is often preferred over Archie's Law when the cementation factor is unknown. The Hashin-Shtrikman upper and lower bounds, abbreviated as HS+ and HS- (or HS-U and HS-L), can be written in terms of effective conductivity (Glover et al., 2000) as

$$\sigma_- = \sigma_r\left(1 + \frac{3\Phi(\sigma_f-\sigma_r)}{3\sigma_r+(1-\Phi)(\sigma_f-\sigma_r)}\right), \qquad \text{(HS-)} \qquad \text{(Eq. 4.8)}$$

$$\sigma_+ = \sigma_f\left(1 - \frac{3(1-\Phi)(\sigma_f-\sigma_r)}{3\sigma_f-\Phi(\sigma_f-\sigma_r)}\right). \qquad \text{(HS+)} \qquad \text{(Eq. 4.9)}$$

Figure 4.2 compares effective resistivities predicted by the mixing laws discussed above for the case of a medium with two phases. At low porosities Archie's Law gives values outside the range of either of the two phases, a clearly unphysical result. This occurs because Archie's Law assumes the host rock is infinitely resistive and that only one conducting pathway exists through the other phase (e.g., the pore fluid). Modified Archie's Law ensures that the resistivity at low porosity is equal to the resistivity of the first phase (e.g., the rock matrix). The Hashin-Shtrikman lower bound is generally preferred over Modified Archie's Law when the cementation factor is unknown, and provides a theoretical lower limit.

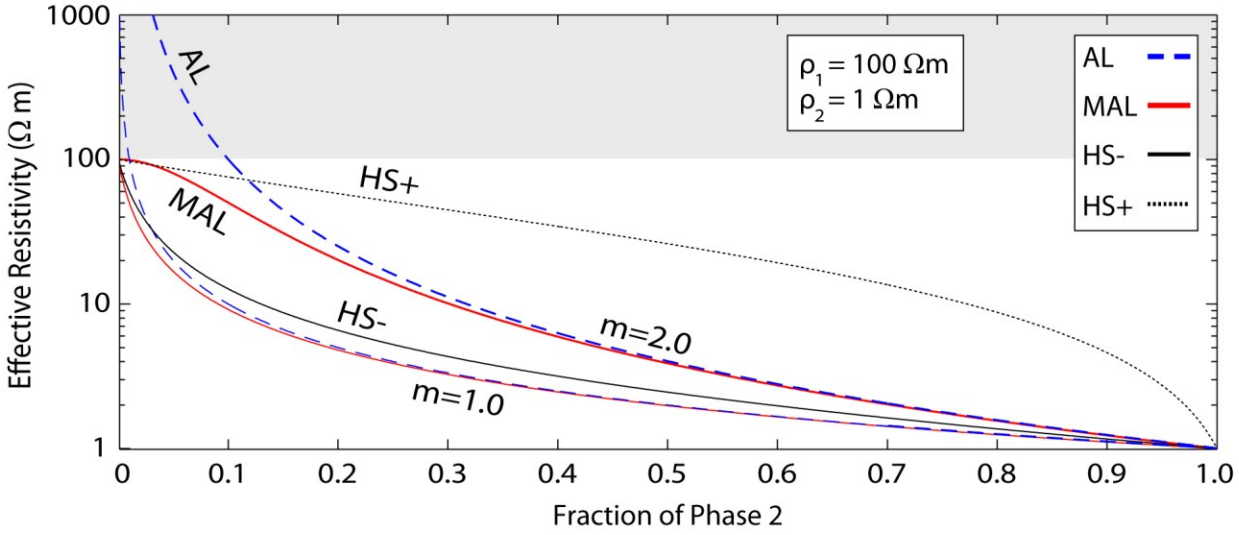

Figure 4.2: Effective resistivities computed by various mixing laws for the case of a medium with two phases (ρ_1=100 Ωm and ρ_2=1 Ωm; for example, conductive pore fluid in a resistive rock matrix). Archie's Law (AL; blue dashed line) and Modified Archie's Law (MAL; red line) are shown for cementation factors of m=1.0 (interconnected) and m=2.0 (isolated). The Hashin-Shtrikman upper bound (HS+; black dotted line) and lower bound (HS-; black line) are also shown. At low porosities Archie's Law gives values outside the range of either of the two phases (i.e., ρ > 100 Ωm; shown with a grey box), an unphysical result.

4.3 Electromagnetic Field Propagation in the Earth

4.3.1 Maxwell's Equations

Current understanding of electricity and magnetism can be succinctly summarized with Maxwell's equations (Maxwell, 1873). This set of equations describes the relationship between electric and magnetic fields and explains their propagation. Maxwell's equations are written below in terms of **E** and **B**:

$$\nabla \times \mathbf{B} = \mu\sigma\mathbf{E} + \mu\varepsilon\frac{\partial}{\partial t}\mathbf{E} \qquad \text{(Ampere's Law)}, \qquad \text{(Eq. 4.10)}$$

$$\nabla \times \mathbf{E} = -\frac{\partial}{\partial t}\mathbf{B} \qquad \text{(Faraday's Law of Induction),} \qquad \text{(Eq. 4.11)}$$

$$\nabla \cdot \mathbf{B} = 0 \qquad \text{(Gauss's Law for Magnetism),} \qquad \text{(Eq. 4.12)}$$

$$\nabla \cdot \mathbf{E} = \frac{\eta}{\varepsilon}, \qquad \text{(Gauss's Law),} \qquad \text{(Eq. 4.13)}$$

where **B** represents the magnetic flux (T), **E** is the electric field strength (V/m), μ is the magnetic permeability (H/m), which is a constant for each material, ε is the electric permittivity (f/m), which is a constant for each material, and η is the density of free electric charges (units of C/m^3) (Griffiths, 1999) (see Section 4.2.1 for more detail on electromagnetic material constants and constitutive equations).

Ampere's Law (Equation 4.10) quantifies how an electric field can create a magnetic field orthogonal to it. The first term is the conduction current, while the second term is the displacement current. The displacement current term was added by Maxwell in 1865, and is necessary to explain the existence of electromagnetic waves. Displacement currents can be considered negligible in MT exploration, as the conduction current has been shown to be dominant (Bahr and Simpson, 2005). Faraday's Law of Induction (Equation 4.11) shows how a time varying magnetic field can create an electric field orthogonal to it. Gauss's Law for Magnetism (Equation 4.12) states that no free magnetic charges exist (i.e., magnetic monopoles). Gauss's Law (Equation 4.13) states that electric charges act as sources for electric fields. These laws underscore the basic principles of electromagnetism.

4.3.2 The Propagation of EM Fields in the Earth

By taking the curl of Faraday's Law (Equation 4.11), substituting in Ampere's Law (Equation 4.10) on the right-hand side, using the vector calculus identity

$$\nabla \times (\nabla \times \mathbf{A}) = \nabla(\nabla \cdot \mathbf{A}) - \nabla \cdot (\nabla \mathbf{A}) = \nabla(\nabla \cdot \mathbf{A}) - \nabla^2 \mathbf{A}\,, \qquad \text{(Eq. 4.14)}$$

on the left-hand side, and assuming there are no free electric charges (i.e., $\eta = 0$, therefore $\nabla \cdot \mathbf{E} = 0$, from Equation 4.13), it can be shown that

$$\nabla^2 E = \mu\sigma \frac{\partial}{\partial t}\boldsymbol{E} + \mu\varepsilon \frac{\partial^2}{\partial t^2}\boldsymbol{E} \,, \qquad \text{(Eq. 4.15)}$$

see Simpson and Bahr (2005) for a complete derivation. Note that the first term comes from the conduction current and the second term comes from the displacement current, showing two distinct propagation methods for EM fields. Assuming a harmonic time dependence (i.e., $e^{-i\omega t}$), the ratio of displacement current to conduction current can be written from Equation 4.14 as $R = \omega\varepsilon/\sigma$. When the conductivity of the medium is very low or zero (e.g., in the air), or the signal frequency is high (e.g., above MHz), the displacement current dominates, and EM fields will propagate as waves (as in ground-penetrating radar methods). When the conductivity of the medium is not low, or the signal frequencies are low, then the conduction current term dominates, and EM fields will propagate diffusively (Simpson and Bahr, 2005). This occurs in all Earth materials.

Neglecting the displacement current, and assuming time variations in the electric and magnetic fields obey a harmonic time dependence (i.e., $e^{-i\omega t}$), Equation 4.14 can be simplified as

$$\nabla^2 \boldsymbol{E} = -i\mu\omega\sigma\boldsymbol{E} \text{ , or} \qquad \text{(Eq. 4.16)}$$

$$\nabla^2 \boldsymbol{E} = k^2 \boldsymbol{E} \qquad \text{(Helmholtz diffusion equation),} \qquad \text{(Eq. 4.17)}$$

where ω is the angular frequency, defined as $\omega = 2\pi f$, for frequency f (Hz), the reciprocal of period, T (s). The derivation can be done for the magnetic field as well. This type of equation is known as a Helmholtz diffusion equation, with a wavenumber $= \sqrt{-i\mu\omega\sigma}$, and a solution $\boldsymbol{E} = E_o e^{kz}$.

4.3.3 Signal Penetration Depth

When an electromagnetic wave intersects the surface of the Earth the majority of its energy is reflected, and only a small amount is transmitted into the Earth (approximately 1 part in 10,000). The energy is transmitted vertically downwards, regardless of the original angle of incidence of the wave. This is shown by Snell's Law and Figure 4.3 illustrates this idea. Snell's Law can be written as,

$$k_1 \cdot \sin\theta_1 = k_2 \cdot \sin\theta_2 \ , \quad \text{or} \quad \sin\theta_2 = \sin\theta_1 \frac{k_1}{k_2} \qquad \text{(Snell's Law).} \qquad \text{(Eq. 4.18)}$$

The wavenumber of the Earth is much higher than the wavenumber of the air (i.e., $k_1 << k_2$, so $k_1/k_2 \approx 0$), so the angle of refraction must be close to normal. Therefore, incoming EM signals travel vertically downward and travel diffusively through the Earth (as explained in Section 4.3.2).

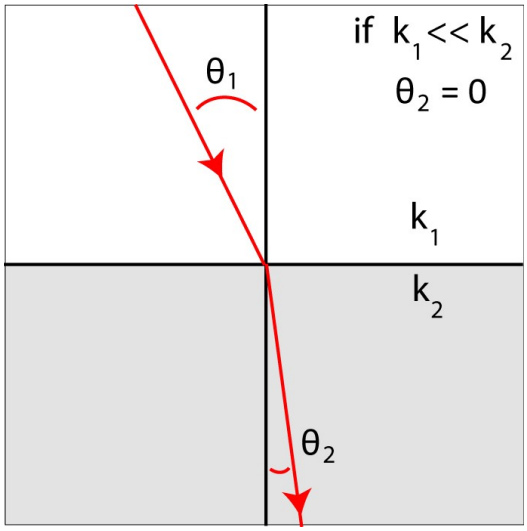

Figure 4.3: An illustration of Snell's Law. Electromagnetic energy incident on the Earth's surface is transmitted vertically downwards ($\theta_2 = 0$), because the wavenumber of the air is much smaller than the wavenumber of the Earth's surface ($k_1 << k_2$).

Once the EM waves enter the Earth they propagate downwards but their penetration is limited. The penetration depth of an electromagnetic wave is called the skin depth, and is defined as the depth at which the amplitude of the electric field decays to 1/e of its original value (approximately 37%) (Griffiths, 1999). This is the commonly accepted depth limit to which the EM signal samples the Earth resistivity in MT exploration. Taking the real part of the wave number from the Helmholtz diffusion equation (Equation 4.16), recalling that

$$\sqrt{-i} = \sqrt{1/2} - \sqrt{i/2}\,, \qquad \text{(Eq. 4.19)}$$

the skin depth in metres can be written as

$$\delta = \sqrt{\frac{2}{\mu_0 \omega \sigma}} = \sqrt{\frac{1}{\mu_0 \pi f \sigma}} = \sqrt{\frac{\rho T}{\mu_0 \pi}}\,, \qquad \text{(Eq. 4.20)}$$

where f is the frequency of the EM signal, T is its period, σ is the conductivity of the Earth, and ρ is the resistivity. Assuming a free space value for the magnetic permeability we can approximate the skin depth of an EM wave in metres as

$$\delta \cong 503\sqrt{\frac{1}{f\sigma}} = 503\sqrt{\frac{\rho}{f}} = 503\sqrt{\rho T}\,. \qquad \text{(Eq. 4.21)}$$

By examining Equation 4.21 it is obvious that the skin depth depends on both the resistivity and the period of the EM signal. The skin depth will be smaller in a less resistive environment, as can be expected as the EM signals decay faster in conductors. The skin depth will also be smaller for EM signals with smaller periods (high frequencies), as these too will decay faster. A layer of conductive material in the Earth can therefore limit the penetration depth of the EM signals, giving very little resolution below it.

4.4 Determining Subsurface Electrical Resistivity

4.4.1 The Electromagnetic Impedance Tensor

Once the horizontal electric and magnetic fields are converted to the frequency domain with a Fourier Transform the complex electromagnetic impedance, Z_{xy}, can then be defined as the ratio of the x-direction electric field and the y-direction magnetic field, written as

$$Z_{xy}(\omega) = \frac{E_x(\omega)}{H_y(\omega)}. \qquad \text{(Eq. 4.22)}$$

The impedance has units of ohms (Ω) and is a complex quantity (having both imaginary and real components) which depends on the angular frequency of the EM signal. We can define individual components of an impedance tensor **Z** in a similar manner. In tensor notation this can be written as

$$\begin{bmatrix} E_x \\ E_y \end{bmatrix} = \begin{bmatrix} Z_{xx} & Z_{xy} \\ Z_{yx} & Z_{yy} \end{bmatrix} \begin{bmatrix} H_x \\ H_y \end{bmatrix}. \qquad \text{(Eq. 4.23)}$$

The impedance tensor (or transfer function) contains information about the electrical structure of the Earth at each location where it is measured and at each frequency of the EM signal.

4.4.2 Apparent Resistivity

The apparent resistivity can be computed from the impedance. The apparent resistivity is equivalent to the average electrical resistivity of the Earth over a hemispherical volume with a radius of one skin depth. Therefore, by measuring the impedance over a range of frequencies the average resistivity over a range of volumes can be computed, showing how resistivity varies with depth. Similarly, by measuring the impedance at different surface locations lateral variations in

the resistivity can be detected and subsurface structures can be identified. From Faraday's Law (Equation 4.11) we can write

$$\mathrm{H_i} = \left(\frac{1}{\mathrm{i}\omega\mu}\right)\frac{\partial}{\partial z}E_j \ , \qquad \text{(Eq. 4.24)}$$

with $E = E_o e^{kz}$ and wavenumber $k = \sqrt{-i\mu\omega\sigma}$ from Equation 4.17, and $Z = E/H$ from Equation 4.22, so

$$\mathrm{Z} = \frac{i\mu\omega}{\sqrt{-i\mu\omega\sigma}} \ , \text{ or } \ \mathrm{Z} = \left(\frac{1-i}{\sqrt{2}}\right)\sqrt{\frac{\mu\omega}{\sigma}} \ , \qquad \text{(Eq. 4.25)}$$

and the apparent resistivity can be calculated as

$$\rho_{\mathrm{ij}}(\omega) = \frac{1}{\omega\cdot\mu}\left|\mathrm{Z_{ij}}(\omega)\right|^2 , \qquad \text{(Eq. 4.26)}$$

where subscripts i and j represent the x-direction or y-direction, in any combination.

4.4.3 Phase Angle

From the impedance data a phase angle can also be computed. Any complex number z, where

$$\mathrm{z} = \mathrm{x} + \mathrm{i}\cdot\mathrm{y} \ , \qquad \text{(Eq. 4.27)}$$

can be written in its polar form

$$\mathrm{z} = |\mathrm{z}|\mathrm{e}^{\mathrm{i}\theta}. \qquad \text{(Eq. 4.28)}$$

The modulus, or magnitude, is given by

$$|z| = \sqrt{x^2 + y^2}. \quad \text{(Eq. 4.29)}$$

While the phase angle, or argument, is given by

$$\theta = \arg(z) = \tan^{-1}\left(\frac{y}{x}\right). \quad \text{(Eq. 4.30)}$$

Similarly, the phase angle of any complex impedance tensor component can be written as

$$\theta_{ij} = \arg(Z_{ij}) = \tan^{-1}\left(\frac{\mathrm{Im}(Z_{ij})}{\mathrm{Re}(Z_{ij})}\right), \quad \text{(Eq. 4.31)}$$

where Im means the imaginary component of the complex number and Re means the real component, or from Equation 4.25,

$$\theta = \tan^{-1}\left[\left(\frac{1-i}{\sqrt{2}}\right)\sqrt{\frac{\mu\omega}{\sigma}}\right]. \quad \text{(Eq. 4.32)}$$

This phase angle represents the phase difference between the orthogonal electric and magnetic field components. For an EM wave traveling in free space (a perfect resistor) the orthogonal electric and magnetic field components will be in-phase (i.e., $\theta = 0°$). If the EM wave is traveling in a material (with $\rho < \infty$), then there will be a lag between the electric and magnetic field components, causing a phase difference. Generally the magnetic field will lag behind the electric field by 45° (Griffiths, 1999).

For a uniform Earth (e.g., a simple 1-D halfspace model) the phase difference will be 45° ($\frac{\pi}{4}$ radians). For an Earth where the resistivity varies with depth, the phase angle will vary from 45°. An increase in the resistivity will cause the phase angle to drop below 45°, while a decrease in the resistivity will cause the phase angle to pass above 45°. The apparent resistivity and phase angle are related through an exact equation (Weidelt, 1972), or also with an Hilbert transform (Boehl, et al., 1977). The phase angle can also be approximated as the slope of the resistivity curve when plotted against period (Weidelt, 1972; Vozoff, 1990). This can be written as

$$\theta \approx \frac{\pi}{4} \cdot \left(1 - \frac{d(\log_{10}\rho)}{d(\log_{10}T)}\right) = 45° \cdot (1 - \frac{d(\log_{10}\rho)}{d(\log_{10}T)}) \quad . \qquad \text{(Eq. 4.33)}$$

4.4.4 Apparent Resistivity and Phase Curves

The apparent resistivity and phase are computed for each frequency, at each MT station. A single MT station's data can be plotted to show how the apparent resistivity varies with frequency (or period) and, by proxy, with depth. The curves start with the shortest periods (shallow depths) and end with the longest periods (greatest depths) recorded by the instrument. Figure 4.4 shows an example of an apparent resistivity curve and a phase curve. Note that apparent resistivity and period are both plotted on a logarithmic scale. Apparent resistivity and phase curves for each component of the impedance tensor (e.g., the xy component, etc.) can also be plotted in a similar way.

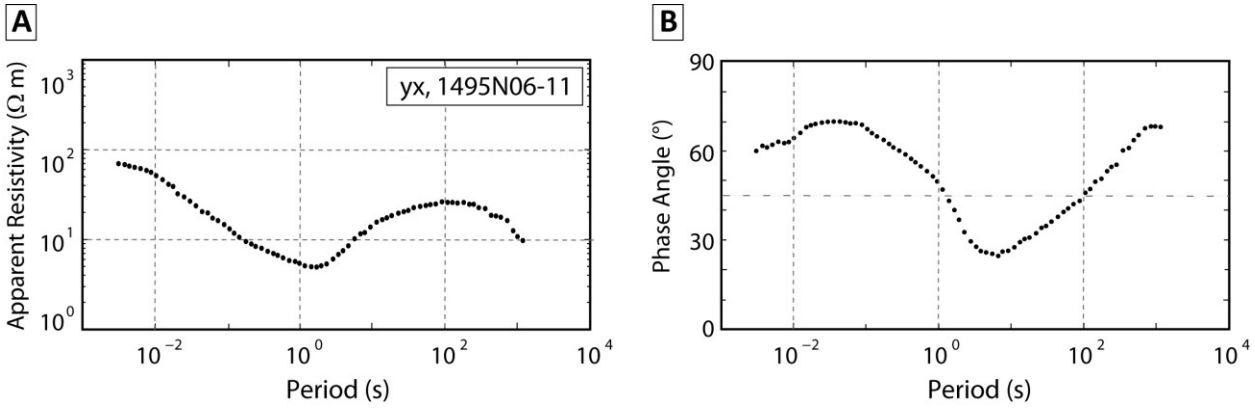

Figure 4.4: Apparent resistivity (A) and phase angle (B) are plotted against period, which acts as a proxy for depth. Shallow structure is seen at lower periods, and deeper structure at longer periods. The phase is below 45° when the apparent resistivity increases, and is above 45° when the apparent resistivity decreases. Note the log scales for both apparent resistivity and period. The MT data shown were collected near Volcan Uturuncu in Southern Bolivia; see Chapter 5 for details.

4.5 The Electromagnetic Impedance Tensor for a 1-D, 2-D, and 3-D Earth

4.5.1 The Electromagnetic Impedance Tensor for a 1-Dimensional Earth

The general form of the impedance tensor was shown in Equation 4.23. However, the impedance tensor can be simplified based on its dimensionality. The simplest form of the impedance tensor is for the case of a 1-D Earth, where the resistivity varies only with depth. In this situation the impedance tensor can be written as

$$\begin{bmatrix} E_x \\ E_y \end{bmatrix} = \begin{bmatrix} 0 & Z \\ -Z & 0 \end{bmatrix} \begin{bmatrix} H_x \\ H_y \end{bmatrix}. \qquad \text{(Eq. 4.34)}$$

Only orthogonal components of the magnetic and electric fields will be related, meaning the diagonal components (Z_{xx} and Z_{yy}) will be zero. The off-diagonal components (Z_{xy} and Z_{yx}) will have equal magnitudes, but opposite signs.

4.5.2 The Electromagnetic Impedance Tensor for a 2-Dimensional Earth

The simple case of a 1-D Earth, where the resistivity varies only with depth, is not very realistic. A better assumption is that the Earth resistivity structure is 2-D, meaning it varies both with depth and in one horizontal direction (for example along a profile). We can choose our coordinate system such that the y-direction is the only horizontal direction in which the resistivity changes (i.e., along profile); the resistivity is constant in the x-direction (i.e., across profile). In this scenario we can define the x-direction as the geo-electric strike direction, because the resistivity does not change along the strike direction. In this case, the impedance tensor can be written as

$$\begin{bmatrix} E_x \\ E_y \end{bmatrix} = \begin{bmatrix} 0 & Z_{xy} \\ Z_{yx} & 0 \end{bmatrix} \begin{bmatrix} H_x \\ H_y \end{bmatrix}. \qquad \text{(Eq. 4.35)}$$

In the perfectly 2-D scenario, only orthogonal components of the magnetic and electric fields are related, so the diagonal components (Z_{xx} and Z_{yy}) are equal to zero. In practice, if the measurement directions do not exactly align parallel and perpendicular to the geo-electric strike direction than the diagonal components will have small non-zero values. However, this simplifying assumption can be considered in many cases, but must first be carefully tested for each data set. Methods for testing dimensionality and geo-electric strike direction will be shown in Section 4.8.

4.5.3 TE and TM modes

In the idealized 2-D scenario it can be shown that Maxwell's equations decouple into two sets. When the electric field is polarized in the x-direction (i.e., the strike direction), known as the transverse electric mode (TE), magnetic field components are confined to the yz plane (i.e., H_y and H_z), and E_x and H_y are related and give the Z_{xy} impedance tensor component. When the magnetic field is polarized in the x-direction, known as the transverse magnetic mode (TM), electric field components are confined to the yz plane (i.e., E_y and E_z), and E_y and H_x are related and give the Z_{yx} impedance tensor component. In this scenario the x-direction is the geo-electric strike direction and so the diagonal elements (Z_{xx} and Z_{yy}) are equal to zero, as described above for an idealized 2-D scenario. We can calculate two different apparent resistivities and two different phase angles (see Section 4.4), one for each mode or direction, ρ_{xy} and ρ_{yx}.

The electric fields in the TM mode flow across the boundaries of a subsurface structure, while the electric fields in the TE mode flow along the structure, as illustrated in Figure 4.5. The TE and TM modes have different sensitivities to subsurface structures. In the TE mode configuration, electric current flows parallel to the geo-electric strike direction and therefore parallel to subsurface structures. The current flow doesn't cross boundaries and can therefore be considered inductive only. The response is completely frequency dependent. The TE mode is particular suited to identify conductors as electric currents are induced in a conductor.

In the TM mode configuration, electric currents flow perpendicular to the geo-electric strike direction. Therefore current flows across subsurface structure boundaries, giving the TM mode both an inductive and a galvanic component. As electric currents cross boundaries, charge build-up occurs, because the electric field is continuous across the boundary. These surface charges (free charges) exist at all frequencies, making the galvanic contribution of the response frequency independent. This is known as galvanic distortion (see Section 4.7). The TM mode has the largest response for resistors.

4.5.4 Tensor Rotation

When MT data are acquired in the field the geo-electric strike direction is usually unknown. In this case the electric and magnetic field components measured may not be aligned parallel or perpendicular to the strike direction, resulting in the case where the MT impedance tensor for a 2-D Earth has non-zero diagonal elements. To correct for this the impedance tensor can be mathematically rotated to a preferred coordinate system. The natural choice is one aligned with the strike direction, which has the advantage of minimizing the diagonal impedance tensor components (for a perfectly 2-D Earth these will equal zero). The rotated impedance tensor, Z_R, can be written as

$$Z_R = RZR^T , \qquad \text{(Eq. 4.36)}$$

where R^T is the transpose of the rotation matrix R. For a rotation angle φ, we can write the rotation matrix R as

$$R = \begin{bmatrix} \cos\varphi & \sin\varphi \\ -\sin\varphi & \cos\varphi \end{bmatrix} . \qquad \text{(Eq. 4.37)}$$

Figure 4.5 illustrates a situation where the magnetotelluric station coordinate system needs to be rotated to align with the 2-D geo-electric strike direction. Rotating the coordinate system to one which aligns with the strike direction is how TE and TM modes are defined.

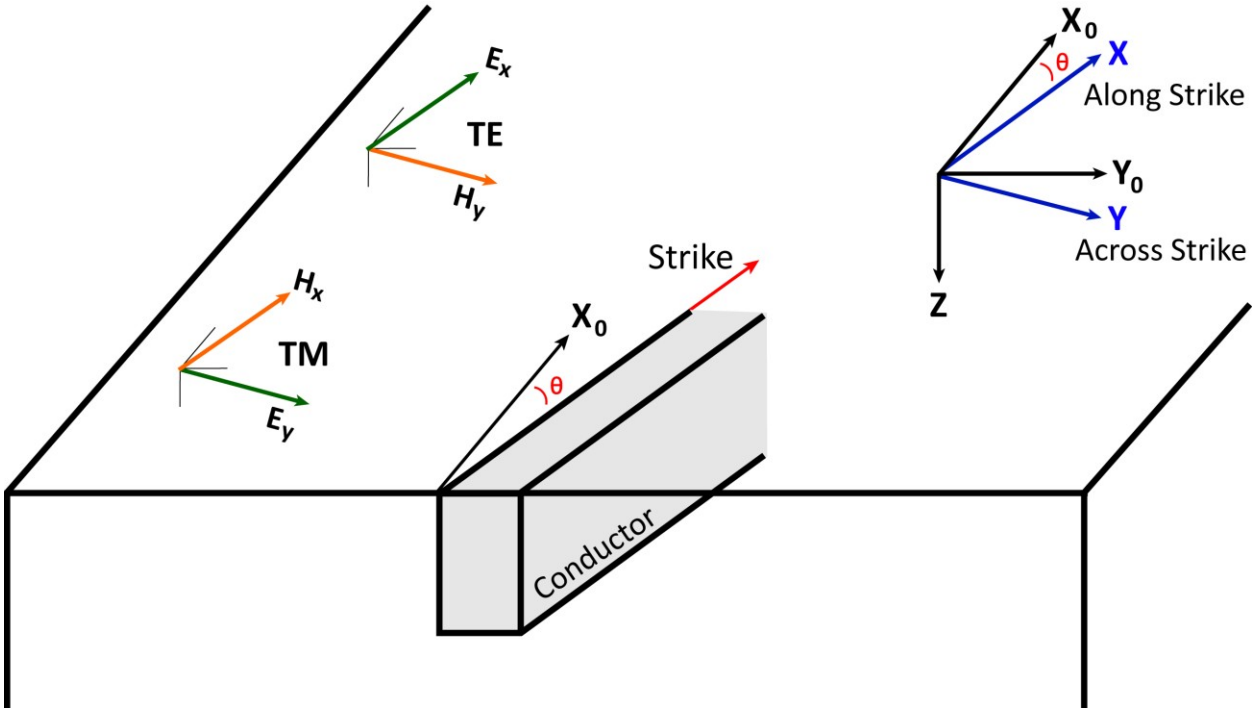

Figure 4.5: A 2-D Earth scenario with a conductor extending along a strike direction that is not aligned with the coordinate system. We can rotate our magnetotelluric station coordinate measurement system (X_0, Y_0) to that defined by the geo-electric strike direction (X, Y). The electric fields are then defined to flow either along strike (TE mode) or across strike (TM mode), simplifying our 2-D analysis.

4.5.5 The Electromagnetic Impedance Tensor for a 3-Dimensional Earth

True Earth structure is generally 3-D, that is, the resistivity varies with depth and in both horizontal directions. In this case the impedance tensor has non-zero values for all four tensor components. We can write this as

$$\begin{bmatrix} E_x \\ E_y \end{bmatrix} = \begin{bmatrix} Z_{xx} & Z_{xy} \\ Z_{yx} & Z_{yy} \end{bmatrix} \begin{bmatrix} H_x \\ H_y \end{bmatrix}. \qquad \text{(Eq. 4.38)}$$

In a 3-D resistivity structure, there is no well defined geo-electric strike direction. Maxwell's equations do not decouple into separate TE and TM modes, as in the 2-D case. Analysis methods for the full impedance tensor are more complicated, and need to only be considered if the data are 3-D and the 2-D approximation cannot be used.

4.6 Induction Vectors

Lateral variations in Earth resistivity will create vertical magnetic fields. These magnetic fields reverse direction when crossing over a conductor, and can therefore give useful information about lateral changes in resistivity. A magnetic transfer function **T** which relates the vertical and horizontal magnetic fields can be written as,

$$H_z = [T_{zx} \quad T_{zy}] \begin{bmatrix} H_x \\ H_y \end{bmatrix}. \qquad \text{(Eq. 4.39)}$$

This is commonly known as the tipper (Parkinson, 1959). The tipper is a frequency-dependent, complex quantity and so has both a real and an imaginary component. The tipper can be plotted in map view using its magnitude and its angle, giving information on the lateral structure of conductors. This is known as an induction vector (IV), and its magnitude is proportional to the strength of the subsurface conductor, which caused the induced vertical magnetic field (Jones and Price, 1970). The real component of IVs can be plotted in either the Parkinson convention so that they point towards conductors (Parkinson, 1959), or in the Wiese convention (Wiese, 1962), pointing away from conductors (used in this thesis).

The IVs contain independent information about the Earth's resistivity structure and are not affected by galvanic distortions (see Section 4.8 below). The IVs can also help to determine the dimensionality of the Earth because they align perpendicular to the geo-electric strike direction in a 2-D Earth (see Chapter 5).

4.7 Measuring and Processing MT Data

MT time series data are acquired by measuring electric field and magnetic field variations at the Earth's surface over hours or days. The time series data must be converted into the frequency domain with a Fourier transform in order to compute the electromagnetic impedance transfer functions, as described in Section 4.4. The apparent resistivity and phase are calculated from impedance values for multiple frequencies, giving insight into the electrical resistivity structure of the Earth's subsurface. Many time series processing schemes have been developed (e.g., Sims et al., 1971) and some incorporate remote reference techniques to reduce noisy data (see Section 4.7.2 below; e.g., Goubau et al., 1979), whereas more modern schemes are based on statistically robust processing (e.g., Egbert and Booker, 1986).

4.7.1 Measuring Time-varying Electromagnetic fields

Induction-coil magnetometers or fluxgate magnetometers are used to measure time variations of the magnetic field in MT exploration. The induction coil consists of a highly permeable ferrite core that acts as a magnetic field line concentrator, surrounded by copper wire windings. When the magnetic field changes along the coil axis, a voltage is induced in the coil windings. Three induction coils oriented orthogonally in the x, y, and z directions can be used to provide measurements of the three components of the magnetic field. Note that the vertical magnetic field data is only required for tipper and induction vector analysis, not impedance and resistivity calculations, and can be omitted if it is impractical. The induction coil magnetometer is a relative instrument because it measures only changes in the magnetic field, not absolute values. Induction coil magnetometers are available within the frequency range of ~ 30,000 Hz to ~3,000 s, practical for most MT exploration studies.

A fluxgate magnetometer has two separate coil windings around a ring-shaped core. By passing an alternating current through the primary coil the core goes through a cycle of magnetic saturation. The second coil measures an induced voltage from the changing magnetic field, and the input and output currents can be compared. In this way the magnitude and direction of the

external magnetic field can be measured. The advantage of this system is that it can measure the absolute magnetic field, not just time variations. Fluxgate magnetometers are commonly used for long-period MT data acquisition because they have a practical frequency range of approximately 1 - 30,000 s.

The electric fields can be measured with a dipole consisting of two electrodes with a known separation distance connected by a wire over which the voltage is measured. The electric field can be computed by the ratio of the voltage measured and dipole separation distance, $E = V/d$. The electrode must remain in contact with the ground and preferably be in an area which does not have high contact resistance (e.g., on rocks, or dry sand), as this will limit the signal strength. Figure 4.6 shows a schematic of a MT station. The voltage measured across electrical dipoles gives the electric field variations, while induction coil magnetometers measure the magnetic field variations.

A number of cycles at any given period must be measured so that errors can be statistically determined from the data distribution. Therefore the duration of the MT recording should be 10 - 100 times longer than the longest period of interest (Simpson and Bahr, 2005). For example, for a signal with a period of 100 s, data must be recorded for 1000+ s to ensure multiple cycles are recorded. Depending on the longest period signals desired, the instrument may be left in position for minutes (~1 s signals), hours (~100 s signals), days (1000+ s signals), or months (10,000+ s signals). See Chapter 5 for more information on data acquisition.

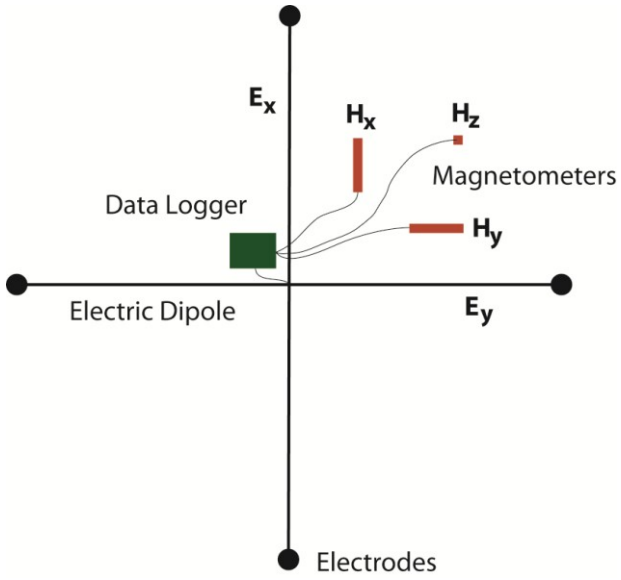

Figure 4.6. A schematic of a magnetotelluric field setup. Long (~100 m) electrical dipoles are used to measure both E_x and E_y field components. Induction coil magnetometers are used to measure H_x, H_y, and H_z field components. A data logger is placed at the centre, representing the station location.

4.7.2 The Remote Reference Technique

Contamination of MT data by noise can occur in a number of ways, such as from cultural sources (e.g., power lines at a frequency of 60 Hz, electric trains) or from atmospheric sources (e.g., local lightning discharges, wind vibrations). The remote reference technique proposed by Gamble et al. (1979) involves recording simultaneous data at two separate locations. When the MT data are being processed, both sets of data are compared and only correlated signals are kept. The noise present at each site will be random and uncorrelated, but the natural MT signal will be correlated, and so noise can be reduced in this way. The magnetic remote reference is preferred over an electric one because the magnetic fields are generally less contaminated by noise and vary less over large distances. Of course, this technique cannot remove noise that is coherent at both sites (Simpson and Bahr, 2005).

In general, the second site should be at a remote or electromagnetically quiet, undisturbed location, and can be run the duration of the survey and compared to each MT station collected. However, in some instances a roving remote reference can be used, as long as the two stations are recording data simultaneously and are far enough apart to record different noise.

4.8 Directionality and Dimensionality

Dimensionality analysis of the impedance tensor is required to determine if a one, two, or three dimensional approach to data analysis is required. If the data are found to be 1-D, then resistivity only varies with depth. If the data represent a 2-D Earth, then the resistivity varies both with depth and horizontally, across the geo-electric strike direction. For the 2-D case, a directionality analysis is required to determine the geo-electric strike direction. When the data are 3-D, there is no defined strike direction.

4.8.1 Dimensionality Parameters

For perfectly 2-D MT data the impedance tensor will have diagonal components equal to zero, when rotated to the geo-electric strike direction (see Section 4.5). If the data are noisy or not exactly 2-D (typically the case), then the diagonal components may be non-zero, but small and negligible (Jones and Groom, 1993). By rotating the impedance tensor to a strike angle which minimizes the diagonal components and maximizes the off-diagonal components, the Earth can be approximated as a 2-D structure.

The Swift skew can help to determine if the data can be considered 2-D (Swift, 1967). This quantity is defined as

$$\kappa = (Z_{xx} + Z_{yy})/(Z_{xy} - Z_{yx}), \qquad \text{(Eq. 4.40)}$$

and compares the diagonal and off-diagonal elements of the impedance tensor. The Swift skew does not depend on the coordinate system used or the rotation angle of the data, and is therefore a rotationally invariant quantity. Values less than 0.3 are commonly interpreted as indicative of 2-D behaviour. This method should be used with caution, as it is sensitive to noise (Chave and Jones, 2012).

The Bahr skew (or phase sensitive skew) uses a similar approach to the Swift skew (Bahr, 1988; Bahr, 1991). It is also a rotationally invariant quantity. It can be written explicitly as

$$H_z = \sqrt{\frac{2\cdot[\mathrm{Re}(Zxx)\cdot\mathrm{Im}(Zyx)-\mathrm{Re}(Zyy)\cdot\mathrm{Im}(Zxy)+\mathrm{Re}(Zxy)\cdot\mathrm{Im}(Zyy)-\mathrm{Re}(Zyx)\cdot\mathrm{Im}(Zxx)]}{[\mathrm{Re}(Zxy)-\mathrm{Re}(Zyx)]^2+[\mathrm{Im}(Zxy)-\mathrm{Im}(Zyx)]^2}}, \quad \text{(Eq. 4.41)}$$

where Re means the real component of a complex number and Im means the imaginary component, and Z_{ij} denotes the components of the impedance tensor (Lezaeta, 2002).

Bahr skew values above 0.3 are commonly interpreted as an indication of 3-D data. Values below 0.1 are considered to be 1-D, 2-D, or 2-D with distortion. Chave and Jones (2012) suggest that for cases of high noise (~10%) mis-interpretation is possible, as 3-D models can give skew values less than 0.3 for a third of the stations, and 2-D models may have values above 0.3 for a third of the stations. See Section 5.5 for an application to MT data.

4.8.2 Tensor Decomposition

Tensor decomposition schemes can be used to test if the data fit a 2-D assumption and to determine the geo-electric strike direction. A tensor decomposition scheme can separate the observed (distorted) tensor Z_0 into two parts, a regional (undistorted, 2-D) tensor Z_2 and a distortion tensor D (Groom and Bailey, 1989), written as

$$Z_0 = DZ_2 . \quad \text{(Eq. 4.42)}$$

The distortion tensor can be parameterized into four independent parameters, written as

$$D=gTSA\ , \qquad \text{(Eq. 4.43)}$$

where g is a constant scale factor known as site gain; T is the twist matrix, representing the rotation of electric currents to align with a regional strike; S is the shear matrix, showing the angular deflection of electric currents such that they are not orthogonal; and A is anisotropy, which occurs when the electric currents preferentially flow in one direction through the material, and results in different resistivities in different directions. The distortion tensor elements are real and independent of frequency (Chave and Smith, 1994). Parameters g and A are non-determinable, while T and S are determinable (Groom and Bailey, 1989). Parameter g can be included in the regional impedance tensor as a static shift (see Section 4.9.1), and may be accounted for in the 3-D inversion modelling. Both g and A have no effect on the geo-electric strike direction.

McNeice and Jones (2001) extended the tensor decomposition scheme to include multiple sites and multiple frequencies using a statistical approach. Geo-electric strike angle determination is therefore possible over any period band of the data and any subset of stations. Therefore, it is possible to see how the strike changes both with depth and along a profile. The assumption of 2-dimenisonality can be tested by measuring the misfit between the measured tensor (potentially distorted) and the regional (undistorted) tensor from the tensor decomposition scheme. If the Earth resistivity structure is truly 2-D, or can be approximated as 2-D, then the misfit should be low.

4.8.3 Phase Tensors

The phase tensor method (Caldwell et al., 2004; Bibby et al., 2005b) is an alternative to the tensor decomposition scheme. The advantage of the phase tensor method is that it gives information on dimensionality and geo-electric strike direction without imposing the condition of 2-dimensionality.

The complex impedance tensor can be written in terms of its real and imaginary components, as $Z = \mathrm{X} + \mathrm{iY}$. The phase tensor is then defined as the ratio of the real and imaginary components of the impedance tensor, and can be written in tensor form

$$\varphi = \frac{Re(Z)}{Im(Z)} = \frac{X}{Y} = \begin{bmatrix} \varphi_{11} & \varphi_{12} \\ \varphi_{21} & \varphi_{22} \end{bmatrix}. \qquad \text{(Eq. 4.44)}$$

The key advantage is that the MT phase tensor is not affected by galvanic distortions (Caldwell et al., 2004; Bibby et al., 2005b; Booker, 2014), so the regional (undistorted) phase tensor and the observed (distorted) phase tensor are identical. The phase tensor is analogous to the MT impedance phase.

The phase tensor can be plotted in map or pseudo-section view as an ellipse, with axes equal to the magnitudes of the maximum and minimum values of the diagonal phase tensor elements, $\varphi_{\min}$ and $\varphi_{\max}$. Figure 4.7 shows the phase tensor represented as an ellipse. We can also define a skew angle β as,

$$\beta = \frac{1}{2}\tan^{-1}\left(\frac{\varphi_{12}-\varphi_{21}}{\varphi_{11}+\varphi_{22}}\right). \qquad \text{(Eq. 4.45)}$$

For a 1-D Earth the phase tensor will plot as a circle, because $\varphi_{\min}$ and $\varphi_{\max}$ (φ_{11} and φ_{22}) have equal magnitudes. The values of φ_{12} and φ_{21} will be exactly zero, and so will the skew value, $\beta = 0$.

For a 2-D Earth, the phase tensor plots as an ellipse with the major axis equal to the magnitude of $\varphi_{\max}$. The skew value will be zero, $\beta = 0$, because the off-diagonal elements are zero. The principal axis will align with angle α, which is related to the geo-electric strike direction (for undistorted data).

For a 3-D Earth, all components of the phase tensor will be non-zero. The skew angle will be non-zero, $\beta \neq 0$, and measures the deviation from two dimensionality. The principal axis of the phase tensor ellipse will align with the angle $\alpha - \beta$. The angle $\alpha - \beta$ is the direction of greatest inductive current flow, the closest equivalent to a 2-D geo-electric strike direction. The phase tensor ellipses will therefore align perpendicular to the most conductive direction (Heise et al., 2006). The orientation of the ellipses will therefore rotate when crossing a conductor.

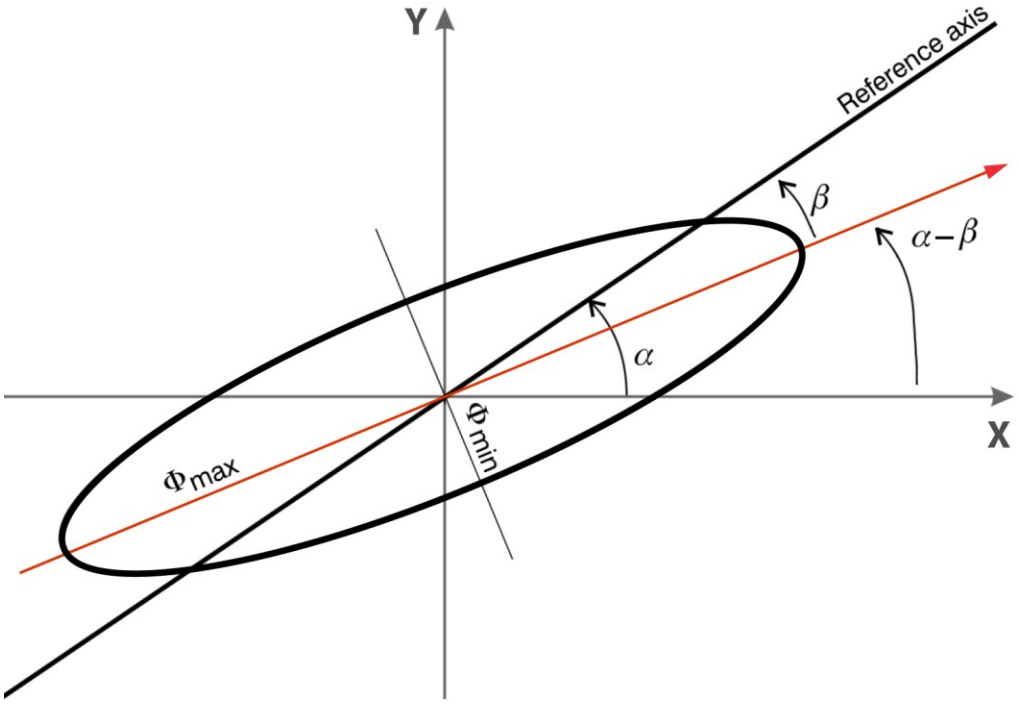

Figure 4.7: The phase tensor represented as an ellipse. The magnitudes of the minor and major axes are given by ϕ_{min} and ϕ_{max}. If the magnetotelluric data are 1-D these are equal and the phase tensor will be a circle. The skew angle β is non-zero if the data are 3-D, and acts as a measure of the deviation from two dimensionality. The angle $\alpha - \beta$ gives the orientation of the major axis, equivalent to a 2-D geo-electric strike direction. (*Figure adapted from Caldwell et al., 2004*).

4.9 Distortion

Near-surface conductors near a MT station which are small, compared to the skin depth, can cause distortion of the electric fields, and therefore of the impedances and apparent resistivities. These distortions are galvanic, and are frequency independent. All MT data can be thought of as a combination of two different effects: frequency dependent inductive effects caused by regional structures, and frequency independent galvanic effects caused by distortion from localized heterogeneities (Wannamaker et al, 1984). In order to eliminate the distortion the regional impedance must be separated from the distortion tensor, as described above (see Section 4.8.2 for details; see Chapter 5 for application to MT data).

4.9.1 Static Shifts

Distortion of the electric fields from localized near surface heterogeneities can cause the impedance and apparent resistivity to be scaled by a frequency-independent factor known as a static shift (Jones, 1988). The term static comes from the fact that the shifts are constant. On a log-log plot of apparent resistivity versus frequency the shape of the apparent resistivity curve remains unchanged, because the distortion is frequency independent, but the curve may be vertically translated (i.e., shifted), because the apparent resistivities (y-axis) are scaled by the static shift coefficient. However, the phase remains unaffected, as do the induction vectors.

Correcting for static shifts is important as they can cause artifacts in the inversion models (Jones, 1988). There are various methods used to correct for static shifts, but a common approach is to use other EM studies, such as time-domain electromagnetic (TDEM) measurements or direct-current (DC) resistivity measurements, to firmly establish the near surface resistivities (equivalent to high frequency in MT), and then shift the apparent resistivity curves accordingly. A popular computational scheme is to invert for both the resistivity and a static shift coefficient simultaneously with an iterative inversion algorithm (Rodi and Mackie, 2001; see Chapter 5 for application).

Topography can also create static shifts (Jiracek, 1990). Electric current lines will be forced to spread out in topography highs (lowering resistivity) and to concentrate in topography lows (increasing resistivity). These effects can be corrected by modeling the topography in the area being analysed. Figure 4.8 shows this effect for two MT stations from Bolivia which are separated by a distance of 3 km. The MT station shown in Panel A (1495N04-11) lies in the valley between San Antonio and Volcan Uturuncu, and the station shown in Panel B (1465O30-11) is located along the top of a 500 m tall ridge on the north slope of Volcan Uturuncu (see Chapter 5 for a map of the area described). The station located on the ridge top (Panel B) has a lower density of electric field lines and therefore exhibits a lower resistivity. The apparent resistivity curves are of similar shapes, but simply translated downwards. Note the phase curves remain unchanged.

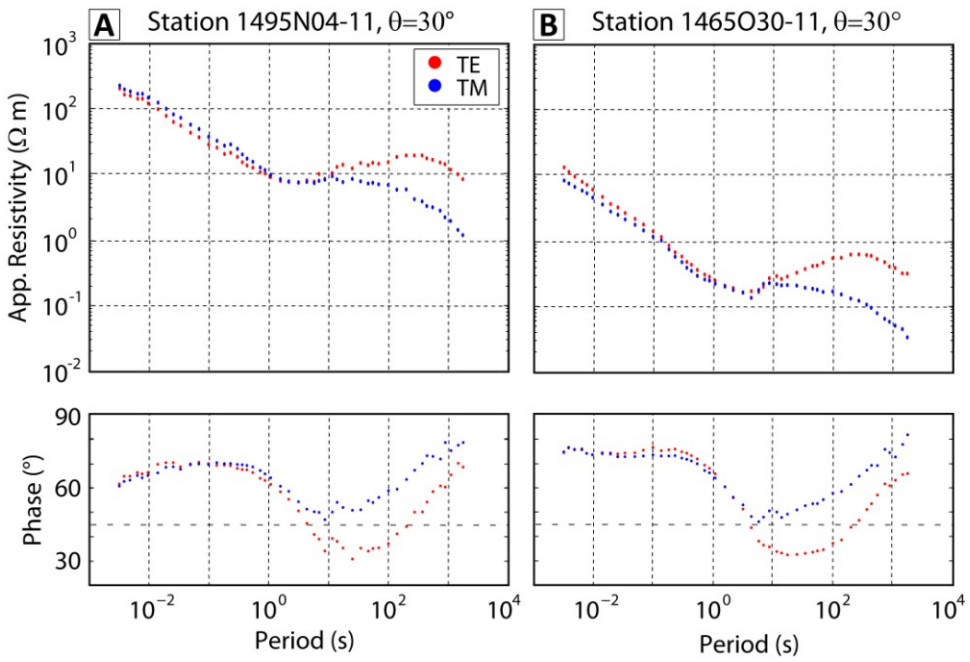

Figure 4.8: Static shifts can be caused by topography. Adjacent MT stations (3 km separation) show similarly shaped apparent resistivity and phase curves. However, the apparent resistivity values for Panel B, which sits on a ridge top, are shifted two orders of magnitude lower.

4.9.2 Electrical Anisotropy

Electrical anisotropy occurs when a material has different electrical resistivities in different directions. In the case of a rock, this can be caused by mineral or grain alignment in a preferred direction. This is very common for many materials in the crust (e.g., graphite layers) and also in the mantle (e.g., olivine) (for more detail refer to Simpson and Bahr, 2005). For an isotropic and 2-D Earth the off-diagonal components of the impedance tensor are non-zero, while the diagonal elements are zero. In practice they are not exactly zero but very small due to mostly noise, and can be set equal to zero. However, in doing this important information may be lost because the diagonal components of the impedance tensor may contain information on anisotropy.

Inversion of anisotropic MT data with a 2-D isotropic inversion algorithm can produce artefacts, because the assumptions being made are invalid. Commonly, the isotropic algorithm will use macro-anisotropy to fit the data, such as large alternating vertical dike features (Heise and Pous, 2001). Such features, when not consistent with the geology of the area, are clear evidence for anisotropic data. Heise et al. (2006) proposed using the shape and orientation of phase tensors to distinguish isotropic and anisotropic data. Unusual impedance phase data can also help to identify anisotropic data. Normally impedance phases from MT data are in the quadrant 0° to 90°, and anything outside this range is known as an out of quadrant phase (OOQP). Electrical anisotropy can cause OOQP, though there may exist other (isotropic) causes, such as complicated geology (Heise and Pous 2003).

4.10 MT Data Modeling and Inversion

After a thorough analysis of the MT data is carried out, including dimensionality and directionally analysis, modeling of the data can begin. To convert the apparent resistivity as a function of period into a resistivity model as a function of depth requires an algorithm such as an inversion algorithm. The inversion problem is non-unique, meaning more than one model can be produced that satisfies the constraints applied. Synthetic modeling can help to show the expected resolution and understand the reliability of certain features.

Mathematically, the inversion algorithm can be described as a minimization problem (e.g., Constable et al., 1987), with the algorithm searching for the minimum misfit between the observed data and the predicted data (from the model). The general approach is described below.

For any resistivity model **m**, forward modeling can give the predicted data ($\mathbf{d_p}$),

$$\mathbf{d}_\mathrm{p} = \mathbf{F}[\mathbf{m}] \, . \qquad \text{(Eq. 4.46)}$$

The inversion algorithm starts with an initial resistivity model (generally a simple halfspace) and iteratively updates the model, checking the fit to the MT data at each iteration step. A fit criterion must be established in order to do this. The fit between the observed data and the predicted data can be evaluated by the chi-squared misfit criterion (e.g., Constable et al., 1987). This is a weighted least squares misfit, with the data being weighted by their respective errors, written as

$$\chi^2 = \left\| \mathbf{W}(\mathbf{d}_\mathrm{o} - \mathbf{d}_\mathrm{p}) \right\|^2 , \qquad \text{(Eq. 4.47)}$$

where **W** is a diagonal weighting matrix, with elements equal to the inverse of the data error. The algorithm is said to have converged when the misfit is no longer reduced appreciable.

If the misfit is distributed statistically as chi squared (χ^2) with Gaussian errors, then the expected misfit value becomes N, the number of data points. This gives a root mean square (r.m.s.) misfit of 1.0. This is the ideal fit requirement, because the data are being fit by the model to within the error of each data point. The r.m.s. misfit expected can be adjusted as needed for noisy data.

The MT method cannot resolve sharp discontinuities, because MT signals travel diffusely through the Earth, and so an additional requirement is imposed by the inversion algorithms on the resistivity models to keep them as smooth as possible (Simpson and Bahr, 2005). Constraints such as smoothness can be added to Equation 4.47 by using the method of Lagrange multipliers. Roughness can be defined in several ways, including as the square of the model gradient. A

parameter, tau, can then be introduced that controls the trade-off between model roughness and data misfit. This ensures the data is fit acceptably, while the resistivity model remains reasonably smooth. The cost function, J, for the inversion algorithm can be written as,

$$J = \left\|\mathbf{W}(\mathbf{d}_o - \mathbf{d}_p)\right\|^2 + \tau\|\partial\mathbf{m}\|^2 , \qquad \text{(Eq. 4.48)}$$

where τ is the trade-off parameter between model roughness and data misfit. The cost function is minimized by taking its gradient. With knowledge of the expected structure we can introduce other constraints, such as horizontal or vertical smoothing (which may be controlled with a parameter alpha, α).

Inversion algorithms are now commonplace and can be run rapidly on modern computers. Two-dimensional inversion is the standard approach to model MT data. A number of algorithms are available (e.g., Constable et al., 1987; Siripunvaraporn and Egbert, 2005; Rodi and Mackie, 2001). It is common for MT data to be approximated as 2-D even when some 3-D effects are observed. If such effects are small, this approximation may not be a problem (Ledo, 2005). A widely used isotropic 2-D inversion algorithm is that of Rodi and Mackie (2001), which uses a non-linear conjugate gradients approach (NLCG). This inversion has been used throughout this thesis.

Algorithms for 3-D inversion are becoming widely used as computer technology is now able to provide the requirements of large amounts of computer memory and computer processing power, which can now be parallelized. The data-space 3-D inversion code of Siripunvaraporn et al., (2005; WSINV3D), used in the academic MT community, was used throughout this thesis.

4.11 Summary

The magnetotelluric (MT) method is a geophysical technique that uses temporal fluctuations of electric and magnetic fields measured at the Earth's surface in order to determine the spatial

variations of the electrical resistivity within the Earth. The theoretical basics of the MT exploration method have been explained and subsequent chapters will rely on these ideas and techniques to analyze and interpret the MT data collected for this thesis.

CHAPTER 5: MAGNETOTELLURIC DATA ACQUISITION AND ANALYSIS

5.1 Introduction

The primary focus of the research presented in this thesis is an investigation of the resistivity structure of the Altiplano-Puna Volcanic Complex, the underlying Altiplano-Puna Magma Body, and of Volcan Uturuncu, which has been observed to be inflating (see Chapter 3). By using magnetotellurics, as described in Chapter 4, the electrical resistivity structure can be studied and used to investigate magmatic processes. In this chapter MT data acquisition undertaken as part of the PLUTONS project in Bolivia and Argentina is described. An introduction to MT instrumentation and time series analysis is provided. The latter part of the chapter focuses on data analysis, with the concepts of dimensionality and directionality explained.

5.2 Magnetotelluric Instrumentation

The magnetotelluric system used for the research presented in this thesis was the V5 System 2000, developed by Phoenix Geophysics of Toronto. The system includes a data acquisition unit (or data logger) known as a MTU, electric sensors (electrodes), magnetic sensors (induction coils), and a power source, as shown in Figure 5.1. The University of Alberta owns two MTUs and two additional units were rented from the Polaris Canadian instrument pool, giving a total of 4 units. The MTUs are independent units that use GPS time signals for synchronization, allowing simultaneous recording for remote reference noise-reduction techniques (details in Section 4.7.2). The MTU weighs 4 kg, and its small size makes it easily portable (23 cm x 23 cm x 11 cm). The construction is rugged, consisting of an aluminum case with military-style connectors, and the broad operating temperature range of -20°C to +50°C makes them suitable for use in the harsh conditions encountered in the study area.

In the field, the configuration and spacing of the MTUs can be varied according to the requirements of the survey. Broad reconnaissance surveys may have station spacing of tens of kilometres, whereas a high-resolution survey may require several stations per kilometre. The standard mode of MTU operation records 5 channels of data (MTU-5; E_x, E_y, H_x, H_y, H_z). The electric field is preferably measured at a closer spacing than the magnetic field, because it shows more spatial variation between adjacent stations. Due to the fact that the magnetic sensors are larger and heavier than the electric sensors and that they require more labour to install, both effort and cost can be reduced by measuring the magnetic fields with a broader station spacing and measuring electric fields only at some stations (MTU-2E configuration, or 2-E type).

The recording operation of the MTU is controlled by a start-up instruction file written to the flash-card memory on the unit ahead of time, allowing the unit to turn on and record at a specified time, or can be directly controlled by a USB or parallel connection to a Windows-based laptop. Field conditions can be tough on a laptop (e.g., dust, rain), but controlling the MTU from a computer has the advantage that the user can see that the data recording is functioning properly and check for errors. All data files are stored on a Compact Flash card for easy data transfer. Recording data for a day gives approximately 100 MB of data.

5.2.1 Magnetic Field and Electric Field Sensors

To measure the magnetic fields induction coil type sensors were employed. The Phoenix MTC-50 magnetic induction coil has an overall length of 144 cm, a diameter of 6 cm, and a weight of 8 kg. Three of these induction coils, placed mutually orthogonal, measured the temporal changes in the magnetic field in the x, y, and z directions by measuring the voltage induced in a wire coiled around a ferrite core, as explained in Chapter 4.

The induction coils were buried in order to stabilize them. This was done for two reasons, the first of which is thermal stability. This is crucial on the Altiplano because the temperature fluctuates greatly from night to day (a change as large as ~50°C). The second reason is for

vibrational stability. Wind can vibrate the sensors, changing their directions and changing the field components they are measuring, which can create noise in the data. The long induction coils are difficult to bury in the often rocky and hard soil of the study area, specifically the vertical magnetic field (H_z) sensor. To overcome this problem shorter induction coils (Phoenix MTC-80H) were used for the vertical sensor after the first field season. In comparison, these induction coils weigh only 5 kg and measure 97 cm long. These shorter coils have a reduced response for periods longer than 3,000 s, and so are not useful for very long period data.

To measure the electric fields non-polarizing porous pot electrodes were used in an X-shaped dipole configuration. To reduce electric field noise and to ensure the signal was measureable, dipole lengths of 100 m in orthogonal arms were used (e.g., distance from North to South electrode). The electrodes were built at the University of Alberta from plastic tubing and a porous ceramic bottom plate. The electrodes measure 20 cm high and 10 cm in diameter, and weigh about 1 kg. The heavy-duty construction protects against weather and temperature variations, making them rugged and reliable in the field.

Following Petiau (2000), the electrodes were filled with a clay slurry to prevent polarization at low frequencies. The slurry consists of kaolin calcined clay (Al_2O_3•$2SiO_2$; 48.6 wt%), water (H_2O; 30.1 wt%), potassium chloride (K_2O; 20.0 wt%), lead chloride ($PbCl_2$; 1.2 wt%), and hydrochloric acid (HCl; 0.11 wt%).

Figure 5.1: (A) Components of the Phoenix V5-2000 MT system. Shown from left to right are: porous-pot electrodes, connection cables, magnetic induction coils (for x, y, and z components), a laptop to process and store data, the MTU data acquisition unit, and a GPS antenna for time synchronization. (*Photo from http://www.phoenix-geophysics.com).* (B) Installing a magnetotelluric site (1495O31-11). Photo was taken October 31, 2011, looking east towards Volcan Uturuncu.

5.2.2 Frequency Range

Broadband frequencies (300 - 0.0003 Hz, or a period of 0.003 - 3,000 s) recorded by Phoenix MT instruments were chosen for this project because they allow for imaging of both shallow features (< 1 km) and features at mid-crustal depths. Periods beyond 3,000 s were not collected because the long period data (10,000+ s) of Brasse et al. (2002) collected across the Altiplano were not able to penetrate the high-conductivity zone observed in the mid-crust (see details in Chapter 3). Furthermore, long-period instruments often do not have the resolution required to image shallow features (i.e., the upper few kilometres) because the fluxgate magnetometers used generally record a minimum period of 1 s (maximum frequency of 1 Hz; see Section 4.7.1). Therefore the broadband MT frequencies were considered an appropriate match for the goals of this thesis.

5.3 Field Campaigns and Data Collection

5.3.1 Study Area and MT Station Maps

This thesis focuses on the data recorded across the Altiplano and around Volcan Uturuncu, as shown in Figure 5.2 and Figure 5.3. Figure 5.2 shows a map of the expanded study area. The locations of all 225 MT stations (representing 254 total runs) are shown (red dots). The approximate limits of the inflation and subsidence around Volcan Uturuncu are shown (pink circle, purple circle; Henderson and Pritchard, 2013). Similarly, the approximate limit of the inflation around Lazufre is shown (pink circle, no subsidence detected; Henderson and Pritchard, 2013). The extent of the Altiplano-Volcanic Complex (APVC, de Silva, 1989) (see Chapter 2 for more detail), and the seismically-inferred limits of the Altiplano-Puna Magma Body (APMB) are also shown (see Chapter 3 for more information). The APVC, the APMB, and the surface deformation pattern are all coincident, with Volcan Uturuncu centered above them. The topographic base maps used for this figure (and other similar figures) was created with the Generic Mapping Tools (GMT) package of Wessel and Smith (1991).

Figure 5.3 shows a topographic map with the location of 187 MT stations deployed in Bolivia and NW Argentina colour coded by year acquired. Locations discussed throughout the thesis are identified for easy reference. A regional profile extending ~250 km across the study area (Profile 1) runs west-east across Volcan Uturuncu, from Laguna Colorado near the Bolivia-Chile border to Abra Pampa in NW Argentina (marked with letters A, B, and C).

Stations located in Bolivia generally have inter-station spacings of ~3 km. The stations in a network on and around Volcan Uturuncu have a denser (~1 km) average spacing. The Vilama line in North-Western Argentina has a MT station spacing of ~4 km, with some wider gaps of ~7 km. The Lazufre profile across the Puna has an inter-station spacing of ~4 km. This dense MT station spacing ensured high-resolution imaging of the near surface structures.

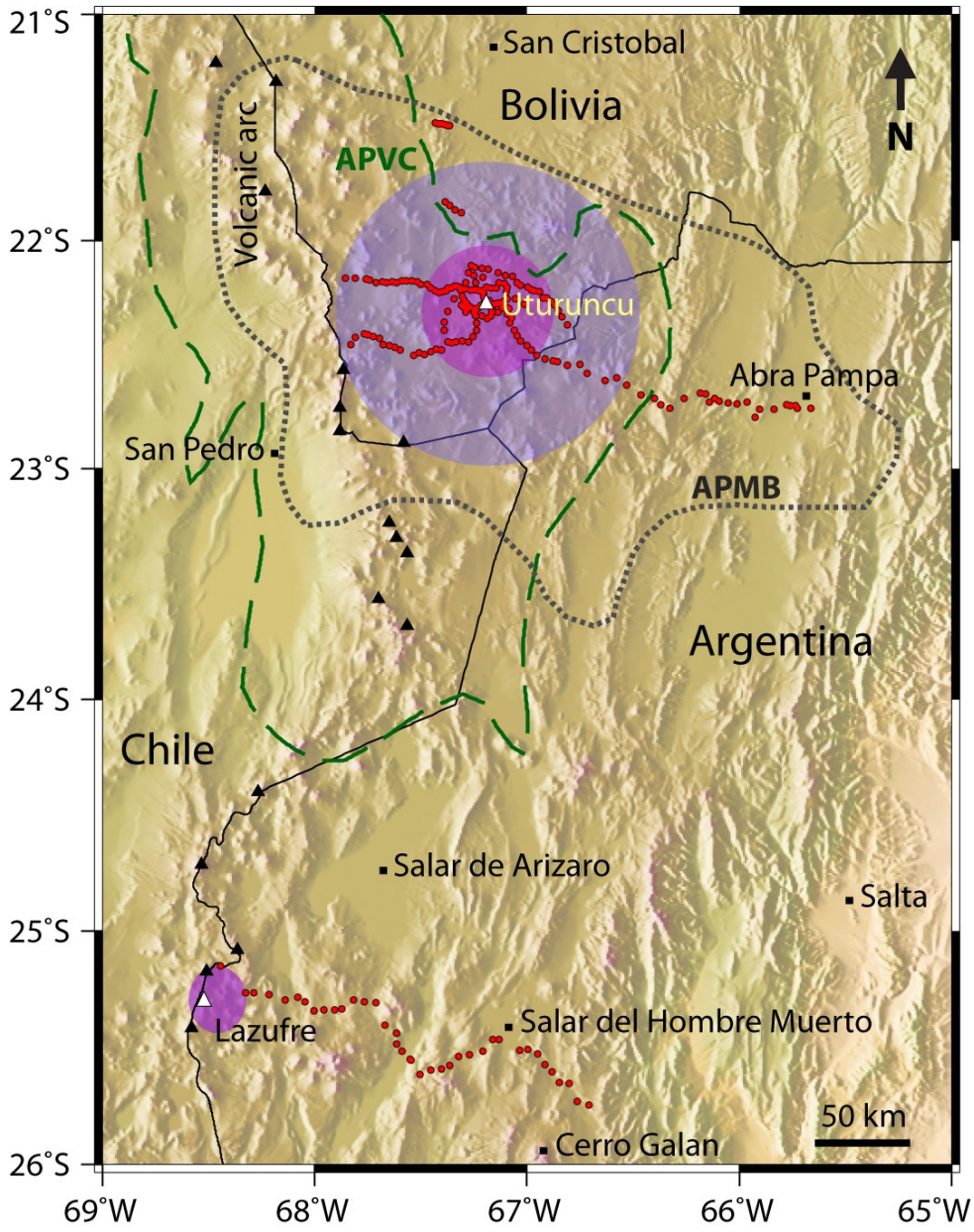

Figure 5.2: A topographic map showing the locations of all 225 magnetotelluric stations (red circles). The thin black line marks the international border. Pink circle shows the approximate limits of inflation deformation for both Uturuncu and Lazufre; purple circle shows the subsidence observed at Uturuncu (Henderson and Pritchard, 2013). Green broken line marks the extent of the Altiplano-Volcanic Complex (APVC; de Silva, 1989). Dotted grey line marks the limit of the seismically-inferred Altiplano-Puna Magma Body (APMB; Zandt et al., 2003). Black triangles mark major volcanoes along the modern volcanic arc. Places of interest are marked with black squares.

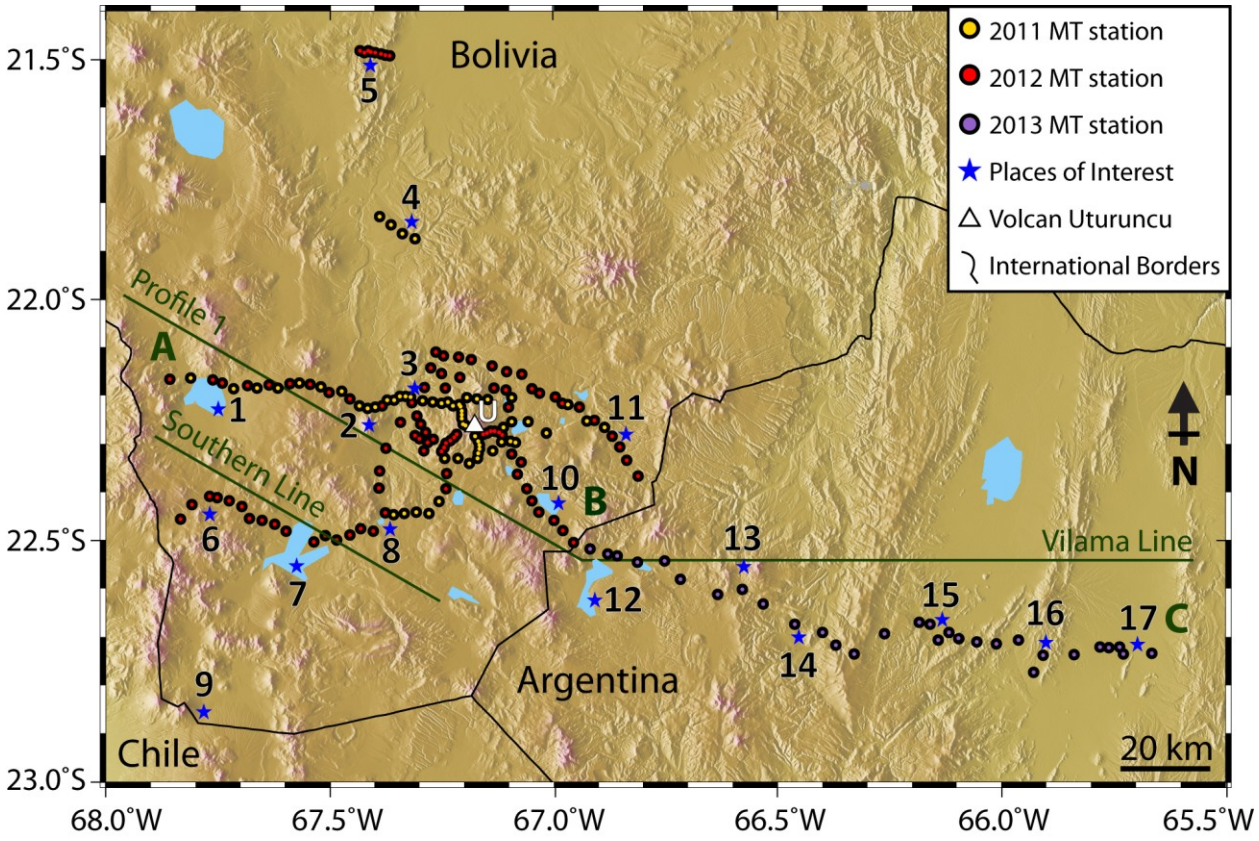

Figure 5.3: A topographic map showing the locations of 187 magnetotelluric stations (circles) collected in 2011 (yellow), 2012 (red), and 2013 (purple) in Bolivia and NW Argentina. Thin black line marks the international borders. Green letters A, B, and C mark the location of Profile 1, a long transect from the western-most station to the eastern-most station over Volcan Uturuncu. Volcan Uturuncu is marked by a white triangle and the letter U. Places of interest are marked by blue stars and identified with a number. 1 - Laguna Colorado; 2 - Volcan Quetena; 3 - Quetena Chico; 4 - Soniquera; 5 - Cerro Gordo; 6 - Sol de Manana; 7 - Salar de Chalviri; 8 - Laguna Hedionda; 9 - Laguna Verde; 10 - Laguna Coruto; 11 - Rio Chilenas; 12 - Laguna Vilama; 13 - Volcan Granada; 14 - Mina Pirquitas; 15 - Mungayoc; 16 - Cochinoca; 17 - Abra Pampa.

5.3.1 2010 Field Season

The Altiplano of Bolivia is a difficult place to work, mostly due to its remote access and the harsh environment. The first excursion to Volcan Uturuncu in the Fall of 2010 was primarily a logistical visit and no MT data were collected. Reconnaissance of the field area near Uturuncu was carried out, and logistical questions such as the availability of water and gasoline, lodging, and road conditions were addressed. Lodging was available in the Alcalde's (municipal magistrate) hostal in Quetena Chico, a small town (population ~300) at the foot of Volcan Quetena, within the bounds of the Area Protegido Eduardo Avaro, Sur Lipez Province. Fuel and food were available in Uyuni (population ~10,000), an eight hour drive northwards. This area has only a few major roads (i.e., Quetena to: Laguna Colorado, Laguna Verde, Soniquera) and identifying easily accessible areas for station deployment was a priority during this field season.

5.3.2 2011 Field Season

The second field excursion occurred in the Fall of 2011. Due to unforeseen delays in shipping equipment to Bolivia and arranging customs clearance, it was only possible to acquire data in the study area around Volcan Uturuncu for 19 days of the 65 days spent in Bolivia. During the 2011 field season MT data were collected at 57 station locations. Some stations were repeated or re-occupied, either to collect higher quality data, more data, or to check consistency, giving a total of 64 instrument runs. Of the 57 stations, 19 were 2-E type stations, where only the electric fields were measured and the magnetic fields needed to compute apparent resistivity values were provided by nearby stations. Vertical magnetic field data (H_z) were recorded at 36 stations. Between Cerro Gordo and Agua de Castilla (~90 km north of Volcan Uturuncu) 8 supplementary stations were acquired over 2 additional days of data collection. This area is thought to host a significant mineral deposit; these MT data are not included in this thesis. Figures 5.2 and 5.3 show the location of MT stations on a topographic map, colour-coded by year collected. Locations discussed in the text are identified there for reference.

The 2011 field season concentrated on a northern transect extending west-east from Laguna Colorado through Quetena, and over Volcan Uturuncu (Profile 1; see Figures 5.2 and 5.3). Volcano Uturuncu (elevation of 6008 m) is accessible by a dirt track which ascends to the col between its twin summits at an elevation of 5700 m. Stations were deployed along this track and at the summit col. A trek on the south side of the volcano was required for the installation of 4 stations on the volcanic edifice. The average elevation of stations was 4670 m, with the highest station at 5760 m and the lowest at 4160 m. Based on the MT data collected in the 2011 field season priority areas for further investigations were determined.

5.3.3 2012 Field Season

The third field excursion to Volcan Uturuncu occured in the Fall of 2012. Approximately two months were spent in Bolivia with 36 days in the field area recording data. Data were collected at 92 station locations (112 total runs), with 42 of these being 2-E type stations. Vertical magnetic field data (H_z) were recorded at 38 stations. The average elevation of stations was 4570 m, with the highest station at 5230 m and the lowest at 4060 m.

During this field season a southern transect was completed from Sol de Manana to Laguna Hedionda (Southern Line, see Figures 5.2 and 5.3). More MT stations were added on the previous year's northern transect, making it more dense, and additional MT stations near Rio Chilenas and Laguna Coruto were installed, extending the transect farther east (segment AB of Profile 1, see Figures 5.2 and 5.3). Two treks were carried out up the volcano's flank on the east side (4 stations) and south-west side (4 stations). In order to assess the northern bounds of the study area, 4 MT stations were deployed near Soniquera, 40 km north of Quetena.

5.3.4 2013 Field Season

The final field campaign took place in the Fall of 2013 in Argentina. Approximately two months were spent in Argentina, with 31 days in the field area recording MT data. Data were collected at

68 station locations (70 total runs), with 14 of these being 2-E type stations. Vertical magnetic field data (H_z) were recorded at 44 stations.

During this field season the west-east profile across Volcan Uturuncu in Bolivia was extended from the Bolivian border near Laguna Coruto and Laguna Vilama through Mina Pirquitas and as far east as Abra Pampa (30 stations; Vilama Line, segment BC of Profile 1, see Figures 5.2 and 5.3). A second profile was collected farther south on a transect from the Lazufre volcanic area on the Chile-Argentina border east through Antofalla and past the Salar de Hombre Muerto to within 25 km of Tacuil, north of Cerro Galan (38 stations; Lazufre/Puna Line). On the Lazufre profile across the Puna, the average elevation of stations was 4060 m, with the highest station at 4550 m and the lowest at 3350 m. In the north, along the Vilama line, the average elevation of stations was 4010 m, with the highest station at 4720 m and the lowest at 3590 m.

5.3.6 Geo-Magnetic Activity Indices

As described in Chapter 4, the MT exploration method uses the time variation of naturally occurring magnetic and electrical fields both from terrestrial and extra-terrestrial signals as energy sources. The K-index measures the amplitude of fluctuations in the horizontal components of the Earth's magnetic field. The K-index is determined by measuring the maximum fluctuation of the geo-magnetic field in nT over a 3-hour time interval and converting it to a logarithmic scale which ranges from 0 to 9 (for more information see Bartels et al., 1939). Over the course of a day, 8 K-indices are measured and these can be averaged to give a daily geo-magnetic fluctuation, known as the A-index. A-indices are measured at 13 geomagnetic observatories around the globe and are averaged globally to provide a daily Planetary A-index, or Ap (Allen, 1982). The A-index ranges from 0 to 400, with values of 0-20 representing quiet magnetic activity, 20-60 representing an active magnetic field, and 60-400 representing a magnetic storm.

Geo-magnetic activity indices are published by the Space Weather Prediction Center of the National Oceanic and Atmospheric Administration and historical values are available online.

Figure 5.4 shows historical Planetary A-index values for the duration of each field season. The median Ap value observed for all three years is 4.0, which represents quiet magnetic activity. Magnetic activity creates good signals for MT, but geomagnetic storms may cause noise or signal saturation at the magnetometer and collecting data during such storms should be avoided.

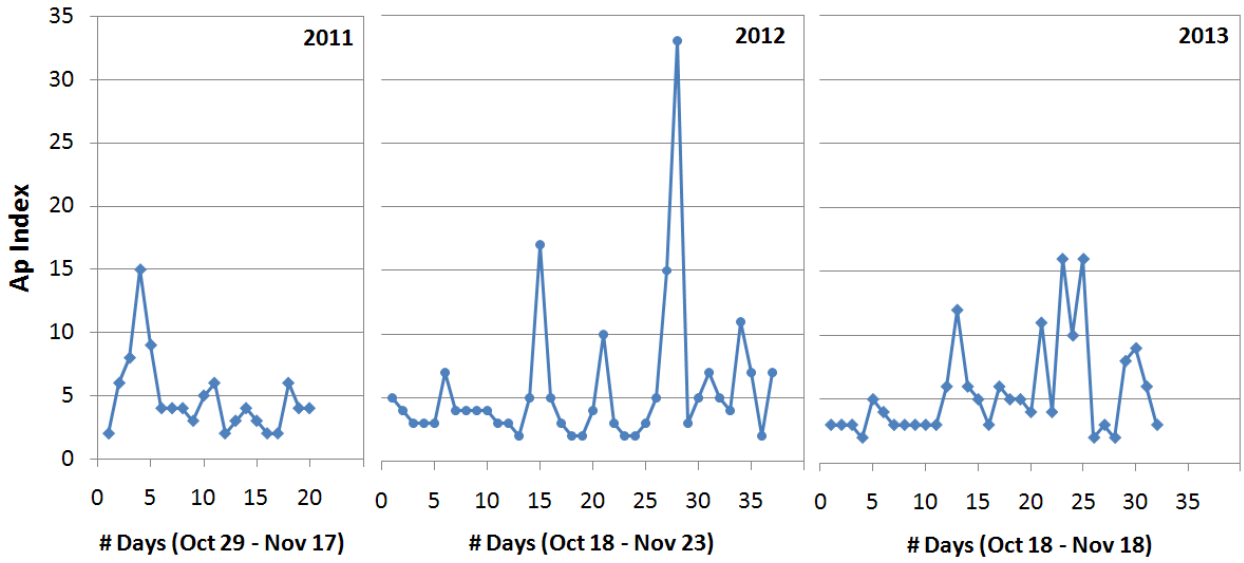

Figure 5.4: Magnetic activity shown as Ap indices during each field season when magnetotelluric data was recorded. Magnetic activity was generally quiet, with a median Ap value of 4.0. (Historical geo-magnetic data is from The Space Weather Prediction Centre, *ftp://ftp.swpc.noaa.gov/pub/indices/old_indices/*).

5.4 Time Series Analysis

MT time series data is acquired in the time domain by measuring electric field and magnetic field variations at the Earth's surface for a period of hours or days. In order to determine the subsurface resistivity the time series data are converted into the frequency domain with a Fourier transform and the electromagnetic impedance transfer functions are computed, as described in

Chapter 4. Calculating the apparent resistivity and phase for multiple frequencies gives insights into the electrical resistivity structure of the Earth's subsurface.

The time series data are inspected closely to ensure that they are not influenced by noise. A visual inspection of the time series data is an important check for data quality and sections containing noise from external sources, broken wires, or otherwise, should be excluded. Data consistency between MT stations can also be checked. The horizontal magnetic fields at adjacent stations should be similar, with only small differences between them. This occurs because the sources for these magnetic fields are far away from the observation point, located within the Earth's ionosphere. This is in contrast to the horizontal electric fields, which can show larger variations from site to site because their amplitudes are controlled by the subsurface electrical resistivity structure of the Earth.

Figure 5.5 shows an example of magnetotelluric time series data from station 1495N06-11, located east of Volcan Uturuncu near Laguna Mama Khumu. The MTU records data in three bands, with sampling rates of 2400 samples/s, 150 samples/s, and 15 samples/s (shown in Figure 5.5). Note that there is strong correlation observed between orthogonal electric and magnetic fields. The signals recorded are composed of various super-imposed periods, with the dominate signal observed at a period of ~30 s, which is caused by a magnetospheric oscillation (Pc3 signal).

In this thesis, MT data processing was implemented with the software package SSMT2000 from Phoenix Geophysics and the results were verified by processing with the statistically robust scheme of Egbert and Booker (1986). After performing a Fourier transform on the time-series data multiple events were robustly stacked and remote reference techniques were applied in order to reduce noise (see Section 4.7.2). The electromagnetic impedance transfer functions were then computed, and apparent resistivity and phase was calculated for each frequency (see Chapter 4 for details).

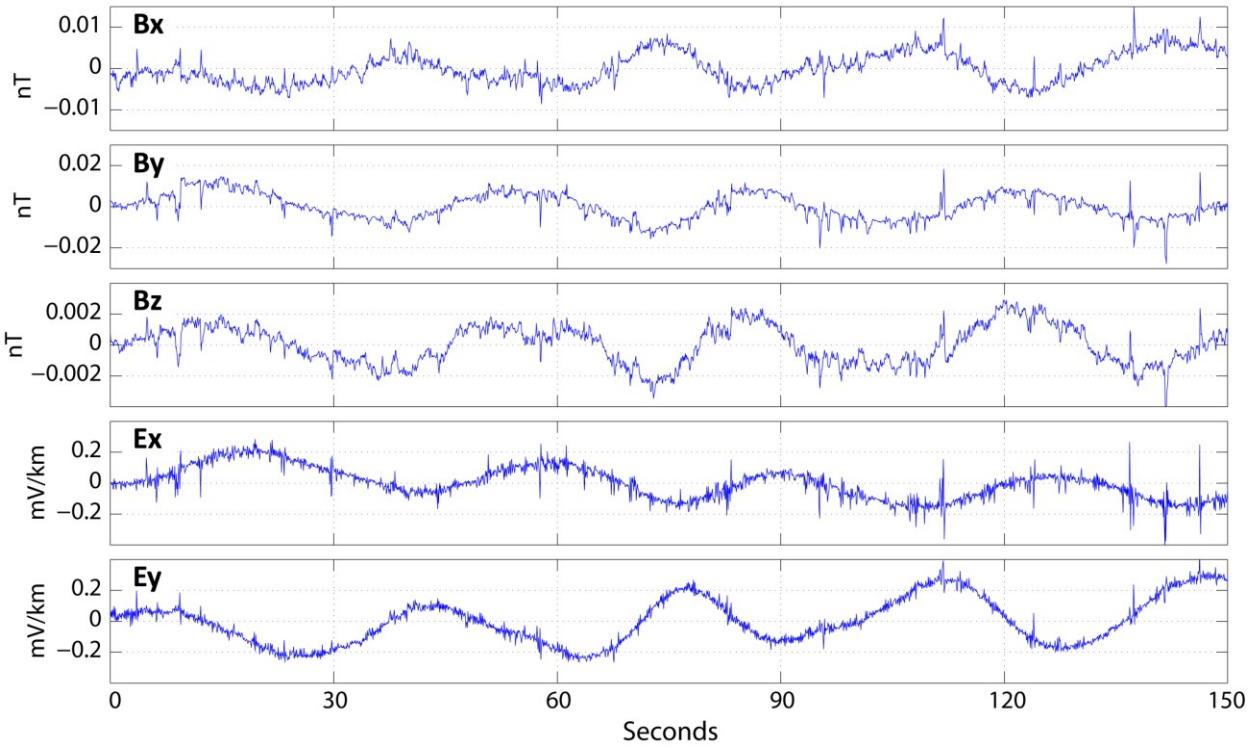

Figure 5.5: Time series for 5 channels of magnetotelluric data from station 1495N06-11. E_x and E_y are the two orthogonal horizontal components of the electric field. B_x, B_y, and B_z, are the three components of the magnetic field. Note the correlation between B_x and E_y, and between B_y and E_x. The sampling rate is 15 Hz, the lowest the instrument can record. Time is measured from 11:25:24 UTC, on November 7, 2011.

5.4.1 Apparent Resistivity and Phase Curve Types

Owing to the remote location, and large distance from sources of electromagnetic noise, most MT stations in the study area produced high quality data. Three distinct types of MT sounding curves were observed across the study area. Figure 5.6 shows apparent resistivity and phase angle plotted against period for three stations that are representative of the distinct styles observed, as described below. As described in Chapter 4, MT data are displayed in a given coordinate system and the curves appear different as they are rotated to a different coordinate system (e.g., in order to align with the geo-electric strike). The data shown in Figure 5.6 have

been rotated to the strike direction determined by the dimensionality analysis in the Section 5.5 (N30°E for Panels A and B; N0°E for Panel C). The transverse electric (TE) mode apparent resistivity is derived from electric currents flowing along strike and the transverse magnetic (TM) mode from currents flowing across strike.

The primary interest in the MT data are low-resistivity zones or conductors, and what may be causing them. Low resistivity in a volcanic environment can be caused by aqueous fluids, partial melt, or hydrothermal alteration, so interpretation must use additional geophysical data and laboratory studies of fluids and melts to distinguish between these possibilities (Chave and Jones, 2012). Chapters 6 and 7 provide a detailed interpretation.

Type 1

The first type of apparent resistivity curve (shown in Figure 5.6 Panel A) is the most commonly observed in the study area. The resistivity is relatively high (~100-1000 Ωm) at the shortest periods (<0.01 s), which represents depths from the surface to less than 1 km. This is due to the fact that most MT stations in the study area were placed on rocky terrain, or in dry sand, which act as resistors. At stations where the soil was less dry (near valley bottoms, or near vegetation) the surface resistivity observed is lower. The resistivity drops to a minimum value around a period of 2 s, representing a shallow conductor (~10 Ωm), labelled C1. This conductor is likely caused by a shallow aquifer or hydrothermal alteration within the ignimbrite layer (see Chapters 6 and 7 for a more detailed interpretation).

The resistivity then increases to moderate values (~30 Ωm), before starting to decrease again around 300 s, and continues decreasing to the longest period data recorded (3,000 s), indicating a strong conductor (< 3 Ωm) located deep in the mid-crust (15-30 km). This conductor is likely caused by the APMB, which is known to be a high conductivity zone at approximately these depths (see Chapter 3; Schilling et al., 2006). The phase angle should show a consistent pattern with the resistivity curves. As described in Chapter 4, as the resistivity drops the phase angle increases, and if the resistivity is constant, then the phase angle will be 45°. The phase curve

shows the phase increasing steadily at the longest periods towards 80°, consistent with a strong, deep conductor.

Type 2

The second type of apparent resistivity curve (Figure 5.6, panel B) is seen at only 27 stations. It shows a particular geographic distribution and can be seen at only two areas: either between Volcan Uturuncu and Volcan Quetena, or near Sol de Manana, at the western edge of the study area. It shows the same layered structure with two resistivity minima seen in the first curve type representing a shallow conductor and a deep conductor interpreted as the APMB, but also includes a third resistivity minimum at a period of ~20 s. This indicates complex structure below the volcanic complex. The conductive anomaly seen at ~20 s (labelled C4) is a subtle effect but tells us important information. This indicates a conductor (<10 Ωm) in the upper crust (depths of 2-10 km).

Type 3

The third type of apparent resistivity curve (Figure 5.6, Panel C) is relatively flat and has very minor resistivity variations with period. This curve type is seen at 9 stations in NW Argentina east of Mungayoc at the eastern-most end of the study area, and also at 3 stations near the western edge of the study area near Laguna Colorado. The flat shape indicates the Earth below the station has a relatively homogenous structure and has no significant conductive anomalies. This is likely caused by the absence of the APMB. This type of curve is observed only at locations near the edges of the study area and therefore helps to define the edges of the APMB. The phase curve shows small oscillations about 45°, never exceeding 55°. This shape indicates no conductive anomaly at depth, consistent with the resistivity curve.

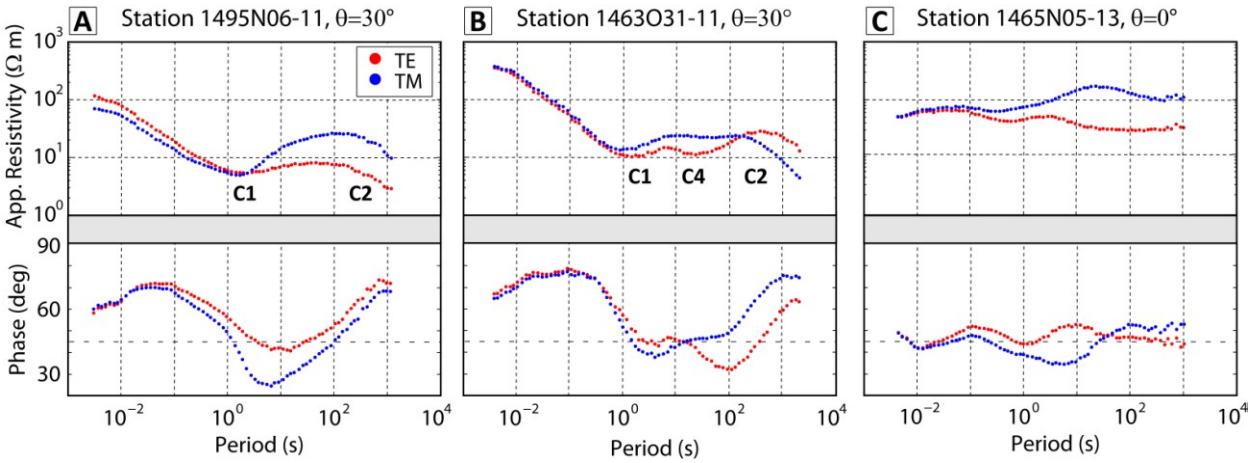

Figure 5.6: Typical magnetotelluric data collected in the study area displayed as apparent resistivity and phase curves. Period acts as a proxy for depth, with short period sensing shallow structures and long periods sensing deeper structures. Low-resistivity zones (conductors) in a volcanic environment can be caused by aqueous fluids, partial melt, or hydrothermal alteration. The data have been rotated to the strike direction. The transverse electric (TE) mode apparent resistivity is derived from electric currents flowing along strike and the transverse magnetic (TM) mode from currents flowing across strike. Panel A, from a station east of Volcan Uturuncu, shows a multi-layered structure with two resistivity minima. The second minimum (C2) is identified as the APMB. Panel B, from a station near Volcan Quetena, shows a third resistivity minimum (C4), indicating an upper-crustal conductor identified as a shallow magma body. Panel C, from a station near the end of the study area in NW Argentina, shows minor resistivity and phase variations. No deep conductor is observed here. See text for further interpretations.

Figure 5.7 shows all 187 MT curves together, with the majority having the same shape as Type 1 discussed above. The consistent shape of all the curves is striking. However it is obvious that different curves have different starting resistivity values. This is due to static shifts at the MT stations, which appear to vary by several orders of magnitude (see Section 4.9.1). One anomalous station that starts at a resistivity of 0.1 Ωm and decreases to almost 0.01 Ωm can be seen. This is the station which was deployed at the col between the twin summits of Uturuncu, at an elevation of 5760 m, possibly the highest MT station in the world.

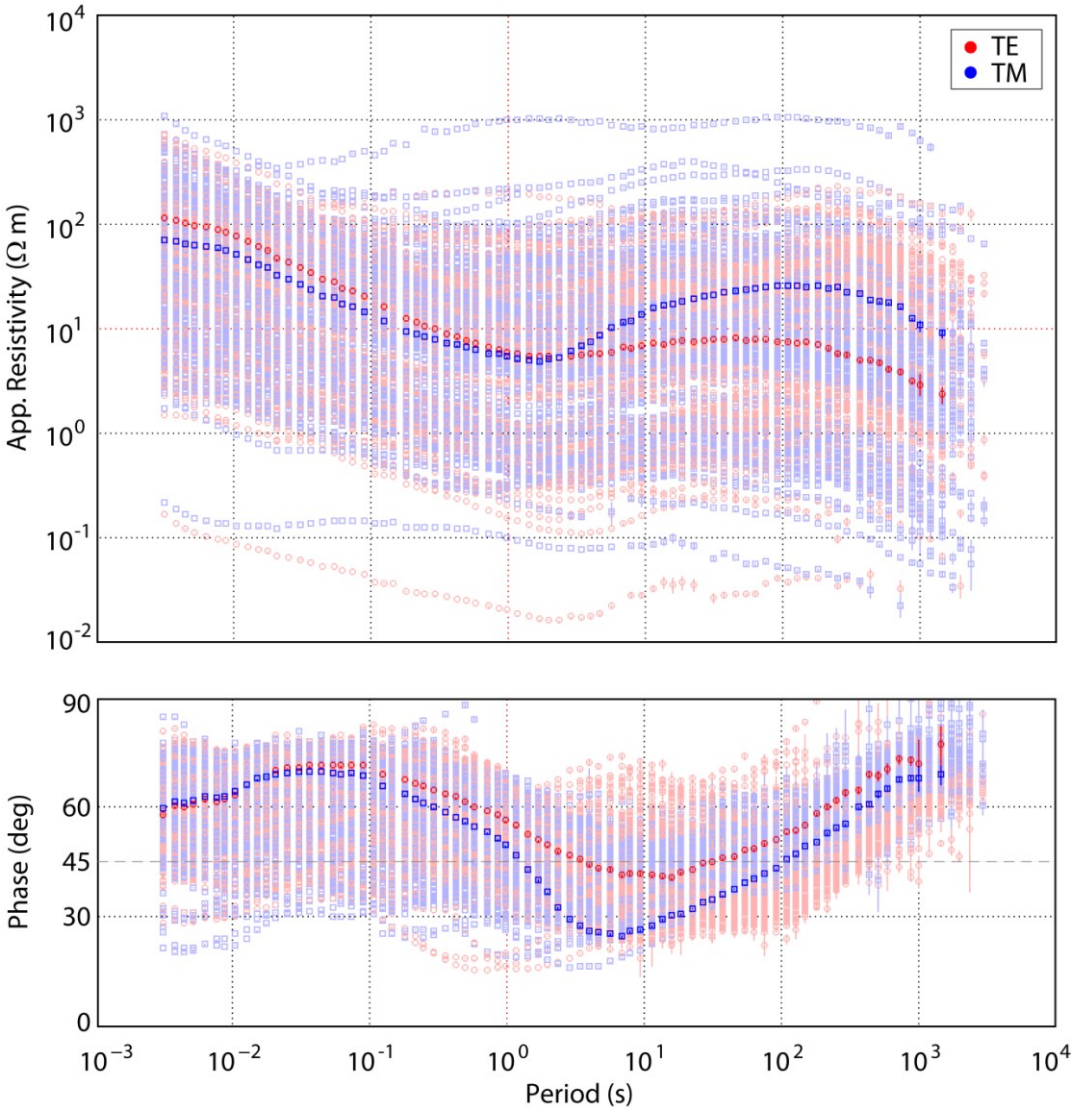

Figure 5.7: Apparent resistivity and phase curves from 187 MT stations plotted atop each other. The bold curve is the Type 1 curve (shown in Figure 5.6 Panel A; station 1495N06-11). The consistent shape of all the curves is striking. However, the different starting resistivity values imply that large static shifts are present.

5.5 Dimensionality and Directionality Analysis

Dimensionality analysis of the impedance tensor is required to determine if a one, two, or three dimensional approach to data analysis is required. For the 2-D case, directionality analysis will determine the geo-electric strike direction that is best for 2-D modeling. The problem with naïvely choosing lower dimensions than the MT data require and proceeding with the analysis is that unpleasant effects may occur in the inversion models, such as artifacts, which can cause difficult or incorrect interpretations (Simpson and Bahr, 2005; Unsworth, 2007). For very simple MT data a 1-D resistivity model may be acceptable, though since the arrival of fast computation 2-D models are commonly used. It has been shown that 2-D modeling of MT data that is overall 2-D but that shows some 3-D effects is still valid (Wannamaker, 1999; Ledo, 2005).

5.5.1 Bahr Phase Sensitive Skew

As discussed previously in Chapter 4, skew values (Swift, 1967; Bahr, 1991) can give information about the dimensionality of the MT impedance tensor. Skew values are rotationally invariant and therefore do not depend on our coordinate system or strike angle. Small Bahr skew values ($\eta < 0.1$) are considered 1-D or 2-D, while large skew values ($\eta > 0.3$) imply that the data is 3-D (Bahr, 1988; Bahr, 1991). Intermediate values ranging from 0.1 to 0.3 can be considered 2-D distorted. Histograms of Bahr skew (Bahr, 1991) for selected period bands are shown in Figure 5.8. Overall, there are only a few stations which show high skew values ($\eta > 0.3$; Panel A). The data for short periods (0.1-10 s, Panels B and C) have skew values mostly below 0.1, indicating shallow 1-D resistivity structure. The period band 10-100 s (Panel D) shows skew values between 0.1 and 0.2, indicating 2-D resistivity structure and possibly distortion. The longest periods (> 100 s, Panel E) show many stations with high skew values, giving evidence for 3-D resistivity structures.

In order to examine the skew values with respect to the spatial location of the MT stations we can plot a Bahr skew pseudosection (vertical axis is period, not depth) along a profile (Figure 5.9). Most skew values for Profile 1 are below 0.1 (blue colours), but there are a few locations

which show high skew values ($\eta > 0.3$, yellow and red colours). The largest departures from 2-D behaviour occurs near Volcan Quetena in Bolivia, and also near Cochinoca in Argentina. However, caution must be exercised when interpreting skew values, because for cases of high error (~10%) the skew values may be misleading and possibly lead to misinterpretation (see Section 4.8 for more details; Chave and Jones, 2012). The data presented in this thesis generally have very low error (a few percent).

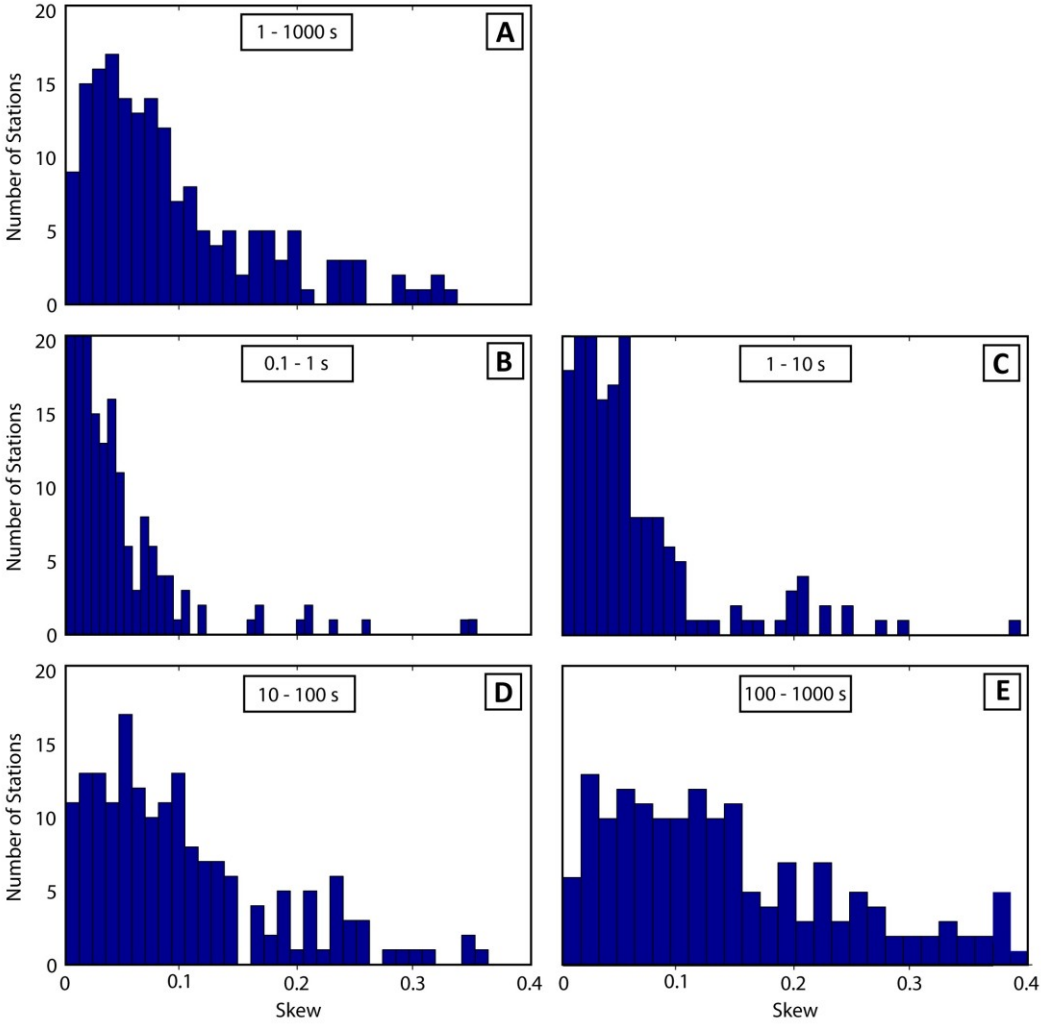

Figure 5.8: Histograms of Bahr skew for a broad period range of (A) 1-1000 s, as well as selected period bands, (B) 0.1-1 s, (C) 1-10 s, (D) 10-100 s, and (E) 100-1000 s. Skew values are mostly less than 0.1 for shorter periods (<10 s), an indication of 1-D or 2-D structure. However, at the longest periods (>100 s), several stations show skew values higher than 0.3, indicating 3-D structure.

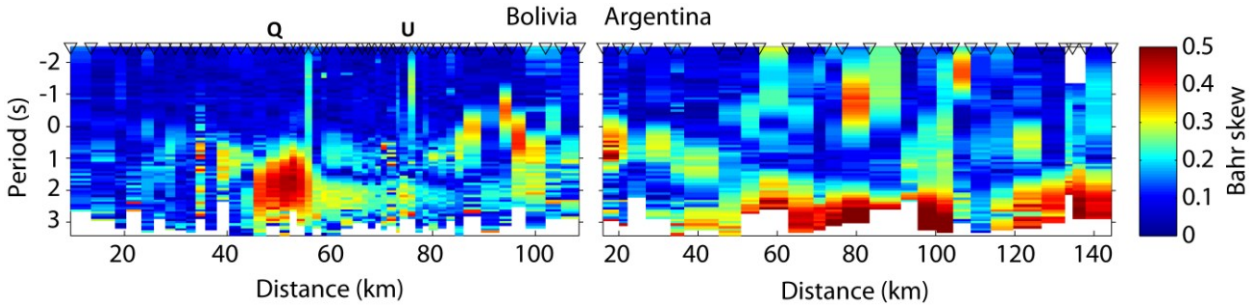

Figure 5.9: A Bahr skew pseudosection along Profile 1 allows the location of the high skew value stations ($\eta > 0.3$, yellow and red colours) to be determined. Q - Volcan Quetena; U - Volcan Uturuncu.

5.5.2 Tensor decomposition

Tensor decomposition is another way to investigate the dimensionality of MT data (Groom and Bailey, 1989; McNeice and Jones, 2001). As outlined in Chapter 4, there are several assumptions inherent in using tensor decomposition, such as assuming that the impedance tensor is 2-D, a potentially erroneous assumption. It is also assumed that the impedance data are galvanically distorted, and that this distortion comes from four parameters, known as twist, shear, anisotropy, and gain. Tensor decomposition techniques are considered more stable than skew value analysis (Jones and Groom, 1993), and are the preferred method to find the dimensionality of the data because the strike can be constrained once the other distortion parameters are known (Jones and Groom, 1993; McNeice and Jones, 2001).

5.5.3 Single Site Tensor Decompositions

The first stage of this dimensionality analysis is to implement the tensor decomposition algorithm of McNeice and Jones (2001) on a site-by-site basis. This allows a different strike direction to be computed at each MT station. The results are shown for selected period bands in

both map view and as rose diagrams in Figure 5.10. Using the skin depth equation with appropriate half-space resistivity values, 1 s, 10 s, 100 s, and 1000 s corresponds roughly to a signal penetration depth of 3 km, 5 km, 15 km, and 30 km. The rose diagram is a type of circular histogram plot that conveniently displays directional data. By examining these diagrams we can get an idea of the average or dominant geo-electric strike direction. It should be noted that strike directions determined with tensor decomposition have an inherent 90° ambiguity, and both possibilities are shown in the rose diagram (red and blue wedges). Given this ambiguity, other information must be used to select the correct strike direction, including regional geological features such as faults and orogens.

In Figure 5.10, the direction of the line indicates the preferred strike direction, chosen from one of the two orthogonal directions found with the tensor decomposition. The preferred direction was chosen as it aligns with the local trend of the Andes in this part of Bolivia. The length of the line represents the maximum difference between TE and TM modes, which is a measure of how 1-D the MT impedance data can be considered. For a 1-D resistivity structure there is no variation of impedance with azimuth and the line will have zero length. The colour of the line shows the root-mean-square (r.m.s.) misfit between the measured MT data and the prediction from the tensor decomposition method. This provides a measure of the validity of the tensor decomposition method, with values of misfit less than ~2 (green color) indicating that the assumptions are valid.

At short periods (1-10 s, Figure 5.10 Panel A), there is no well defined strike direction because the EM signals are only sampling the near surface resistivity structure, which is approximately 1-D. The lines in Figure 5.10 are scattered in different directions and the rose diagram shows no dominant direction. At longer periods (10-100 s, Panel B) the signals sample deeper in the Earth and a clear and consistent regional trend begins to emerge - a strike direction of 20°-30° NE. At the longest periods (100-1000 s, Panel C) almost all the MT stations in the dataset fit one strike direction - about 30° NE.

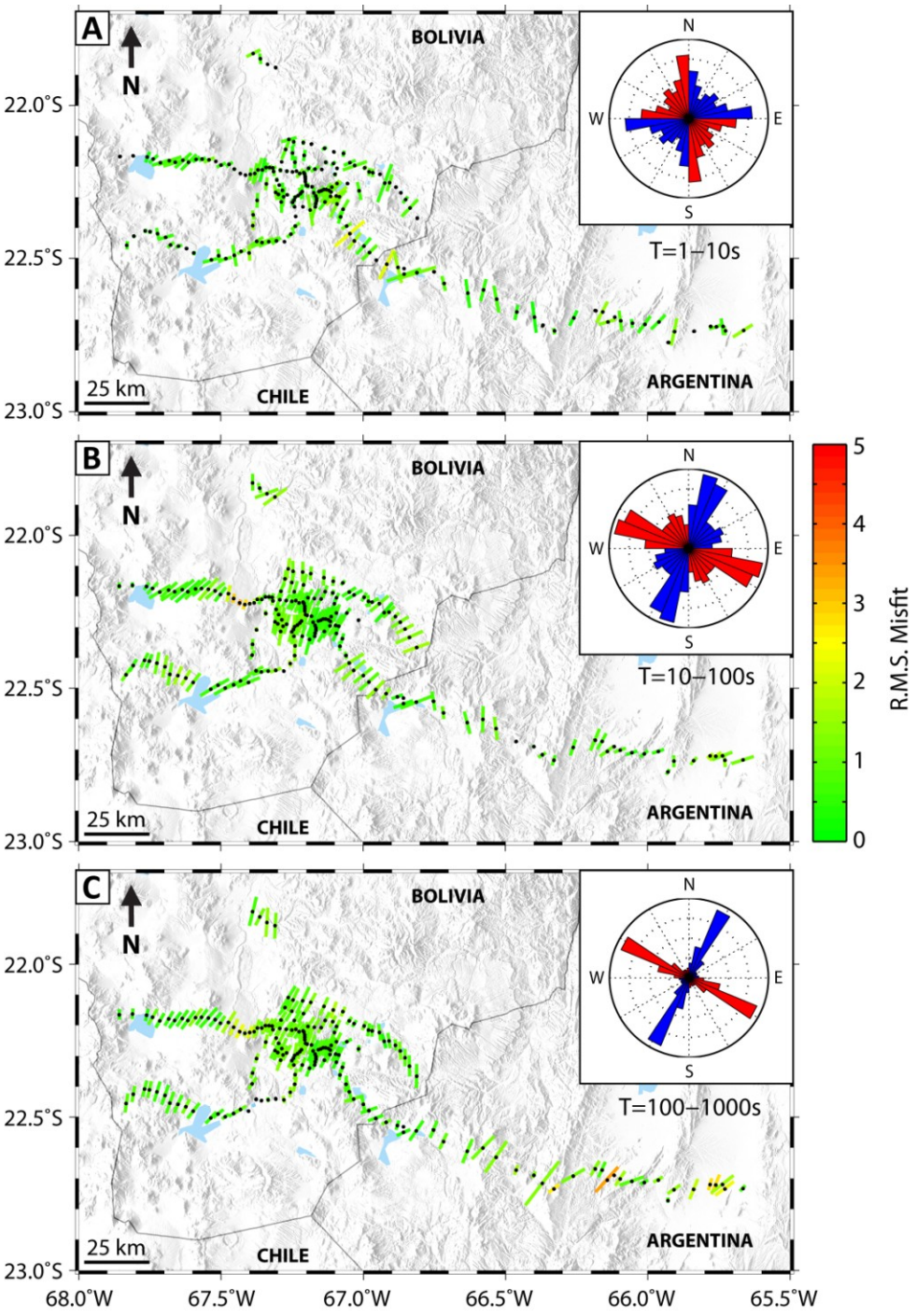

Figure 5.10: Results of tensor decomposition of the MT impedance data around Volcan Uturuncu. Bins of periods from 1-10 s (A), 10-100 s (B), and 100-1000 s (C) are shown. There is no well defined strike direction for short periods (< 10 s). At longer periods (10-1000 s) a clear strike direction of N30°E is observed. The strike is closer to N0°E in Argentina, however the rose diagram is dominated by the more numerous stations in Bolivia.

An examination of the single site decomposition results shows that the data appear to be separable into two regions that show slightly different trends, a western region including the stations in Bolivia, and an eastern region including the stations in Argentina. The tensor decomposition analysis was done for each region separately, and Figure 5.11 shows rose diagrams of the strike angle for each subset over a broad period range of 1 - 3,000 s.

The western region (Bolivia, 149 sites; Figure 5.11, Panel B) exhibits the same strike direction as that of the whole dataset (Figure 5.11, Panel A), which is a well defined strike angle of ~N26°E. This is no surprise because this subset consists of the majority of the MT stations and dominates the average. The eastern region (Argentina, 29 sites) is markedly different (Panel C), showing a strike angle of N88°E (or N02°W). Only at the longest periods (100 - 3,000 s; see Figure 5.10 Panel C) does a strike direction of N20°E - N40°E emerge. It would appear that this region is distinct from the western one, and that a strike angle of ~N0°E is better suited to the majority of the data in this region.

The Mann-Whitney U test (or Wilcoxon rank-sum test) can be used to test the null hypothesis that the data in two different sets come from independent random samples of a single, normally distributed (Gaussian) set and have equal or similar means (Mardia, 1972; Mardia and Jupp, 2000; see also Lowry, 2015). The alternative hypothesis being that the two sets of data come from different populations with different means (Mardia, 1972). The test was carried out as a two-sample test to show whether the strike angles measured in the Eastern area (29 samples) could be from the same distribution as the strike angles measured in the Western area (149 samples). The test rejects the null hypothesis (at a 5% significance level), implying that the two data sets come from separate distributions with different means. Therefore, geo-electric strike angles of N0°E will be used for Profile 1 segment BC, and N30°E will be used for Profile 1 segment AB.

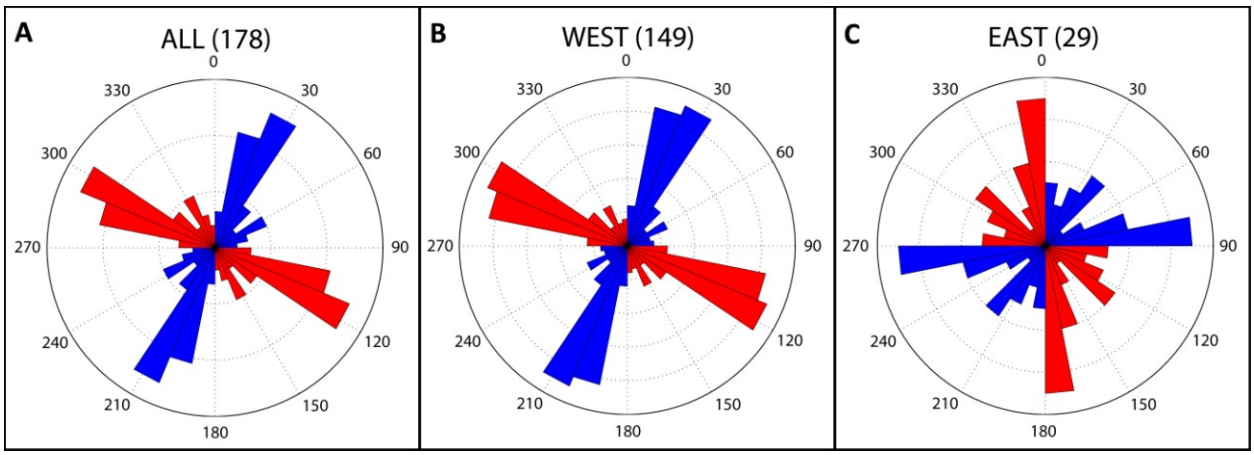

Figure 5.11: Rose diagram plots for 1 - 3,000 s showing the long period trend for the whole data set (A), as well as two subsections, the western portion (B) and the eastern portion (C).

5.5.4 Multi Site Tensor Decompositions

A second stage of the tensor decomposition analysis is to determine if there is a single strike direction that is applicable to all MT stations and frequencies. This is required if a 2-D inversion is to be undertaken, as the data need to be rotated to the geo-electric strike direction. The multi-site decomposition was implemented by fixing the strike direction at a given angle and determining the misfit between the decomposition model and the observed MT data for all stations and all periods. Figure 5.12 shows the results for both the Bolivia and Argentina regions. As the fixed strike direction is varied a clear minimum in the r.m.s. misfit can be seen for both regions.

For the western region (149 sites, Bolivia), the minimum r.m.s. misfit (~1.2) lies between N20°E and N35°E. This agrees with the single-site analysis preformed above which found a strike angle of approximately N30°E for this region. In the eastern region (29 sites, Argentina), the minimum r.m.s. misfit (~1.9) is found for strike angles of N10°W to N0°E. When the strike angle is near 30° the misfit is higher (~2.2), indicating that this region is distinct from the western one, and that a strike angle of N0°E is better suited to the data in this region.

A single r.m.s. value does not fully describe how well the data is fit. Therefore, Figure 5.13 shows a pseudosections (vertical axis is period, not depth) along Profile 1 of the fit of the tensor decomposition to the measured impedance data for the preferred strike directions of N30°E along segment AB and N0°E along segment BC. The generally low misfit values (< 2) indicate that a 2-D approach using these strike angle can be considered valid. Some areas with 3-D effects can be identified, such as near Volcan Quetena at distance of 40 km on segment AB, and at isolated stations and at long periods on segment BC.

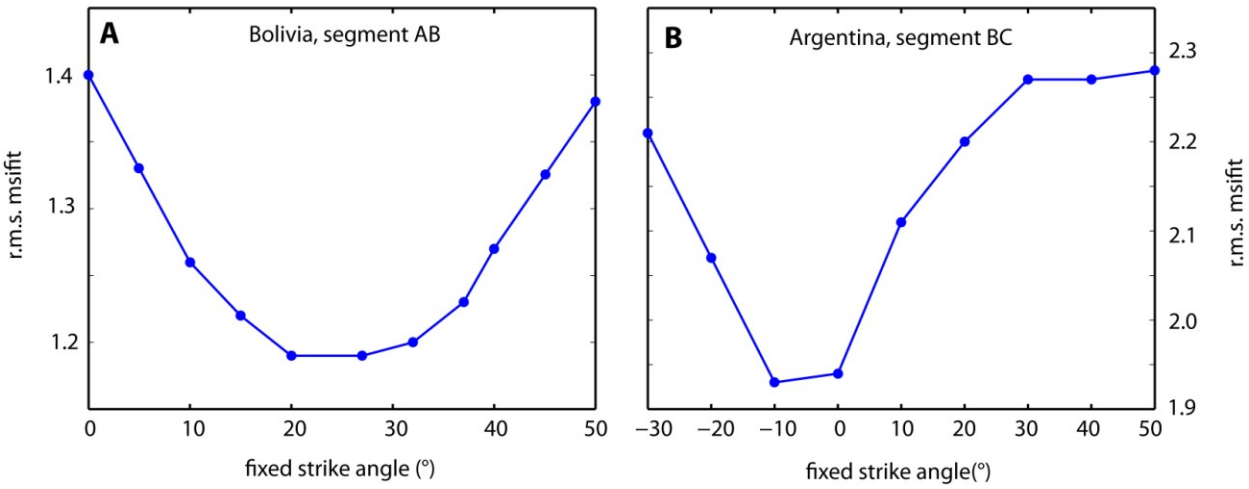

Figure 5.12: Fit of the measured impedance to the values predicted by a multi-site / multi-period tensor decomposition in the period band 1-1000 s for fixed strike angles. Panel A shows the results using the MT data in Bolivia, and Panel B uses the data in Argentina (B). The minima shows the preferred strike direction for all sites and all periods included in the calculation. An error floor of 3% was used.

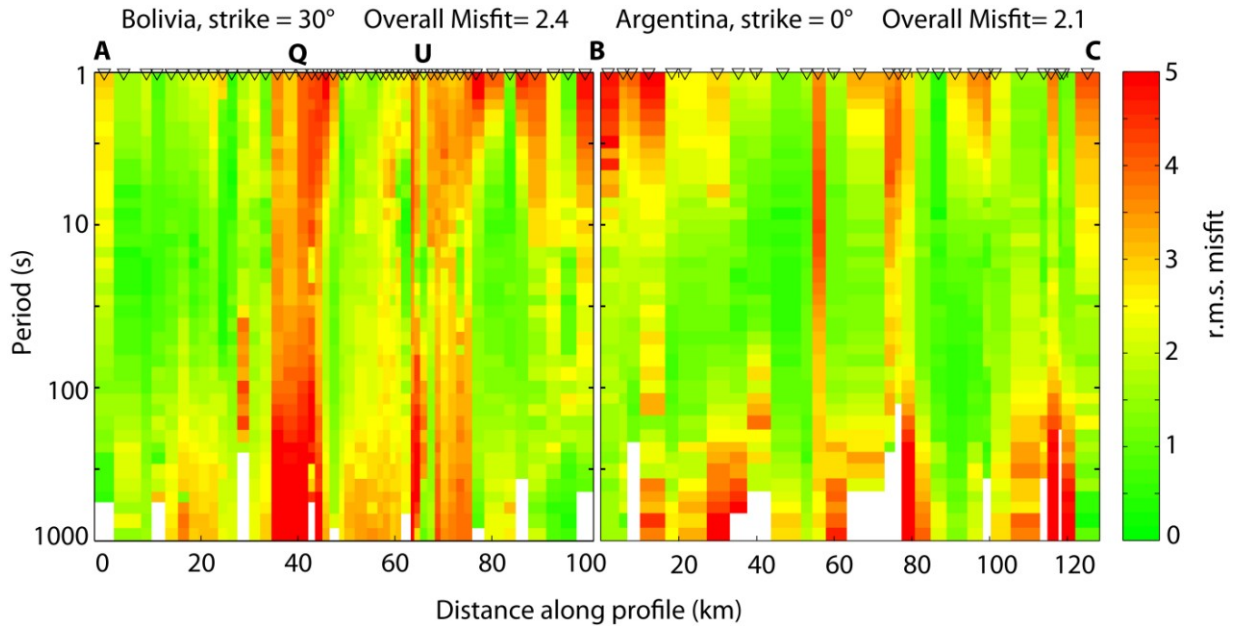

Figure 5.13: Pseudosection showing the fit of the tensor decomposition to the measured impedance data on Profile 1. Profile 1 has two distinct segments: AB and BC, see Figure 5.3. A strike direction of N30°E was used for segment AB and N0°E for segment BC. The generally low misfit values (< 2) indicate that a 2-D approach can be considered valid. Q = Volcan Quetena; U= Volcan Uturuncu. White triangles indicate the position of MT sites.

5.5.5 Induction Vectors

As described in Chapter 4, an induction vector (IV) can be computed from the vertical magnetic field (H_z) and the horizontal magnetic fields generated by electric currents induced in the Earth. The orientation of an IV can help eliminate the ambiguity in the geo-electric strike direction which is inherent in the tensor decomposition. The real component of the IV will be orthogonal to the geo-electric strike direction if the Earth has a 2-D resistivity structure. Whereas the impedance is sensitive to structure directly below the MT station, the IV is sensitive to lateral changes in subsurface resistivity. Therefore the IVs should point away from the edges of a conductor (when plotted in Weise convention in map view). The IVs located above a conductor

will not be sensitive to it, but rather to the small variations within it, and will therefore appear scattered.

The real component of the IVs are plotted in Figure 5.14 for a period of 55 s and 294 s (Weise convention, pointing away from conductors). At a period of 55 s the IVs show a complicated pattern. However, at longer periods (such as 294 s in Figure 5.14) the IVs are pointing away from a conductor which is located below Volcan Uturuncu. The large amplitude IVs seen at the east end of the profile near Mungayoc point eastward and define the eastern edge of a major crustal conductor. The western edge of this large conductor can also be detected near Laguna Colorado where the IVs are pointing westward. Unfortunately, the vertical magnetic fields (H_z) were not recorded at all MT stations, and so the IV data are sparse.

The IVs at the edges of the conductor are found to be pointing N120°E at the eastern edge and N60°W at the western edge. The real components of IVs are expected to be orthogonal to the geo-electric strike direction and this is therefore consistent with a strike direction of N30°E. Some along-strike IV components are seen above the conductor, indicating a possible 3-D conductivity structure. If these stations are to be included in a 2-D inversion model, a very thorough judgment of the model features is required to determine if the features are truly required by the data, or are only artifacts due to the violation of model assumptions.

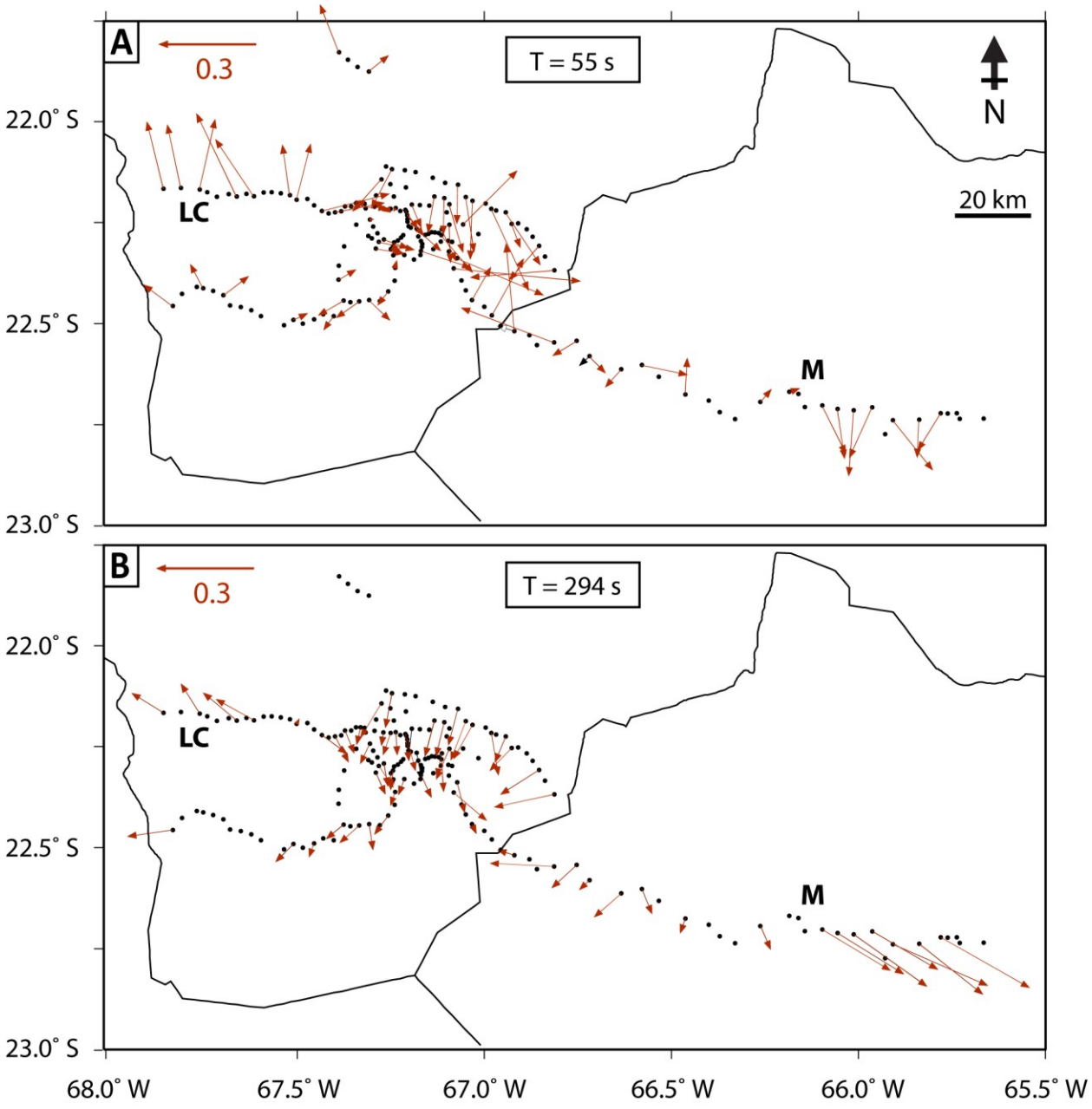

Figure 5.14: Real induction vectors at periods of 55 s (A) and 294 s (B) plotted using the Weise convention (i.e., pointing away from conductors). A scale arrow of magnitude 0.3 is shown for reference. At long periods (i.e., 294s) the induction vectors point away from a large conductor, thought to be the APMB, and define its edges near Laguna Colorado (LC) and Mungayoc (M).

5.5.6 Phase tensor

The phase tensor method (Caldwell et al., 2004; Bibby et al., 2005) is an alternative method to tensor decomposition for dimensionality analysis (refer to Chapter 4 for a more detailed explanation of the theory). The phase tensor method has the advantage that it is not necessary to assume that the regional resistivity structure is 2-D. The phase tensor is often displayed in map view or in a pseudo-section as an ellipse. The direction of greatest inductive response (the equivalent to the 2-D geo-electric strike direction) aligns with one of the axes of the ellipse. The ellipse may be coloured to show other parameters, such as skew angle (β), maximum phase angle, or minimum phase angle. Maps of the phase tensor ellipses at representative periods are shown in Figure 5.15.

At a period of 3 s (Panel A, Figure 5.15) most of the phase tensors plot as circles or very close to circular (median eccentricity value of 0.64), indicating that there is no defined strike at the shallow depths sampled by these EM signals. The inset rose diagram shows the angle α-β which is equivalent to the strike direction in tensor decomposition, and shows that there is no preferred orientation. The colour fill indicates the skew angle is small ($\beta < 3°$), signifying a 1-D or 2-D resistivity structure. A skew angle of $\beta < 3°$ implies the diagonal values of the phase tensor are an order of magnitude larger than the off-diagonal values, which can be considered negligible (Booker, 2014).

At a period of 31 s (Panel B, Figure 5.15) the phase tensors appear more elliptical (median eccentricity value of 0.75). The rose diagram of α-β shows less scatter but there is still no clear dominant direction. Skew values are generally remain low (1-3°), excepted locally around Volcan Quetena (west of Volcan Uturuncu), where they are very high (7° - 10°). The high skew values imply that there exists 3-D effects in the MT impedance data near that location.

At a period of 294 s (Panel C, Figure 5.15) the phase tensors show a strong azimuthal dependence, with a preferred direction of N30°E. Some departure from this trend can be seen at selected stations near Volcan Quetena. Other changes are observed near Laguna Coruto, possibly

indicating that this area may have a complex resistivity structure. Skew values are generally < 5°, but are higher (7° - 10°) in a couple of areas, notably close to Volcan Quetena (west of Volcan Uturuncu) and also in NW Argentina. A skew value of $\beta = 10°$ implies the off-diagonals are one third as big as the diagonal values, and ignoring these may cause problems (Booker, 2014).

Histograms of the phase tensor ellipse axis ratios (major axis over minor axis) are shown in Figure 5.16 for selected periods. At short periods (e.g., 0.3 s) the phase tensor ellipse are nearly circular, implying 1-D structure. At longer periods (e.g., 294 s) the ellipses have similar shape, implying a well-defined strike direction. Histograms of the phase tensor skew angle for selected periods are also shown in Figure 5.16.

It is important to note that both tensor decomposition and phase tensor analysis give consistent estimates of the dimensionality and directionality of the subsurface resistivity structure. It appears that a 2-D MT inversion of these data is valid, although this can be verified by using a 3-D MT inversion for selected parts of the study area.

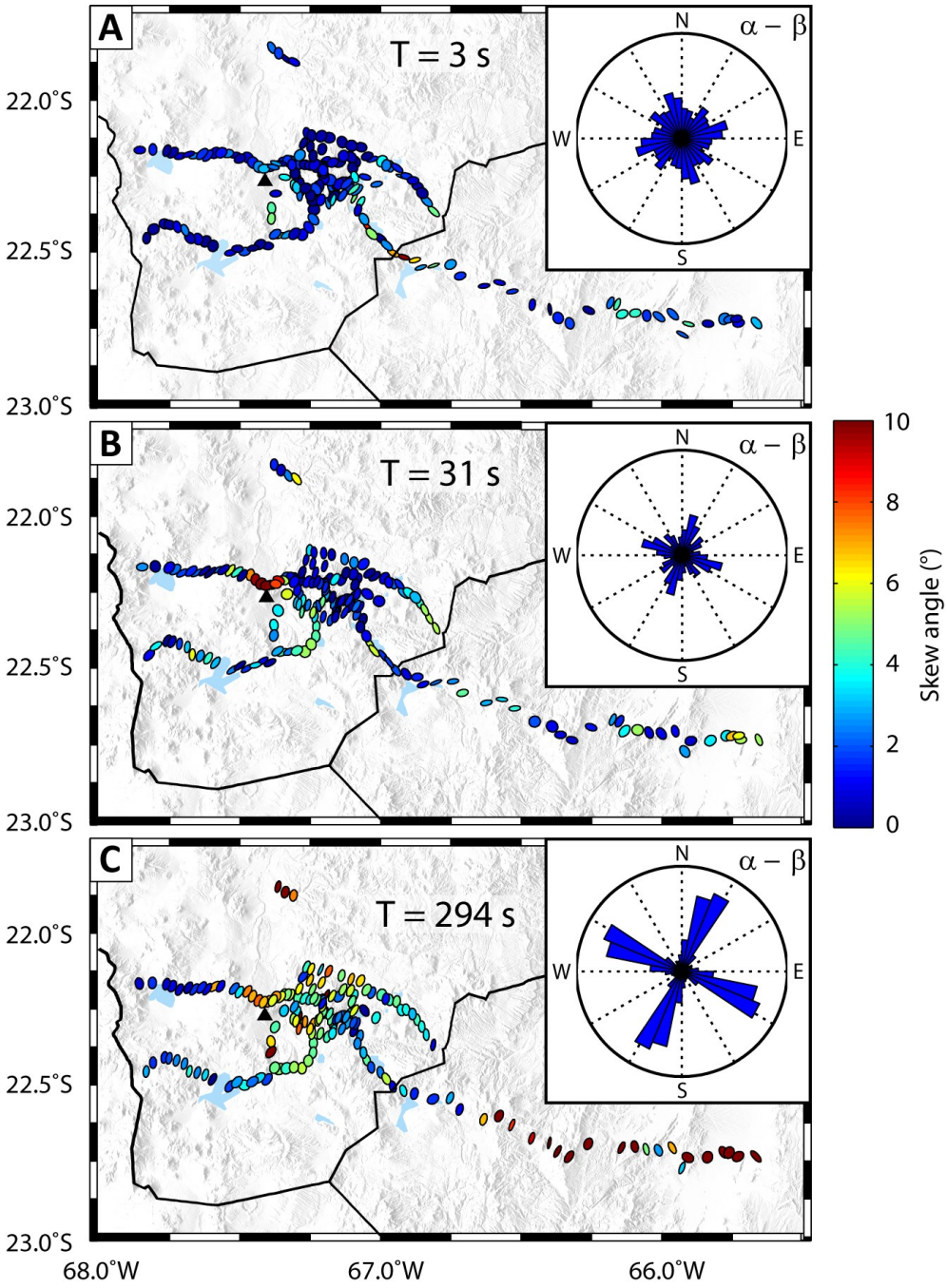

Figure 5.15: Phase tensors calculated for periods of 3 s (A), 31 s (B), and 294 s (C). The ellipse axes indicate the direction of maximum induction, equivalent to a 2-D geo-electric strike direction, also shown on the rose diagram. At longer periods the phase tensors show a preferred direction of N30°E. Ellipses are coloured with skew value. Skew is generally low, but is locally very high west of Volcan Uturuncu near Volcan Quetena (black triangle) and near the profile end in NW Argentina.

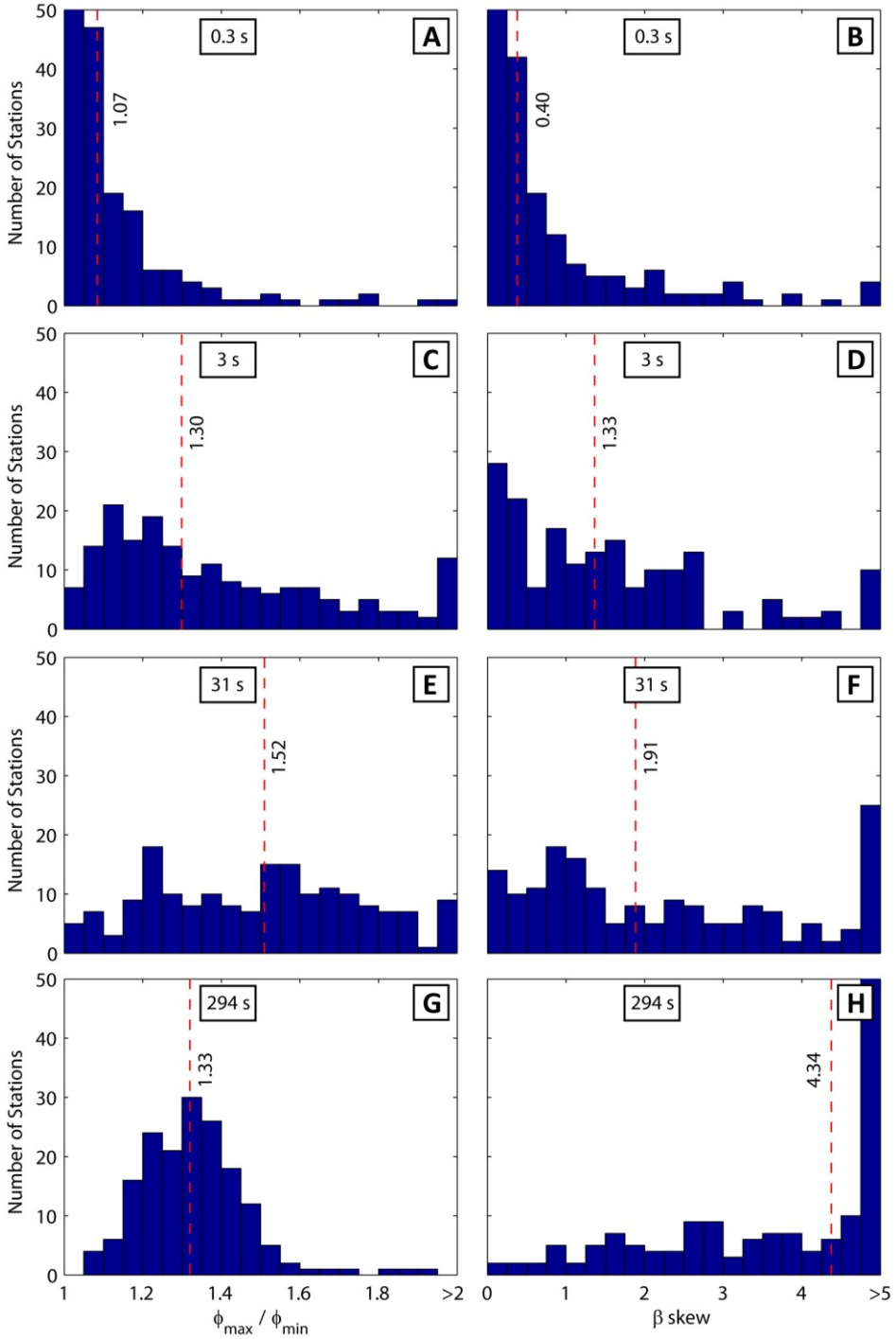

Figure 5.16: Histograms of the phase tensor ellipse axis ratio for selected periods (A, C, E, G). Histograms of phase tensor skew angle for selected periods (B, D, F, H). Dashed red lines show the median values. The last bins show all values equal to or larger than that value. Skew values are mostly small (<2), except at long periods (e.g., 294 s). At short periods (e.g., 0.3 s) the phase tensor ellipse are nearly circular, implying 1-D structure.

5.6 Summary

Magnetotelluric data were collected across the Altiplano-Puna Volcanic Complex in Bolivia and Argentina from 2011-2013. The Phoenix MT system was used and frequencies in the range 300 Hz - 3,000 s were recorded. The quality of the data collected was good and three distinct types of apparent resistivity curves were identified. Type 1 was the most commonly observed and showed a conductor at a period of 2 s and a strong, deep conductor at a period of 300 s. Type 2 curves showed another prominent conductor at a period of 20 s. Type 3 curves were essentially flat, and showed no conductors. Taken together these apparent resistivity curves showed a large conductor at depth believed to be the APMB under most of the study area, a shallow conductor directly beneath Volcan Uturuncu, and the absence of a deep conductor near the edges of the study area.

Tensor decomposition indicated that the MT data may be fit by a 2-D resistivity model, with a well-defined geo-electric strike direction of N30°E for the western region (Bolivia) and N0°E for the eastern region (Argentina). The α-β angle from phase tensor analysis also showed a consistent orientation for long-period data of N30°E. Furthermore, the geo-electric strike direction appeared to remain constant over all period bands > 10 s. The orientation of induction vectors at both the western and eastern edges of the study area, which point away from a deep conductor, are aligned orthogonally with 30° and are consistent with this strike angle.

The independent methods of strike direction determination give consistent results. This uniform result, from tensor decomposition, the alignment of the induction vectors, and α-β phase tensor angles, shows that the MT data may be fit by a 2-D resistivity model. However, it can be noticed that significant 3-D effects do exist at several stations. This implies that the resistivity structure is at least partially 3-D. These 3-D effects include select high skew values and the non-perpendicular alignment of some induction vectors. Most of these 3-D effects are near Volcan Uturuncu and Volcan Quetena, giving motivation for a 3-D resistivity model of the area around Uturuncu. Both 2-D and 3-D MT inversion models are described and shown in Chapter 6.

CHAPTER 6: MAGNETOTELLURIC DATA INVERSION

6.1 Introduction

In this chapter, resistivity models derived from both 2-D and 3-D inversion of the MT data are presented, and their resistivity features interpreted. The fit of the measured MT data to the model response is discussed, and synthetic inversions are used to investigate model resolution. As described in Section 4.10, most MT inversion algorithms start with an initial resistivity model and iteratively update that resistivity model, checking the fit to the measured data at each iteration step. The algorithm is said to have converged when the misfit is no longer reduced appreciably, and the resistivity model stops changing. Throughout this thesis the isotropic non-linear conjugate gradients inversion algorithm of Rodi and Mackie (2001) is used for the 2-D inversions. The algorithm of Siripunvaraporn et al. (2005) is used for the 3-D inversions.

6.2 2-D MT Inversion

6.2.1 Regional Profile, Profile 1

The dimensionality analysis in Chapter 5 suggested that a 2-D inversion would be valid for the MT data along a regional profile across the study area. The regional profile, Profile 1, stretches ~300 km from the western-most site near the Chilean border, across Volcan Uturuncu, to the eastern-most site in Argentina. Based on geo-electric strike analysis (see Section 5.5.3), the regional profile was separated into two segments, with different strike directions determined for each. Segment AB contains 47 MT sites in Bolivia and was found to have a geo-electric strike of N30°E. Segment BC contains 26 MT sites in Argentina, and was found to have a geo-electric strike of N0°E. Figure 6.1 shows the orientation of the regional profile, its segments, and which MT sites were used in the preferred 2-D inversion model.

Separate inversions were run on each profile segment, then combined together to form one long profile. The inversion for segment AB (in Bolivia) included additional MT sites at the eastern edge (the first 10 sites along segment BC), and also 2 sites at the western edge in Chile (sites PEA and VIR, not shown in Figure 6.1; from Brasse et al., 2002). Using additional MT sites beyond the area of interest can help to control unconstrained edge effects. Similarly, the inversion for segment BC (in Argentina) included additional MT sites at the western edge (the last 12 sites along segment AB).

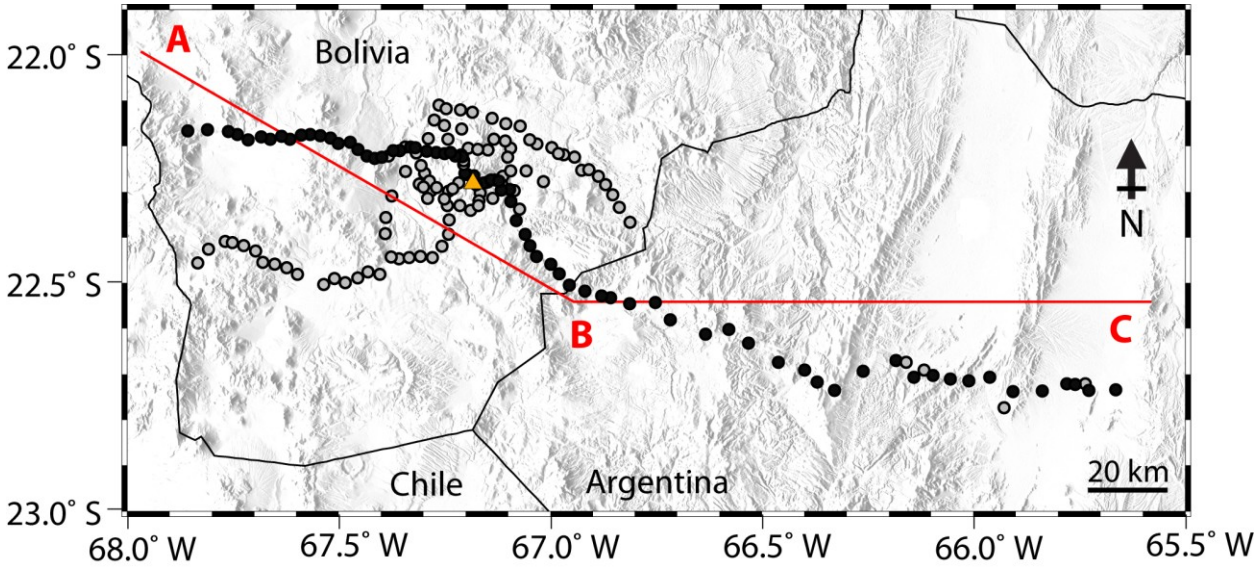

Figure 6.1: Regional profile (Profile 1) with two segments, AB and BC. The magnetotelluric (MT) data were rotated to the determined geo-electric strike directions (AB = N30°E; BC = N0°E, see Section 5.5), and projected onto profile segments oriented perpendicular to the strike direction (N120°E for segment AB and N90°E for segment BC). Circles mark the location of MT sites. MT data from the sites marked by black circles were used for the 2-D inversion model. Volcan Uturuncu is marked with an orange triangle.

6.2.2 Preferred 2-D Resistivity Model along Profile 1

Many combinations of inversion parameters were investigated and a set of preferred parameters that worked best for this data set were determined (see Section 6.2.4 for details). The resistivity model presented in this section is the preferred model and is representative of most models produced (see Sections 6.2.8 to 6.2.13 for a discussion of the other models). The main resistivity features do not depend on any specific choice of parameters, implying they are robust and required by the MT data.

The preferred 2-D resistivity model is shown in Figure 6.2. This model was obtained from the joint inversion of TE and TM mode MT data at 73 sites along the regional profile, Profile 1. After 200 iterations the r.m.s. misfit for segment AB was reduced from 13.4 to 1.49, and for segment BC from 10.4 to 1.48. This low misfit indicates an acceptable fit to the measured MT data. The approximate limits of uplift and subsidence are shown above the 2-D model for reference (Henderson and Pritchard, 2013). It is noteworthy that Volcan Uturuncu sits at the centre of this uplift ring (see maps in Section 5.3 for more information). The inferred limits of the APVC (de Silva, 1989) are also shown. Significantly, the edges of the large deep conductor align with the limits of the APVC. As explained in Chapter 4, there is a penetration limit for EM signals (the skin depth), below which there is limited resolution. The hatched pattern in Figure 6.2 shows this approximate limit for EM signals with a period of 1000 s.

The 2-D resistivity model shows three distinct layers: (1) a shallow heterogeneous surface conductor (C1); (2) a deep, spatially uniform conductor (C2) that begins at a depth of 15-20 km below sea-level, within and below which there is no resolution; (3) an intermediate layer with spatially variable resistivity consisting of series of conductors (C3-C7) and resistors (R1, R2). See Section 6.4 and Chapter 7 for a full interpretation of these features and their magmatic implications.

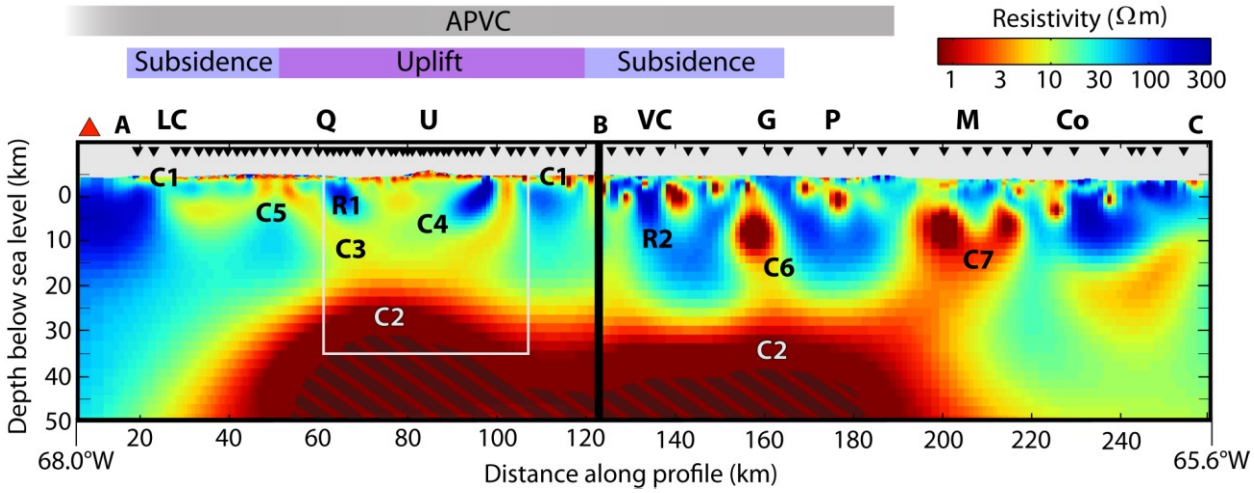

Figure 6.2: The preferred 2-D resistivity model obtained from the joint inversion of transverse electric (TE) and transverse magnetic (TM) mode magnetotelluric (MT) data, along Profile 1 (segment AB and BC are joined), see Figure 6.1 for a location map. A combined r.m.s. misfit of 1.49 was achieved after 200 iterations, indicating an acceptable fit to the measured MT data. The approximate limits of uplift and subsidence are shown as pink and purple bars above the resistivity model (Henderson and Pritchard, 2013). The limits of the Altiplano-Puna Volcanic Complex is shown as a grey bar above the resistivity model, note it extends westward beyond the figure (de Silva, 1989). The red triangle at the western edge of the profile marks the modern-day volcanic arc. Note that the depths are referenced to sea-level. Hatched pattern shows approximate limit of penetration for EM signals with a period of 1000 s, and there is minimal resolution in this region. Black triangles indicate MT sites locations used in the inversion. The white box shows the limits of the 3-D inversion discussed below in Section 6.3 (see Figure 6.19). Labelled conductors and resistors (e.g., C1, R1) are discussed in the text. The large deep conductor has an east-west extent of ~170 km, extending from Laguna Colorado, Bolivia, to Mungayoc, Argentina. LC - Laguna Colorado; Q - Volcan Quetena; U - Volcan Uturuncu; VC - Vilama Caldera; G - Volcan Granada; P - Pirquitas; M - Mungayoc; Co - Cochinoca.

6.2.3 MT Data Pseudo-sections

Figure 6.3 shows pseudosections of the MT data and of the model response for the profile segments AB and BC. This is a useful way to look at the resistivity and phase data and how they vary both with period (i.e., pseudo-depth) and distance along a profile. As explained in Chapter 4, TE and TM modes are derived from electric current flowing parallel to the strike direction, or across the strike direction, respectively, in a 2-D analysis.

At short periods (~0.1-1 s; shallow features) the data from both TE and TM modes show low apparent resistivity (<10 Ωm, red colour). This feature can be associated with a shallow near-surface conductor. At long periods (100-3000 s; deep features) the data from both TE and TM modes show low apparent resistivity and high phases (>45° degrees, yellow and red colours). The phase above 45° degrees indicates that the resistivity is continuing to drop. This feature can be associated with a strong, deep conductor. Evidence of static shifts can be seen in the apparent resistivity data for both the TE and TM modes. This can be seen as drastic variations in apparent resistivity at adjacent stations. Overall, the modeled data response closely match the observed data.

A useful way to compare both the modeled and observed data is by computing the residuals and plotting these as a pseudosections. Figure 6.4 shows the residuals (difference of modeled and measured data) scaled by the error. It can be seen that the difference between the observed data and the model in apparent resistivity is generally within +/- 3, and the phase is within +/- 5. These low residuals indicate an acceptable fit to the measured data.

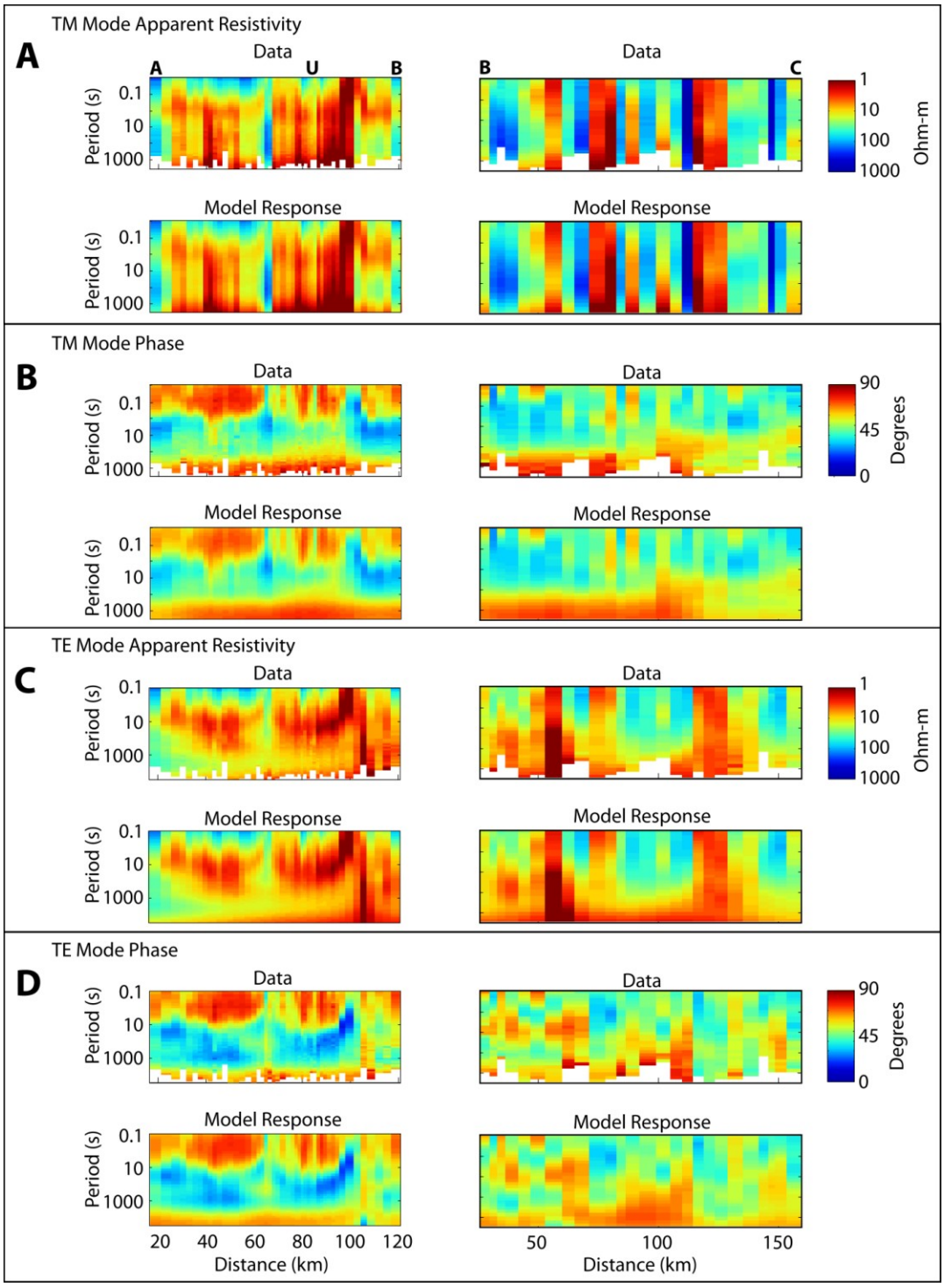

Figure 6.3: Pseudosections of both the measured magnetotelluric data and the modeled data for Profile 1 (segments AB and BC) for both TM mode (Panels A and B) and TE mode (Panels C and D). U - Volcan Uturuncu. Profile location as indicated in Figure 6.1. Segment AB is rotated to N30°E; segment BC is rotated to N0°E).

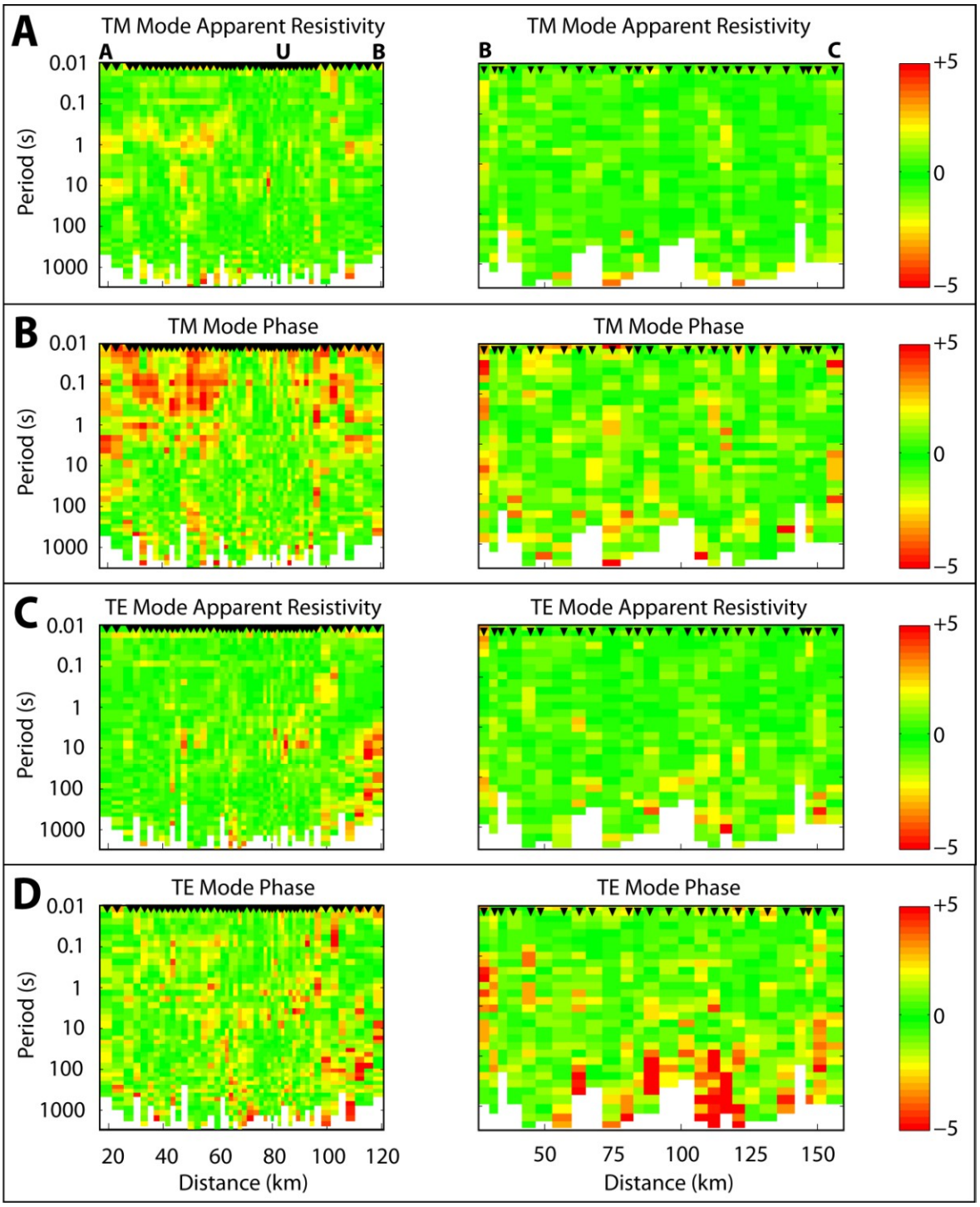

Figure 6.4: Pseudosection residuals showing fit of the MT observed data to the response of the inversion model for Profile 1 (segments AB and BC). The residuals are scaled by the data error. Black triangles mark the location of the MT stations. U - Volcan Uturuncu.

6.2.4 2-D Inversion Parameters

For the segment AB of Profile 1, a dense mesh was designed with 111 rows and 267 columns (~30,000 cells), including topography. Horizontal mesh cells were designed so that there were at least 2 cells between adjacent MT stations, which allows the inversion to fit MT data at stations which have significantly different resistivity values. For example, the mesh used for the segment AB had cells with a horizontal dimension of 250 m to 1000 m, depending on the MT site spacing. Outside the region of interest, mesh cell sizes are increased geometrically (by a factor of ~1.5) in both the horizontal directions until a distance of at least three skin depths at the longest period (lowest frequency) has been reached. This part of the mesh is known as padding, and helps to stabilize the inversion and its boundary conditions (Weaver, 1994).

Vertical mesh cells were designed with small sizes near the surface and increasing in size with depth, in order to mimic the diffusive nature of the EM signals used in MT. The smallest vertical size is determined by one third of the smallest skin depth at the highest frequencies, and the depth extent is a distance of at least three skin depths at the longest period (lowest frequency). These extents help stabilize the inversion and its boundary conditions (Weaver, 1994). In many cases the vertical cell sizes are kept fixed throughout the region of interest. For example, the mesh used for the segment AB had cells with a vertical dimension of 50 m at the surface, then increased in size slowly to optimize resolution (cell thickness of 400 m at sea-level; 1000 m at 6 km BSL; 2000 m at 17 km BSL; 3000 m at 58 km BSL, etc.).

In the inversion each data point carries a weight inversely proportional to its assigned error (uncertainty). To equalize the influence of all data points which have an acceptable error, and to minimize the potentially dominating effect of points with small error bars, an error floor is used. This is an imposed minimum error; data errors above this threshold will not be changed. Data error floors for the preferred inversion were set to 10% for the apparent resistivity and 5% for the phase. Having a lower error floor on the phase helps eliminate distortion effects, because the apparent resistivity data may be galvanically distorted (see Section 4.9).

For the segment BC, a mesh with less cells was designed (due to the larger site spacing than segment AB), with 89 rows and 188 columns (~17,000 cells). Horizontal cell sizes ranged from 500 m to 1500 m, depending on station spacing; vertical cell sizes were the same as segment AB. Data error floors were set to 20% for the apparent resistivity and 10% for the phase, due to the larger site spacing on this segment.

For both segments, MT data from the entire recorded frequency range, 100 Hz to 3,000 s, were inverted. For both segments, the inversion model began from a 10 Ωm halfspace, and topography was also included. This is illustrated in Figure 6.5. The inversion algorithm also solved for static shifts, using a damping factor of 10,000 and a variance of 10% for the preferred resistivity model (see Section 6.2.7 for more details).

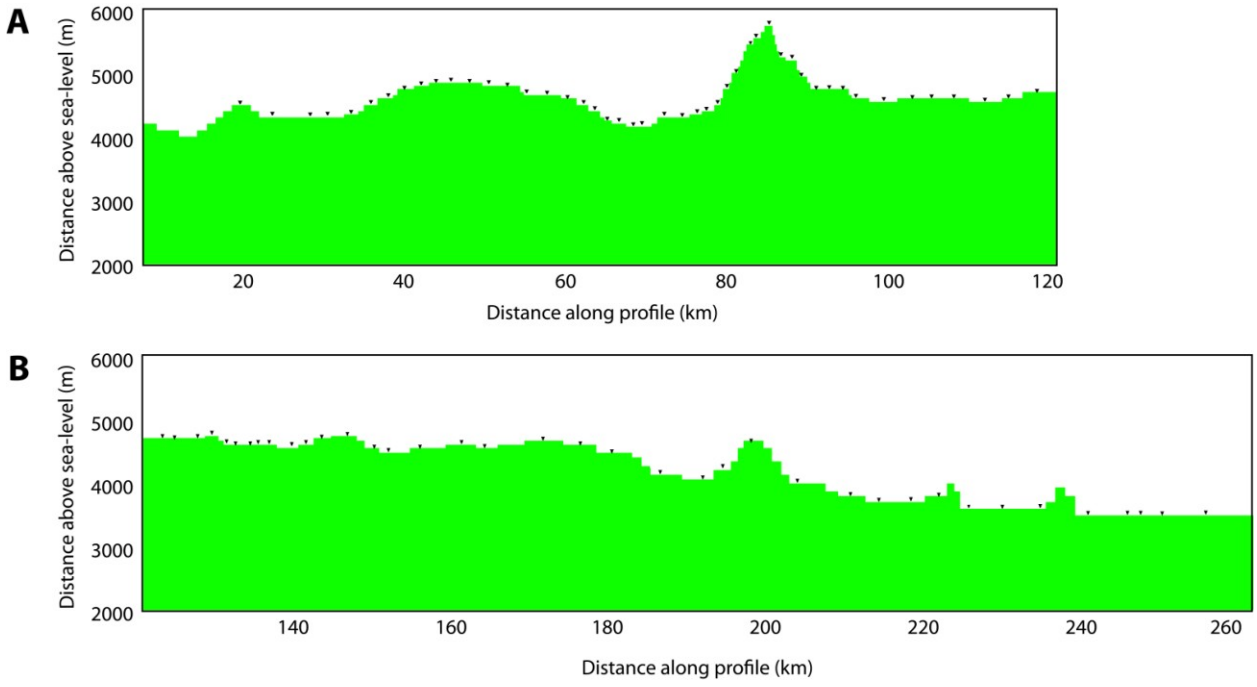

Figure 6.5: Profile 1 used a mesh which included topography. The starting model used for the preferred inversion was a 10 Ωm halfspace. Panel A shows the mesh design with topography for segment AB, and panel B shows the mesh for segment BC. Black triangles are MT sites.

The 2-D inversion was repeated for a range of model regularization parameters, τ, which controls model smoothness (see Section 4.10 for more details). Figure 6.6 shows how the r.m.s. misfit varies with model roughness for a selection of τ values, known as an L-curve. After examining the L-curve, a value of τ = 10 was chosen for segment AB, representing the preferred compromise between fitting the measured MT data and producing a spatially smooth resistivity model, free of artefacts. The optimal value lies near the centre of the L-curve where the curvature starts to change. A value of τ = 3 was chosen for segment BC.

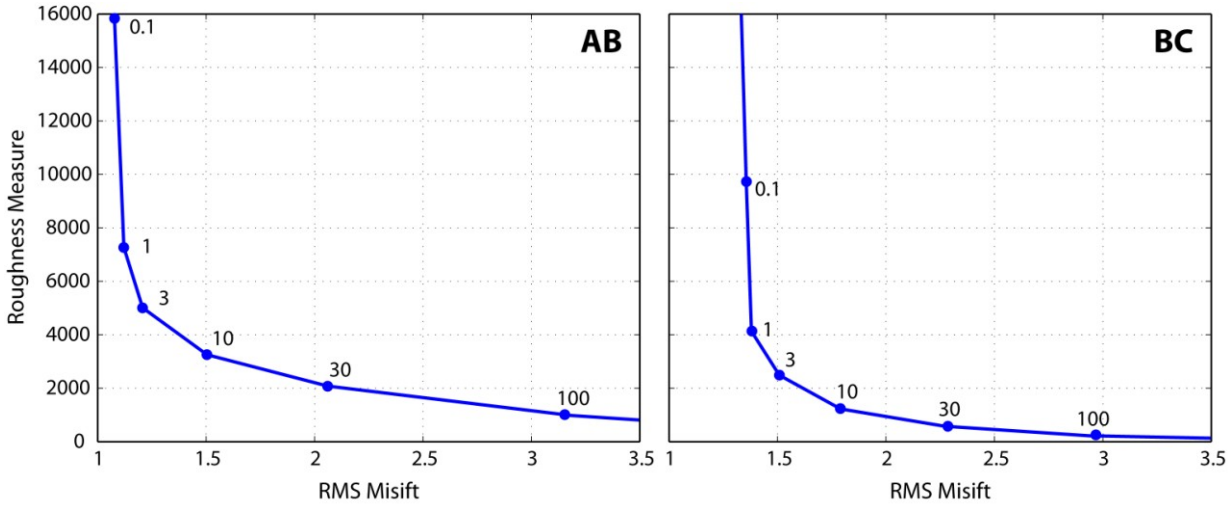

Figure 6.6: The L-curve represents the compromise between fitting the measured magnetotelluric data (r.m.s. misfit) and producing a spatially smooth resistivity model (roughness), by varying the regularization parameter, τ, identified with blue dots. A value of τ = 10 was chosen for segment AB, and a value of τ = 3 was chosen for segment BC.

6.2.5 Model Convergence

The preferred 2-D inversion was run for 200 iterations to ensure convergence to an unchanging misfit value was reached. Figure 6.7 shows that both segments of Profile 1 achieved convergence to an r.m.s. misfit of 1.49 within the first 50 iterations. A smoothly decreasing r.m.s. misfit is a sign of a stable inversion.

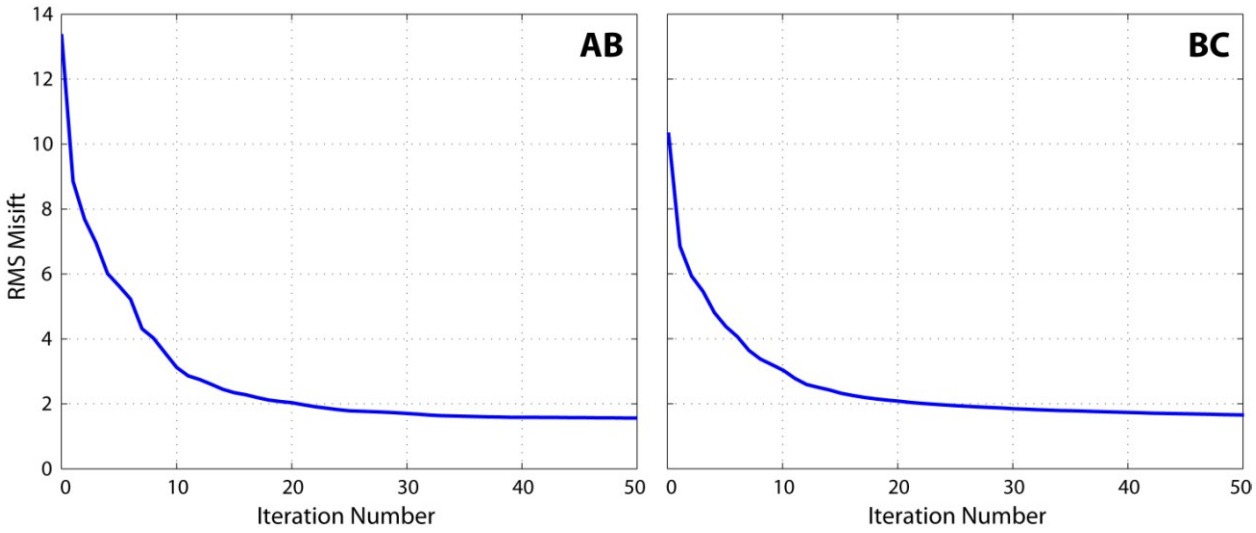

Figure 6.7: A convergence curve for the preferred 2-D inversion shows both segments of Profile 1 (AB and BC) smoothly converged to an r.m.s. misfit of 1.49 within the first 50 iterations, although the inversion algorithm was run for 200 iterations, see text for details.

6.2.6 MT Data Fit

The r.m.s. misfits at each MT site for both TE and TM modes of the preferred 2-D model are shown in Figure 6.8. It can be seen that the MT data is fit relatively uniformly. Most misfit values are between 1 and 2, indicating an acceptable fit to the measured MT data. Figure 6.9 shows the data fit at three MT sites, representing each of the three curve types, as discussed in Section 5.4.1.

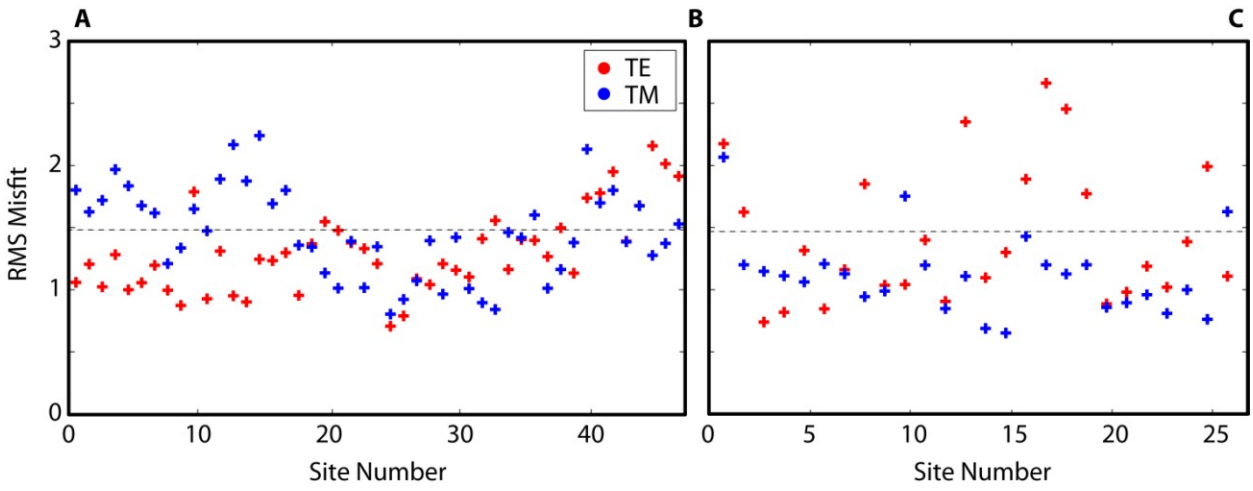

Figure 6.8:. The r.m.s. misfit for each MT site in the preferred 2-D inversion along Profile 1 for both the TE mode (red dots) and the TM mode (blue dots). The average misfit of 1.49 is shown as a dashed grey line.

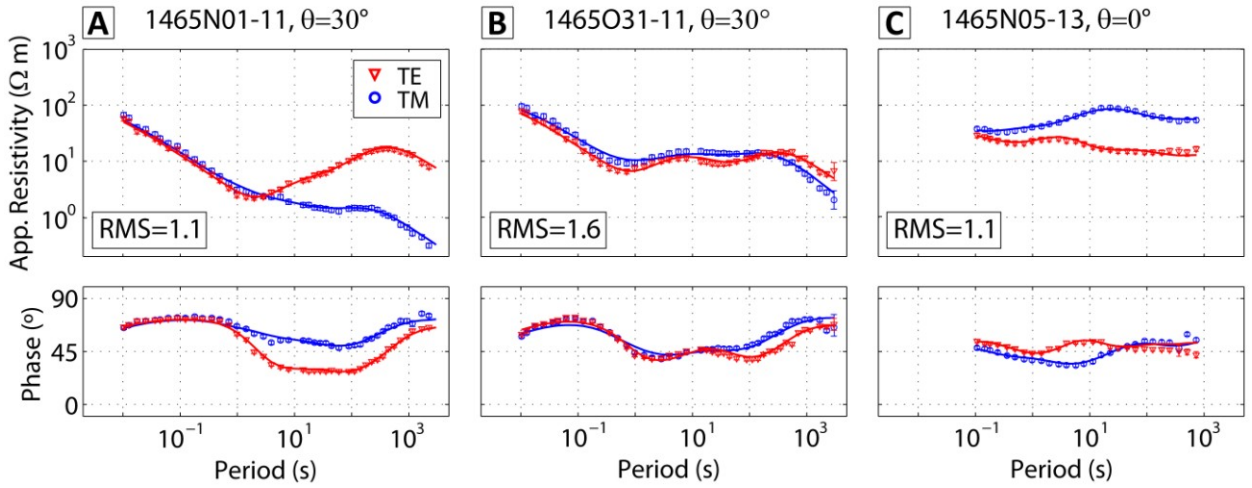

Figure 6.9: Data fit for the preferred 2-D MT inversion model at three sites, one for each identified curve type (see Chapter 5). The line shows the model response and the points are the measured data with error bars. The model generally fits the data well.

6.2.7 Static Shifts Coefficients

MT data are often influenced by static shifts, see Section 4.9 and Jones, (1988). These are due to near-surface resistivity structure that occurs at a small spatial length scale. That is, at scales smaller than the skin depth of the highest frequency measured. Static shifts are common in this data set because the study area is a volcanic environment, where there can be large changes in resistivity over short horizontal distance (e.g., alternating high resistivity lava flows and low resistivity zones of hydrothermal alteration).

One approach is to allow the inversion algorithm to solve for static shifts. The algorithm of Rodi and Mackie (2001) has two control parameters: a damping factor and a variance value. A high damping factor forces the algorithm to first fit the measured MT data with resistivity structure, then solve for static shifts. This is preferred, so that the data control the resistivity model structure. A low variance value keeps the static shifts close to a Gaussian distribution with a sum equal to zero (in the log domain), an inherent assumption of static shifts (see Section 4.9.1). For the preferred resistivity model a damping factor of 10,000 was used and a variance of 10% was used. This allowed the inversion to solve for static shifts only after first solving for model structure, and ensured that the static shifts followed a Gaussian distribution.

The estimated static shift coefficients are shown in Figure 6.10. These values are multiplicative, i.e., a value of 1 corresponds to no static shift of the apparent resistivity. No systematic trends in the static shifts are observed, and both TE and TM modes appear to be shifted together at most sites. Other methods were used to estimate static shifts and gave similar values (see Section 6.2.10).

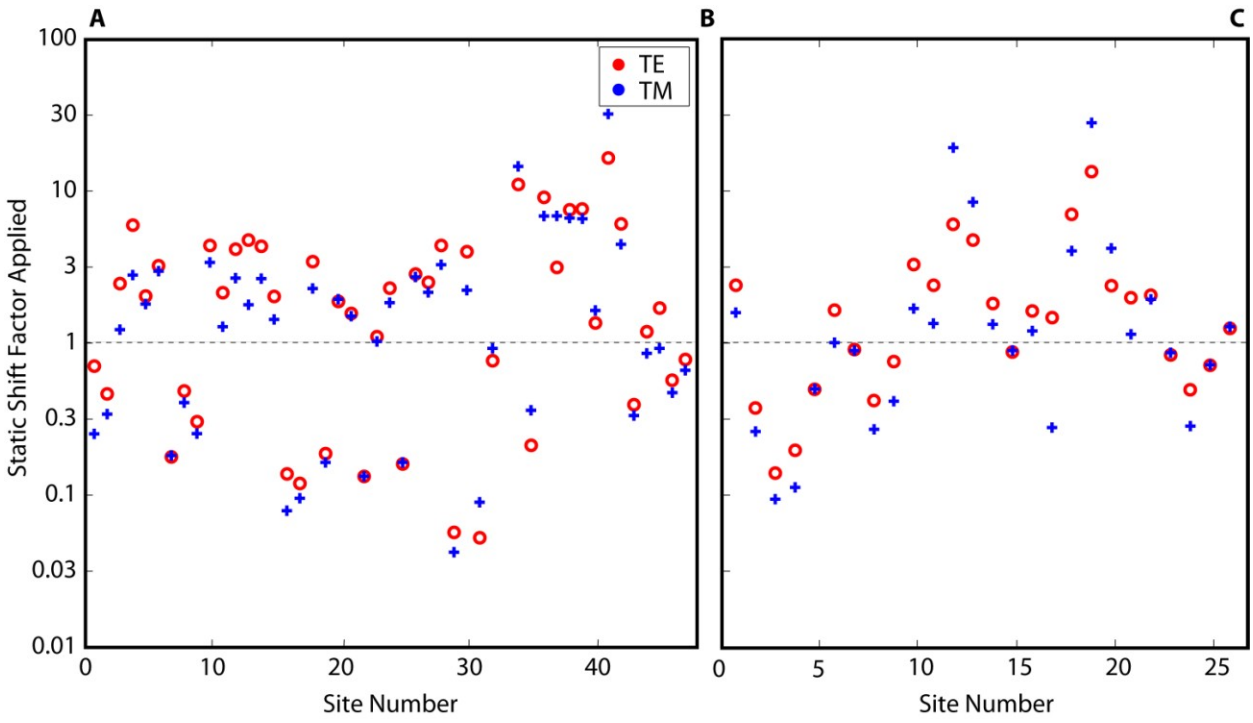

Figure 6.10: Static shift coefficients estimated by the 2-D inversion for the preferred model. A value of 1 corresponds to no shift of the apparent resistivity. Damping parameter = 10,000; variance constraint = 10%.

6.2.8 Inversion Parameter Variations

Many inversion models were produced for a range of inversion parameters, in order to find the best parameters for this data set. Examples of parameters investigated include: varying the tau parameter to find an optimal balance of smoothing and data misfit, multiple strategies for dealing with static shifts, changing the inversion starting model, different error floor limits on both resistivity and phase, and variations in the strike direction. Examples are shown in the following sections, but are not exhaustive. The main resistivity features of the models did not depend on any specific choice of inversion parameters or combination of parameters; they were always present to some degree. This gives confidence that the main features are robust and required by the MT data. The following sections will illustrate this with a few examples.

6.2.9 Effect of Varying the Tau Parameter

As described in Section 6.2.4, the tau parameter can be varied and acts as a trade-off between resistivity model smoothing and data misfit (see L-curve, Figure 6.6). Figure 6.11 shows models produced for profile segment AB with differing values of tau. Besides the tau parameter, all the resistivity models shown used the same inversion parameters as the preferred model. As the tau parameter becomes smaller the resistivity model becomes very rough, while larger tau values give very smooth resistivity models which begin to smear features. However, the main resistivity features are seen in each model.

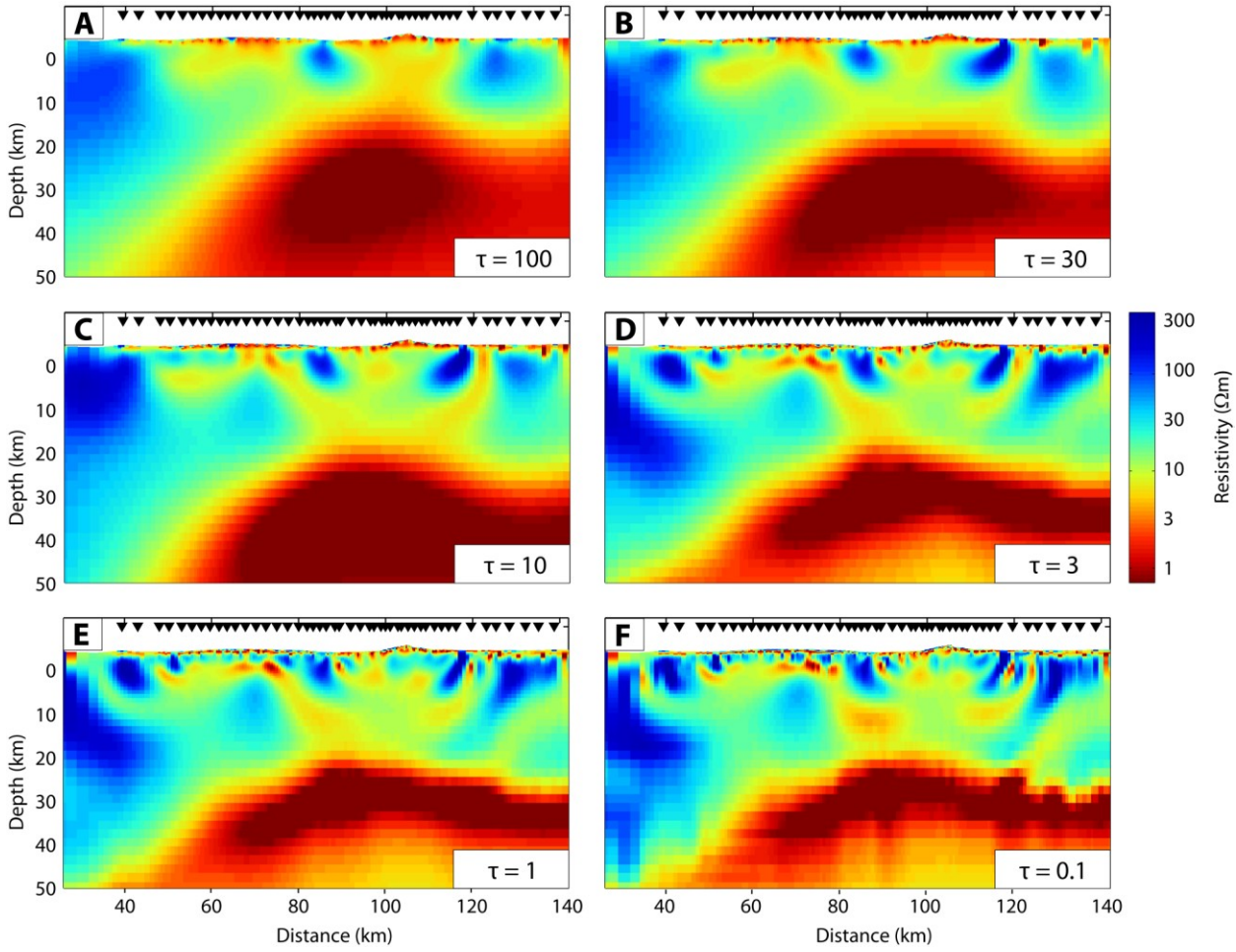

Figure 6.11: Resistivity models produced by varying the tau parameter, which controls model roughness. Panel C shows the preferred 2-D model with a tau value of τ=10. The main resistivity features are seen in each model.

6.2.10 Solving for Statics Shifts

Various strategies exist for solving static shifts, and several different approaches were used. Figure 6.12 shows examples of models produced with different static shift strategies; the models shown have the same inversion parameters as the preferred model. Allowing the inversion algorithm to solve for the statics after first solving for the structure seemed to work best for this dataset. As explained above, a low damping value (< 1000) allows the inversion algorithm to first fit the data with static shifts, while a high damping value (> 1000) forces the inversion to first fit the data with structure. A high damping value is preferred, so that the data control the model structure. The variance constraint measures how closely the static shifts coefficients fit around a Gaussian distribution with a sum equal to zero.

Panel A of Figure 6.12 shows the preferred model, with a damping value of 10,000 and a variance of 10%. Decreasing the damping value (Panel B) allows the algorithm to solve for static shifts at earlier iterations; no significant changes in the model features are noticed. Increasing the variance (Panel D) lessens the constraint that the static shifts values be kept near a Gaussian distribution; almost no change in the model is noticed, nor the r.m.s. misfit.

Panel C shows a different approach. Here the inversion algorithm does not solve for static shifts, instead the error floors are manipulated to account for static shift effects. In this case, the TE mode resistivity error floor is set very high (90%), while the TM mode error floor is set as normal (10%). The r.m.s. misfit is much higher because the error floor is higher, but the main features of the resistivity model are recovered.

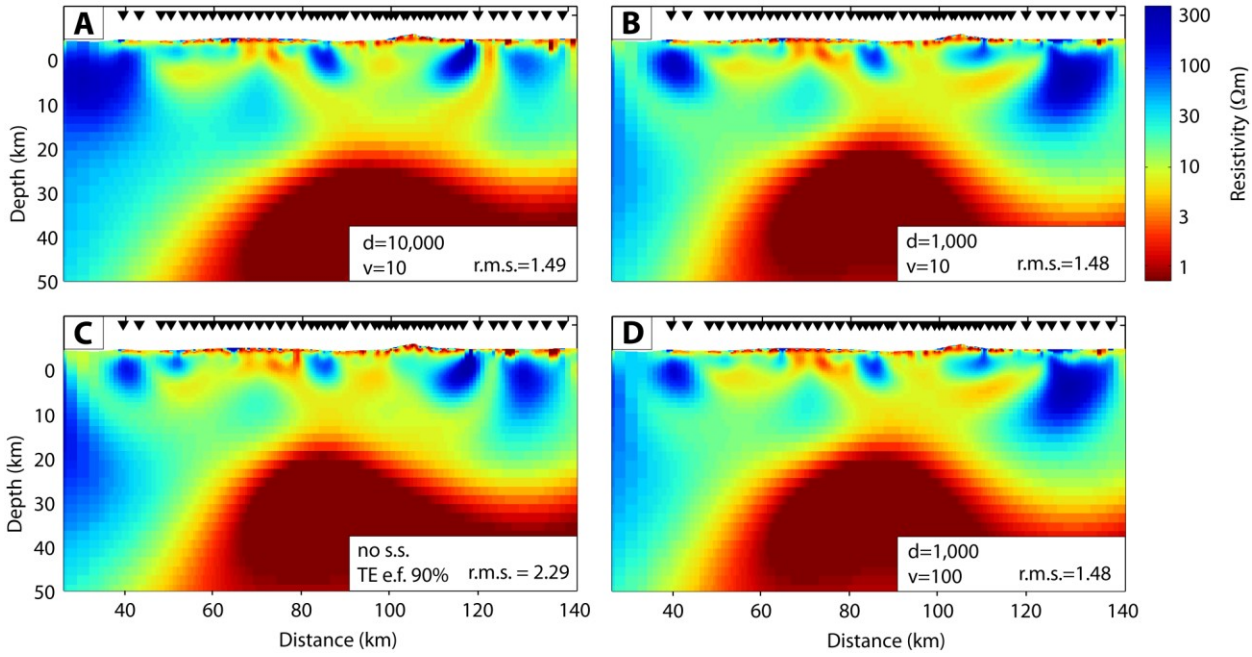

Figure 6.12: Resistivity models produced with various strategies for correcting static shifts, see text for details. Panel A shows the preferred 2-D resistivity model. The main features are observed in each model, indicating they are required by the MT data.

6.2.11 Effect of Varying the Starting Model

Varying the starting model had little effect on the main features of the inversion model. If the starting model was too high (e.g., 1000 Ωm), then more iterations were required for model convergence. As expected, the model misfit did not vary significantly when using different starting models. Figure 6.13 shows this graphically as a comparison of model roughness, r.m.s. misfit, and the starting model halfspace resistivity chosen. As can be seen, the variations are minimal. The models had the same inversion parameters as the preferred model, with the exception that topography was not included in this example. Inversions were all run for 100 iterations to ensure convergence.

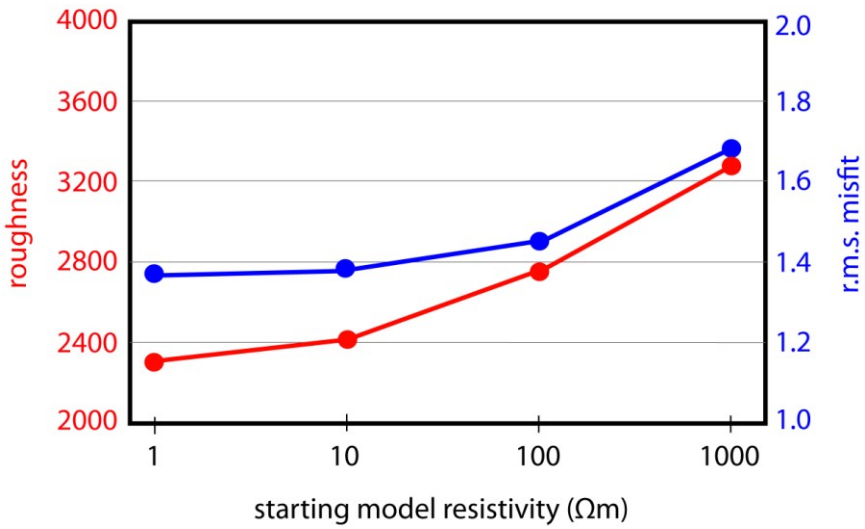

Figure 6.13: Varying the starting model halfspace resistivity of the 2-D inversion has only a small effect on the r.m.s. misfit of the model (blue line; right-hand y-axis) or the roughness (red line; left-hand y-axis).

6.2.12 Effect of Varying the Strike Angle

Before carrying out a 2-D inversion the data must be rotated to the geo-electric strike direction determined (as explained in Section 4.8). Directionality analysis carried out in Section 5.5 showed that a range of strike angles were compatible with the majority of MT sites. Variations in the strike direction were investigated by running multiple inversions with the data rotated to different strike angles. Figure 6.14 shows this along the AB profile segment of Profile 1 for angles of N20°E (r.m.s. misfit of 1.49), N30°E (r.m.s. misfit of 1.49; preferred model), and N40°E (r.m.s. misfit of 1.51). Inversion parameters used were the same as the preferred model. No significant changes in the resistivity model features are observed when geo-electric strike is varied over this range.

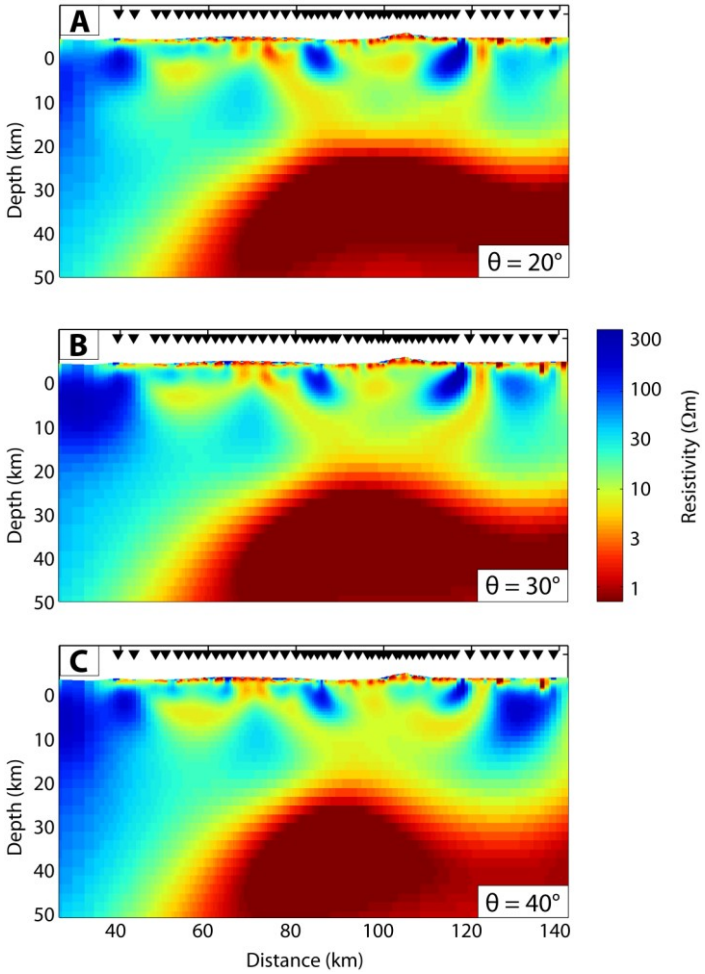

Figure 6.14: Varying the strike angle used in the inversion has minimal change on the model. The r.m.s. misfit for a strike angle of 20° (Panel A) is 1.49; for a strike angle of 20° (Panel B; preferred model) is 1.49; a strike angle of 40° (Panel C) is 1.51.

6.2.13 Resistivity Features Required by the MT Data

One last test to ensure that the features present in the preferred inversion model were required by the data was to run the inversion starting with the preferred model but with the intermediate depth features removed. To do this the intermediate features from 3 to 20 km depth below surface were set to a resistivity of 25 Ωm. Inversion parameters were the same as in the preferred model, with the exception that topography was omitted (for simplicity). Figure 6.15 shows the results of this analysis. The model from this test shows the same features, with identical

geometry and resistivities. This test shows that the main features of the inversion model are required by the MT data. Figure 6.16 shows the apparent resistivity and phase curves for the MT data at one station (1463N16-11, just south of Volcan Uturuncu's summit), the fit to the data from the inversion model (Panel A in Figure 6.15), and the forward response when the intermediate features are removed (as in Panel B, Figure 6.15). The figure clearly shows that the MT response with and without the intermediate depth resistivity features is very different.

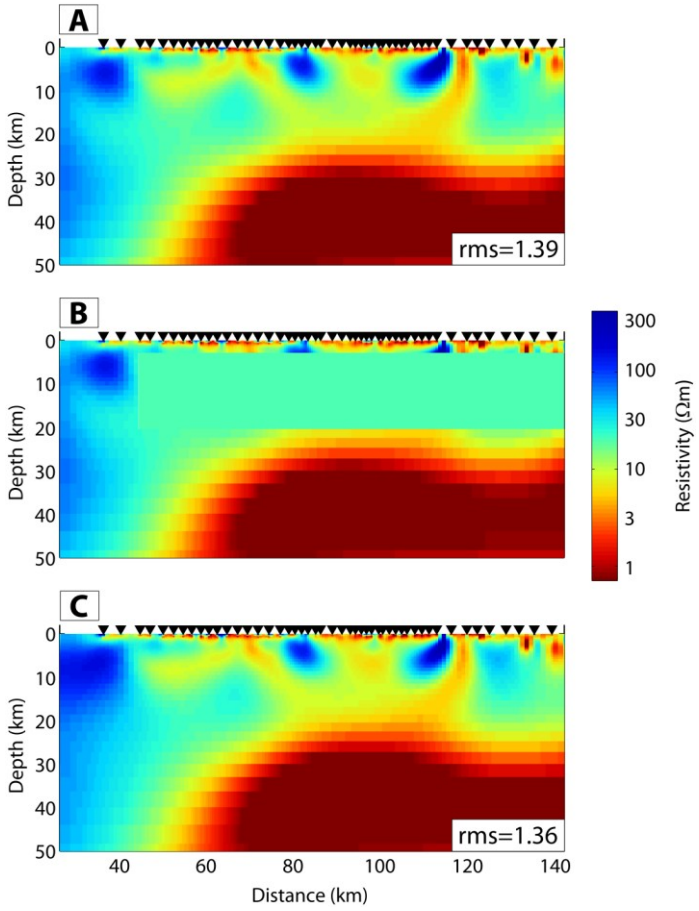

Figure 6.15: A test for the requirement of the intermediate depth resistivity features in the preferred 2-D model. Panel A shows the first inversion model (similar to the preferred model, but with no topography). Note the depths are measured from surface, not sea-level as in Figure 6.2. Panel B shows the inversion model edited to eliminate the intermediate depth features. This model is then used as the starting model for a second inversion run (Panel C). The intermediate depth features are recovered completely, showing that they are required by the inversion in order to fit the MT data.

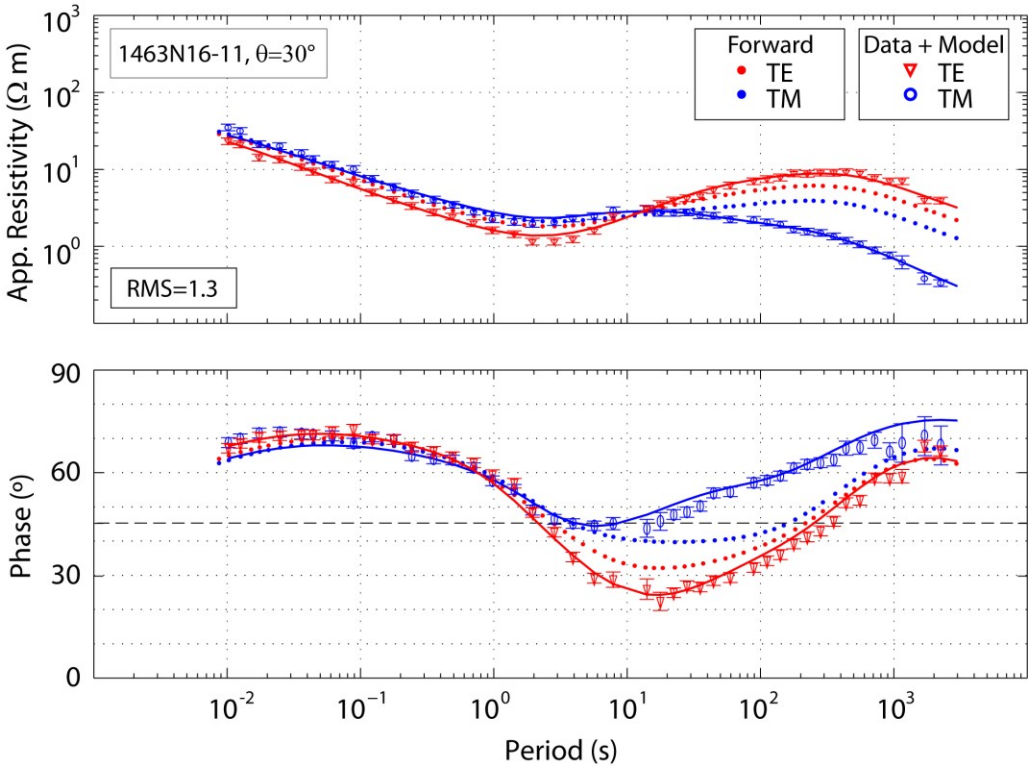

Figure 6.16: Apparent resistivity and phase curves for the MT data at station 1463N16-11, south of Volcan Uturuncu. The fit to the data from the inversion model (Panel A in Figure 6.14) is shown, and the forward response when the intermediate features are removed (as in Panel B, Figure 6.14). The MT response with and without the intermediate features is very different, and they are required by the model in order to fit the measured MT data.

6.2.14 Southern Line, Profile 2

Many other 2-D inversion models were created along other profiles. The majority of the profiles running west-east showed similar features to the preferred model (for example, a line from Laguna Colorado to Rio Chilenas, passing north of Volcan Uturuncu). Figure 6.17 shows the 2-D inversion model of the southern profile (Profile 2) as an example, as it is the most distinct and has several interesting features. The model uses the same inversion parameters as the preferred model discussed above, although it does not include topography. A final r.m.s. misfit of 1.64 was achieved, reduced from 10.8. The Sol de Manana geothermal field can be identified as shallow conductive body at a distance of 30 km. Salar de Chalviri, a large salt flat, also appears as a very

strong surface conductor. As in the preferred model, there exists an intermediate depth conductor below Volcan Uturuncu, but it is smaller. The bulge below Uturuncu is absent, with the surface of the deeper conductor being mostly flat. Differences also exist in the western edge extent of the deep conductor, ending ~30 km farther east than was seen on Profile 1 (near Laguna Hedionda, 67.4°W - 67.3°W, a distance of ~60-70 km along the profile). This matches the seismic models of Zandt et al. (2003) and Ward et al. (2014) (see Section 3.2.3 and 3.2.4) which show that the maximum westward extent of the APMB is near latitude 22°, and narrows significantly from 22.5° to 30° latitude.

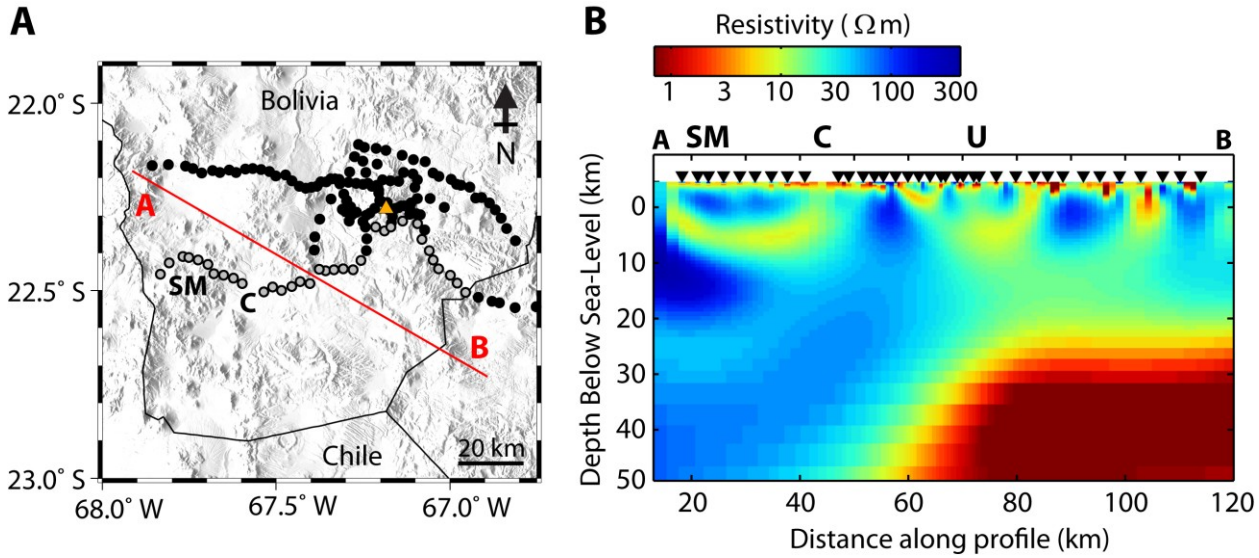

Figure 6.17: Profile 2 (red line, AB) runs along the southern line roughly parallel to Profile 1, but offset southwards by about ~30 km. Panel A shows the location of the magnetotelluric sites used in the 2-D model (grey circles). Volcan Uturuncu is marked with an orange triangle. SM - Sol de Manana geothermal field; C - Salar de Chalviri. Panel B shows the 2-D inversion model. Data were rotated to the geo-electric strike direction of N30°E and projected onto the 2-D profile (line AB). Note the differences in the western edge of the conductive body, and the lack of a bulge below Volcan Uturuncu.

6.2.15 Summary of 2-D Inversions

The regional profile, Profile 1, across Volcan Uturuncu was separated into two segments, AB and BC, based on the observed geo-electric strike angles. The preferred 2-D resistivity model, shown in Figure 6.2, was obtained from the joint inversion of TE and TM mode magnetotelluric data at 73 sites and had an r.m.s. misfit of 1.49 along segment AB, and 1.48 along segment BC, indicating an acceptable fit to the measured data. Many combinations of inversion parameters were investigated and a set of preferred parameters was determined. The main resistivity features do not depend on any specific choice of inversion parameters, giving confidence that the main resistivity features are robust and are required by the MT data. The preferred 2-D resistivity model shows three distinct layers: a shallow, variable surface conductor; a deep, spatially uniform conductor at a depth of 15-20 km below sea-level; and an intermediate layer consisting of series of conductors and resistors. A more thorough explanation of resistivity model features will be presented in Section 6.4.

6.3 3-D MT Inversion

Dimensionality analysis showed that a 2-D inversion was valid on a regional scale (i.e., Profile 1), but that 3-D resistivity structure was locally present around Volcan Uturuncu and nearby Volcan Quetena (see Section 5.5). Therefore, a subset of the MT data on a network of stations around Volcan Uturuncu was inverted using the 3-D inversion algorithm of Siripunvaraporn et al. (2005) (WSINV3DMT). The details of the 3-D inversions are presented in this section.

6.3.1 Network of MT Sites Around Volcan Uturuncu

The 3-D inversion algorithm used (WSINV3DMT) was computationally intensive and required a large amount of resources and time to run (e.g., 18 processors, 144 GB of RAM, running for up to 336 hours on a WestGrid cluster). It was not feasible to run the 3-D inversion for all of the MT sites. Therefore, only a subset of MT sites were chosen for a 3-D inversion. A dense network of

MT sites both on and around Volcan Uturuncu was chosen for the 3-D inversion, as shown in Figure 6.18. An area of roughly 40 x 40 km centred around the volcano contained 73 MT sites; this network of MT sites was named S73. A expanded network with 96 MT sites was also examined (S96), which had a larger area of roughly 50 x 50 km (see Section 6.3.10).

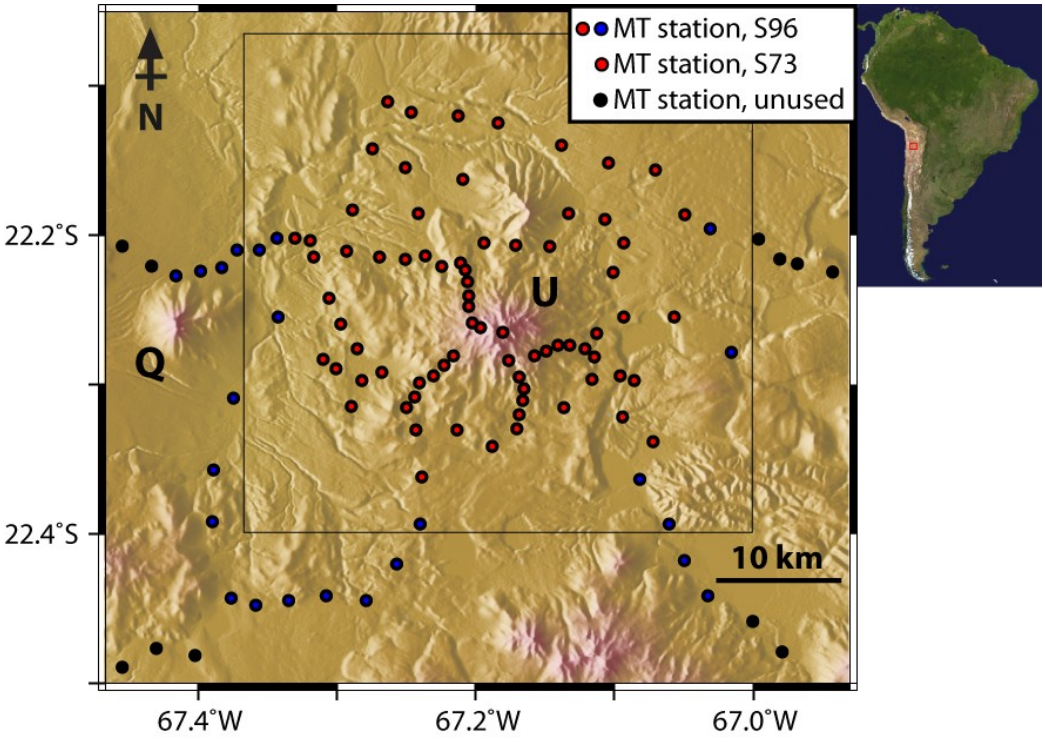

Figure 6.18: A set of 73 magnetotelluric sites around Volcan Uturuncu (red circles, S73), and an extended set of 96 sites (blue and red circles, S96), are used in the 3-D MT inversion. Black circles are MT stations which are not used in the 3-D inversion. The grey box marks the area (approximately 40 x 40 km) shown in the preferred 3-D resistivity model. Volcan Uturuncu (U) is located at near the middle of this grid of stations and Volcan Quetena (Q) is to the west. Inset map shows the location of the study are within South America.

6.3.2 Preferred 3-D Resistivity Model

Many combinations of inversion parameters were investigated and a set of preferred parameters that worked best was determined. The 3-D resistivity model presented in this section is the preferred model, and is representative of most models produced (a total of 49 inversion runs were done, experimenting with different parameters). Other resistivity models produced from inversion parameter variations are discussed and shown in Section 6.3.6. The main resistivity features do not depend on any specific choice of inversion parameters, implying the features are required by the MT data.

The preferred 3-D resistivity model obtained from the joint inversion of all elements of the impedance tensor (i.e., Z_{xx}, Z_{xy}, Z_{yx}, Z_{yy}) for a network of 73 sites around Volcan Uturuncu (S73) is shown in Figure 6.19. This 3-D resistivity model was first shown by Comeau et al. (2015). After a total of 10 iterations the r.m.s. misfit was reduced from 9.30 to 0.95, indicating an acceptable fit to the data (see Section 6.3.4 for more detail on model convergence). The 3-D resistivity model shows three distinct layers: (1) a shallow surface conductor; (2) a deep, spatially uniform conductor (C2) at a depth of 10-15 km below sea-level; (3) an intermediate layer with a prominent set of dyke-like conductors located at approximately sea-level (C4 and others). See Section 6.4 and Chapter 7 for a full interpretation and implications. Figure 6.19 panel A shows a West-East vertical cross-section and panel B shows a South-North vertical cross-section through the 3-D model. Panels C and D show two horizontal slices at depths of 1700 m above sea-level (3.3 km below surface) and 900 m BSL (5.9 km below surface). Earthquake hypocenters from Jay et al. (2012) are also shown. See Figures A.4 and A.5 in the Appendix for larger figures of the preferred 3-D resistivity model.

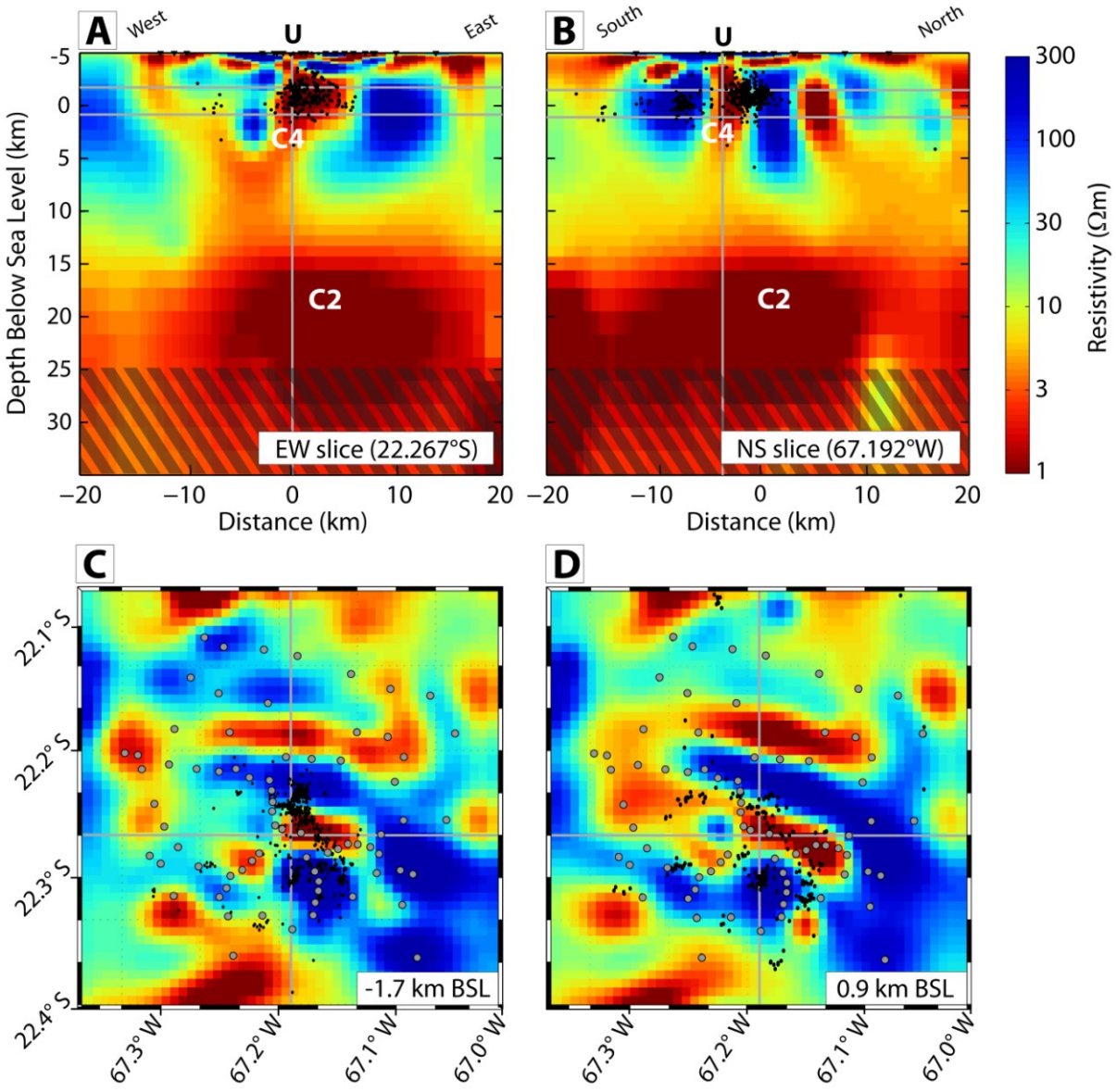

Figure 6.19: The preferred 3-D resistivity model (S73), as shown by Comeau et al. (2015). The upper panels show vertical slices through the inversion model, both West-East (Panel A) and South-North (Panel B). The lower panels show depth slices 1700 m above sea-level (Panel C) and 900 m below sea-level (Panel D). The 73 MT sites used in the inversion are shown as grey circles. Black dots are earthquake hypocenters from Jay et al. (2012). A r.m.s misfit error of 0.95 was achieved, indicating an acceptable fit to the measured MT data. The locations of each slice are indicated by grey lines on the other slices. Depths are measured from sea-level, assuming a mean surface elevation of 5000 m. U = Volcan Uturuncu. The hatched pattern shows the skin depth limit for EM signals, below this limit there is no resolution.

6.3.3 3-D Inversion Parameters

The inversion model mesh grid had cells with horizontal dimensions of 750 m x 750 m, with 62 cells in each horizontal direction. This spacing ensured that at least 2 cells existed between adjacent MT stations, helping the inversion to fit MT data at adjacent stations which have different resistivities. The vertical cells increase in size with depth in order to mimic the diffusive nature of the EM signals used in MT. There were 51 vertical Earth cells and 7 air cells in the model. Vertical cells were 50 m thick at the surface and were increased by a factor of 1.2 to a thickness of 1000 m at a total depth of ~5 km, then they were set to a uniform thickness of 1000 m to a total depth of ~20 km, then increased to a thickness of 2200 m to a total depth ~40 km, after which they were set to increase by a factor of 1.5 at each step. The total number of cells was ~3,600. The 3-D inversion used the full impedance tensor (4 components) with an error floor set at 10%. A total of 18 periods were used, spread across the band 0.01 - 1200 s. The inversion began from a uniform 10 Ωm halfspace. The fit of the model response to the measured apparent resistivity and phase data is discussed in Section 6.3.5.

6.3.4 Model Convergence

The 3-D inversion used the algorithm of Siripunvaraporn et al. (2005), and a 2-stage approach was used. For the first stage, the initial model used was a uniform halfspace (10 Ωm) and the inversion algorithm searched for spatially smooth models varying from this. After 4 iterations the r.m.s. misfit was reduced from 9.30 to 1.45. A second inversion run was then begun, using the final model from the first stage as the prior model (instead of the usual halfspace). The inversion algorithm then searched for a new smooth model that was close to the prior model, but the initial model used is still a halfspace. After 6 iterations the r.m.s. misfit was reduced to 0.95. Figure 6.20 shows this 2-stage approach for the preferred 3-D model.

The two-stage approach was used because the prior model in the first stage, about which the inversion algorithm searches for a solution, is essentially a starting guess. The second stage uses

a prior model which has been shown to fit the data, and represents a guess which is much closer to the true model. In most cases, the first stage does a good job of fitting the measured MT data; the second stage simply acts to refine and accentuate the resistivity features. Figure 6.21 compares both a vertical and horizontal slice of the inversion model produced from each stage in order to illustrate their similarities.

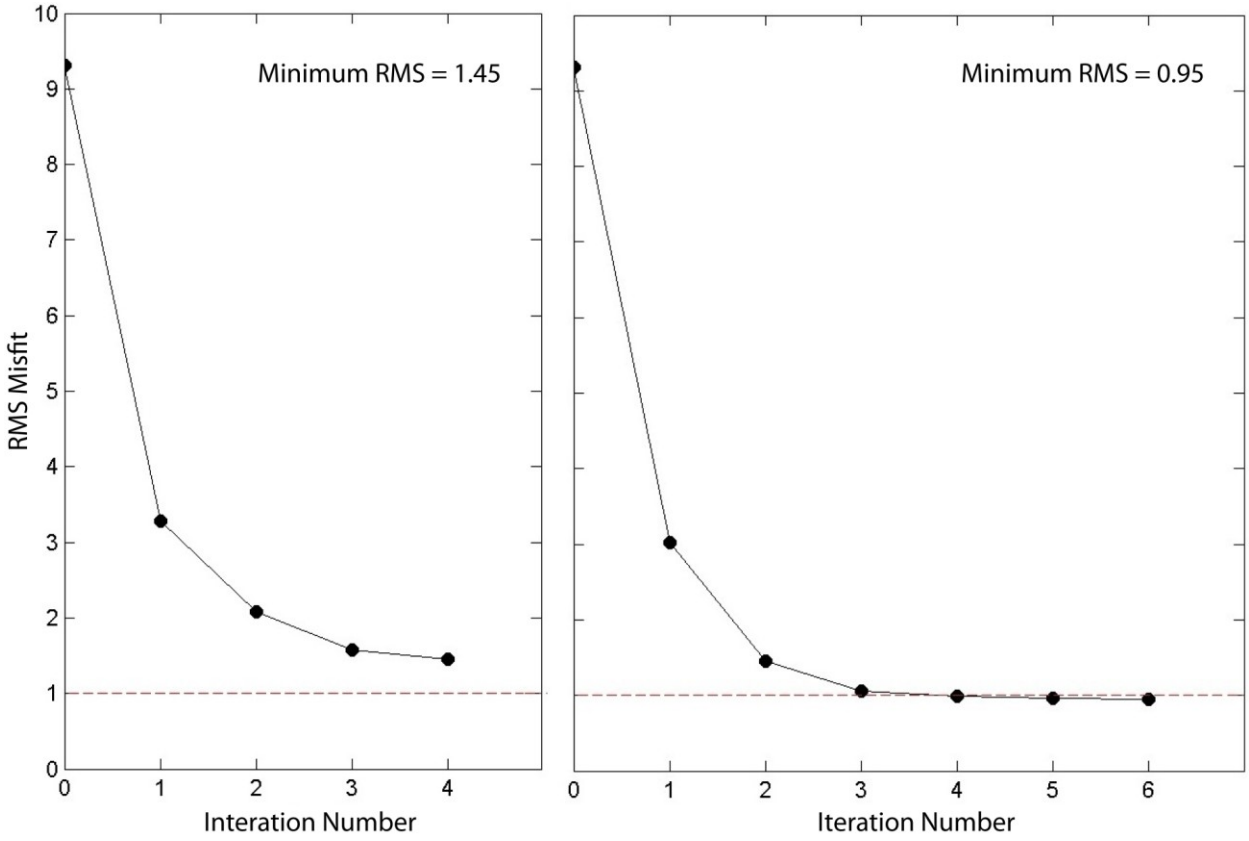

Figure 6.20: The 3-D inversion of the preferred model shows convergence with a 2-stage approach. The left panel shows the first stage, with 4 iterations. The right panel shows the second stage, when the inversion is run a second time, starting with the final model from the first stage as the prior model. After 6 iterations, the r.m.s. misfit converges to 0.95.

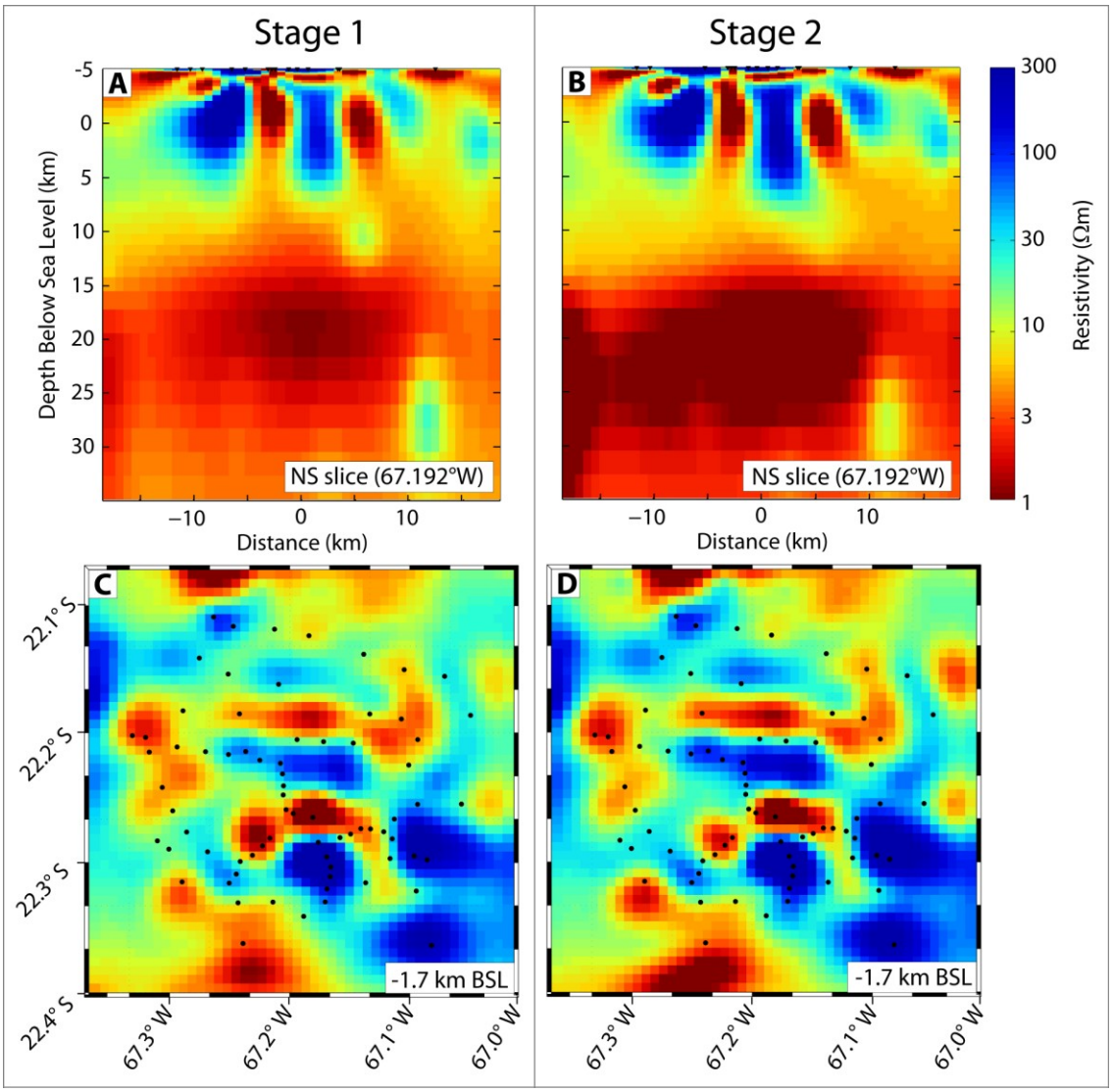

Figure 6.21: The preferred 3-D inversion used a 2-stage approach, using the final model from the first stage as the prior model for the second stage, see text for details. The left side shows the first stage model; the right side shows the second stage model. The second stage acts to refine and accentuate the resistivity features. Panels A and B compare a vertical south-north slice; Panels C and D compare a horizontal slice at a depth of -1700 m below sea-level.

6.3.5 MT Data Fit

The preferred 3-D model generally fits the measured MT data well, with an overall r.m.s. misfit of 0.95. Table 6.1 shows individual misfits for each MT station. Figure 6.22 shows the data fit at four representative MT sites. The diagonal components (Z_{xx} and Z_{yy}; indicative of non-2-D effects, see Chapter 4) are much smaller than the off-diagonal components, implying mainly 2-D structure. This can be seen in Figure 6.22 where ρ_{xx} and ρ_{yy} are smaller (often by one or two orders of magnitude) than ρ_{xy} and ρ_{yx}, specifically at short periods. The diagonal components also have larger error bars and subsequently are not fit as well as the off-diagonal components, although they are still fit within error.

SITE	RMS
'1463N03_11b'	0.878
'1463N04_12'	0.488
'1463N05_11b'	0.810
'1463N07_12'	1.125
'1463N08_12'	0.406
'1463N09_11b'	1.825
'1463N09_12'	0.503
'1463N10_11b'	0.939
'1463N12_11b'	0.684
'1463N13_11b'	0.781
'1463N14_11b'	0.615
'1463N14_12'	0.385
'1463N15_11b'	0.998
'1463N16_11b'	1.907
'1463N16_12'	0.720
'1463N17_12'	0.597
'1463O30_11'	0.613
'1465029_11b'	0.675
'1465N04_11b'	0.506
'1465N04_12'	0.510
'1465N05_11b'	0.549
'1465N05_12'	0.749
'1465N06_11b'	0.726
'1465N06_12'	1.288
'1465N07_12'	1.336

SITE	RMS
'1465N09_11b'	2.624
'1465N09_12'	0.404
'1465N10_11b'	1.772
'1465N10_12'	0.549
'1465N11_11b'	0.694
'1465N11_12'	0.602
'1465N14_12'	0.614
'1465N15_11b'	0.650
'1465N15_12'	0.950
'1465N16_12'	1.270
'1465N17_12'	1.770
'1465N23_12'	0.676
'1465O18_12'	0.413
'1465O19_12'	0.374
'1465O22_12'	0.690
'1465O23_12'	0.697
'1493N06_12'	2.564
'1493N07_12'	1.749
'1493N09_11b'	0.593
'1493N10_11b'	0.831
'1493N10_12'	0.450
'1493N11_11b'	0.510
'1493N12_11b'	0.542
'1493N13_11b'	1.306
'1493N14_11b'	0.692

SITE	RMS
'1493N16_11b'	0.677
'1493N16_12'	1.375
'1493N23_12'	0.446
'1493O22_12'	0.512
'1493O23_12'	0.367
'1495N04_11b'	0.643
'1495N05_11b'	0.755
'1495N06_11'	0.597
'1495N09_11b'	0.667
'1495N11_11b'	0.364
'1495N12_11b'	0.377
'1495N13_11b'	0.581
'1495N14_11b'	0.702
'1495O30_11b'	0.596
'1496N05_12'	0.707
'1496N07_12'	1.584
'1496N10_12'	0.584
'1496N14_12'	0.663
'1496N16_12'	0.934
'1496N23_12'	0.883
'1496O19_12'	0.596
'1496O22_12'	0.598
'1496O23_12'	0.363

Table 6.1: Root mean square (RMS) misfits for each MT site of the preferred 3-D inversion.

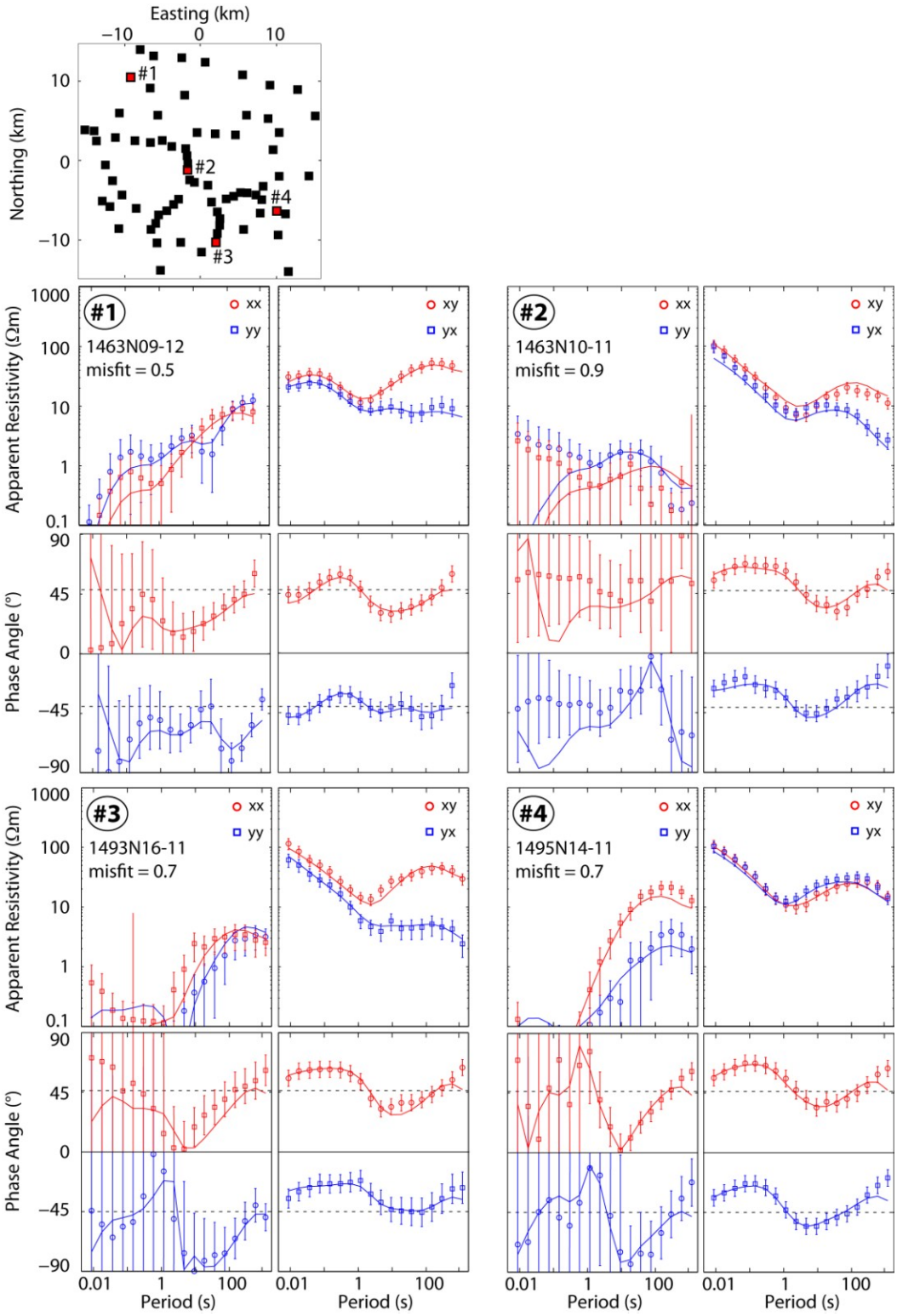

Figure 6.22: Data fit for the preferred 3-D inversion at four representative MT sites. The map shows their location on the S73 grid of MT sites. The line shows the model response and the points are the measured data with error bars. The model generally fits the data well.

6.3.6 Inversion Parameter Variations

Many inversion models were produced for a range of inversion parameters. In total, 75 models were computed and compared. Examples of parameters investigated include: changing the inversion starting model, adding tipper (H_z) response, varying model smoothing, and different error floor limits for diagonal and off-diagonal impedance components. The trade-off between model smoothing and data misfit, which is controlled by the tau parameter for the 2-D inversions, is solved iteratively by the algorithm for the 3-D inversion. The main resistivity features of the models did not depend on any specific choice of inversion parameters or combination of parameters. This gives confidence that the main features are robust and required by the MT data. Small differences arise in the geometry of the structures or their resistivity values, but are within the limitations of the inversion and do not affect the interpretation. Examples are illustrated in the following sections, but are not exhaustive.

6.3.7 Inclusion of Tipper Data

The preferred 3-D inversion model uses the full MT impedance tensor data (Figure 6.19). The tipper (H_z) data can also be included in the joint inversion. An error floor of 0.02 (absolute units) was used, and the starting model was a uniform 10 Ωm halfspace. After a total of 6 iterations, using the two-stage approach, the r.m.s. misfit was reduced from 7.67 to 0.99, indicating an acceptable fit to the data (stage 1 reduced the misfit from 7.67 to 1.37 after 4 iterations). Figure 6.23 shows the result of the inversion when tipper data were included. Panel A shows a West-East vertical cross-section and panel B shows a South-North vertical cross-section. Panels C and D show two horizontal slices at depths of -1700 m BSL (i.e., 1700 m above sea-level) and 900 m BSL. Figure 6.24 shows the fit of the IVs for three select periods, showing that the response and the data are generally close. Note that tipper data were not recorded at every site.

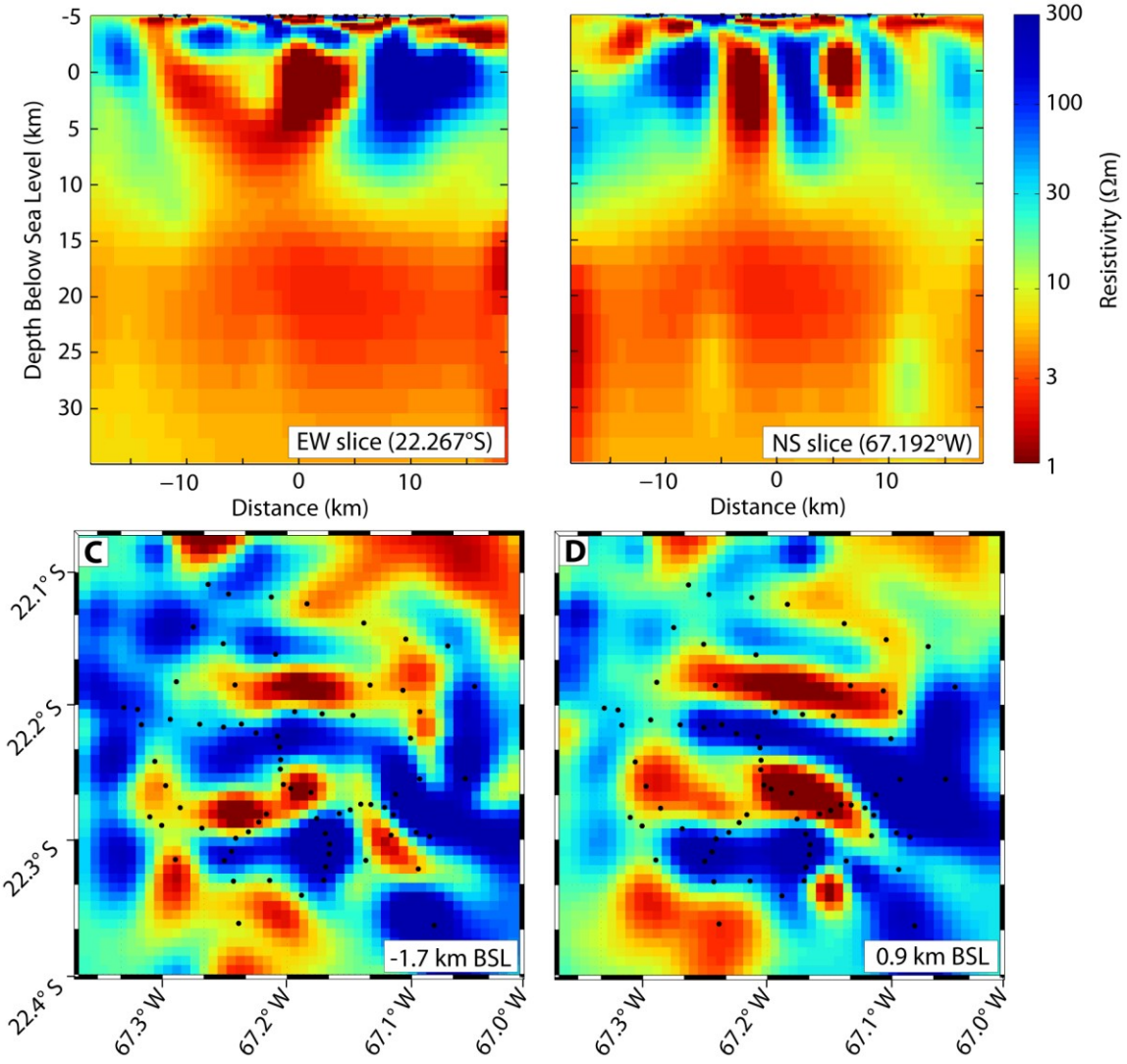

Figure 6.23: The 3-D inversion model including tipper data. The main resistivity features are similar to the preferred model (Figure 6.19). Panels A and B are west-east and south-north vertical slices through the 3-D model. Panels C and D are horizontal slices at -1700 m below sea-level and 900 m below sea-level. The location of magnetotelluric sites used in the inversion are shown as black circles.

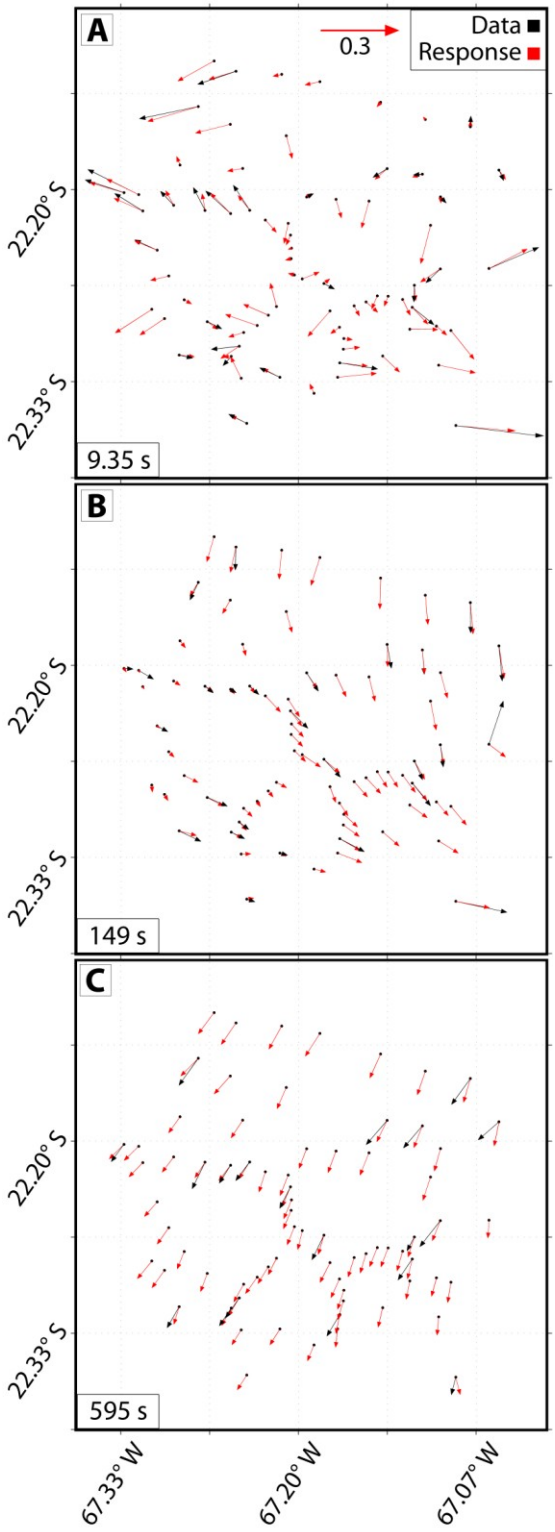

Figure 6.24: The fit of the induction vectors for a period of 9.35 s (Panel A), 149 s (Panel B), and 595 s (Panel C). An induction vector of length 0.3 is shown for scale. The response and the data are generally close. Note that tipper data was not recorded at every MT site.

6.3.8 Effect of Varying Model Smoothing

The 3-D inversion algorithm contains three parameters to control horizontal (x and y) and vertical (z) smoothing. Default smoothing for all three directions is set to a value of 0.1 (unitless ratio). By increasing or decreasing the value of smoothing in the x and y directions and keeping the z direction smoothing fixed the ratio and magnitude of smoothing in the vertical or horizontal direction can be altered. The preferred model used equal smoothing of 0.1, 0.1 and 0.1, for x, y, and z directions.

Figure 6.25 shows the effect of increasing and decreasing the smoothing parameters. When the horizontal smoothing parameters (both x and y) were decreased (panels A and B; e.g., 0.05) and the vertical smoothing parameter was fixed (0.1), vertical smoothing became more dominant and the model resistivity features appear smeared vertically. When the horizontal smoothing parameters (both x and y) were increased (panels E and F; e.g., 0.15), the horizontal smoothing became dominant and model resistivity features appear smeared horizontally. Panels C and D show the model with default smoothing, when the three parameters were equal (all set to 0.1). The models appear visually different, but the r.m.s. misfit values are all similar. For panels A and B, vertical smoothing, the r.m.s. misfit was 1.54; for panels C and D, no smoothing, the r.m.s. misfit was 1.59; for panels E and F, vertical smoothing, the r.m.s. misfit was 1.61.

These resistivity models used a slightly different approach than the 3-D model discussed thus far. Rather than using MT data from a uniformly spaced range of frequencies, a specific frequency set was chosen which had more emphasis on the lower frequencies. For example, using this approach only 5 frequencies used (of 18 total) were above 0.5 Hz, compared to 9 frequencies (of 18 total) used in the preferred 3-D model. The intent of this approach was to better fit the long period MT data, rather than the short period data. The resistivity model features are similar to those of the preferred model.

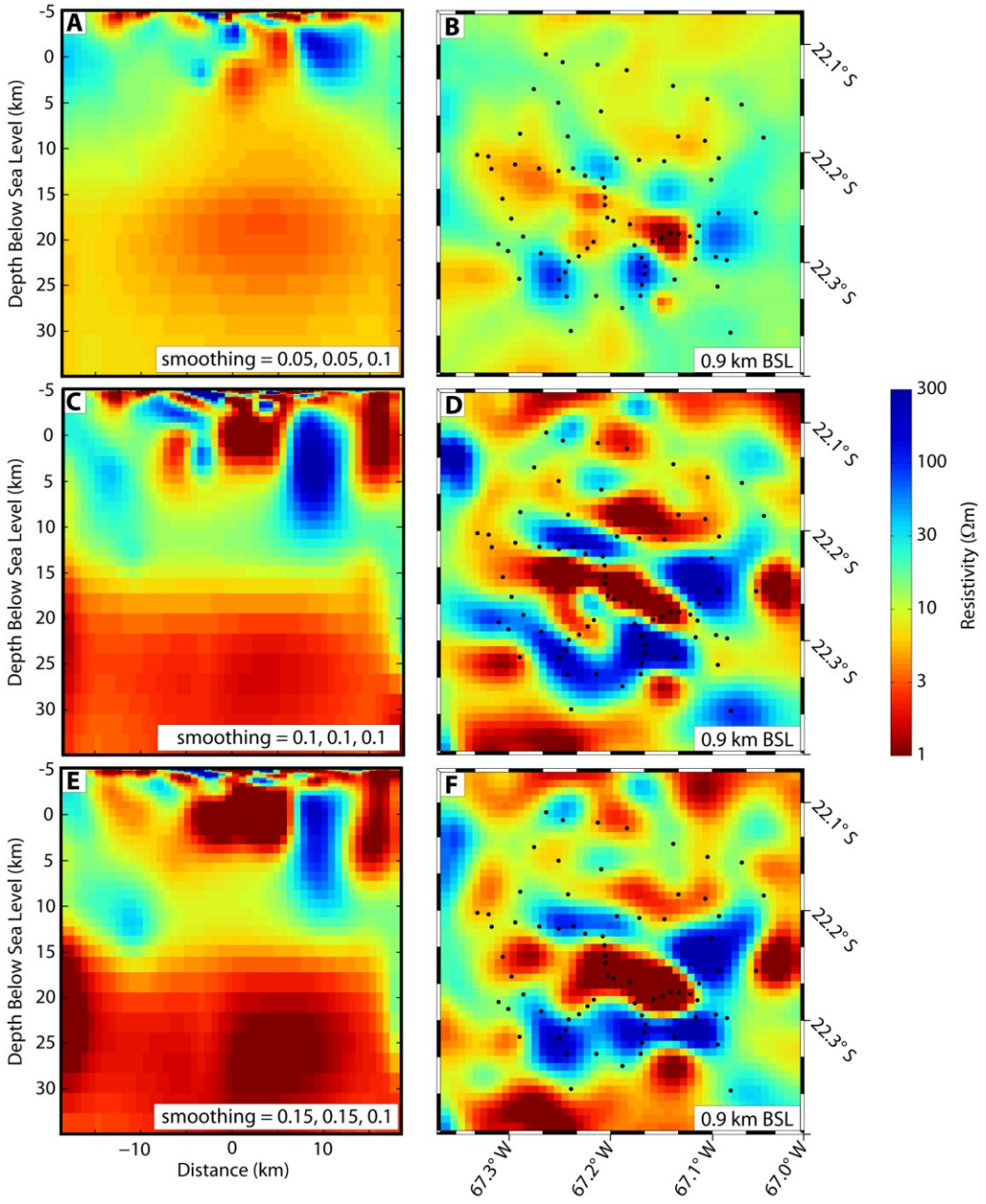

Figure 6.25: Resistivity models produced by varying the smoothing parameters in the inversion algorithm. The models are made smoother in the vertical direction (panels A and B) by decreasing the ratio of the horizontal (x and y) to vertical (z) smoothing parameters. Default smoothing with all directions given equal weight is shown in panels C and D. Making the model smoother in the horizontal directions is shown in panels E and F. These models used a modified approach with emphasis on fitting longer period data. Panels A, C, and E are west-east vertical slices through the 3-D model along latitude 22.267°S. Panels B, D, and F are horizontal slices at 900 m below sea-level. The location of magnetotelluric sites used are shown as black circles.

6.3.9 Effect of Varying Error Floor

In the inversion algorithm each data point is weighted based on its error. A minimum error, or error floor, can be set in order to equalize the influence from all points within an acceptable error range, and to minimize the potentially dominating effect of points with small error bars. If the error of the data point is above this error floor then its actual error will be used in the inversion algorithm. The preferred model uses an error floor of 10% for both the diagonal and off-diagonal impedance components.

When 5% error floor was used (Panels A and B) the r.m.s. misfit was 3.56 (5 iterations, one stage); for 10% error floor (Panels C and D) the r.m.s. misfit was 1.65 (6 iterations); for 20% error floor (panels E and F) the r.m.s. misfit was 1.09 (3 iterations). The r.m.s. misfit decreases as the error floor increases, because the r.m.s. misfit is normalized by the error. Therefore, a more meaningful way to determine the error for comparison between models would be to take the product of the r.m.s. misfit and the error floor used for that inversion. Doing so for 5%, 10%, and 20% error floors gives errors of 17.8%, 16.5%, and 21.8%, showing that they are of similar magnitude, and that the error is lowest for the 10% error floor case, see Table 6.2. Figure 6.26 shows how the resistivity models change when the error floor is varied.

ERROR FLOOR (%)	RMS MISFIT	PRODUCT
5	3.56	17.8
10	1.65	16.5
20	1.09	21.8

Table 6.2: The r.m.s. misfit is lower for models that have higher error floors. Therefore, a more meaningful way to determine the error for comparison between models is the product of the r.m.s. misfit and the error floor used.

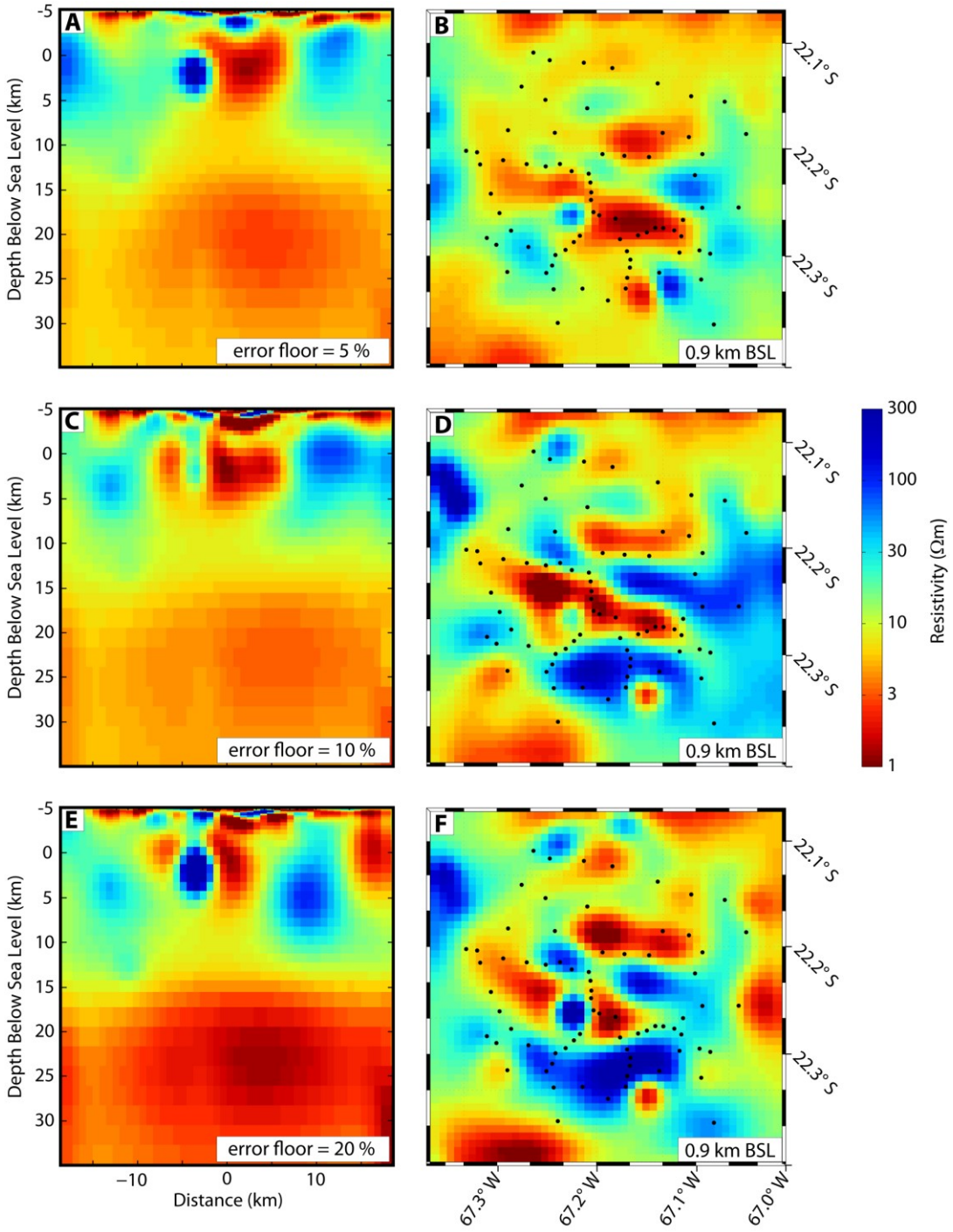

Figure 6.26: Resistivity models produced by varying the error floor applied to the magnetotelluric (MT) data used in the inversion algorithm. The main features were recovered in each case. Panels A, C, and E are west-east vertical slices through the 3-D model along latitude 22.267 °S. Panels B, D, and F are horizontal slices at 900 m below sea-level. The location of MT sites used in the inversion are shown as black circles.

6.3.10 Expanded Area S96 Inversion

An expanded network with a subset of 96 MT sites (S96) was also examined. The area covered is significantly larger than the preferred model (S73), but the MT site distribution is less dense. The 3-D resistivity model obtained from the full impedance tensor MT data is shown in Figure 6.27. The inversion parameters used are the same as in the preferred 3-D inversion (S73). After a total of 11 iterations (using a two-stage approach) the r.m.s. misfit was reduced from 8.74 to 0.95 (the first stage reduced the misfit to 1.47 in 8 iterations). The resistivity model shows similar features to the preferred 3-D model (S73). However, the extended model shows a third dyke-like conductor to the south, that was at the edge of the smaller S73 grid. It also resolves more clearly the resistor below Volcan Quetena (R1 on the 2-D profile, Figure 6.2).

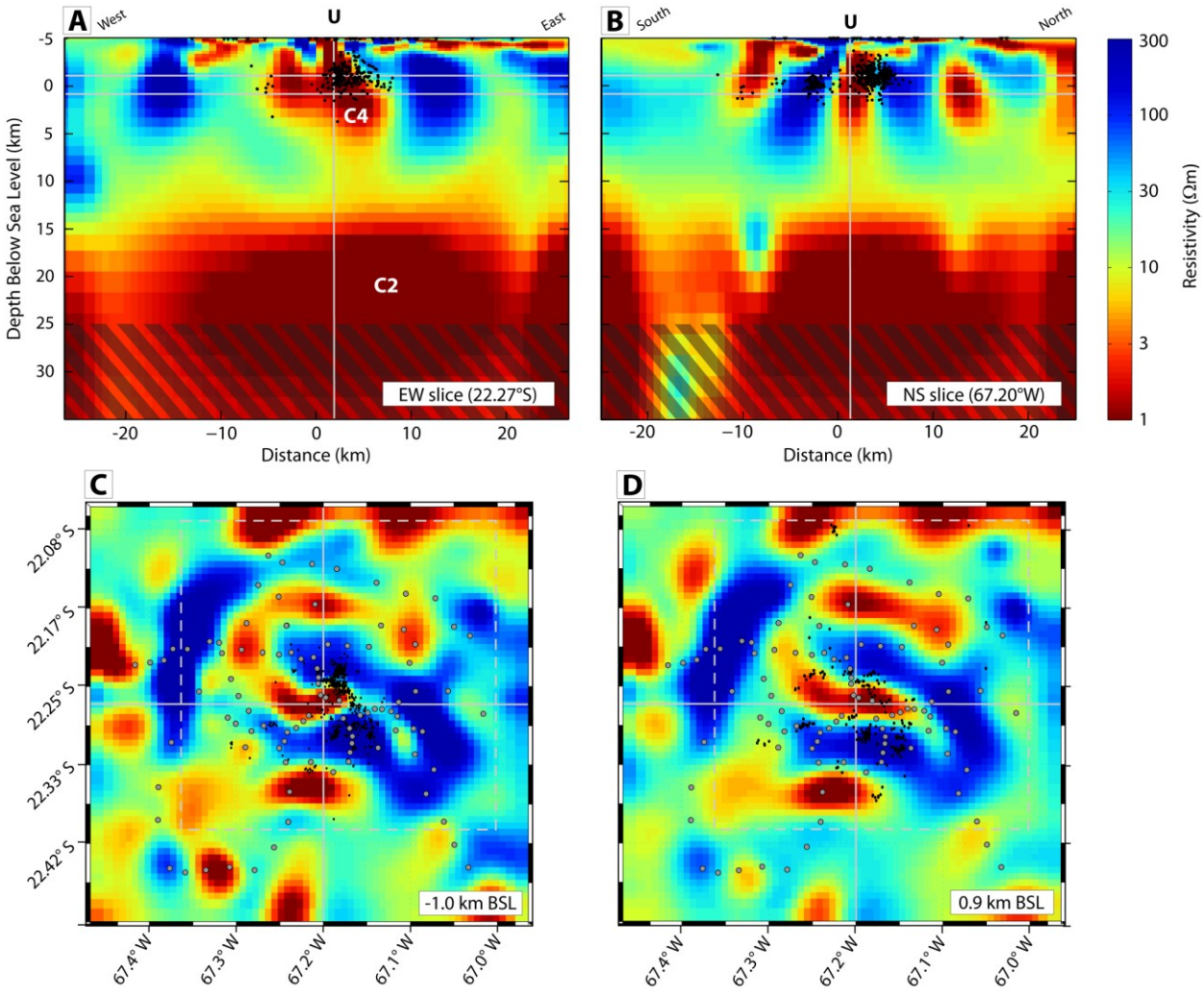

Figure 6.27: The extended S96 3-D resistivity model. The upper panels show vertical slices through the inversion model, while the lower panels show depth slices. The location of the 96 magnetotelluric sites used in the inversion are shown as grey circles. Black dots are earthquake hypocenters from Jay et al., (2012). The locations of each section or slice are indicated by grey lines on the other slices. The hatched pattern shows the skin depth limit for EM signals, below this limit there is no resolution. The grey dashed boxed outlines the area of preferred inversion (S73) for comparison.

6.3.11 Resistivity Features Required by the MT Data

A test was performed to ensure that the features present in the 3-D resistivity model were required by the MT data by removing the intermediate depth features from the resistivity model and forward modelling the MT responses to see if they fit the data. When the intermediate features from 2-12 km depth below surface were set to a resistivity of 30 Ωm the response of the forward modelled data had an overall r.m.s. misfit of 2.11. Figure 6.28 shows the results of this analysis for station 1463N09-11 (#1 in Figure 6.22, north of Volcan Uturuncu). The response of the forward modeled MT data is shown as apparent resistivity and phase curves. This station had a r.m.s. misfit of 1.40. The fit to the data from the inversion model response at the same station (S73; Figure 6.19), with r.m.s. misfit of 0.50, is also shown. The model does not fit the data at periods of ~3-300s, the approximate period range of the intermediate features removed. Furthermore, it is clear that the yx component is poorly fit, compared to the xy component. This is significant as it is the yx component ("TE mode") which is sensitive to east-west electric fields and east-west oriented conductors, like those removed from the model. This implies the intermediate depth features are required, and are required to be oriented east-west. Overall, by removing conductive features the apparent resistivity would be expected to increase, and the phase to decrease. This is seen in the forward model. The figure clearly shows that the MT response with and without the intermediate depth resistivity features is distinguishable, and that a model without those features does not fit the data well.

The next step in the analysis was to run an inversion, to test whether the inversion algorithm would introduce the intermediate features again in order to fit the measured data, or whether it would fit the measured data in some other way. The inversion was run again with the prior model set to the edited model where the intermediate depth features have been removed. Inversion parameters were the same as in the preferred 3-D model. The output resistivity model, shown in Figure 6.29, has an r.m.s. misfit of 1.85 and shows the same resistivity features, with similar geometry and resistivities, as the preferred resistivity model. This test shows that the main features of the inversion model are required by the MT data.

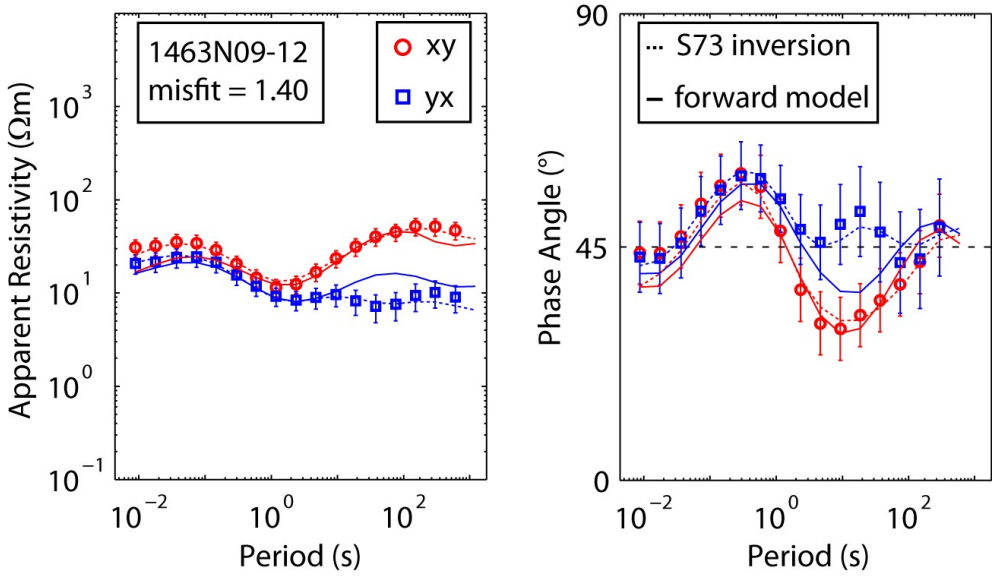

Figure 6.28: Apparent resistivity and phase curves for the MT data (points) at station 1463N09-11 (#1 in Figure 6.22), north of Volcan Uturuncu. The fit to the data from the forward response (solid lines) when the intermediate features are removed, and the inversion response (dashed lines) are shown. The MT response with and without the intermediate features is different, and they are required by the model in order to fit the measured MT data.

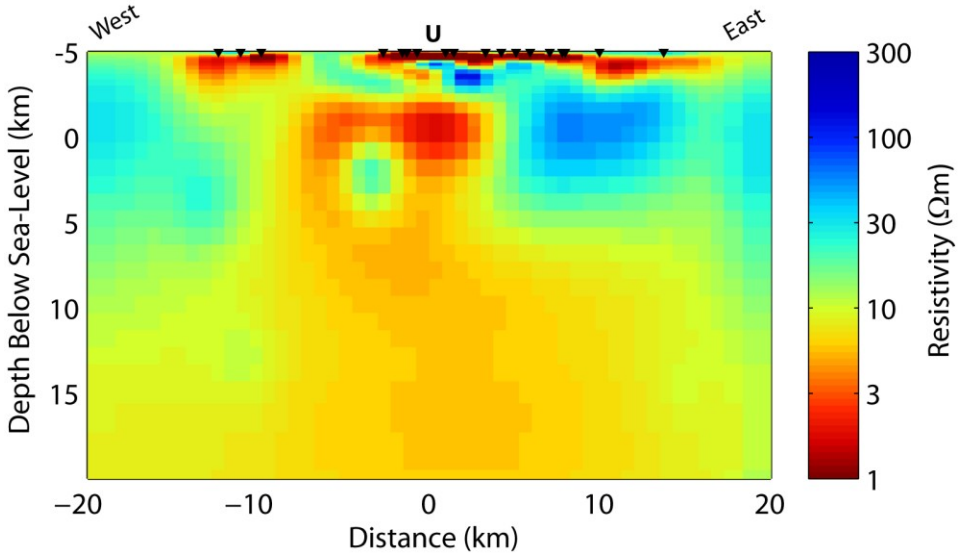

Figure 6.29: A test for the requirement of the intermediate depth features in the 3-D resistivity model. The inversion prior model used was the preferred 3-D model edited to eliminate the intermediate depth features from 2-12 km below surface. The intermediate depth features are recovered in this model, showing that they are required in order to fit the MT data.

6.3.12 Other 3-D MT Inversion Algorithms Used

The 3-D MT inversion algorithm of Siripunvaraporn et al. (2005; WSINV3DMT) was used to produce the 3-D resistivity models presented in this thesis thus far (i.e., Figure 6.19 and 6.27). The 3-D MODEM inversion algorithm of Kelbert el al. (2014) was also used for comparison. This algorithm is computationally faster than WSINV3DMT (days versus weeks) and allows more user control of the resistivity model characteristics. The main advantage of MODEM compared to WSINV3DMT is that it allows topography to be included. Preliminary resistivity models produced show the same resistivity features as the preferred inversion presented above (i.e., Figure 6.19 and 6.27) run with WSINV3DMT. The r.m.s. misfit was reduced from 9.97 to 1.03, in 25 iterations. The resistivity model images the APMB at a slightly shallower depth, and shows the same bulge beneath Volcan Uturuncu. Some small-scale features, such as the intermediate dike-like conductors seen below Volcan Uturuncu in the preferred inversion model, are not seen as clearly, and the resistivity model appears overly smoothed. This may be due to grid cell size differences or to other parameter differences, and more models must be run to better understand the inversion algorithm and the results.

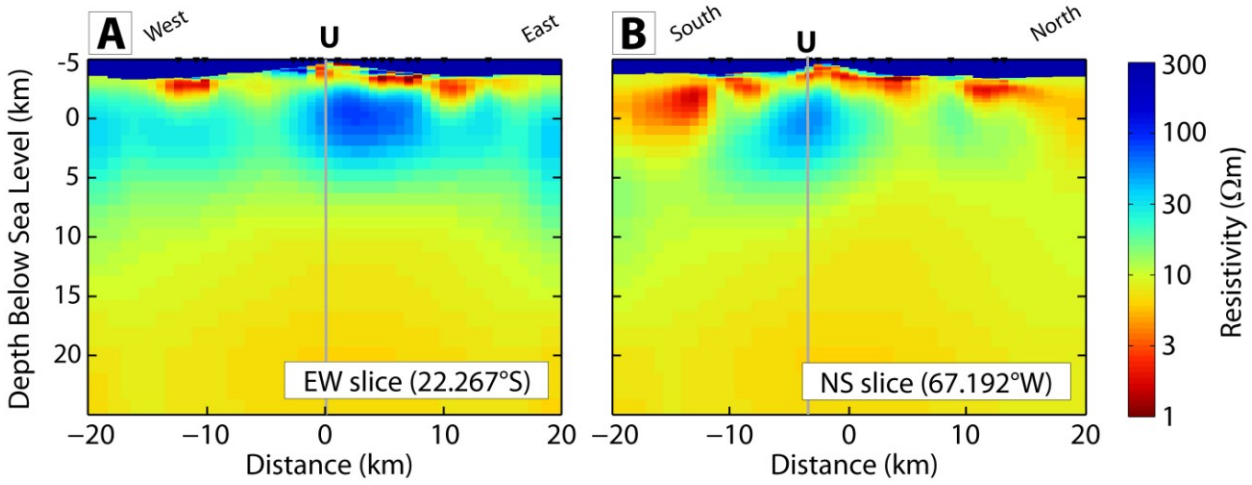

Figure 6.30: Resistivity model with topography produced by the MODEM inversion algorithm of Kelbert el al. (2014).

6.4 Resistivity Model Features

Both the preferred 2-D resistivity model (Figure 6.2) and the preferred 3-D resistivity model (Figure 6.19) show similar major resistivity features. A description and interpretation is provided here which follows that of Comeau et al. (2015), with a full discussion of the implications given in Chapter 7. The resistivity models shows three distinct layers: (1) a shallow heterogeneous surface conductor (C1), about 1 km thick; (2) a deep, spatially uniform conductor (C2) that begins at a depth of 15-20 km below sea-level, within and below this there is no resolution; (3) an intermediate layer with spatially variable resistivity consisting of series of conductors (C3-C7) and resistors (R1, R2).

6.4.1 Shallow Resistivity Features

The near-surface layer (C1) is confined to the upper kilometre and has highly variable but low resistivity (< 10 Ωm). It is likely caused by a shallow aquifer and hydrothermal alteration within the regionally extensive ignimbrite layer. One explanation may be that over a timescale of ~1 m.y. ignimbrites form highly conductive clays by undergoing low-temperature hydrothermal alteration (Bibby et al., 2005). This layer causes the minimum in the apparent resistivity curve observed at a period of ~2 s (see Section 5.4).

6.4.2 Deep Resistivity Features

The prominent conductor C2 is resolved by both the 2-D and 3-D inversions. The resistivity values of the 2-D model appear lower than those of the 3-D model. The depth to the top of C2 is also slightly different (see Chapter 7 for a full discussion). If the top is defined as the 3 Ωm contour in the 3-D model, then this conductor is located at a depth of ~14 km BSL. The 8 Ωm contour of the 2-D model also gives the top at a depth of ~14 km BSL, while the 3 Ωm contour

occurs deeper at ~20 km BSL. For the 3-D model, the 5 Ωm contour occurs at a depth of ~11 km BSL.

As explained in Chapter 4, the exploration depth of MT is controlled by the EM skin depth which is dependent on both the period of the signal and the ground resistivity. MT data can give a reliable estimate of the top of a conductor, but it is not always possible to record long enough periods to detect the base of a conductor. This is the case with the deepest conductor (C2), and the hatched pattern on both models indicates where there is minimal resolution (calculated from one skin depth at 1000 s period).

Based on the horizontal extent, the location of the edges, the very low resistivity values observed, and the laterally uniform resistivity, C2 is believe to be the Altiplano-Puna Magma Body (APMB) (Chmielowski et al., 1999). The low resistivity zone can be interpreted as a zone of partial melt. The western edge of the APMB (i.e., conductor C2) is located east of the modern volcanic arc near Laguna Colorado, at a distance of ~25-40 km along the profile (67.8°W - 67.6°W). The APMB extends ~170 km across Bolivia and NW Argentina, with its eastern edge near Mungayoc, at a distance of ~195-210 km along the profile (66.3°W - 66.1°W). The southern line (Profile 2) shows the western edge much closer to Volcan Uturuncu near Laguna Hedionda (67.4°W - 67.3°W, a distance of ~60-70 km along the profile), showing that south of Volcan Uturuncu the APMB starts to narrow considerably. MT data near Soniquera (latitude of ~21.9°S, ~50 km North of Uturuncu) show only a weak conductor, implying this is the northern edge of the APMB. The southern edge of the APMB is not constrained by the MT data due to a lack of MT station coverage, but is believed to extend to the Bolivian border (latitude of ~22.8°S, ~60 km south of Uturuncu).

The APMB limits proposed by Zandt et al. (2003) based on receiver function analysis show overall similar limits (see Section 3.2), and are compared in Figure 6.31. However the western edge of the APMB as predicted by Zandt et al. (2003) is ~30 km farther west (in Chile) than that seen with MT data. The velocity model of Ward et al. (2014) shows an APMB with a much smaller area than that of Zandt et al. (2003) (although its thickness is larger, giving it a large volume, see Section 3.2.5). The western edge of the APMB as predicted by Ward et al. (2014) is

~30 km farther west than that seen with MT data, the eastern edge is ~30 km farther east than that seen with MT data, and the northern edge is ~30 km farther south than that seen with MT data.

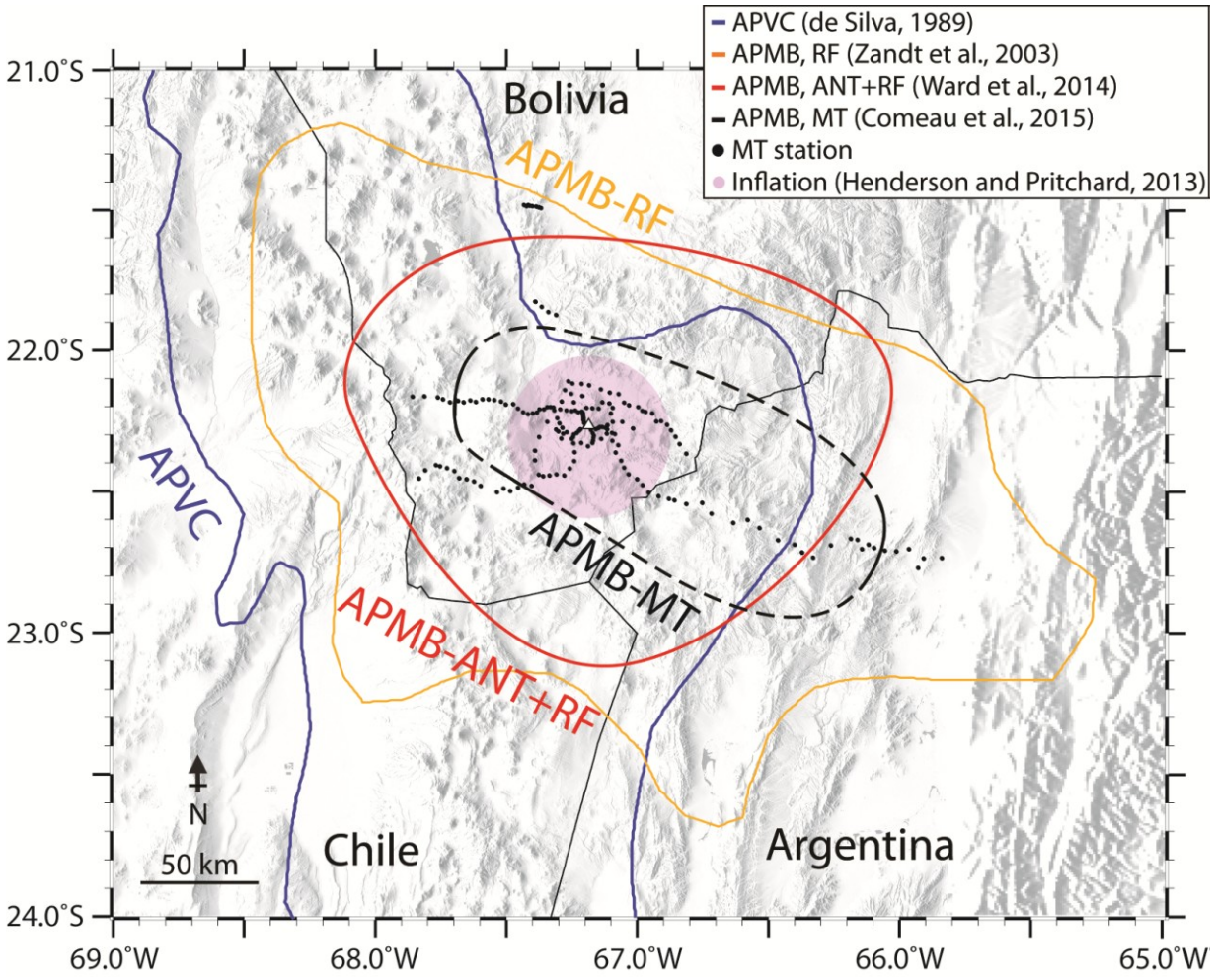

Figure 6.31: Map showing the inferred extents of the APMB from different methods. The magnetotelluric (MT; black line) data show smaller horizontal extents for the APMB then either the receiver functions analysis (RF; orange line) of Zandt et al. (2003) or the joint ambient noise tomography and receiver function analysis (ANT+RF; red line, 2.7 km/s velocity contour) of Ward et al. (2014). The MT data can constrain the east and west extents, where there is station coverage (solid black lines), but not the north and south boundaries (dashed black line). MT stations are shown as black dots. The Altiplano-Puna volcanic complex (APVC; de Silva, 1989) is shown as a blue line. Approximate limits of the inflation pattern are shown (Henderson and Pritchard, 2013).

6.4.3 Intermediate Depth Resistivity Features

At intermediate depths a series of conductors (C3-C7) are imaged (see Figure 6.2 and Figure 6.19). These conductive features between the APMB and the surface are significant because they may represent pathways of past or present fluid motion. A conductor exists near sea-level beneath Volcan Uturuncu (C4), as seen in both the 2-D and 3-D models. This can be interpreted as a shallow pre-eruptive magma chamber, as predicted by other researchers based on geochemical evidence (e.g., Muir et al., 2014), shallow seismic events (Jay et al., 2012), and a low-velocity zone identified with a local ANT network (Jay et al., 2012). The 2-D model shows this feature has a resistivity of about 6 Ωm. The 3-D model shows a resistivity of about 3 Ωm. For sub-volcanic structures, the 3-D model gives the most robust description of conductor geometry. In the 3-D model, the geometry of C4 is more complex; it actually consists of a series of dike-shaped conductors striking approximately east-west (more specifically WNW-ESE). This direction matches with an analysis by Walter and Motagh (2014) who identified a strike angle of N72°W (N108°E) for structural lineaments located around Volcan Uturuncu. These conductors are seen in both the North-South cross-sections and the horizontal slices. These conductors extend vertically downwards towards the APMB with the seismicity confined to their edges. These conductive conduits ("fingers") seem to be feeding the volcanic system from below, rising from the bulge in the APMB below the inflation centre.

A number of other discrete low resistivity zones (e.g., C5, C6, and C7) can be seen as well. Low resistivity in a volcanic environment can be caused by aqueous fluids, partial melt, or hydrothermal alteration, so any interpretation must use additional information to distinguish between these possibilities (Evans, 2012). Zones of hydrothermal alteration or saline fluids left from past eruptive events, because any original magma would have likely long since solidified, could explain the conductors beneath northwestern Argentina (i.e., C6, C7). Conductor C6 is associated with the Granadas caldera, which is dated to 10 Ma, and C7 is associated with the Rachaite caldera dated to 7 Ma. Similarly, conductor C5 is spatially associated with the vent that produced the Laguna Colorado ignimbrite 2 Ma (Salisbury et al., 2011). These conductors could also be new batches of magma moving upwards from the APMB. Regions where past eruptions

took place must have contained shallow magma chambers, and these would have since solidified and become resistive because of the lack of volatiles in the crystallized intrusion. Vilama caldera, straddling the Bolivia-Argentina border, appears to be underlain by a relatively resistive zone (R2), perhaps related to solidification of magma associated with eruptive events dated to 8.4 Ma (Salisbury et al., 2011). Resistor R1 beneath Volcán Quetena may be similarly explained.

6.5 Synthetic 3-D MT Inversion

The 3-D resistivity model was investigated using a set of synthetic inversions. These allow the model resolution and sensitivity of the model to the measured MT data to be investigated. The synthetic model was limited to a few layers and block shapes for simplicity, but was designed to exhibit the main resistivity features seen in the real-data inversion model (preferred 3-D model; Figure 6.19). It included three main layers, as described below.

1. A thin, 1 km thick, surface layer with a resistivity of 3 Ωm.
2. A 100 Ωm resistive layer with two narrow, parallel conductors, each with a resistivity of 3 Ωm. These conductors were 15 km long, 4.5 km wide, and were positioned at a depth of -3 to 3 km BSL (2-8 km below surface).
3. The final layer was a halfspace, with a resistivity of 3 Ωm to represent a deeper conductor. The depth of this was varied from 15 km BSL to 10 km BSL.

Synthetic MT data were computed in the period band 0.01-1500 s (similarly to the real-data inversion) and 5% Gaussian noise was added to the clean synthetic data to make the inversion more realistic. The actual MT site distribution was used (S73). Smoothing parameters were set for horizontal smoothing (x = 0.2, y = 0.2, z = 0.1), in order to better distinguish the known flat layers. Other inversion parameters were set identically to those of the preferred 3-D inversion model.

The synthetic inversion began from a 10 Ωm starting model. When the deep conductor was set at a depth of 15 km BSL, the r.m.s. misfit was reduced from 6.38 to 0.91, after a total of 8 iterations (the first stage reduced the misfit to 1.38 after 5 iterations). When the depth was set to 10 km BSL, the r.m.s. misfit was reduced from 6.32 to 0.97, after a total of 8 iterations (the first stage reduced the misfit to 1.00 after 5 iterations). The synthetic forward model and the inversion results are compared in Figure 6.32, for both vertical slices and horizontal slices of the 3-D model. The depth of the deep conductor was recovered reliably, and the two intermediate conductors are also distinguished and located at their expected positions. The geometry of the dyke-like shape was not fully recovered, owing to the irregular distribution of MT sites, but the resistivity values and the structure was well resolved.

Figure 6.33 shows a similar synthetic inversion using the extended site distribution of S96, and three intermediate depth conductors. Parameters were set as above. The r.m.s. misfit was reduced from 6.38 to 0.95 after a total of 8 iterations (the first stage reduced the misfit to 1.44 after 5 iterations). The depth of the deep conductor was recovered reliably (at 15 km BSL), and all three of the dyke-like conductors were recovered at their expected positions. The geometry of the dyke-like conductors is not fully recovered, due to the irregular distribution of MT sites, but the resistivity values and the structure is well resolved.

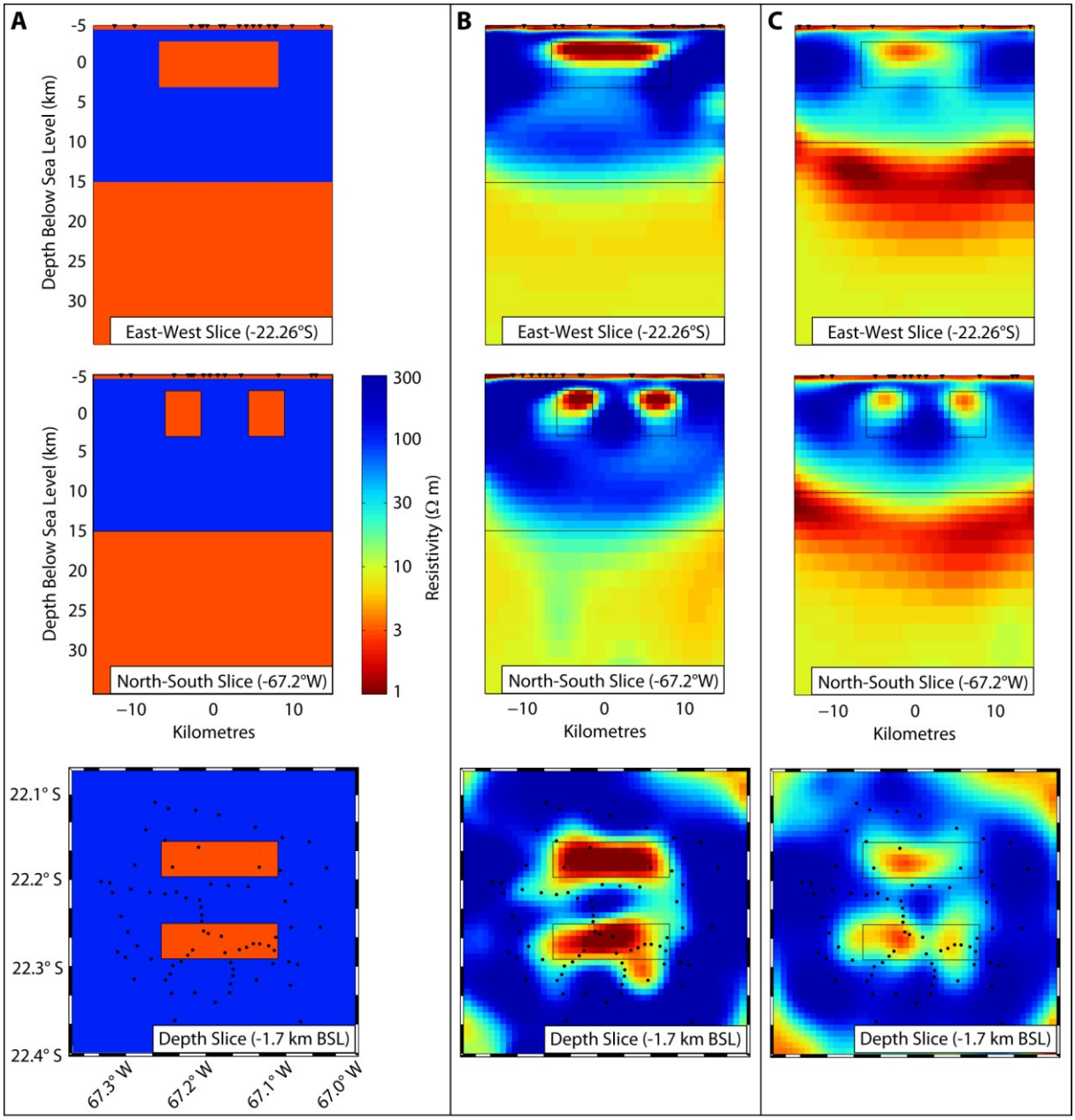

Figure 6.32: Results of a synthetic inversion study. Column A shows the synthetic resistivity model, with intermediate conductors positioned at a depth of -3 km BSL to 3 km BSL, and with a deeper conductor at a depth of 15 km BSL. Column B shows the recovered inversion model. The expected geometry of the intermediate and deep conductors are outlined in gray. Column C shows the recovered inversion model when the deeper conductor is raised to a depth of 10 km BSL. Rows, from top to bottom, show West-East vertical slices, South-North vertical slices, and a horizontal slice at a depth of -1.7 km BSL. The resistivity values and the geometry of the structure is fairly well resolved.

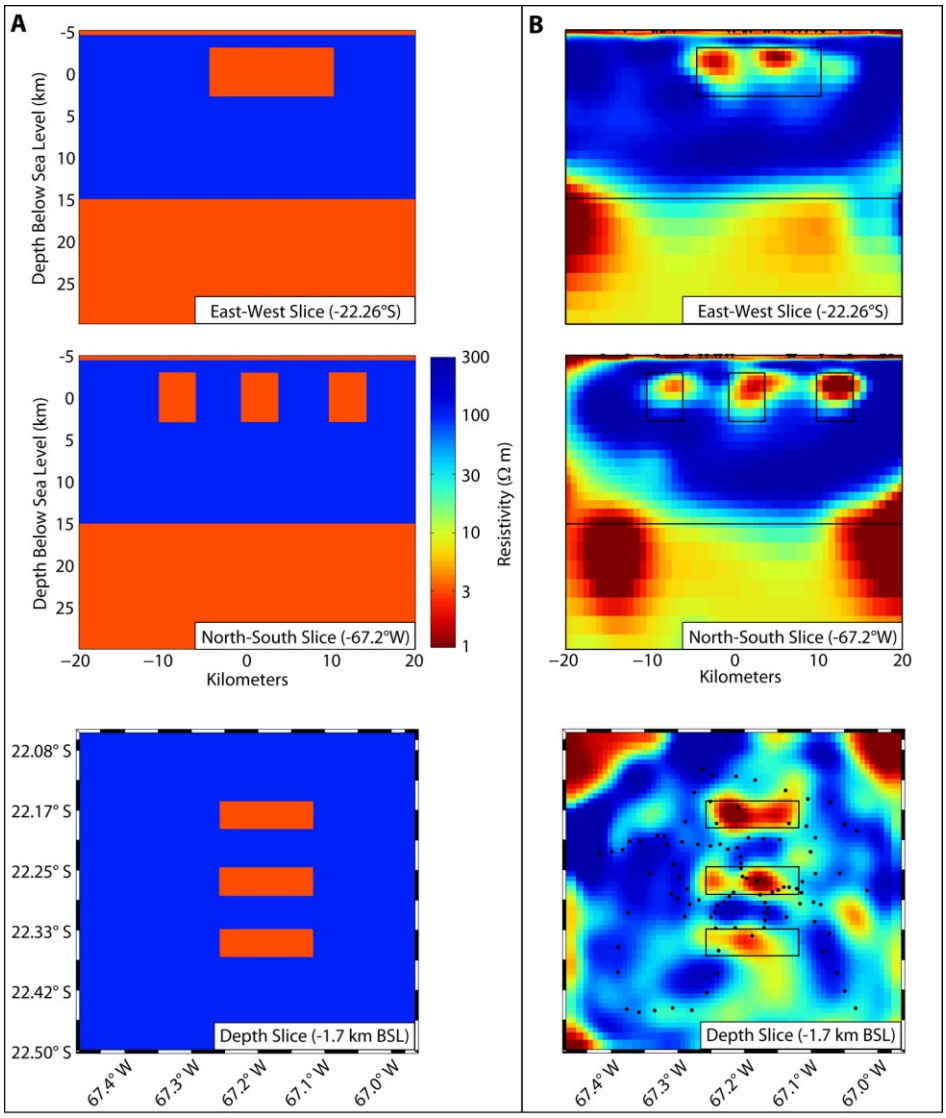

Figure 6.33: Results of a synthetic inversion as in Figure 6.32 but with the site distribution of S96 and three intermediate depth dyke-like conductors. Column A shows the synthetic resistivity model and column B shows the recovered 3-D inversion model. The expected geometry of the conductors are outlined in gray. The resistivity values and the geometry of the structure is fairly well resolved.

6.5.1 Infinite Extent Conductor Model

Another 3-D synthetic model was created which used the same set up as the model above, but with the exception that the intermediate dyke-like conductors extended beyond the edges of the model. This synthetic model shows whether the MT data can reliably show whether the dyke-like features are finite in extent or not.

Inversions parameters were set as above, and 5% Gaussian noise was added to the MT data. The r.m.s. misfit was reduced from 6.08 to 0.91, after a total of 10 iterations (the first stage reduced the misfit to 1.47 after 5 iterations). The synthetic forward model and the inversion results are compared in Figure 6.34, for both vertical slices and horizontal slices of the 3-D model. The depth of the deep conductors and the two intermediate conductors are distinguished at the expected positions. The geometry of the dyke-like conductor with a non-finite extent is fully recovered. However, owing to the irregular distribution of MT sites, the structure is not as uniform as in the true model, but appears split up into several pieces. Despite this, it is clear that the inversion shows the intermediate conductor continues beyond the model edges, and is not finite in extent. This gives confidence that the 3-D inversion model of the field data can properly define the limits of the intermediate dyke-like conductive features.

Another 3-D synthetic model was created which used the same set up as the model above, but with a single intermediate dyke-like conductor extended in a North-South direction beyond the edges of the model. This synthetic model shows whether the data and MT site distribution can reliably determine whether the intermediate depth features are connected or not. Inversions parameters were set as above. The r.m.s. misfit was reduced from 5.99 to 0.99, after a total of 8 iterations (the first stage reduced the misfit to 1.43 after 5 iterations). The synthetic forward model and the inversion results are compared in Figure 6.35 for horizontal slices of the 3-D model. The geometry of the dyke-like conductor with a non-finite extent and its position is fully recovered. However, owing to the irregular distribution of MT sites, the structure is not uniform. Despite this, it is clear that the inversion shows the intermediate conductor is continuous and continues beyond the model edges. This gives confidence that the 3-D inversion model for the real collected data can defined separate intermediate depth dyke-like conductors.

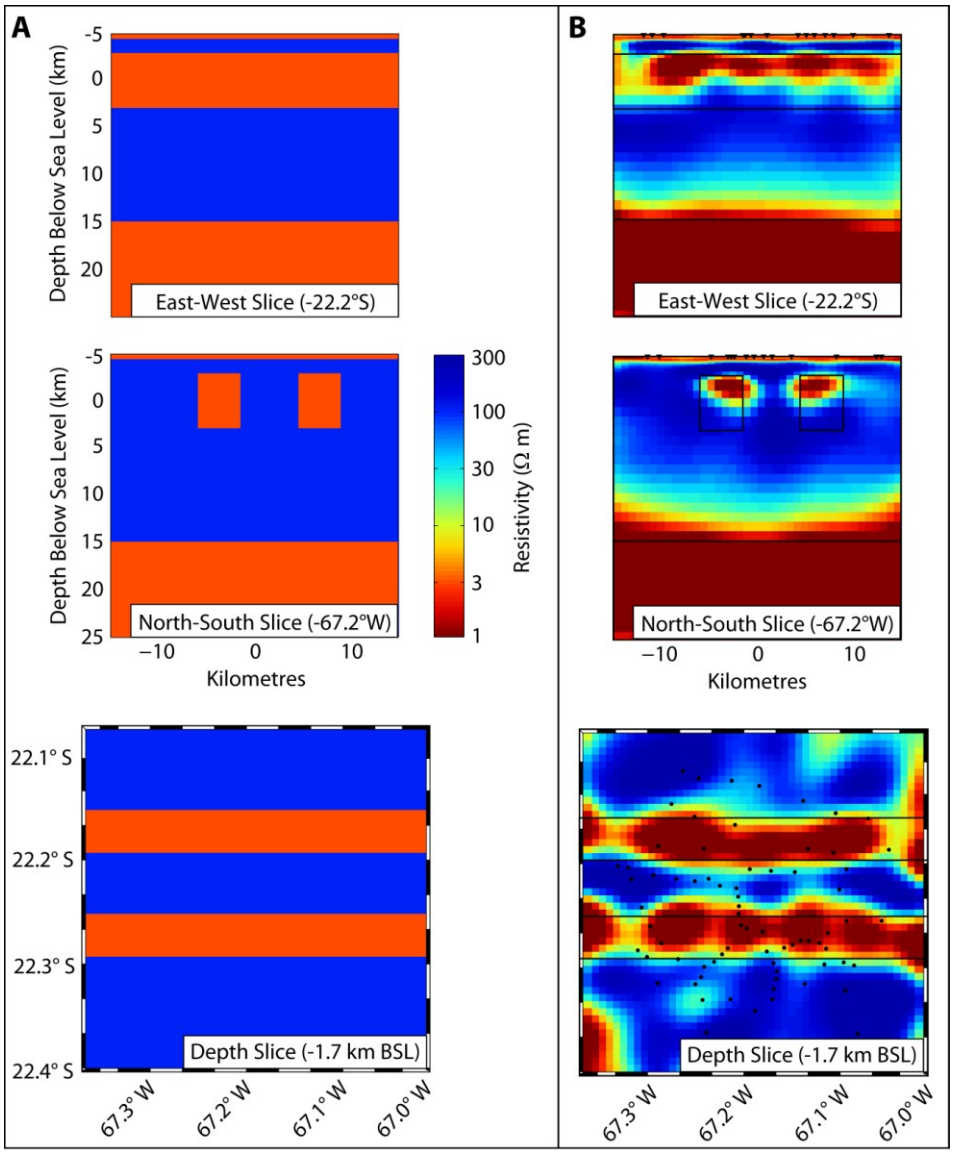

Figure 6.34: Results of a synthetic inversion study. Column A shows the synthetic model, with intermediate conductors positioned at a depth of -3 km BSL to 3 km BSL, and with a deeper conductor at a depth of 15 km BSL. The intermediate conductors extend East-West beyond the edges of the model. Column B shows the recovered 3-D inversion model. The expected geometry of the intermediate and deep conductors are outlined in gray. Rows, from top to bottom, show West-East vertical slices, South-North vertical slices, and a horizontal slice at a depth of -1.7 km BSL. The resistivity values and the geometry of the structure is fairly well resolved.

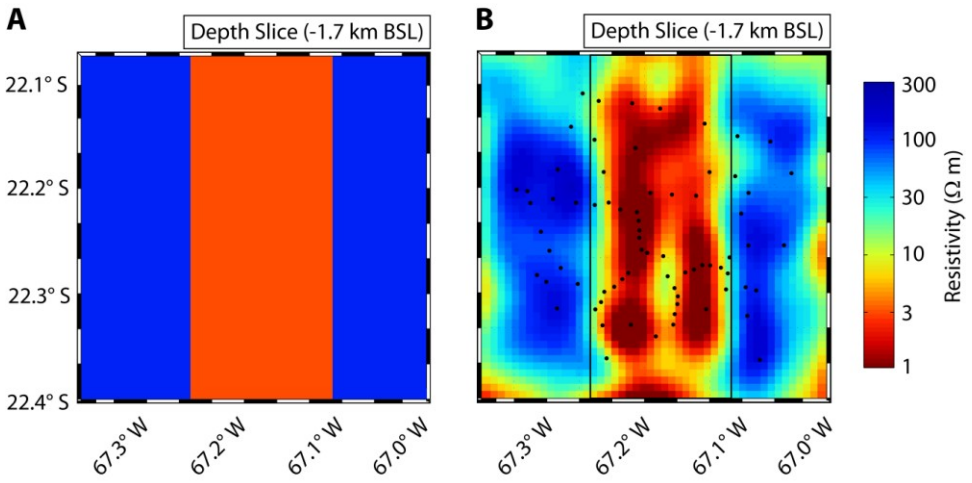

Figure 6.35: Results of a synthetic inversion study as in Figure 6.34 but with a single continuous intermediate depth conductor which extends North-South beyond the model. Panel A shows the synthetic model and Panel B shows a horizontal depth slice through the recovered 3-D inversion model. The expected geometry of the conductor is outlined in gray. The resistivity values and the geometry of the structure is fairly well resolved.

6.7 Summary of Results

In this chapter, both 2-D and 3-D inversion models of the MT data were presented. The preferred 2-D resistivity model along Profile 1 (Figure 6.2) achieved a combined r.m.s. misfit of 1.49. A subset of the MT data on a network around Volcan Uturuncu were inverted using a 3-D inversion (Figure 6.14), which produced a preferred 3-D resistivity model with a r.m.s. misfit of 0.95. These r.m.s. misfit values indicate an acceptable fit to the measured MT data. Many combinations of inversion parameters were investigated for both the 2-D and 3-D inversions. The main resistivity features were found to not depend on any specific choice of inversion parameters. This indicates that the main features are required by the MT data. Both the 2-D and 3-D resistivity model shows three distinct layers: a shallow surface conductor, an intermediate layer consisting of a series of conductors and resistors, and a deep conductor at a depth of 15-20 km BSL. The deep conductor is interpreted as being the APMB, with the low resistivity zone

interpreted as a zone of partial melt. Synthetic 3-D inversions allowed the model resolution to be investigated. The top of the low resistivity layer was recovered reliably, as were the intermediate depth dyke-like conductors. This gives confidence that the inversions are resolving the subsurface structure properly.

CHAPTER 7: RESULTS AND INTERPRETATIONS

7.1 Introduction

This chapter describes the interpretation of the MT data and the resistivity models presented in Chapter 6, and focuses on a synthesis with other data from Volcan Uturuncu and the APVC. Interpreting subsurface resistivity is an intrinsically non-unique process because a low resistivity zone can be caused by a number of distinct compositions and physical conditions. However, the uncertainty associated with non-unique processes can be reduced by using other geophysical data or laboratory measurements to constrain the resistivity models derived from the MT data. In this chapter melt fraction and melt viscosity are inferred from the MT data in order to aid the interpretation. Comparison and quantitative correlation with seismic velocity models and a comparison with geodetic models is carried out, and helps to constrain on the resistivity models derived from MT data.

7.2 MT Inversion Model Interpretations

Both 2-D and 3-D MT inversion models for the region around Volcan Uturuncu were presented in Chapter 6 (see Figures 6.2 and 6.19). A description of their resistivity features was provided in Section 6.4 and a brief summary is given here. Refer to Section 5.3.1 and Figure 5.3 for MT station locations and the location of places referred to in the text.

Shallow Resistivity Features

Both the 2-D and 3-D electrical resistivity models show a shallow layer (< 1 km) with a highly variable but low resistivity (resistivity of < 10 Ωm). It may be caused by either a shallow aquifer or hydrothermal alteration within, or around, the regionally extensive ignimbrite layer, as

ignimbrites are known to form highly conductive clays by undergoing low-temperature alteration (Bibby et al., 2005).

Intermediate Depth Resistivity Features

Below Volcan Uturuncu, at a depth near sea-level, a conductor (e.g., C4; resistivity range of 3-7 Ωm) is imaged in both the 2-D and 3-D resistivity models. This is interpreted as a shallow magma chamber. The 3-D resistivity model shows that the geometry of this feature is complex and reveals a series of dike-shaped conductors striking east-west. Furthermore, seismicity appears confined to the edges of these features, giving additional evidence for a region of melt or fluid.

The 2-D resistivity model along the regional profile shows a number of other discrete conductors at similar depths. These can be related to specific volcanic events or current-day calderas and may be caused by zones of hydrothermal alteration or saline fluids left from past eruptive events, because any original magma would have solidified.

Deep Resistivity Features

The prominent uniform conductor (resistivity range of < 3 Ωm) at a depth of ~15-20 km BSL is interpreted as a zone of partial melt and believed to be the large magma body below the Altiplano, the APMB. Although MT can give a reliable estimate of the depth to the top of the conductor and the total conductance, its thickness cannot be well constrained because there is minimal resolution within and below the conductor. The APMB's eastern edge (near Mungayoc) and western edge (near Laguna Colorado) are clearly seen in the 2-D resistivity model, placing the entire extent of the APMB east of the present-day volcanic arc.

7.2.1 Interpreting Depths from MT Resistivity Models

If the top of the APMB is defined as the 3 Ωm contour, the depth to the top calculated from the electrical resistivity inversion models presented in Chapter 6 is 13.5 km BSL and 18.5 km BSL

for the 3-D model and 2-D model, respectively (see Figures 6.2 and 6.19). As discussed in Chapter 6, the 2-D resistivity model gives greater depths to the APMB, but the 3-D model may be more reliable because the MT data are affected by static shifts. By varying the resistivity contour which defines the top of the APMB a range of values can be determined. The 5 Ωm contour corresponds to depth of 11-16 km BSL (3D/2D); the 10 Ωm contour corresponds to depth of 9-10 km BSL; the 1 Ωm contour corresponds to depth of 14.5-22 km BSL. These depths agree with other MT studies over the Altiplano, which indicate a large conductor at depths of 10-30 km BSL (e.g., Brasse et al., 2002; Schwarz and Kruger, 1997).

However, defining the depth to the top of the APMB as a resistivity contour can be misleading, and a better approach is to use the inflection point of the resistivity-depth curves from the resistivity model, as shown in Figure 7.1, because the inversion algorithm seeks a smooth model. Thus even if the true model was a layer with sharp edges, it would appear in the inversion model as smooth gradational feature. This point is illustrated in Figure 7.1 for simple 1-D synthetic models.

Resistivity-depth profiles for each station in the real-data inversion model are shown in Figure 7.1 Panel A. The major resistivity feature seen clearly at all sites at depth is the prominent conductor C2. There is a lot of variability in the upper 10 km of the resistivity model, where different MT stations detect intermediate conductors near sea-level (e.g., C4) in some places but not in others. The surface layer (i.e., C1) can be seen to be highly variable, either being highly conductive or highly resistive. Based on the above discussion, it can be seen that the inflection point of the deeper conductor (i.e., C2, the APMB) for the MT inversion resistivity model occurs at a depth of 13-14 km BSL (see Figure 7.1, Panel A).

Figure 7.1 Panels B and C show the true (synthetic) resistivity model and the inversion model resistivity-depth profile. Gaussian noise (5%) has been added to the data. The top of the conductive layer is identified by the inflection point of the resistivity-depth curve. Panels D and E show the synthetic 1-D resistivity models (with noise added) as a colour plot with the same colour-scale used throughout this thesis. It is clear that the deeper conductor is not identified as a sharp boundary (as in the true model), but rather as a smooth gradational boundary.

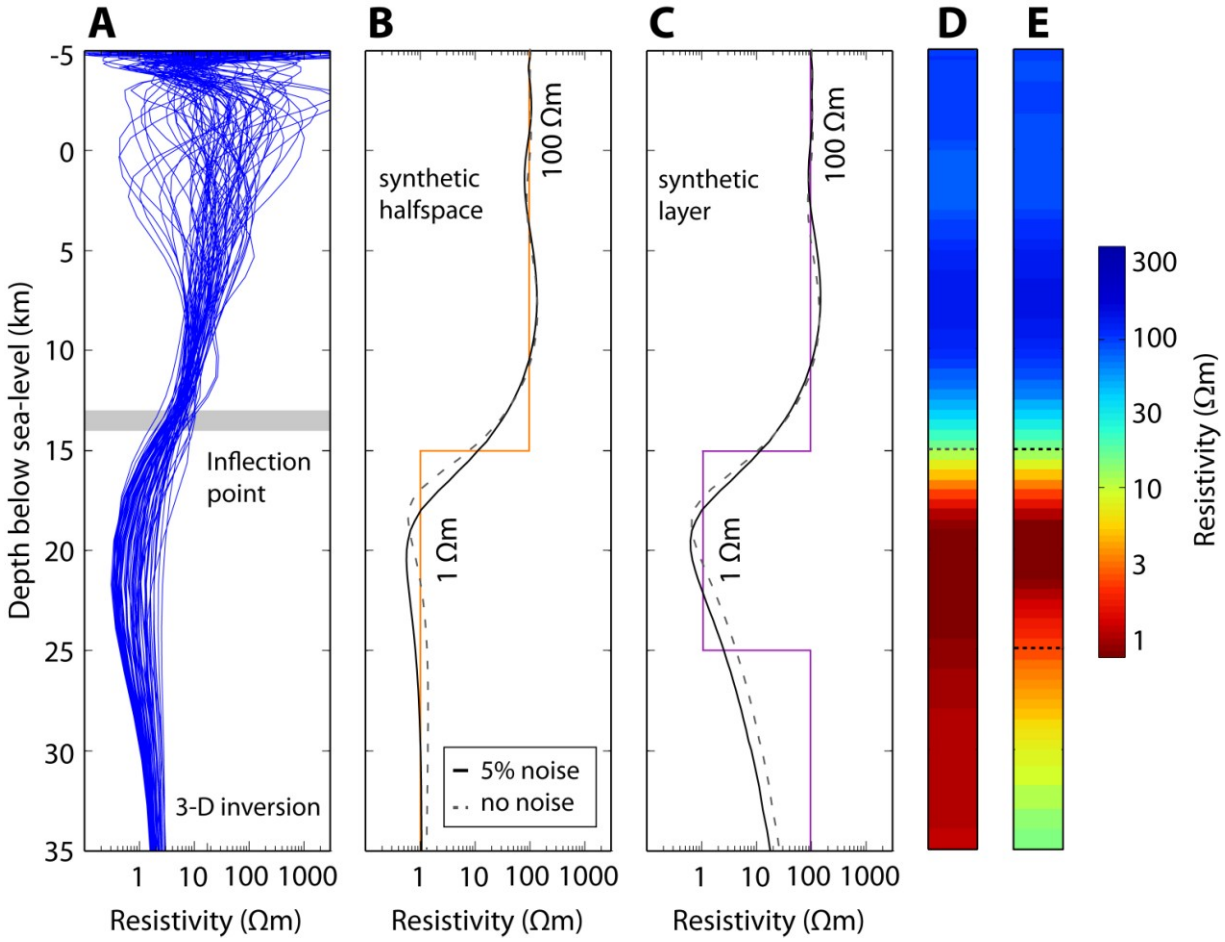

Figure 7.1: Resistivity-depth profiles for each MT station from the MT response of the inversion resistivity model is shown in Panel A. The depth to the top of the prominent deep conductor (i.e., C2, the APMB) is given by the inflection point of the resistivity curve, shown as a grey box at a depth of 13-14 km below sea-level. Panels B and C show simple 1-D synthetic models with a halfspace (Panel B, orange line) and a layer (Panel C, purple line) with the inversion model resistivity-depth profile shown as a black line, both with 5% Gaussian noise added (solid line) and without (dashed line). The top of the conductive layer is identified with the inflection point of the resistivity-depth curve. Panels D and E show the synthetic 1-D resistivity models (with noise added) with the same colour-scale used throughout this thesis, with dashed lines indicated the sharp boundaries in the true model.

7.2.2 APMB Thickness

MT data can give a reliable estimate of the depth to the top of a conductor, but it is not always possible to record data at long enough periods to detect the base of a conductor. Therefore the thickness of the APMB is not well constrained.

However, the APMB has a very high conductance of ~30,000 S (the product of a layer's conductivity and its thickness). The resistivity of the APMB is known from the measured MT data and can also be calculated theoretically from the pure melt resistivity predicted by the SIGMELTS model based on known magma composition and using Archie's law with an estimated melt fraction (i.e. 30 % melt). If the APMB is assumed to have a minimum resistivity of 0.1-0.3 Ωm (conductivity of 3 - 10 S/m) this gives a minimum thickness of 3-10 km. A maximum resistivity of 1 Ωm (conductivity of 1 S/m) would give a thickness of 30 km. In stable continental regions the average crustal conductance is no more than 1,000 S, although a conductance of up to 20,000 S has been seen in Tibet (Wei et al., 2001). Previous MT studies of the Altiplano found a conductance of 20,000-23,000 S (Schwarz and Kruger, 1997; Brasse et al., 2002), and resistivities of 0.5-2 Ωm in a HCZ, giving a minimum thickness of 10-46 km (see Schilling et al., 1997).

Alternatively it is possible to estimate the thickness of the APMB from its lateral extent seen with MT data (area) and its volume estimated from the plutonic to volcanic ratio (intrusive to extrusive ratio; see Section 2.3). A plutonic to volcanic ratio of 2:1 to 5:1 is commonly used in the Andes, but could be within the range of 1:1 to 10:1 (e.g., Francis and Hawkesworth, 1994; de Silva and Gosnold, 2007; Kay et al., 2010). The APVC ignimbrite volume estimated by de Silva et al. (2006) is 15,000 km^3 (extrusive), while the area of the APMB is estimated from MT measurements to be ~14,000 km^2, giving a range of thickness of 2 - 5 km, and possibly as high as 10 km. Schilling et al. (2006) estimate 30,000 km^3 of erupted ignimbrites in the APVC, requiring the thickness to double (giving a total range thickness of 2-20 km). Using the plutonic volume estimate of 50,000-60,000 km^3 from de Silva and Gosnold (2007) gives a thickness of 3.5 - 5.5 km. See Table 7.1 for a summary of thicknesses derived from the MT data.

Several receiver function studies (e.g., Chmielowski et al., 1999; Zandt et al., 2003) imaged the APMB as a thin sill with a thickness of ~1 km, while others detected a broader low-velocity zone of 10-20 km thickness (e.g., McFarlin et al., 2014; Beck and Zandt, 2002), see Section 3.2.3 for more details. Ward et al. (2014) estimated a very high plutonic to volcanic ratio of 35:1 for the APMB with an area of ~60,000 km^2, giving a thickness of 9 km. Their velocity model shows the thickest part of the APMB, located beneath Volcan Uturuncu, is 20 km thick (see Section 3.2.4 for more details). See Table 3.3 for a summary of APMB thickness as determined by other methods.

METHOD		THICKNESS (KM)
Intrusive to extrusive ratio (2:1 - 5:1)	Extrusive volume from de Silva et al. (2006) Extrusive volume from Schilling et al. (2006)	2-5 4-10
Plutonic volume	Plutonic volume from de Silva and Gosnold (2007)	3.5-5.5
Magnetotelluric data	High Conductivity Zone, from Conductance	3-10

Table 7.1: Summary of thickness estimates for the Altiplano-Puna Magma Body derived from magnetotelluric data, as described in Section 7.2.2. See Table 3.3 to compared to thicknesses derived from other methods.

7.3 Comparison of Electrical Resistivity and Seismic Velocity Models

Comparison of electrical resistivity models with seismic velocity models is useful, because the amount of melt present in the crust will have an influence on both the electrical resistivity and the seismic velocity. This allows non-uniqueness to be addressed and can help to constrain model interpretations. Furthermore, it allows the resolution of both model types to be assessed. In this section the 3D MT models introduced in Chapter 6 are compared to the joint ambient noise tomography and receiver function (ANT+RF) seismic velocity model of Ward et al. (2014) (see Section 3.2.4). The velocity model of Ward et al. (2014) has excellent spatial coverage over Volcan Uturuncu and has enough resolution to identify shallow and deep features. A range of seismic models exists for this region (see Section 3.2; receiver functions, e.g., Chmielowski et

al., 1999; Zandt et al., 2003; ambient noise tomography, Ward et al., 2013) but the ANT+RF model has the best resolution and coverage in the vicinity of Volcan Uturuncu and was chosen for the comparison with the MT resistivity models.

7.3.1 Seismic Velocity Model

As discussed in Section 3.2.4, Ward et al. (2014) produced a joint ANT and RF S-wave velocity (ANT+RF) model across the APVC and Volcan Uturuncu. Figure 3.4 showed a smoothed vertical slice through the velocity model along a profile which corresponds to Profile 1 (azimuth direction ~120°). The 2.9 km/s velocity contour defines a large low velocity zone that was identified as the APMB (Ward et al., 2014). Figure 7.2 Panel A shows a horizontal slice through the velocity model at a depth of 15 km BSL, with MT sites for reference. Panel B shows a vertical section across the APMB. Velocities are estimated on a 0.1° x 0.1° horizontal grid (roughly 11 km by 11 km), which is coarse spatial resolution compared to the 3D MT model (which has 750 m by 750 m cells horizontally). For example, all of the 73 MT sites around Volcan Uturuncu used to produce the preferred 3-D resistivity model (i.e., S73, Figure 6.19) would fit within 9 grid boxes of the seismic model.

The low velocity layer below the APVC and Uturuncu is remarkably homogenous. The western edge of the low velocity zone correlates well with the edge of the APMB identified in the resistivity model (near Laguna Colorado, see Figure 6.2). The eastern edge of the low velocity zone also correlates well and seems to end near Mungayoc, as seen in the resistivity model. Unfortunately, the velocity model does not extend east of longitude 66°W. The velocity model also shows the east-west width of the APMB decreases southward, which the MT data also show (compare with Profile 2, Southern Line, see Section 6.2.14).

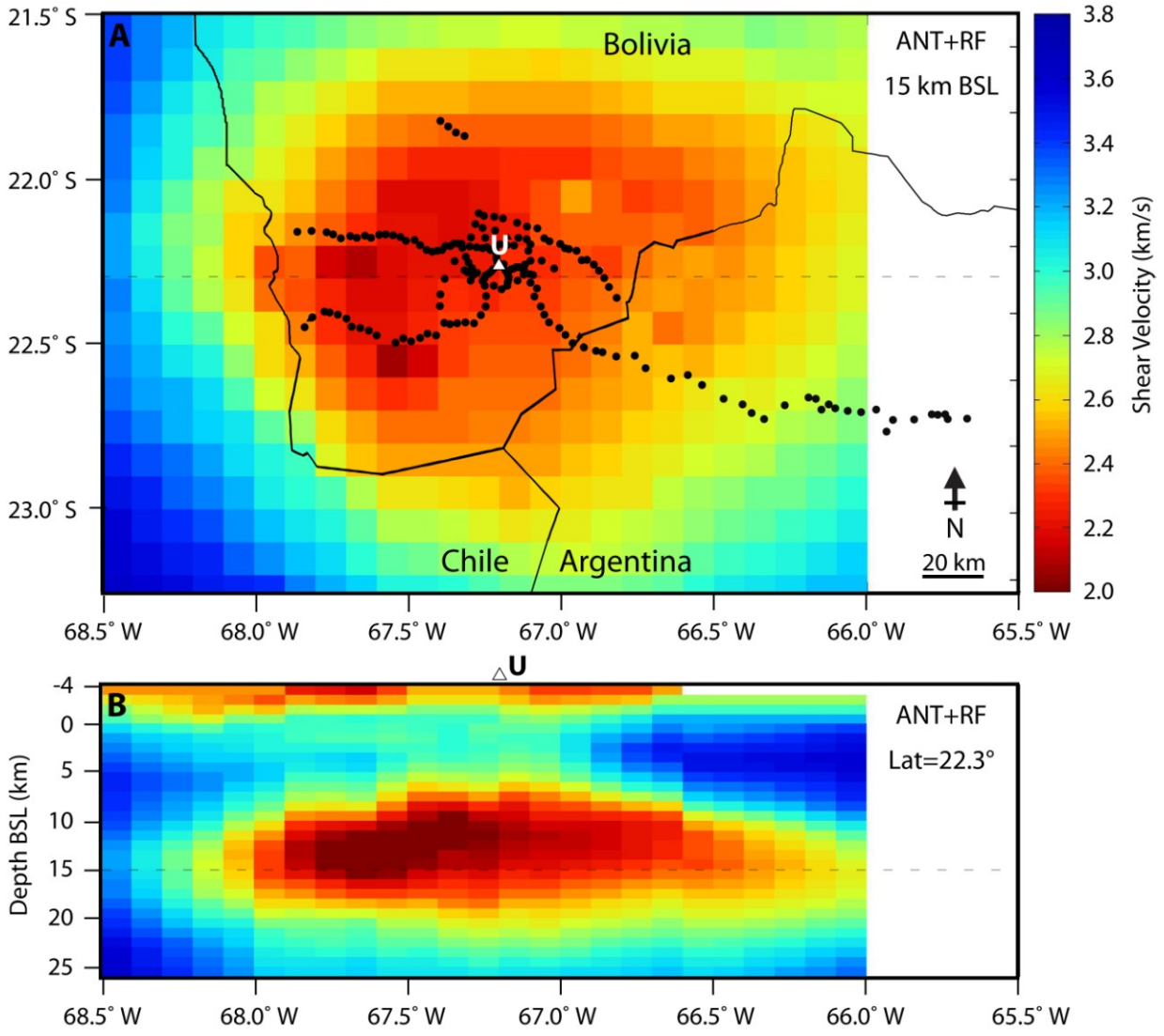

Figure 7.2: Ambient noise and receiver function joint inversion (ANT+RF) velocity model (Ward et al., 2014). Panel A shows a horizontal slice at 15 km BSL. Panel B shows a vertical section along latitude 22.3°, with a vertical exaggeration of 3. The 2.9 km/s contour (green colour) encompasses a large low-velocity zone attributed to the Altiplano-Puna Magma Body. Black dots indicate MT sites, for reference purposes. Volcan Uturuncu is marked with a white triangle and labelled U. The velocity model does not extend east of longitude 66° W.

7.3.2 Comparing Electrical Resistivity and Velocity Models

It can often be difficult to interpret physical rock properties with only one geophysical method and so multiple methods can be used to constrain the interpretation. Both electrical resistivity and seismic velocity are sensitive to the properties of rock, and are therefore directly comparable (Bedrosian et al., 2007). Although no universal relationship between resistivity and velocity exists, they are known to be linked through the amount of fluid present in a rock (Bedrosian et al., 2007). As porosity increases, both electrical resistivity and velocity decrease. This occurs for rocks that contain either aqueous fluids and melt (e.g., Simpson and Bahr, 2005; Dvorkin, 2008). Some compositional changes of the fluid or melt, such as the silica and sodium content, will influence the resistivity (Unsworth and Rondenay, 2013; Pommier, 2014), but will not affect the velocity (Dvorkin, 2008; Takei, 2000).

A joint inversion of velocity and resistivity data is possible, but can be difficult (e.g., Roux et al., 2011; Moorkamp et al., 2007). In this thesis a visual comparison and a quantitative correlation will be used to show the similarities and differences between the velocity and resistivity models. Figure 7.3 shows a comparison of the S-wave velocity model from Ward et al. (2014) (Panel A) and the S96 3-D electrical resistivity model (Panel B) on a common grid (the S96 model, shown in Figure 6.27, was used in this analysis due to its larger coverage area). The grid is spatially coarse (x = 11 km, y = 11 km, z = 1 km) in comparison to the original resistivity model (see Figure 6.27), which was interpolated onto the velocity model grid.

At first glance, the resistivity model and seismic model show some correlation. The low resistivity region (below a depth of 15 km) is correlated with the broad low velocity region (below 15 km), both interpreted as the APMB (red colour in Figure 7.3). The higher velocity lid above the APMB is correlated with the higher resistivity region above a depth of 15 km (blue colour in Figure 7.3). Because of the resolution differences between the two models, the resistivity model shows much finer structures above the APMB which are not seen in the velocity model.

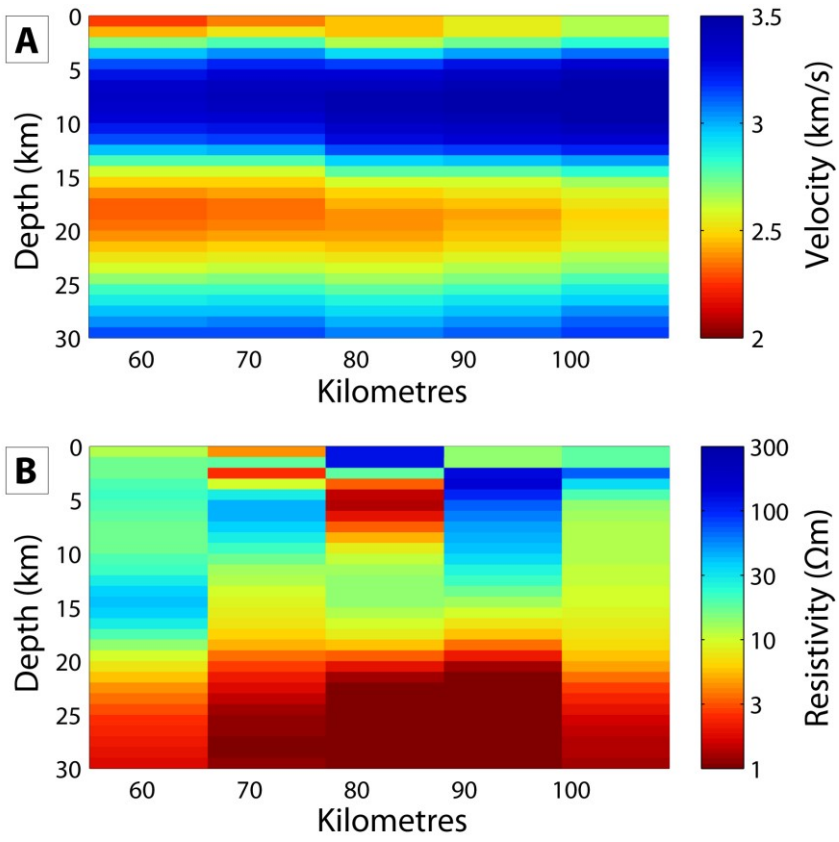

Figure 7.3: Comparing the shear-wave velocity model of Ward et al. (2014) (Panel A) and the S96 3-D MT resistivity model (Panel B), on a common grid. A general trend of increasing resistivity with increasing velocity can be seen. Note that the depth is defined with reference to the ground surface, not sea-level, as in other figures.

7.3.3 Quantitative Correlation of Resistivity and Velocity

A quantitative approach to correlating two independent geophysical data sets was presented by Bedrosian et al. (2004; see also Bedrosian et al., 2007; Bertrand et al., 2009). By correlating both parameters with each other, distinct domains can be defined with certain ranges of resistivity and velocity. In order to do this type of quantitative correlation the finer resolution resistivity model needs to be interpolated so that it shares a common set of grid points with the velocity model (as in Figure 7.3). Next the poorly resolved areas of the models must be masked to avoid inaccurate

correlation. In the analysis shown here the edges of the resistivity model, where it is not well constrained by MT sites, and the region below the large conductor (< 27 km), where there is minimal resolution, have been removed to ensure proper correlation. The correlation results are then presented as a two-parameter histogram which shows the number of occurrences of each specific combination of resistivity and velocity (Figure 7.4, Panel A). Lastly, distinct domains can be identified and mapped back onto the resistivity or velocity models to better understand which zones are correlated (Figure 7.4, Panel B).

The correlation results for the S-wave velocity model and the 3-D electrical resistivity model (Figure 7.4, Panel A) show a general trend of increasing resistivity with increasing velocity. Zone 1 is identified with APMB, a correlation of low velocity (< 2.75 km/s) and low resistivity (< 10 Ωm). Zone 2 is identified with the lid above the APMB, a correlation of higher velocities and higher resistivities. Zone 3 is an anomalous zone which does not follow the expected trend. It shows a correlation of low resistivity (< 10 Ωm) with high velocity (> 2.75 km/s). This zone is caused by the small scale low resistivity features above the APMB seen in the resistivity model but not in the velocity model. Therefore the explanation of this anomalous zone is due to the resolution difference between the methods. As discussed previously, the two methods are able to resolve structures of different scales. Mapping the zones spatially back onto the model confirms the identification of the zones (Figure 7.4, Panel B).

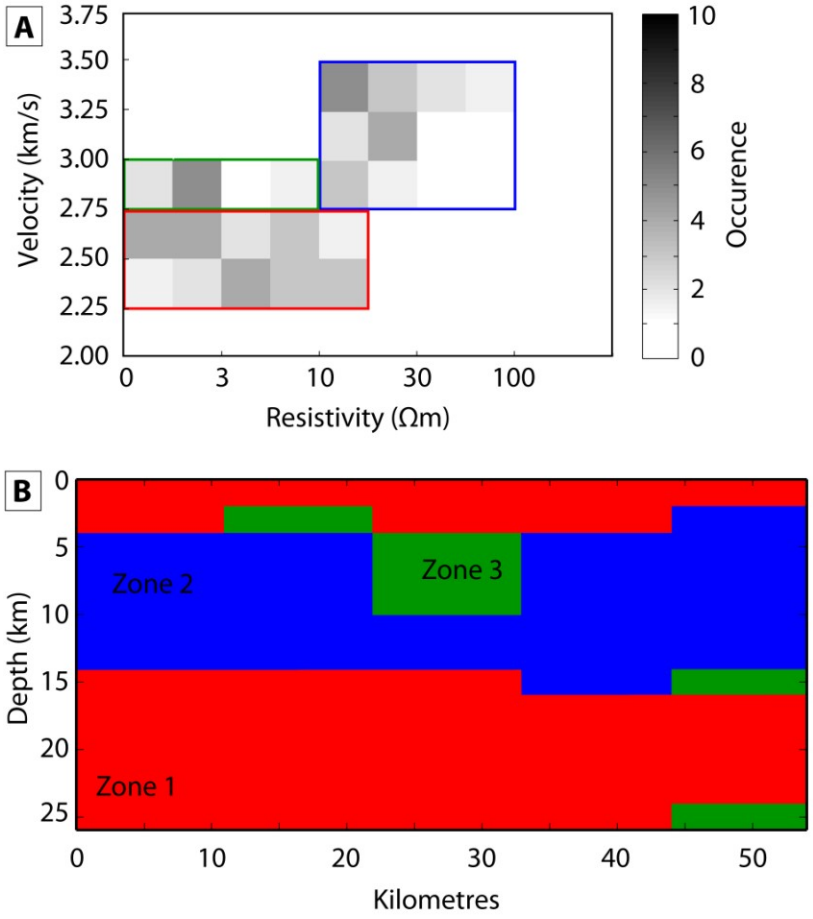

Figure 7.4: Quantitative resistivity-velocity correlation for the S96 3-D MT resistivity model and the velocity model of Ward et al. (2014). Panel A shows the resistivity-velocity correlation histogram. A general trend of increasing resistivity with increasing velocity can be seen. Zones of correlation are colour coded. Panel B shows the spatial location of the outlined zones. Zone 1 (red) maps to the APMB; zone 2 (blue) maps to the lid above the APMB; zone 3 (green) coincides with the small scale features above the APMB.

7.3.4 Comparison of Resistivity Model and ANT LVZ Below Volcan Uturuncu

A seismic ANT survey from a local seismometer network around Volcan Uturuncu imaged a low-velocity zone at a depth of 2-4 km depth below surface (Jay et al., 2012) (see Figure 3.6). Figure 7.5 shows the 2.9 km/s velocity contour from the ANT model at a depth of 4 km below

surface overlain on a horizontal depth slice of the preferred 3D MT resistivity model at a depth of 5.9 km (as in Figure 6.19). The low-velocity zone is spatially correlated with the conductive dyke-like features seen in the MT resistivity model. However, the low-velocity zone is one continuous feature encompassing both separate dyke-like features, likely smearing across them due to resolution differences of both methods. The northern and southern edges of the LVZ align very well with the edges of the dyke-like features

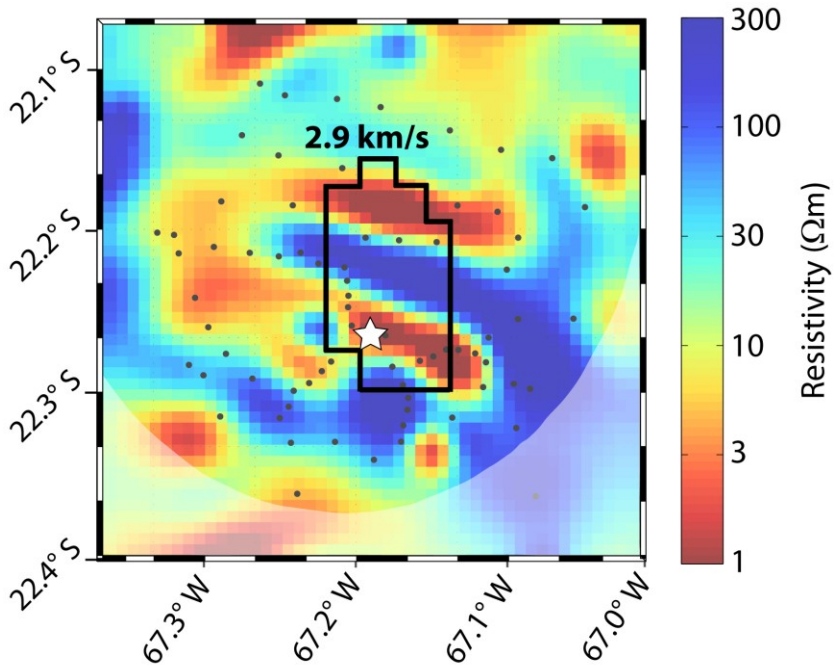

Figure 7.5: The low velocity zone identified as the 2.9 km/s velocity contour in the ambient noise tomography (ANT) model of Jay et al. (2012) at a depth of 4 km below surface is spatially correlated with the conductive dyke-like features seen in the preferred 3D magnetotelluric resistivity model (depth of 6 km below surface). Black circles are magnetotelluric site locations (S73). Volcan Uturuncu is marked with a white star. Shaded area on the figure indicates region outside the bounds of the ANT velocity model.

7.3.5 Correlation of Electrical Resistivity and Earthquake Locations

The resistivity models derived from MT data shows that the volcano-tectonic earthquake hypocenters below Volcan Uturuncu are clustered at the perimeters of conductors (see Figures 6.19 and 6.27). Volcano-tectonic earthquakes are thought to occur because of stresses from the migration of magma through the crust, for example as dike propagation, or from the injection of new magma into the crust from a deeper source (Roman and Cashman, 2006). Both horizontal slices and vertical sections through the 3-D resistivity model show that the earthquakes surround the shallow conductive body below Volcan Uturuncu (e.g., C4), which is thought to represent a magma storage region.

A number of other MT studies have observed that seismicity occurs at the perimeters of conductors that are interpreted as fluid-bearing zones (e.g., Wannamaker et al., 2009; Ogawa et al., 2001) or conduits for fluid migration (Bertrand et al., 2009). Turkoglu et al. (2008) note that two mechanisms are possible to link electrical resistivity due to fluids and seismic activity: either (a) fluids are controlling crustal deformation causing seismicity by weakening the crust, or (b) deformation produces a network of interconnected cracks enhancing the effect of fluids on electrical resistivity. Below Volcan Uturuncu it is likely the first mechanism that is dominant, although both mechanisms are possible. The shallow seismicity observed below Volcan Uturuncu is likely due the migration of magma and fluids through the crust, for example as dike propagation (Roman and Cashman, 2006).

7.3.6 Reconciling Seismic and MT Estimates of the Depth to the APMB

In Chapter 3, the depth to the APMB as measured by various methods was summarized in Table 3.1. Geodetic modeling gave depths of 16-20 km BSL for inflation sources (e.g., Pritchard and Simons, 2004), whereas seismic models gave slightly shallower depths of 10-20 km BSL to the top of a low-velocity layer (e.g., Zandt et al., 2003). As discussed above, the top of the APMB is detected in the 3-D resistivity model at a depth of 13-14 km BSL, based on the inflection point of the resistivity-depth curves. If resistivity contours of 1-5 Ωm are used a range of 11-15 km depth

BSL is found. These depths agree with other MT studies over the Altiplano, which indicate a large conductor at depths of 10-30 km BSL (e.g., Brasse et al., 2002; Schwarz and Kruger, 1997).

Receiver function models give a depth of 13-15 km BSL for the top of the APMB (e.g., Zandt et al., 2003; Chmielowski et al., 1999; Leidig and Zandt, 2003). The ambient noise tomography and receiver function joint inversion (ANT+RF) of Ward et al. (2014) gives a depth of 14-15 km BSL for the slowest velocities, but those within the 2.9 km/s velocity contour, selected by Ward et al. (2014) to define the APMB, range in depth from 6-20 km BSL for station LCOL and 10-23 km BSL for station PTLP. One issue with the ANT results is that this method is not sensitive to small vertical structures, and therefore only shows one smooth and continuous LVZ. The model only shows the long-wavelength structure of the APMB, and likely smears the small scale features seen in the MT models, which explains why it shows a shallower depth to the LVZ compared to the other seismic models and the MT models, as shown in Figure 7.6.

Besides the resolution differences between the MT and ANT methods, the methods are sensitive to different parameters, and it may be that the depth difference is physical and can give important information about the APMB, or the layer above it. The depth difference between the ANT and MT results can be reconciled by allowing the area above the top of the APMB (as seen by MT data) to be a low-velocity zone, but not a low-resistivity zone. This can be achieved in three ways: (1) by varying the composition (i.e., increasing the silica content, lowering the water content) of the layer above the APMB or the top layer within the APMB, (2) by varying the porosity (i.e., a lower fraction of melt or fluids present), or (3) by varying the connectivity (i.e., melt/fluid in isolation). This analysis is carried out in more detail in Section 7.5.

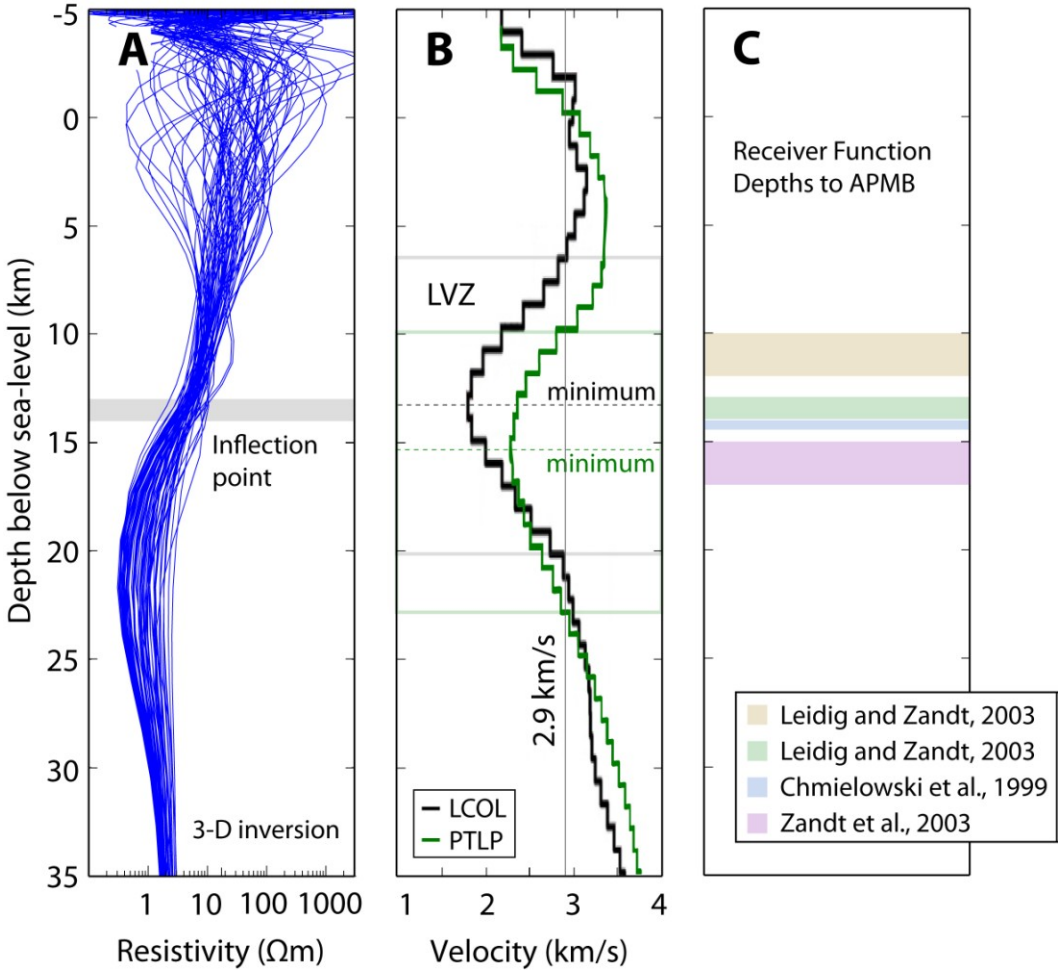

Figure 7.6: Panel A: the preferred 3-D electrical resistivity plotted as depth-resistivity profiles for all MT stations. The inflection point of the resistivity-depth profile is at 13-14 km BSL (gray box). Panel B: the S-wave velocity model of Ward et al. (2014) for 2 stations, LCOL near Laguna Colorado and PTLP north of Volcan Uturuncu. The slowest velocities for both stations (dashed lines, minimum) occur at a depth of ~14 km BSL, but the low-velocity zone (LVZ) of Ward et al. (2014) defined by the 2.9 km/s contour (solid lines) encompasses a large region, as the ANT results are smeared vertically. Panel C: published depths to the APMB from seismic receiver functions analysis show depths of 10-17 km BSL.

7.4 Inferring Melt Properties from MT Resistivity Models

7.4.1 Melt Resistivity Predictions

The resistivity values derived from MT exploration can be used to determine the composition of magma bodies. However, this is a non-unique process because the bulk resistivity depends on several variables, including the melt composition, melt quantity, and melt geometry (see review by Pommier, 2014). Pure melt resistivity is dominated by both water content and sodium content (Pommier and Le Trong, 2011). An online portal, SIGMELTS (Pommier and Le Trong, 2011), allows the computation of electrical conductivity of silicate melts as a function of composition, temperature, and pressure (see the Appendix Section A.4, and Figure A.4). A geochemical analysis of erupted lavas around Volcan Uturuncu provides compositional values for silicate rocks in the study area and allows the melt resistivity to be predicted (Muir et al., 2014; Sparks et al., 2008), as shown in Figure 7.7.

Dacite lava samples (silica content of ~65%) were inferred to be derived from a shallow magma chamber beneath Volcan Uturuncu (Muir et al., 2014; Sparks et al., 2008), corresponding to the feature C4 in Figure 6.2 and Figure 6.19. This shallow chamber is at a depth of 5 km below surface (about sea-level), equivalent to a pressure of ~100 MPa (Muir et al., 2014). The dacite samples had water contents of 2.5-4 weight percent (wt%), and a low sodium content of 2-3 wt% (Muir et al., 2014). Thermo-barometry from Sparks et al. (2008) gives an average temperature of 838°C for these dacite samples. Muir et al. (2014) give a similar average temperature of 858°C. Based on these values, a pure melt resistivity of 5-15 Ωm can be predicted from SIGMELTS, as shown in Panel A of Figure 7.7. These melt resistivity values match the laboratory studies of Laumonier et al. (2014), who used slightly different parameters (e.g., 870°C, 130 MPa), giving a predicted pure dacitic melt resistivity of 2.5-6.5 Ωm (see Figure 7.8 for a comparison). These resistivity values are relatively high for arc magmas, and likely reflect the relatively low sodium content of the Uturuncu lavas, compared to other systems (e.g., 3.5-5 wt% for Mount St. Helens, Pinatubo, Unzen) (Muir et al., 2014, and references therein).

The analysis was repeated for andesite samples (silica content of ~60%), which were inferred to have been erupted from the deeper magma body beneath Volcan Uturuncu, corresponding to the APMB, labelled C2 in Figure 6.2 and Figure 6.19. This body is at a depth of 15 km below surface, equivalent to a pressure of ~375 MPa (Sparks et al., 2008). Based on mineral assemblages and melt inclusion data, the andesite magmas had estimated temperatures of 980°C, a sodium content of 2-3 wt%, and were water-rich, possibly with water contents > 7 wt% (Sparks et al., 2008). Water contents for the deeper andesite samples can be hard to determine, as some water is lost during the crystallization of the magma upon ascent through the crust and eruption (Sparks et al., 2008). Muir et al. (2015) show that water contents of 5.0-9.2 wt% are possible for Uturuncu lava samples, reaching the solubility limits of Newman and Lowenstern (2002), see Section 7.4.3. Laumonier et al. (2014) believe that water contents as high as 10+ wt% are feasible. These input values predict a pure melt resistivity of 0.1-2 Ωm, as shown in Panel B of Figure 7.7. These melt resistivity values match the laboratory studies of Laumonier et al. (2014), who used slightly different parameters (e.g., 870°C, 1000 MPa), and assumed dacite melt, and predicted a pure melt resistivity of 0.2-2 Ωm (see Figure 7.8 for a comparison). The combination of higher temperature and an elevated water content gives the andesite magma a lower resistivity than the dacite magma.

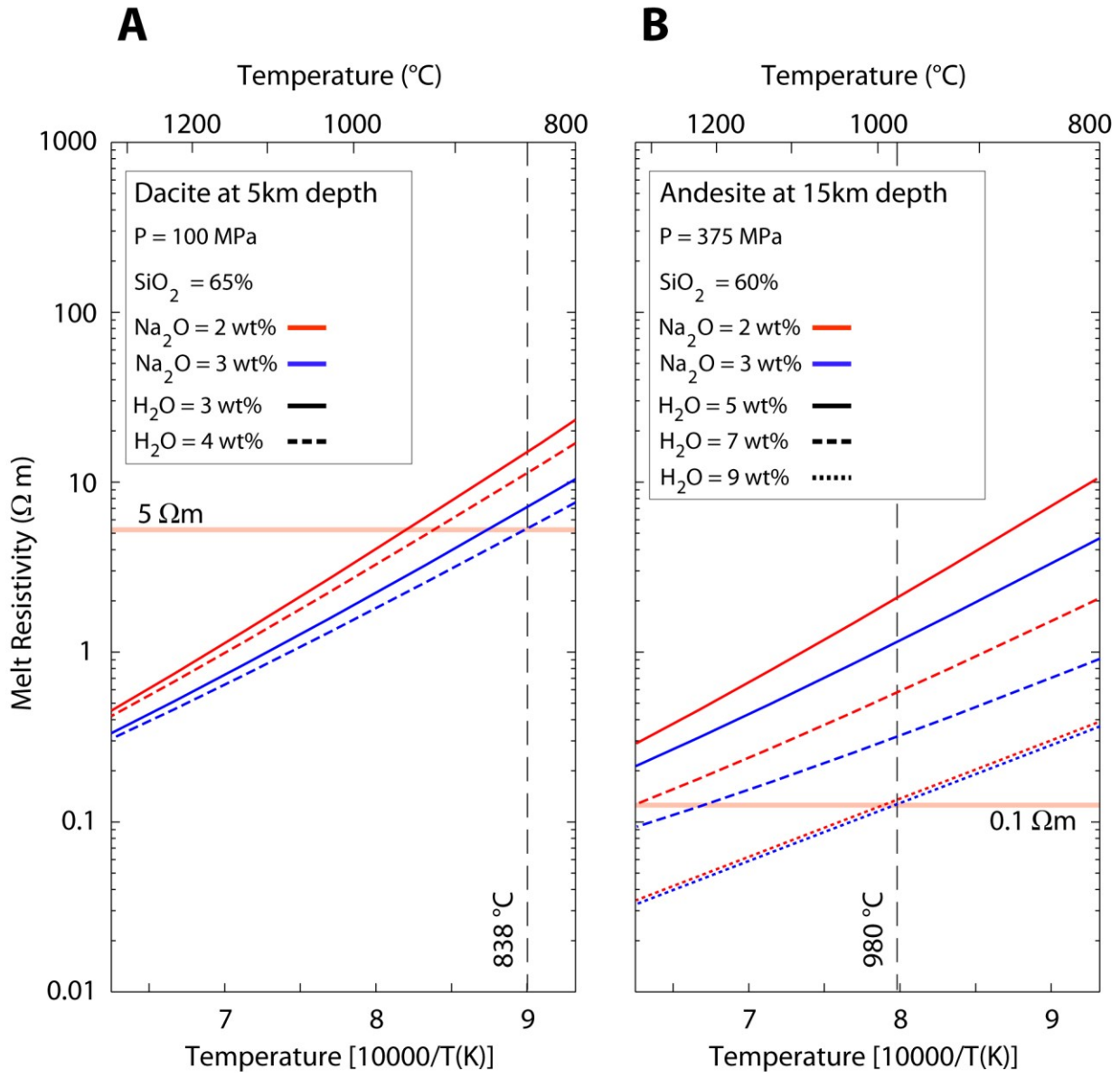

Figure 7.7: Variation of melt resistivity as a function of temperature for dacite and andesite melt with a range of water and sodium contents. The resistivity data were calculated using the SIGMELTS database of Pommier and Le Trong (2011). The lava composition was taken from Muir et al. (2014) and Sparks et al. (2008). Temperatures measurements are from Sparks et al. (2008). Depths are below surface (rather than sea-level), as this controls the pressure. Minimum resistivity values possible for the compositions and temperatures tested are shown.

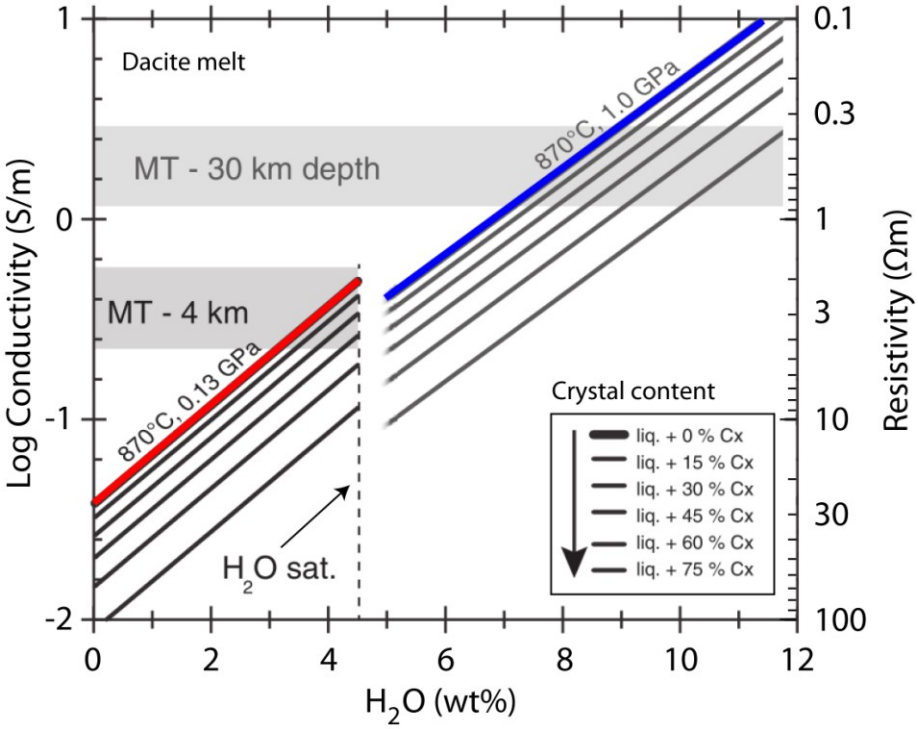

Figure 7.8: Conductivity values from the model of Laumonier et al. (2014) for dacite samples from Volcan Uturuncu with varying water content, measured as weight percent (H_2O wt%). Temperature is fixed at 870°C, and pressure is based on the depth to both a shallow magma body (~4 km depth; 130 MPa) and a deep magma body (~30 km depth; 1000 MPa). The red and blue lines show the pure melt conductivity (and resistivity) values for the shallow body and deep magma body, respectively. Thin grey lines represent the conductivity of a melt and crystal (Cx) mixture, as identified in the legend. Gray bands represent values which are compatible with MT measurements, according to Laumonier et al. (2014). These values are consistent with the SIGMELTS model of Pommier and Le Trong (2011), as shown in Figure 7.7. *(Figure adapted from Laumonier et al., 2014).*

7.4.2 Melt Fraction Measurements

Melt fraction can be estimated by combining the observed resistivity values from the MT inversion models with the estimated resistivity of pure melt based on the compositions of rock samples (see discussion above, Figure 7.7). Using the minimum values of resistivity for the melt will allow the determination of the minimum percentage of partial melt required to explain the observed MT data.

The bulk resistivity for different melt fractions was computed assuming pure dacite melt at a depth of 5 km with a resistivity of 5 Ωm and pure andesitic melt at a depth of 15 km with a resistivity of 0.1 Ωm (as described above and shown in Figure 7.7). The resistivity of the rock matrix was computed from the resistivity-temperature relation derived from the Arrhenius expression (Hashim et al., 2013; see Section 7.5.2 for more details), and was 780 Ωm for the shallow body (T = 838°C), and 325 Ωm for the deeper body (T = 980°C). These computations were made using the Modified Archie's Law (MAL; Glover et al., 2000) for various degrees of melt interconnection (cementation factor m=1.0 for interconnected melts; m=2.0 for isolated melts), and also with the Hashin-Shtrikman upper and lower bounds (HS-U, HS-L; Hashin and Shtrikman, 1963), see Section 4.2.3 for more details. The Hashin-Shtrikman lower bound is the preferred value because crustal melts are generally interconnected (e.g., ten Grotenhuis, 2005; Unsworth and Rondenay, 2013).

Figure 7.9 shows the melt fraction required to explain the observed resistivity values of the shallow dacite body (Panel A) and the deeper andesite body (Panel B). The dyke-like conductor beneath Uturuncu (i.e., C4 in Figure 6.2 and 6.19) has an observed resistivity of 3-7 Ωm in the inversion models, and dacite melt cannot explain the observed resistivity without having an exorbitantly high minimum melt percentage of 80%, or a much higher and unphysical water content. Another conducting phase is clearly needed to explain the results, as 80% melt is physically unlikely, because the rock becomes too weak above a rheological critical melt percentage (RCMP) of ~50% (see Petford, 2003) and becomes eruptible (Bachmann and Bergantz, 2008). Saline aqueous fluids, in addition to magma or alone, can possibly explain the

observed resistivity values, although MT data cannot distinguish between the two. Saline fluids would be more conductive, helping to explain the observed resistivity value. The fluids could be exsolved from magma crystallizing in C4, or perhaps the APMB. Aranovich et al., (2013) suggested that such fluids can move vertically over significant distances and accumulate in such a location. Jay et al. (2012) interpreted the shallow low-velocity zone detected beneath Uturuncu (see Section 3.2.6) as a hydrothermal system. This agrees with the above analysis indicating that saline or hydrothermal fluids are required to explain the resistivity values observed with MT.

The deeper conductor beneath Uturuncu (i.e., the APMB, C2) has an observed resistivity of < 1 Ωm in the inversion models. Assuming the melt is very well connected (m=1.0), a minimum melt fraction of 10% is required if andesitic melt is the cause of this conductive anomaly (see Panel B, Figure 7.9). The Hashin-Shtrikman lower bound predicts 15-45% andesitic melt is required to explain resistivity values of 0.3-1 Ωm. These results are consistent with the results of other MT studies which have suggested that 14-27% melt is required to explain the high conductivity anomaly detected below the Altiplano (i.e., the APMB), see Section 3.3.1 (e.g., Schilling, 2006; Schilling et al., 1997). Ward et al. (2014) determined that a melt fraction of 10-25% is required to explain the low velocities detected in the APMB. An analysis of the gravity data from del Potro et al (2013) shows that a melt fraction of 22-49% can explain the observed gravity low (Muir et al., 2015; Caricchi et al., 2014), as shown in Section 3.4.1. If higher values of melt resistivity are assumed (e.g., 0.3 Ωm) then a higher melt fraction is required. Therefore these values represent the minimum percent partial melt required by the MT data. For example, if the melt resistivity is assumed to be 0.3 Ωm, instead of 0.1 Ωm (for example if the melt is assumed to have 7 wt% water, see Figure 7.7), then the Modified Archie's Law (m=1.0, interconnected) predicts 30-100% andesitic melt is required to explain the observed resistivity values. In comparison, Yellowstone's shallow magma chamber (3-12 km depth) was found to contain 9-32% rhyolitic melt (Huang et al., 2015; Farrell et al., 2014; Chu et al., 2010). At Mount St. Helens, Hill et al. (2009) inferred 12% dacitic melt within a shallow magma chamber (5-10 km depth).

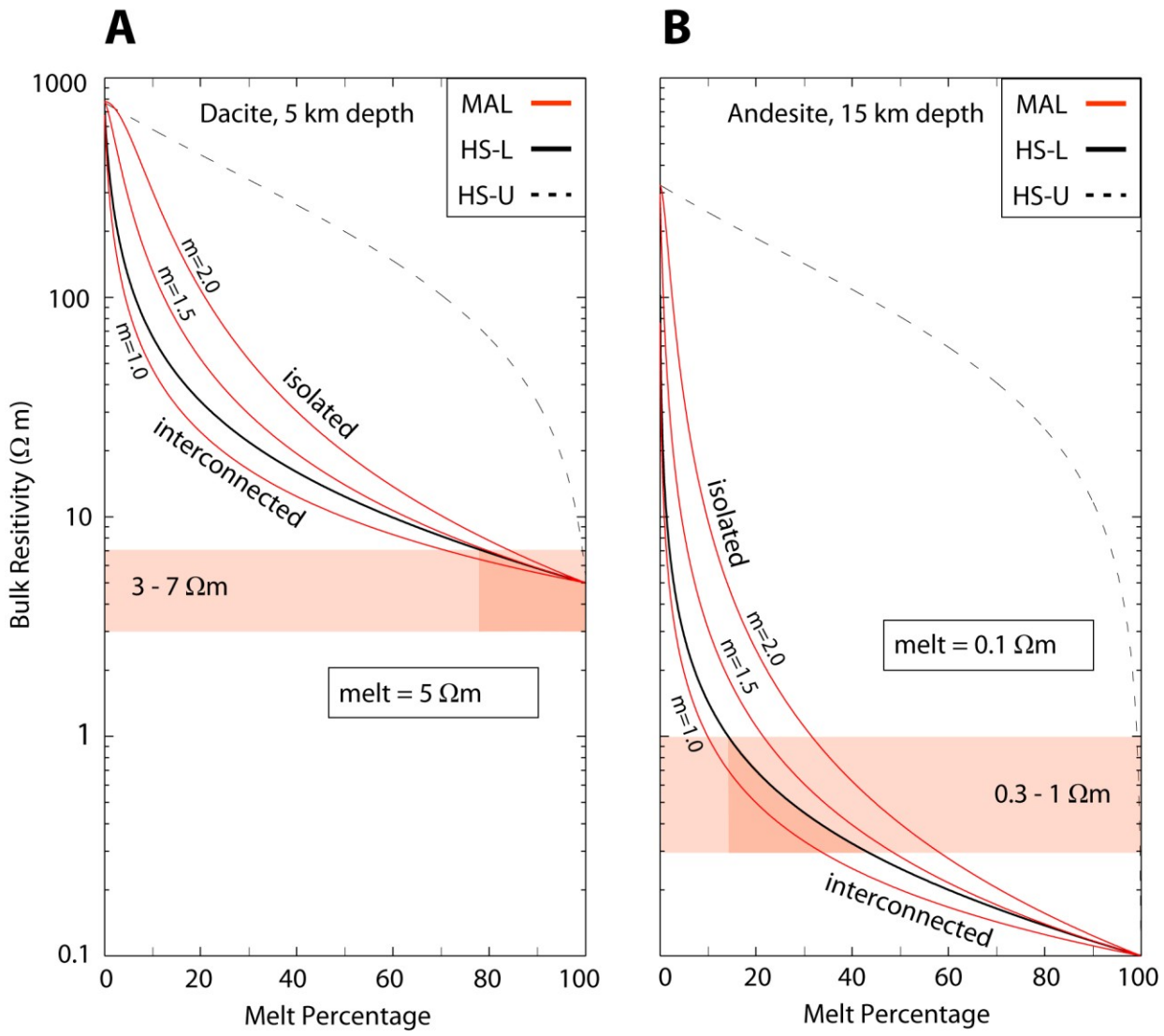

Figure 7.9: Bulk resistivity of a partially molten rock as a function of melt percentage. Panel A shows pure dacite melt with a resistivity of 5 Ωm. Panel B shows pure andesitic melt with resistivity of 0.1 Ωm. Red lines show the bulk resistivity computed using Modified Archie's Law (MAL; Glover et al., 2000), for various degrees of melt interconnection (cementation factor m=1.0, 1.5, 2.0). The solid black line shows the Hashin-Shtrikman lower bound (HS-L), and the dashed line shows the upper bound (HS-U). HS-L is the preferred value, see text for details. Depths are below surface, as this controls the pressure (~5 km below surface = sea-level). The minimum melt percentage for dacite is 80%, implying that a second conducting phase may be required to explain the data. The minimum melt percentage for the andesite is 15%.

7.4.3 Solubility of Water and Carbon Dioxide

Dacite lava samples (silica content of ~65%) from a shallow magma chamber beneath Volcan Uturuncu (5 km below surface, pressure of ~100 MPa, temperature of 858°C) had water contents of 2.5-4 wt% (Muir et al., 2014), see Section 7.4.1 and Figure 7.7 for more details. Whereas andesite samples (silica content of ~60%) from a deeper magma chamber (the APMB; 15 km below surface, pressure of ~375 MPa, temperature of 980°C) had water contents as high as 7-9 wt% (Sparks et al., 2008; Muir et al., 2014), and can possibly hold more than 10 wt% water (Laumonier et al., 2014). Water contents of magma can be difficult to determine from surface lava samples (Sparks et al., 2008), and it is an open question as to whether the lavas erupted at the surface are truly representative of the magma at depth. In order to understand the possible saturation levels of water content in these samples the solubility of silicate melts must be investigated.

The solubility of water in silicate melts of different compositions (e.g., water content, silica content) under different conditions (e.g., temperature, pressure) can be explored with the VolatileCalc model of Newman and Lowenstern (2002). Other similar relations are available from King and Holloway (2002) and Botcharnikov et al. (2006). VolatileCalc models volatile (i.e., water and carbon dioxide) solubility for both rhyolitic (VolatileCalc assumes 73% silica) and basaltic (49% silica) melts, but is also applicable to andesitic/dacitic (~63% silica) melts. Figure 7.10 shows the model of Newman and Lowenstern (2002), which confirms that melt at a pressure of 400 MPa and a temperature of 1000°C (e.g., the APMB) could contain 9.5 wt% water, while at lower pressures of ~100 MPa (e.g., a shallow magma body) the melt is limited to less than 4 wt% water.

The model of Newman and Lowenstern (2002) also allows the calculation of carbon dioxide (CO_2) solubility, shown in Figure 7.10, Panel B. A maximum of 2130-2190 parts per million (ppm) of CO_2 can be dissolved in basaltic or rhyolitic melt. However, adding CO_2 decreases the amount of water that can be contained in the melt. Volatile contents in the Uturuncu lava samples other than water, such as CO_2, are believed to be very low (Sparks et al., 2008). The results from the model of Newman and Lowenstern (2002), as shown in Figure 7.10, give

credibility to the compositional values assumed in Section 7.4, and show that the melt percentages calculated in Section 7.4.2 are minimum values.

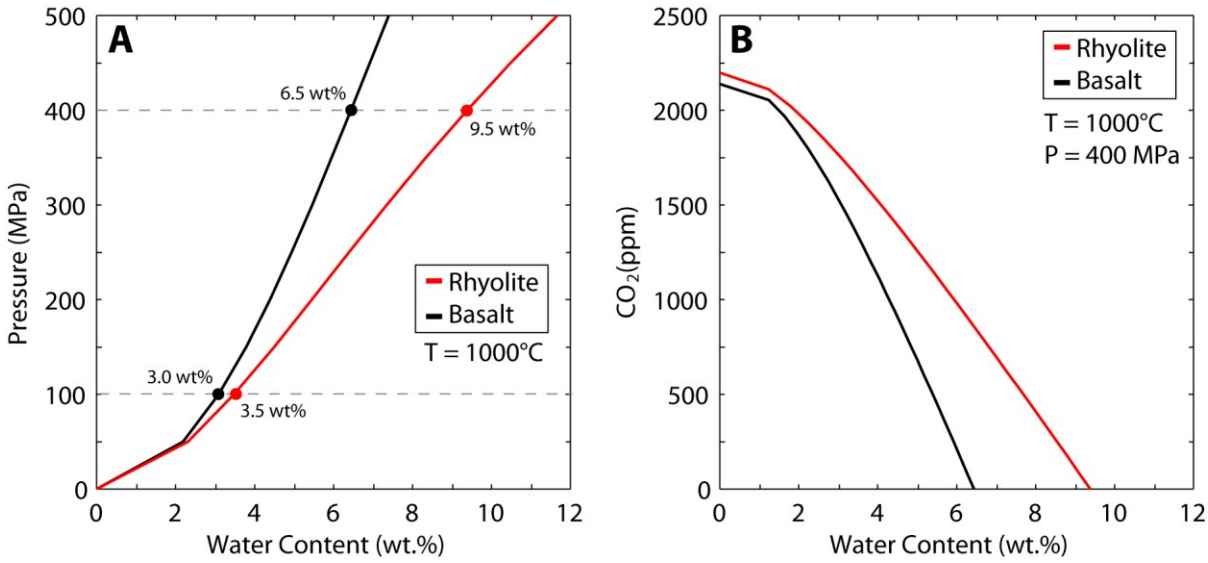

Figure 7.10: Panel A shows the solubility of water for varying pressures for both basaltic and rhyolitic melts, from the model of Newman and Lowenstern (2002). Panel B shows an isobaric (constant pressure) solubility plot for both water and carbon dioxide (CO_2).

7.5 Modeling a Layered Magma Chamber

As seen in Section 7.3, there is a small difference (a few kilometres) in the depth to the top of the APMB as determined with MT data (top of a high-conductivity zone) and with ANT+RF data (top of a low-velocity layer). One explanation for this discrepancy, given in Section 7.3, is that the resolution between the two geophysical methods is different; that is, the ANT results are not sensitive to small vertical structures and therefore show one smooth and continuous low-velocity layer. However a second explanation is that the APMB has a more complicated structure that is detected differently by each geophysical method, due to the fact that MT is sensitive to electrical resistivity and seismic methods are sensitive to (acoustic) velocity. A layered magma body that

had a relatively more resistive top layer would cause the MT method to detect the top of a high-conductivity zone at a greater depth than the seismic method, without affecting the seismic velocities. There are several ways to achieve this, such as having a layered magma body with a silica-rich, water-poor, or melt-poor top layer, or a top layer where the melt is not well-connected. All of these effects will make the top layer more resistive. The following sections will explore this idea in detail.

7.5.1 Modeling Shear-Wave Velocity

A velocity model can be computed from the forward model input parameters and compared to the observed velocity from the ANT+RF data of Ward et al. (2014), see Figure 7.6. Following Dvorkin (2008), the shear-wave velocity can be computed for any melt fraction if the melt density and rock matrix density are known. This relation is written as

$$V_s = (1-\varphi)^2 V_{so} \sqrt{\frac{(1-\varphi)p_s}{(1-\varphi)p_s + \varphi p_f}}, \qquad \text{(Eq. 7.1)}$$

where V_s is the bulk shear wave velocity, V_{so} is the shear wave velocity of the rock matrix with no melt, p_s is the density of the rock matrix, p_f is the density of the fluid, and φ is the melt fraction.

Bottinga and Weill (1970) give equations which allow the calculation of magma density based on its chemical composition and temperature. Using the composition and temperature values from Sparks et al. (2008), the density of andesitic magma is found to be 2392 kg/m^3, and the density of dacitic magma is 2431 kg/m^3. Assuming a rock matrix density of andesite, 2700 kg/m^3, and a rock matrix velocity of 3.5 km/s, the shear-wave velocity can be computed for any melt fraction with the relation of Dvorkin (2008), as shown in Figure 7.11.

Takei (2000) gives a more complex relationship which depends not only on the density but also on the shear modulus of the rock matrix and the shear modulus of the fluid saturated rock. This relation is written as

$$V_s/V_{so} = \sqrt{\frac{N}{p}}\sqrt{\frac{p_s}{N_s}}, \text{ or} \quad \text{(Eq. 7.2)}$$

$$V_s = V_{so}\sqrt{\frac{N}{N_s}}\sqrt{\frac{p_s}{(1-\varphi)p_s+\varphi p_f}}, \quad \text{(Eq. 7.3)}$$

where V_s is the bulk shear wave velocity, V_{so} is the shear wave velocity of the rock matrix with no melt, p_s is the density of the rock matrix, p_f is the density of the fluid, p is the combined density of the rock matrix and fluid, φ is the melt fraction, N is the bulk shear modulus, and N_s is the shear modulus of the rock matrix.

Using shear modulus values from the compilation of Bass (1995) and from Schmitt (2015), the shear-wave velocity can be computed for any melt fraction with the relation of Takei (2000), as shown in Figure 7.11. A layer with 25% melt fraction results in a velocity of 1.52 km/s and 1.65 km/s for the Dvorkin and Takei relations, respectively, which matches the ANT+RF results of Ward et al. (2014), as shown in Figure 7.6. A 15% melt fraction gives a velocity of ~2.2 km/s, still within the values for the LVZ as defined by Ward et al. (2014). The shear-wave velocity is sensitive to the fluid content (e.g., water content, melt fraction), but not its chemical composition (e.g., silica content, sodium content), implying the velocity will be constant within a uniform or layered magma body.

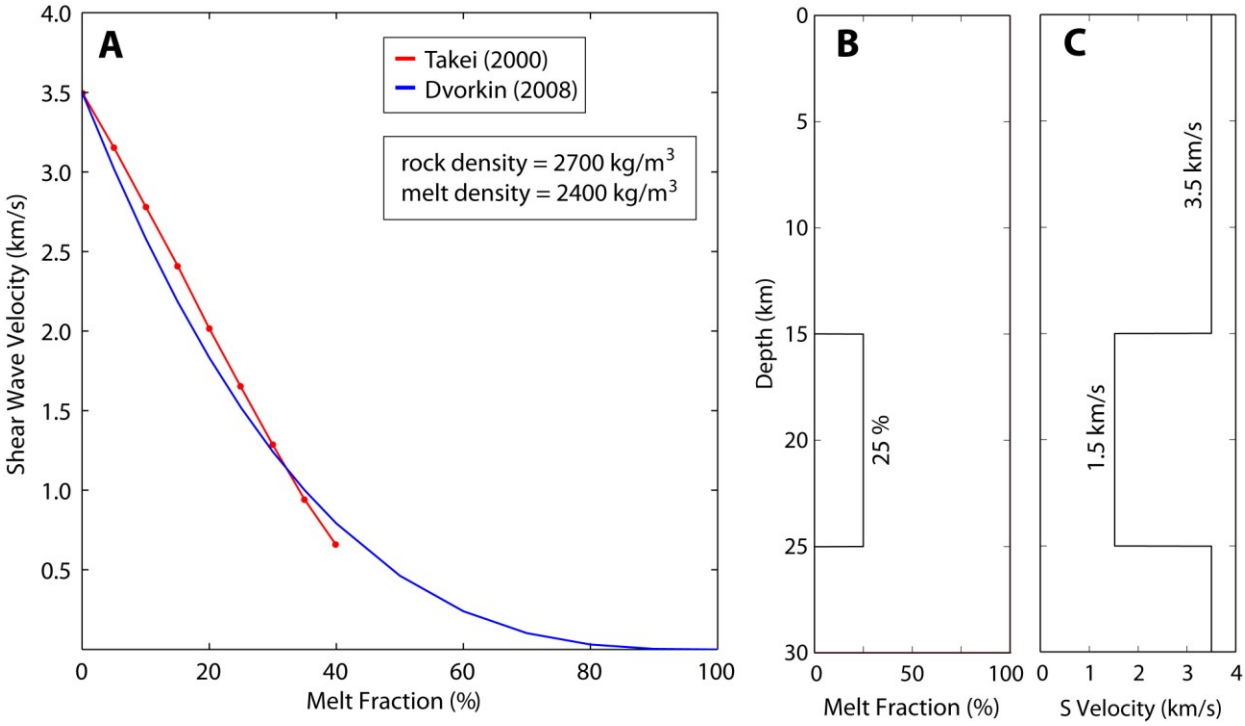

Figure 7.11: Panel A shows shear wave velocity (Vs) as a function of melt fraction. The relations of Dvorkin (2008) and Takei (2000) give similar results. Panels B and C show that the shear-wave velocity is sensitive to the fluid content and will be constant in a layer of melt, despite the melt's composition or inhomogeneities within the melt.

7.5.2 Modeling Resistivity for a Layered Magma Chamber

Calculating the bulk resistivity of a partially molten rock (what can be measured with MT data) can be modeled as a forward problem. By specifying the composition of the melt (e.g., water content, sodium content, silica content) and the conditions where the melt is found (e.g., temperature, pressure) the melt resistivity can be determined from various semi-empirical relations. In this thesis, the widely used SIGMELTS model (Pommier and Le Trong, 2011) is used, although other relations exist (e.g., Gaillard, 2004). The observed bulk resistivity can then be calculated using the rock matrix resistivity (which depends on temperature), the melt

geometry, the melt fraction (porosity), and the pure melt resistivity using mixing laws such as the Modified Archie's Law (see Section 4.2.3 and Equation 4.6).

These steps were carried out above in Section 7.4 and the predicted melt resistivity for varying temperature is shown in Figure 7.7, and the predicted bulk resistivity for varying melt percentage is shown in Figure 7.9. However, a model which can compute the bulk resistivity over a range of depths as various input parameters are varied and can then forward model MT data would be useful to compare the effect small parameter changes have on a measured MT response. The input parameters (e.g., water content, sodium content, silica content, temperature, pressure, rock density, rock matrix resistivity, melt geometry, melt fraction) depend on depth. In contrast, as seen above in Section 7.5.1, shear-wave velocity depends primarily on the density of the rock matrix and the pore fluid (e.g., Takei, 2000; Dvorkin, 2008), and not on compositional differences (i.e., water content, sodium content, silica content) or melt geometry.

The pressure is calculated from the depth, assuming a simple lithostatic relation (e.g., pressure = density·depth·g, where g is the acceleration due to gravity, g = 9.81 m/s^2); a density of 2700 g/m^3 can be used for the andesitic rock matrix (del Potro et al., 2013). The rock matrix conductivity (i.e., inverse of resistivity) depends on the temperature, and can be calculated assuming an Arrhenius-like behaviour (Nover, 2005). The theoretical relationship can be written for conductivity as

$$\sigma = A \cdot e^{-Ea/kT} , \qquad \text{(Eq. 7.4)}$$

and depends on a constant (A), the activation energy (Ea), the temperature in Kelvin (T), and the Boltzmann constant (k = 1.381x10^{-23} J/K) (e.g., Nover, 2005). The relation of Hashim et al. (2013) is used for the analysis in this section, with experimentally derived values for crustal rocks. The relation for the resistivity of crustal rocks as a function of temperature is

$$\rho_r = e^{[-\ln(2.9)+8581.8/T]} , \qquad \text{(Eq. 7.5)}$$

where T is temperature in Kelvin (Hashim et al., 2013). It is important to consider the resistivity of the rock matrix because it can also act as a conducting phase at high temperatures (as described in Section 4.2.3). The melt geometry can be highly interconnected, using a cementation factor of m = 1.0 in Modified Archie's Law, or the melt may be located in isolated pores, where a cementation factor of m = 2.0 is more appropriate (Glover et al., 2000). The temperature can be increased linearly at a gradient of ~65°C/km until it reaches the magma body at a temperature of 980°C (Sparks et al., 2008) at a depth of ~15 km, where it becomes isothermal due to convection.

7.5.3 Layered Magma Chamber: Varying Silica Content

Figure 7.12 shows three models where the silica content varies vertically within the magma body. Model 1 is a simple model which consists of a uniform magma body (i.e., melt reservoir) at a depth of 15 km below the surface. Within this body the melt fraction is 25 %, the melt geometry is interconnected (m = 1.0), the sodium content is 3 wt%, the water content is 6 wt%, and the silica content is 60% throughout. Models 2 and 3 are similar but have a layered magma chamber which has a more felsic upper layer. Specifically, Model 2 has an upper layer (15 - 20 km depth) with 65 % silica and Model 3 has an upper layer with 70 % silica. The SIGMELTS model (Pommier and Le Trong, 2011) uses a different relation for high silica content (70 - 80 %) compared to intermediate silica contents (50 - 70 %), so a value of 69.999 % was used in place of 70 %, in order to stay within the same regime, see Figure A.4 in Section A.4 of the Appendix.

The bulk resistivity is constant in the upper portion of the model (Figure 7.12, Panel E), as it equals the resistivity of the host rock (1000 Ωm), but begins to decreases smoothly as the increasing temperature makes conduction through the host rock possible (325 Ωm at 15 km depth). The predicted bulk resistivity decreases drastically at the depth of the magma chamber as partial melts are encountered (shown in Figure 7.12, Panel E). Model 1 shows a constant resistivity within the magma chamber. For Model 2 and Model 3 the predicted bulk resistivity is higher in the upper layer due to the higher silica content.

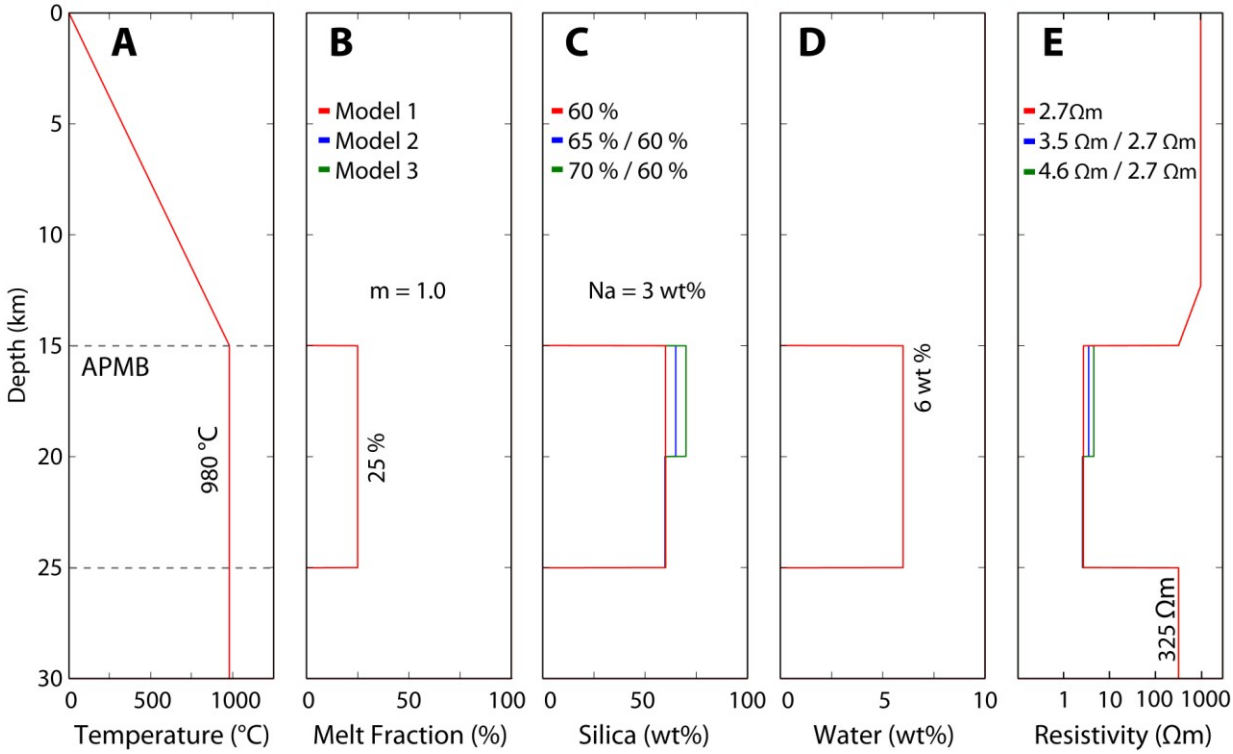

Figure 7.12: Bulk resistivity forward model for varying silica contents. Input parameters of temperature, melt fraction, silica content, and water content are shown in Panels A-D. The predicted bulk resistivity of a magma chamber is shown in Panel E for three models. Each model has the same temperature profile, a melt fraction of 25 %, water content of 6 wt%, and sodium content of 3 wt%. Model 1 (red) is uniform with 60 % silica; Model 2 (blue) is a layered magma chamber with 65 % silica in the upper portion; Model 3 (green) is a layered chamber with 70 % silica in the upper portion.

7.5.4 Layered Magma Chamber: Varying Water Content

Within the magma chamber Models 1, 2, and 3 use a constant water content of 6 wt%. It is plausible that within the magma chamber the water is partitioned such that the upper silica-rich portions are also water-rich. Model 4 has 9 wt% water in the upper portion and 6 wt% water in the lower portion, as shown in Figure 7.13. The resistivity of the upper and lower portions are

0.6 Ωm and 2.7 Ωm. Obviously a water-poor upper layer is required within or above the magma chamber to make the top portion more resistive than the lower portion. The area immediately above the magma chamber may have a different composition then the magma chamber, and if melt exists above the magma chamber, but is water-poor, this upper portion will become more resistive. Model 5 has water partitioned in the opposite way, with 4 wt% water in the upper portion and 6 wt% water in the lower portion.

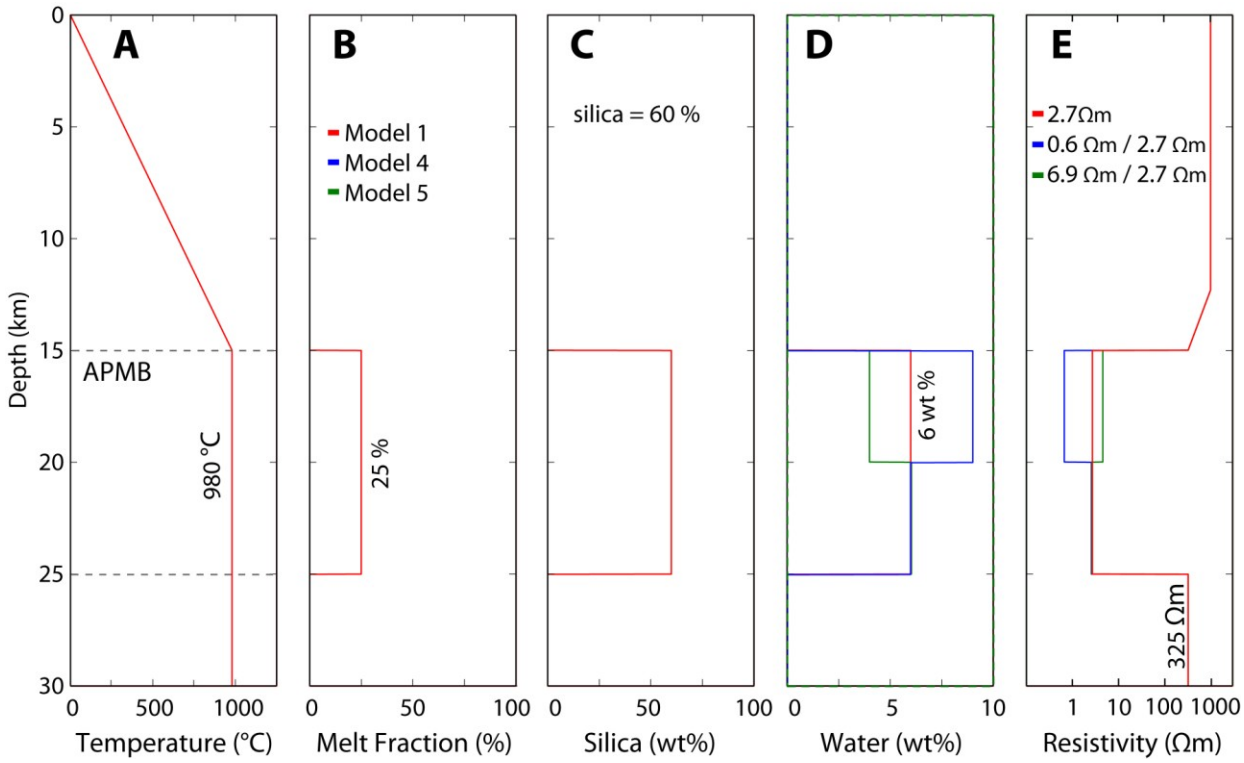

Figure 7.13: Bulk resistivity forward model for varying water contents. Input parameters of temperature, melt fraction, silica content, and water content are shown in Panels A-D. The predicted bulk resistivity of a magma chamber is shown in Panel E, as in Figure 7.12.

7.5.5 Layered Magma Chamber: Varying Melt Geometry and Melt Fraction

If the melt is not well connected the electrical resistivity will be higher. Model 6 is similar to Model 1 but has somewhat isolated melt (m = 2.0) in the upper portion of the magma chamber. Model 7 is similar to Model 3 (70% silica in the upper portion) but has isolated melt (m = 2.0) in the upper portion.

As shown in Section 7.5.1, the shear-wave velocity depends on the amount of melt present. Therefore, if the melt fraction is kept constant, as in the models above, the velocity will be constant. However, if the melt fraction decreases the shear-wave velocity will increase. The relation of Dvorkin (2008) gives a velocity of 1.5 km/s for a 25% melt fraction and a velocity of 2.2 km/s for a 15% melt fraction. These are both considered "low-velocity" based on the 2.9 km/s velocity contour of Ward et al. (2014). Model 8 is similar to Model 1 but has a melt fraction of 15% in the upper portion (rather than 25%, as in Model 1).

Figure 7.14 shows the relationships between silica content, water content, melt fraction, melt connectivity, and resistivity from the SIGMELTS model for the entire model space. It can be seen that silica content and water content have the strongest impact on resistivity. For water contents of 9wt% and above the melt saturates and the resistivity is constant for any silica content (within the SIGMELTS model). Table 7.2 shows a list of models and their parameters. The values for an upper and lower layer are given (if only one value is given then that parameter is the same for both layers), as well as the ratio of upper layer resistivity to lower layer resistivity.

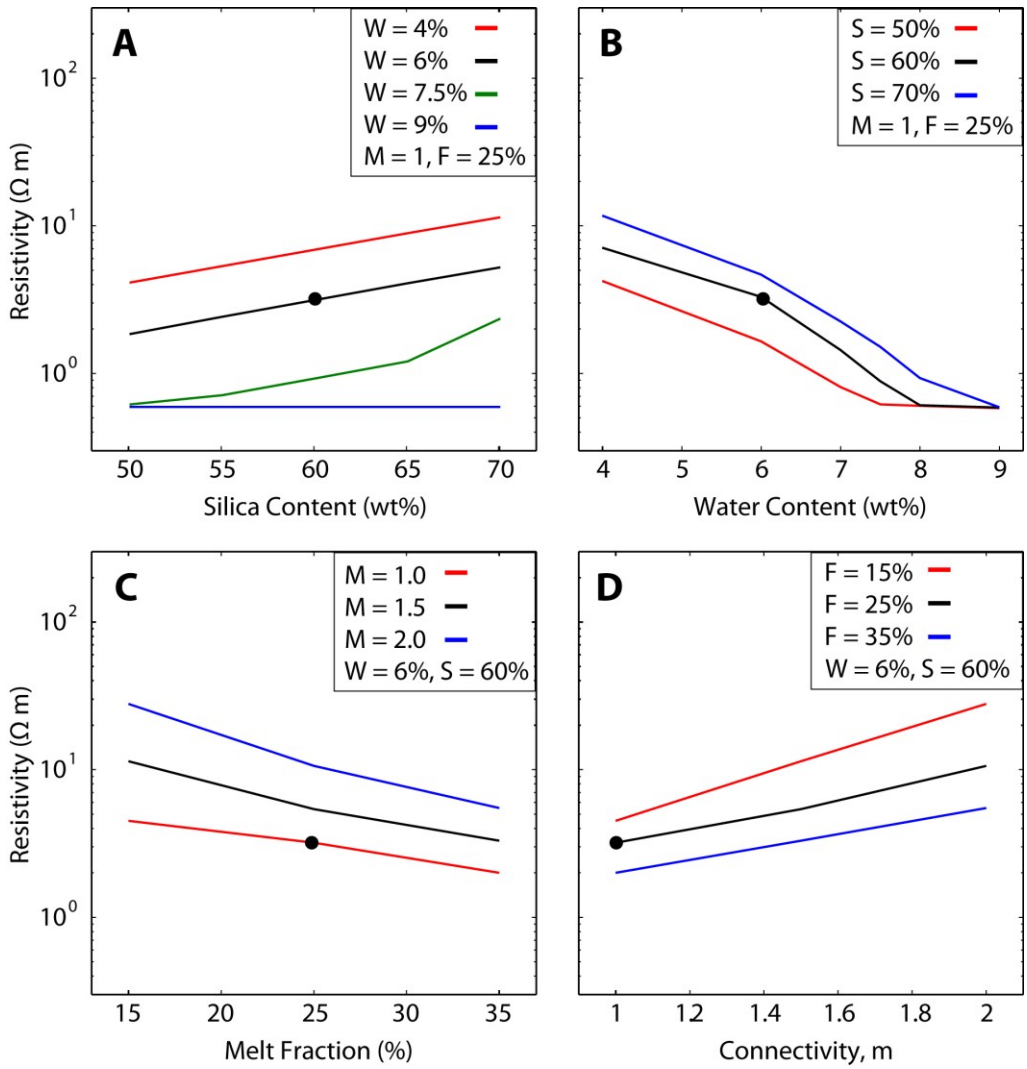

Figure 7.14: Melt resistivity values for the whole model space computed from SIGMELTS are shown. Panel A shows how the resistivity varies as a function of silica content, for different water contents (W). A connectivity of m=1 and a melt fraction of 25% is assumed. Panel B shows how the resistivity varies as a function of water content, for different silica contents (S). Panel C assumes a silica content of 60% and a water content of 6% and shows how the resistivity varies with melt fraction, for different connectivity values (M). Panel D shows how the resistivity varies as a function of the connectivity parameter m from Archie's law, for different melt fractions (F). The black dot represents the values used in Model 1. Resistivity values cover a large range: from ~0.5 to 20 Ωm.

MODEL #	SILICA (wt%)	WATER (wt%)	MELT FRACTION (%)	MELT GEOMETRY (m)	SODIUM (wt%)	RESISTIVITY (Ωm)	RATIO
1	60	6	25	1	3	2.7	
2	65/60	6	25	1	3	3.5/2.7	1.3
3	70/60	6	25	1	3	4.6/2.7	1.7
4	60	9/6	25	1	3	0.6/2.7	0.2
5	60	4/6	25	1	3	6.9/2.7	2.6
6	60	6	25	2/1	3	10.6/2.7	3.9
7	70/60	6	25	2/1	3	17.5/2.7	6.5
8	60	6	15/25	1	3	4.5/2.7	1.7
9	70/60	6	15/25	2/1	3	44.4/2.7	16.4
10	60	6	15/25	2/1	3	28/2.7	10.4
11	65/55	6	25	1	3	3.5/2.1	1.5
12	70/50	6	25	1	3	4.6/1.6	2.9
13	60	9/4	25	1	3	0.6/6.9	0.1
14	60	6	15/35	1	3	4.5/2.0	2.3
15	70/50	6	25	2/1	3	17.5/1.6	10.9
16	70/50	6	15/25	2/1	3	44.4/1.6	27.8
17	70/50	9/4	25	1	3	1/4.1	0.2
18	70/50	4/9	25	1	3	94.7/0.6	157.8

Table 7.2: Models created in the forward modeling exercise of Section 7.5 and their parameters. values for an upper and lower layer, when different, are given. The final column gives the ratio of upper layer resistivity to lower layer resistivity.

7.5.6 Forward Modelled MT Data

Figure 7.15 shows the forward model MT responses as apparent resistivity and phase curves for various models. A conductive surface layer (3 Ωm from 500 m to 1000 m) was included to represent the surface layer seen in the measured (real) MT data. The surface layer acts to reduce the resolution in the lower layer, making the study more realistic. The responses from Models 1, 2, and 3 (Panel A) show that silica differences within the magma chamber are reliably resolvable. Panel B compares water differences, and Panel C compares changes in the melt fraction and melt geometry.

The higher resistivity layer at the top of a layered magma body, as seen in Models 3, 7, and 8, can cause MT measurements to detect the top of the conductive zone at a greater depth then the top of the magma body (i.e., 20 km below surface rather than 15 km). Forward modeling MT responses from these 1-D models shows that small differences within the magma chamber can be resolved reliably (Figure 7.15). The apparent resistivity curves for most models are very similar because they represent a smoothly varying average of the true resistivity. At the longest periods (100+ s) the apparent resistivity and phase curves show a separation.

At long periods (100+ s) the apparent resistivities of Model 1 and Model 3 are different by a factor of 2 (10 Ωm and 20 Ωm), but it is difficult to see this on the log-scale plot. The phase curves a show large separation between the two models of up to 10°. These difference would typically be above the error of MT data (e.g., 10 % error for 30 Ωm = 3 Ωm; 10 % error for 45° = 4.5°). The apparent resistivity curves for Model 1 and Model 4 differ by a factor of 5, while Model 1 and Model 5 differ by a factor of 2. The phase curves for Model 1 and Model 4 differ by a up to 22°, while Model 1 and Model 5 differ by up to 7°. Model 7 shows a large difference in apparent resistivity compared to Model 1 of a factor of 3, and a phase difference of up to 11°.

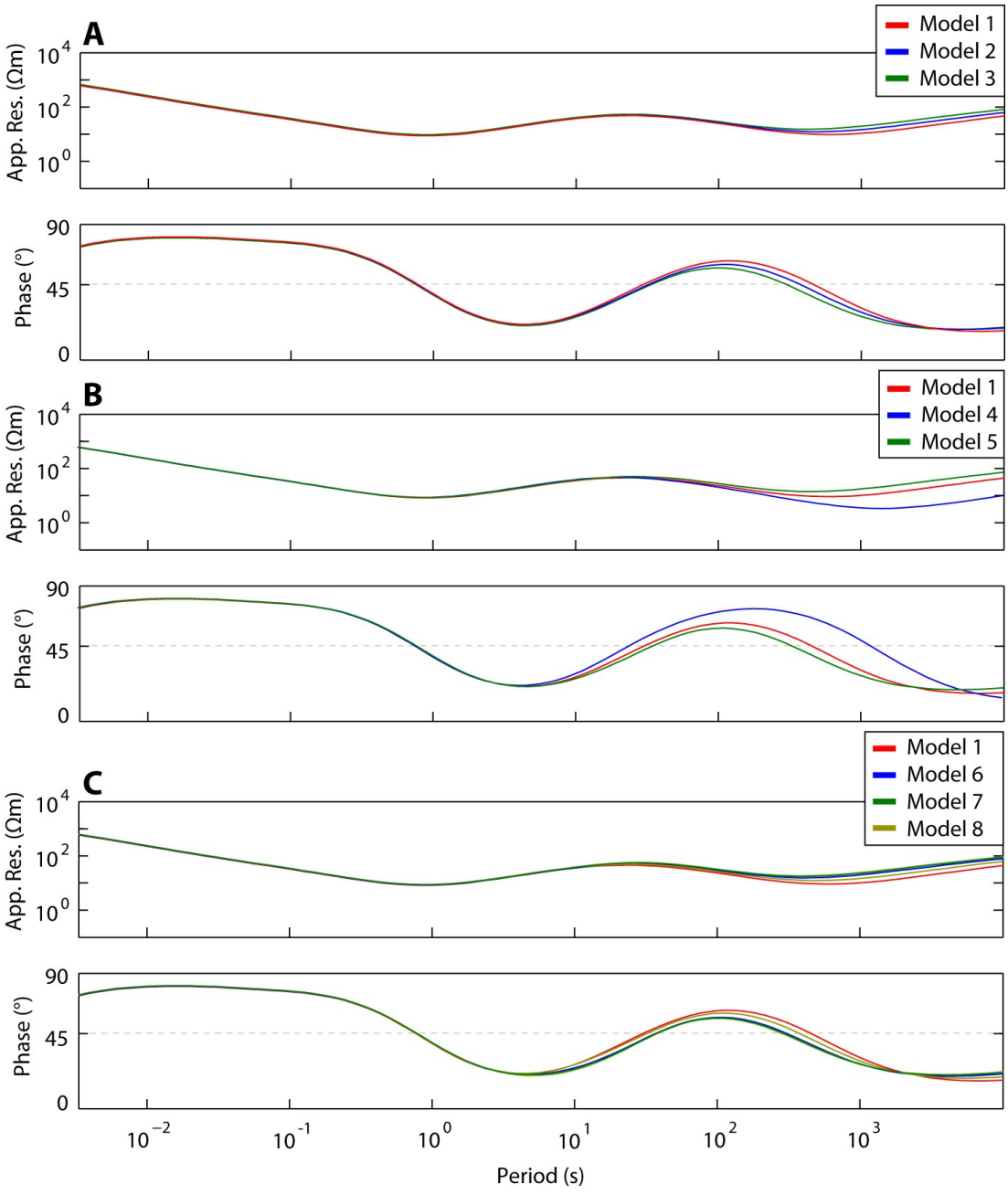

Figure 7.15: Forward model MT curves for various models shown as apparent resistivity and phases curves, see text for details. Panels show variations in silica content (A), variations in water content (B), and variations in melt fraction and melt geometry (C). The models are very similar but the differences are large enough to distinguish between models with MT data.

7.5.7 MT Inversion Model for a Layered and Uniform Magma Chamber

The forward modeling exercise above showed that differences within a magma chamber (i.e., a uniform chamber versus a layered chamber due to changes in silica, water content, melt fraction, or melt geometry) are distinguishable with MT data. A synthetic inversion is needed to test whether the resistivity values and geometry of the different models can be recovered satisfactorily. The MT data responses (see Figure 7.15) for the magma chamber resistivity models (see Figure 7.11) were used in a synthetic MT inversion. Model 1 (uniform chamber; silica = 60 wt%, H_2O = 6 wt%) and Model 7 (layered chamber; upper layer with 70% silica, lower layer with 60% silica) were run and compared, as these represent the cases of a uniform magma chamber and a layered magma chamber with a resistive top layer.

The synthetic models were run with the 2-D inversion algorithm of Rodi and Mackie (2001). The synthetic profile had MT stations at 1 km intervals, with a minimum horizontal mesh cell spacing of ~350 m and a vertical cell spacing of 500-1000 m in the area of interest. However, the model is 1-D, and so each site shows the same resistivity profile. The conductive surface layer (3 Ωm from 500 m to 1000 m), representing the surface layer seen in the measured (real) MT data, acts to mask the signal causing the lower layers to be less resolved. The synthetic MT data had 5% random Gaussian noise added in order to give an example of a more realistic case. The inversion was constrained with a layered starting model having a resistivity of 100 Ωm from 0-15 km and a 1 Ωm halfspace below 15 km depth.

The synthetic true model is shown in Figure 7.16 Panel A as a resistivity-depth curve and in Panels C and E using a colour scale for the uniform magma chamber (Model 1) and the layered magma chamber (Model 7). Figure 7.16 Panels D and F show the results of the inversion of the synthetic data. The results show for the uniform case (Panel D) the depth to the top of the magma chamber is well resolved. However, for the layered case (Panel F), the model shows the depth to the lower layer is resolved, because it is a strong conductor, but the depth to the top of the upper layer is not interpreted as readily, because it is more resistive. The results for this extreme case show that for the layered case the depth to the top of the upper layer is lower than for the uniform case.

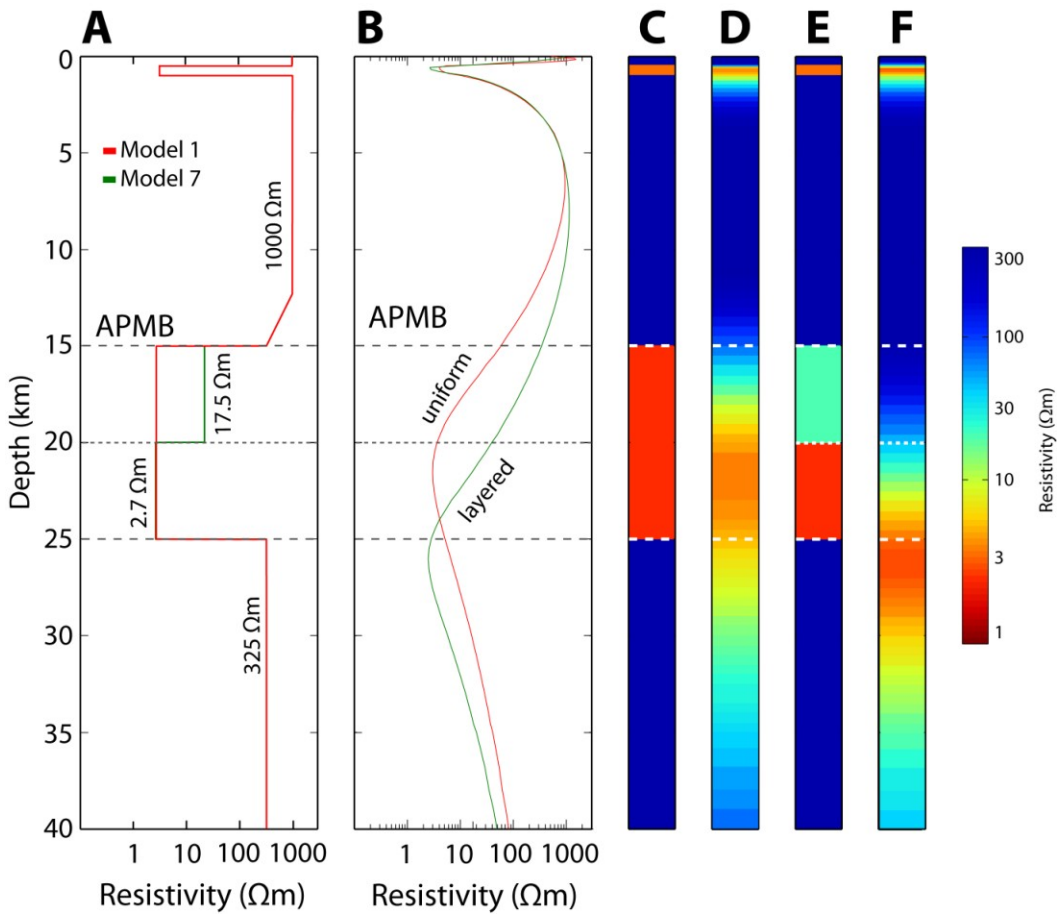

Figure 7.16: Panel A: synthetic models for a uniform magma chamber (Model 1, red line) and a layered magma chamber (Model 7, green line), with the addition of a conductive surface layer. Panel B: resistivity-depth profile for the 1-D synthetic inversion resistivity model. The depth to the top of the prominent deep conductor (i.e., the APMB) is given by the inflection point of the resistivity curve. Random Gaussian noise (5%) was added to the data in order to create a more realistic model. True synthetic models are shown in Panels C and E as colour plots, whereas inversion resistivity models are shown in Panels D and F. Dashed lines indicated sharp boundaries in the true model of magma chamber location and its upper and lower portions for the layered case. The surface conductor acts to mask the signal, reducing the resolution in the magma chamber. The models show that MT data can reliably show a layered magma chamber at a greater depth than a uniform one, when the lower layer is more conductive.

7.5.8 Can Depth Differences be Explained by a Layered Magma Chamber?

Both the forward modeling of the MT data (i.e., Figure 7.15) and the synthetic MT inversions (i.e., Figure 7.16) clearly show that MT data can distinguish between a uniform magma body (i.e., Model 1) and a layered magma body (i.e., Model 7), provided the difference between the resistivity of the upper and lower layers is substantial (e.g., ratio of upper layer resistivity to lower layer larger than a factor of ~2). However the predicted MT response for Model 3 (layered with 70 % and 60 % silica; resistivities of 11.4 Ωm and 2.7 Ωm) and Model 7 (where the water content was also partitioned; resistivities of 6.9 Ωm and 2.7 Ωm) were both easily distinguishable from Model 1 (uniform case, silica = 60 %, water = 6 wt%), differing in apparent resistivity by a factor of 3 and up to 10° in phase, at longer periods (> 100 s). These differences would typically be above the error of MT data (e.g., 10 % error 30 Ωm = 3 Ωm; 10 % error 45° = 4.5°). The synthetic inversion models unequivocally show a depth difference between the layered magma body (Model 7) and the uniform magma body (Model 1).

These results show that one explanation for the small difference in depth to the top of the APMB from seismic ANT+RF and MT results can be explained by a layered magma body. If the APMB has a silica-rich upper layer or if the water content is higher in the lower portion of the magma body this can drastically affect the resistivity and therefore the MT data, showing a greater depth to the top of a conductive layer. On the other hand, the seismic velocities will be relatively unaffected by this compositional layering, showing a shallower depth to the top of a low-velocity zone, resulting in a difference in depths between the two geophysical methods.

7.6 Determining the Viscosity of Partial Melts

Viscosity is an important physical property that controls the speed at which magma moves through the Earth, and can give insights into the occurrence of magma mixing within magma chambers, and establish the explosivity and potential hazards of volcanoes (Pommier et al., 2013, and references therein). Viscosity is a measure of the resistance of a substance to flow, and is

measured in Pa·s. It can be thought of as the time it takes for a substance to flow, for a given force over a given area (Lowrie, 2004). By observing everyday fluids such as water (10^{-5} - 10^{-2} Pa·s), oil (10^{0} - 10^{1} Pa·s), or syrup (10^{1} - 10^{2} Pa·s), it is obvious that viscosity varies over many orders of magnitude (Lowrie, 2004). For Earth materials, which are not true fluids, the viscosity is much higher. Estimates of the viscosity of the crust and mantle range from 10^{19} - 10^{21} Pa·s or higher (Lowrie, 2004).

While the electrical conductivity of melt is controlled by charge carriers (i.e., sodium, water; as described in the previous section), it is the silica framework of a melt that controls the viscosity (Pommier et al., 2013). When the melt has a higher silica content the viscosity is increased, because the structure becomes more rigid and its ability to flow is limited. The viscosity of a melt has an inverse relation with the temperature; that is, the viscosity increases as the temperature decreases, because the melt begins to crystallize as it cools, limiting its ability to flow (Dingwell, 2006). The viscosity also has an inverse relationship with the water content. Water acts to break down the silica network, making the silica more mobile and decreasing the viscosity, so the viscosity increases as the water content decreases (Dingwell, 2006). In comparison, electrical resistivity depends on silica content, water content, and temperature in much the same way as viscosity, showing a similar general trend. As seen in the previous section, the resistivity increases as silica content is increased, the resistivity increases as temperature is decreased, and the resistivity increases as water content is decreased.

Figure 7.17 shows how melt viscosity varies temperature, water content, and silica content, using the model of Giordano et al. (2008). The compositions of andesite, dacite, and rhyolite samples were taken from Sparks et al. (2008), and is shown in Table 7.3. The model of Giordano et al. (2008), with the input values given above, gives a viscosity for the pure melt in the deeper magma reservoir of ~10^{3} Pa·s, and for the pure melt in the shallow magma reservoir of $10^{5.5}$ Pa·s. These values are within the range of expected values for melt viscosities (Pommier et al., 2013). In comparison, Pommier et al. (2013) calculate a value of $10^{5.7}$ Pa·s for the viscosity of a pure rhyolite melt with 3 wt% water at 900°C.

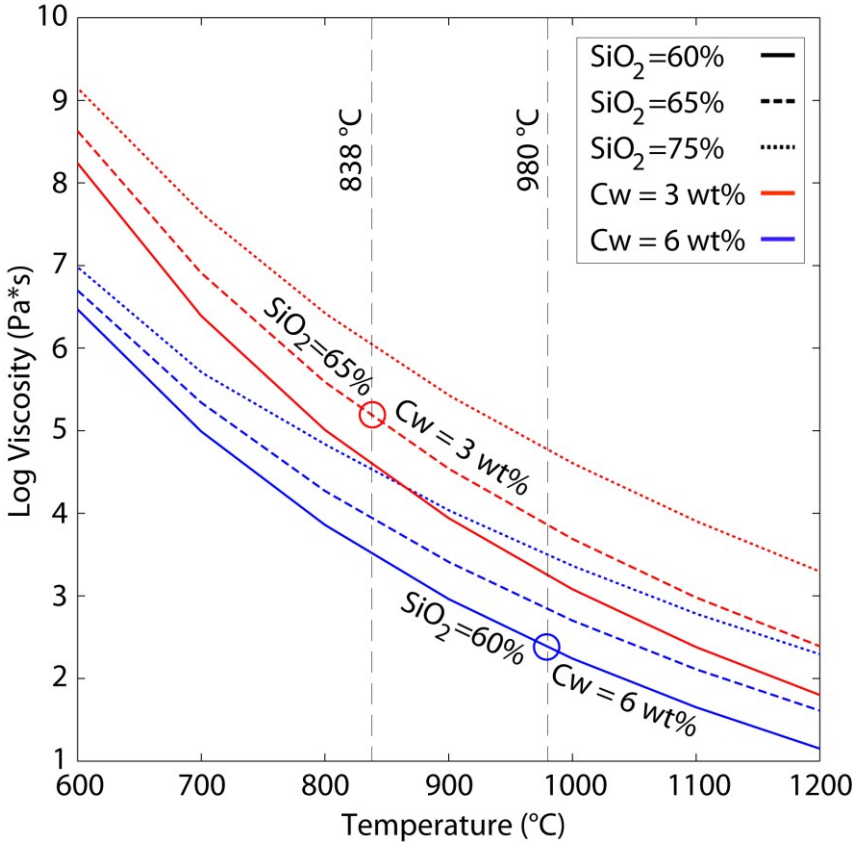

Figure 7.17: Variation of melt viscosity with temperature for various melt compositions, using the model of Giordano et al. (2008). Note that there are multiple ways to lower the viscosity: a higher temperature leads to a lower viscosity; a higher water content (weight percent, wt%) leads to a lower viscosity; a lower silica fraction (% SiO_2) leads to a lower viscosity.

wt%	Andesite	Dacite	Rhyolite
SiO_2	60	65	75
AlO_2	17	14	11
FeO_2	6	5	1.5
MgO	3	2	0.1
CaO	5	3	0.5
Na_2O	2	2	1.5
K_2O	3	3	6
H_2O	3-6	3-6	3-6

Table 7.3: The composition values in weight percent (wt%) were taken from Sparks et al. (2008), andesite samples UTU5 and UTU2, Table 4b; dacite lava samples UTU16 and UTU25, Table 4a, rhyolite inclusion sample UTU2, Table 4c.

7.6.1 Calculating Viscosity of Melt from Resistivity Measurements

Determining the viscosity of a melt in the laboratory is relatively simple (e.g., Dingwell and Hess, 1998). However, when considering the structure at depth in the crust, geophysical constraints must be used. Ryder et al. (2007) used post-seismic crustal deformation to estimate viscosity, while Rippe and Unsworth (2010) were able to link MT resistivity measurements and crustal viscosity by estimating crustal flow due to a pressure gradient from surface topography.

Viscosity and conductivity are theoretically related through the modified Stokes-Einstein equation, which can be written as

$$\eta \propto A \cdot \sigma^{-B} \text{ , or} \qquad \text{(Eq. 7.6)}$$

$$\log(\eta) \propto \log(A) - B \cdot \log(\sigma) \text{ ,} \qquad \text{(Eq. 7.7)}$$

where η is the viscosity (Pa·s), σ is the electrical conductivity (S/m; the inverse of resistivity), and A and B are empirical constants, which are tabulated for many materials (Pommier et al., 2013, and references therein). However, a relation which clearly expresses the dependence on measurable quantities from the rock composition is more appropriate to geophysical interpretations.

Pommier et al., (2013) proposed a semi-empirical relation between viscosity of melt and electrical conductivity, for a given melt composition, water content, and temperature. The relation can be written as follows,

$$\log(\eta) = 41.09 - 1.5 \cdot \frac{10^5}{T} + 2.84 \cdot Cw + 139.4 \cdot OB - 31.25 \cdot \log(\sigma) \text{ ,} \qquad \text{(Eq. 7.8)}$$

where η is the viscosity (Pa·s), T is the temperature in degrees Kelvin, Cw is the water content in wt%, OB is the optical basicity which encompasses the melt composition (explained below), and σ is the electrical conductivity of the pure melt (S/m; the inverse of resistivity).

Equation 7.8 is complicated by the fact that the conductivity has a large dependence on the water content, composition, and temperature as well (Pommier and Le Trong, 2011). This means that it is not possible to keep the resistivity fixed as the water content is varied, for example, to see the effect on the viscosity, as the resistivity will change as the water content is varied. This relation is based on empirical evidence from laboratory studies of silicate melt conductivity and viscosity models (Pommier and Le Trong, 2011). Acceptable ranges of values for the relation suggested by Pommier et al. (2013) are 0-6 wt% for water content and a temperature range of 900-1600°C. The relation is most appropriate for pure melt or for high melt fraction zones (i.e., > 70%), where the bulk conductivity can be assumed to be controlled mostly by the melt conductivity (Pommier et al., 2013; Costa et al., 2009).

The optical basicity (OB) parameter is an estimation of oxide ion activities, and encompasses the chemical composition of the melt (Pommier et al., 2013; Duffy and Ingram, 1975; Zhang and Chou, 2010). The OB parameter depends mainly on the silica dioxide content (SiO_2). For pure SiO_2 the OB value is 0.478, and as the SiO_2 content decreases, the value of OB increases. The OB value also increases as water content increases. For the dacite and andesite samples from the study area the OB value ranges from 0.56 to 0.67, as shown in Table 7.4.

Optical basicity (OB) composition parameter

Water	Basalt	Andesite	Dacite	Rhyolite
(wt%)	50%	60%	65%	75%
0	0.609	0.576	0.562	0.534
1	0.618	0.585	0.570	0.542
2	0.627	0.594	0.579	0.551
3	0.636	0.602	0.588	0.559
4	0.646	0.611	0.596	0.568
5	0.655	0.620	0.605	0.576
6	0.664	0.629	0.614	0.585
9	0.693	0.656	0.640	0.612

Table 7.4: The optical basicity (OB) parameter encompasses the chemical composition of the melt; see text and references for details. The compositions were taken from Sparks et al. (2008) (see Table 7.3) and were scaled to attain 100% composition as varying amounts of water were added, keeping the silica content fixed.

Both electrical conductivity and viscosity are parameters which depend on the chemical composition of the sample, but viscosity has a much higher sensitivity to chemical composition then electrical conductivity, with small changes in any parameter creating drastic changes of several log units for viscosity. This can be seen in Figure 7.18, which shows the predicted viscosity for various resistivity values of both andesitic and dacitic melts. The viscosity can vary by several factors of ten (i.e., 10^{10}) if the resistivity is varied by only a factor of ~2. Using a resistivity value of ~0.2 Ωm for the pure melt (as determined previously for the APMB), Equation 7.8 gives a viscosity of 10^6 Pa·s for the APMB. This seems plausible, in comparison to values found by other researchers (e.g., Pommier et al., 2013). For the shallow dacite body a temperature of 900°C is used as this is the lowest acceptable value for the relation (Pommier et al., 2013), a resistivity value of ~1.0 Ωm gives a viscosity value of 10^8 Pa·s. These values are higher (2-3 orders of magnitude) than those discussed above using the model of Giordano et al. (2008), but may be more realistic because the resistivities are accounted for. For comparison, Pommier et al. (2013) estimates a viscosity of $10^{5.7}$ Pa·s for a rhyolite melt (3 wt% water and 900°C). The addition of useful rheological information (i.e., viscosity) to the interpretation of conductivity anomalies from MT data can provided constraints on magma motion in the crust above the APMB. These viscosity values will later be used to compare proposed geodynamics models.

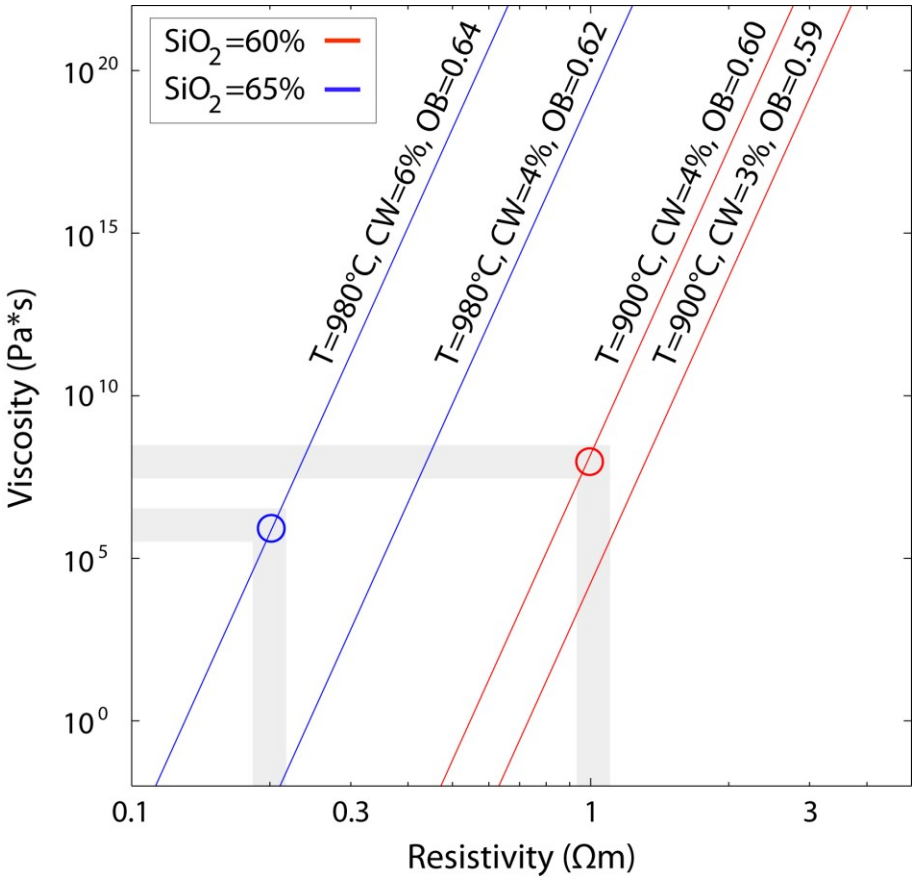

Figure 7.18: Variation of melt viscosity and electrical resistivity for a deep andesite body (blue lines) and shallow dacite body (red lines) for fixed temperatures, water content (CW, in weight percent, wt%), and composition (the OB parameter) using the relation of Pommier et al. (2013), see text for details. Note the resistivity also depends on the temperature, water content, and composition. A resistivity value of 0.2 Ωm for the deep andesite body with 6 wt% water gives a viscosity value of 10^6 Pa·s; a resistivity value of 1.0 Ωm for the shallow dacite body with 4 wt% water gives a viscosity value of 10^8 Pa·s.

7.6.2 Viscosity of Crystal-Rich Melts

Thus far the viscosity of pure silicate melts has been discussed, but the viscosity of a partial melt can also be calculated. There are several semi-empirical relations that show how viscosity varies

with the fraction of solid particles (e.g., crystals) in a fluid (e.g., melt) (e.g., Costa, 2005; Einstein, 1906). Caricchi et al. (2007) performed a series of experiments in order to understand the relation between the viscosity of a pure melt and one that contains a high crystal fraction (i.e., low porosity). The authors used rhyolitic melt with ~3 wt% water containing quartz crystals in order to simulate magma rising inside a volcanic conduit. Costa (2005) compared experimental viscosity measurements in the literature (mostly for granite) and developed an empirical relationship for viscosity and crystal fraction, which was later modified and improved by Costa et al. (2009). Experimental results generally show relative viscosity by comparing the viscosity of the sample (measured) with the viscosity of the pure melt (with no crystals), which allows different experimental setups and different sample compositions to be compared. Figure 7.19 shows the relative viscosity as a function of crystal fraction (melt fraction = 1 - crystal fraction) based on the works of Costa (2005), Caricchi et al. (2007), and Costa et al. (2009).

Examining Figure 7.19, the viscosity increases as the crystal fraction is increased, as expected (e.g., Caricchi et al., 2007; Costa et al., 2009). Viscosity increases slowly and linearly at low crystal fractions until a crystal fraction of approximately 40-50 % is reached, at which point the crystal grains begin to interact and the fluid no longer acts as a pure liquid (Costa et al., 2009). Viscosity then begins to increase exponentially until approximately 80 % crystal fraction, after which the viscosity doe not vary very much as the fluid is no longer well-connected (Costa et al., 2009). A crystal fraction of 35-50 % can increase the viscosity of the melt by an order of magnitude (i.e., 10 times the value of the pure melt; relative viscosity = 10^1). A crystal fraction of 60 % (melt fraction of 40 %) can increase the viscosity of the melt by a factor of 10^2-10^4, while a crystal fraction of 80 % (melt fraction of 20 %) can increase the viscosity of the melt by a factor of 10^6-10^8. These values give an idea of the viscosity difference between a pure melt and a partial melt (e.g., a rock with 30 % melt fraction). The models described here are for relatively high strain rate non-Newtonian systems, where the viscosity decreases as strain rate increases, whereas magma addition and reservoir inflation of the APMB is likely a case of low strain rate. Therefore, these relations provide a minimum constraint on the relative viscosity of the APMB.

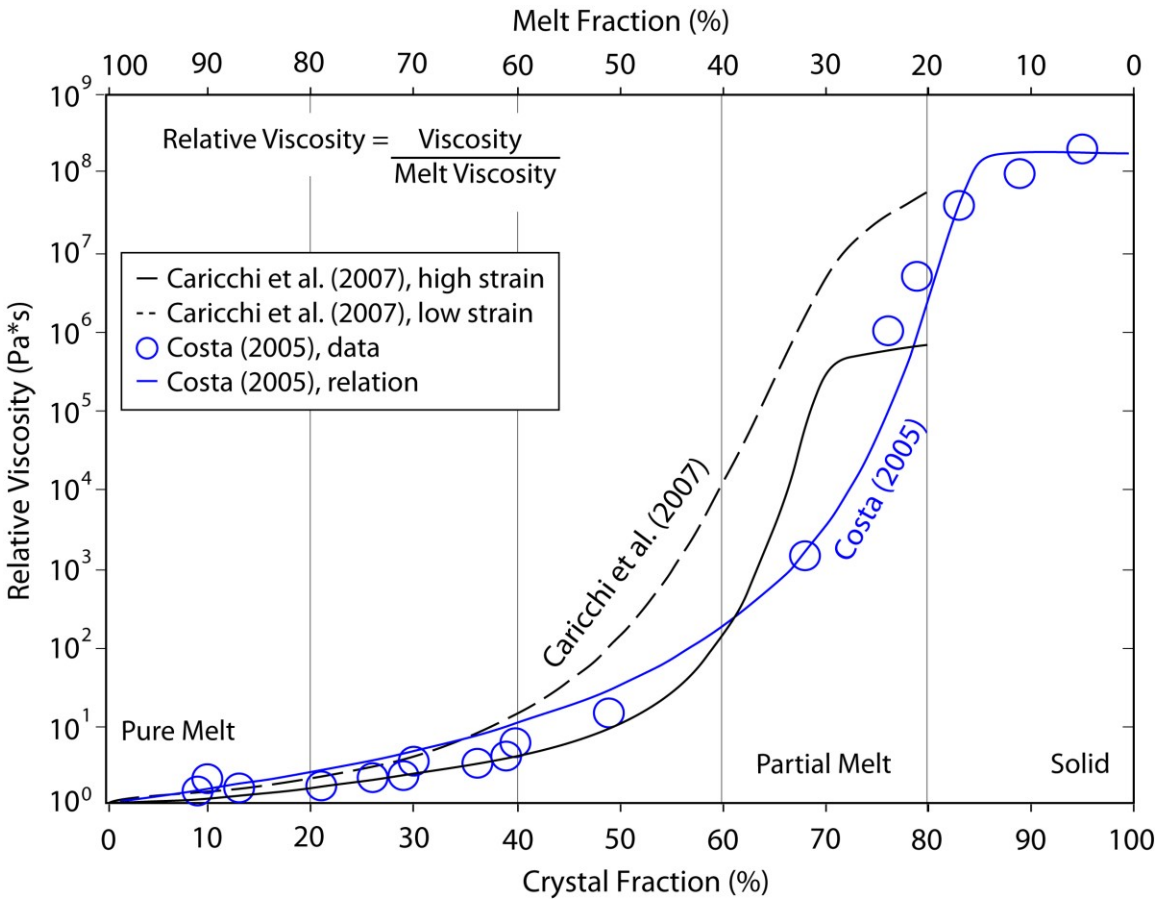

Figure 7.19: The relative viscosity (ratio of viscosity to melt viscosity) as a function of melt fraction and crystal fraction. The experimental values of Caricchi et al. (2007) are shown with black lines for a high strain rate ($8x10^{-4}$ s^{-1}; solid line) and a low strain rate ($0.005x10^{-4}$ s^{-1}; dashed line). Experimental values from Costa (2005) (strain rate of $0.01x10^{-4}$ s^{-1}) are shown as blue circles, while the empirical relation of Costa (2005) is shown as a blue line.

7.6.3 Determining the Viscosity of the Partial Melts of the APMB

The viscosity of the partial melt in both the APMB and the shallow upper magma reservoir can now be calculated by combining the results of the previous sections. Using the models of Giordano et al. (2008) and of Pommier et al. (2013), the viscosity of pure melt for the deeper reservoir was calculated to be 10^3-10^6 Pa·s, and for the pure melt in the shallow magma reservoir the viscosity was $10^{5.5}$-10^8 Pa·s. The model of Caricchi et al. (2007) shows that if the magma

reservoir has a melt fraction of 20% (crystal fraction of 80%) then the partial melt viscosity increases by a factor of 10^6-10^8; for a melt fraction of 40% (crystal fraction of 60 %) the partial melt viscosity increases by a factor of 10^2-10^4. This gives a final effective viscosity for the partial melt in the shallow magma reservoir of $10^{7.5}$-10^{12} Pa·s for a 40 % melt fraction and $10^{11.5}$-10^{16} Pa·s for 20 % melt fraction. Correspondingly, the partial melt in the deeper magma reservoir will have an effective viscosity of 10^5-10^{10} Pa·s for a 40 % melt fraction and 10^9-10^{14} Pa·s for 20 % melt fraction.

7.6.4 Implications of MT derived viscosities for the APMB

Assuming a minimum melt fraction of 20%, the effective viscosity of the APMB has been calculated to be a maximum of 10^{14} Pa·s, while the shallow magma reservoir has an effective viscosity of 10^{16} Pa·s (see above for details). These values are in good agreement with the geodynamic model of Fialko and Pearse (2012) which estimated a viscosity of 10^{16} - 10^{18} Pa·s for the APMB and the magma in the crust above it.

These viscosity values can be compared to those in Tibet, which is an active convergent orogen with a high plateau and thick crust, similar to the Altiplano, although no large magma bodies have been detected there. Post-seismic deformation in northern Tibet was modelled by Ryder et al. (2007) and gave a mid-crustal viscosity of 10^{18} Pa·s. Geodynamic modeling studies estimated the viscosity of the crust beneath the central part of the Tibetan plateau as 10^{16} Pa·s (Clark and Royden, 2000). Beneath eastern Tibet Rippe and Unsworth (2010) calculated viscosities of 10^{17} - 10^{20} Pa·s from crustal flow using their resistivity-viscosity relation with conductances of 30,000 S measured from MT data.

The viscosity values determined for the APMB are lower than those of the crust (10^{19} - 10^{21} Pa·s; e.g., Lowrie, 2004), as expected, given the hydrous state of the APMB magma and its high temperatures. The addition of rheological information is useful when interpreting the conductivity anomalies from MT data as it can provided constraints on magma motion in the crust above the APMB.

7.7 Synthesis with Geodetic Measurements

As explained in Chapter 3, multiple geodetic models have been proposed to explain the deformation pattern around Volcan Uturuncu observed with InSAR. Figure 7.18 shows several of these models overlain with the preferred 3-D resistivity model (details of this model were presented in Chapter 6; see Figure 6.19). Details of the geodetic models proposed can be found in Section 3.6.2, but a summary is provided here: Model 1 is a spherical inflation source centered at 17 km BSL (Pritchard and Simons, 2004), Model 2 is a horizontal ellipsoid source centered at 19 km BSL (Pritchard and Simons, 2004), Model 3 is a vertical ellipsoid source centered at 16 km BSL (Hickey et al., 2013), Model 4 is a diapir extending vertically from the APMB (Fialko and Pearse, 2012), Model 5 is a flat topped body rising 7 km from the APMB (Walter and Motagh, 2014).

The MT model does not disagree with models 1 and 2 as sources for the inflation, although these are likely oversimplifications. Hickey et al. (2013) used a realistic visco-elastic layered model to propose the broad surface deformation pattern observed can be fit with a vertically elongated inflation source driven by the lateral motion of magma (Model 3). This model predicts a shallowing in the upper surface of the APMB that is consistent with the MT results and seen in both the 3-D and 2-D resistivity models. Significantly, the 2-D resistivity model (see Figure 6.2) reveals that Uturuncu is located above the highest point of a long-wavelength upwelling of the APMB. This "bulge" is likely caused by the inflation source.

The 3-D model shows that, at a local scale, the MT results are consistent with a diapir geometry (Model 4) with the dimensions proposed by Fialko and Pearse (2012). The MT model shows that the diapir is more resistive than the APMB, which may imply that it has a lower melt fraction, or a different composition than the APMB. Fialko and Pearse (2012) modelled the APMB with a viscosity of 10^{16} Pa·s and the diapir with a viscosity of 10^{18} Pa·s. These values are higher than the values predicted by the analysis above ($<10^{16}$ Pa·s for the shallow magma viscosity) by a few orders of magnitude, but are within error, giving credibility to this model.

A flat-topped magma reservoir extending above the top of the APMB does not match the MT data at the scale proposed by Walter and Motagh (2014). Although, it is possible that this geometry would be difficult to resolve at smaller scales, so the MT model does not preclude this geometry.

The deformation source may be radially symmetric and located within the APMB. However above a depth of 10 km BSL the magma distribution pattern does not appear to be radially symmetric. Instead the MT model shows that magma and fluids are moving upwards in a series of discrete dyke-like zones striking roughly east-west, as opposed to a broad homogenous upwelling as expected from a diapir (see Figure 6.19).

Figure 7.20 also shows the depths to the APMB as predicted by seismic models (discussed above). Seismic RF models give depths to the APMB which match the MT results (i.e., ~15 km BSL), whereas ANT+RF models give a thick diffuse layer for the APMB. Earthquakes hypocenters below Volcan Uturuncu from Jay et al. (2012; see Chapter 3) are also shown. The shallow pre-eruptive magma storage chamber predicted by Muir et al. (2014) from geo-barometry of erupted dacites is also shown. Its location correlates with the shallow conductor of the MT model and also with the earthquakes hypocenters.

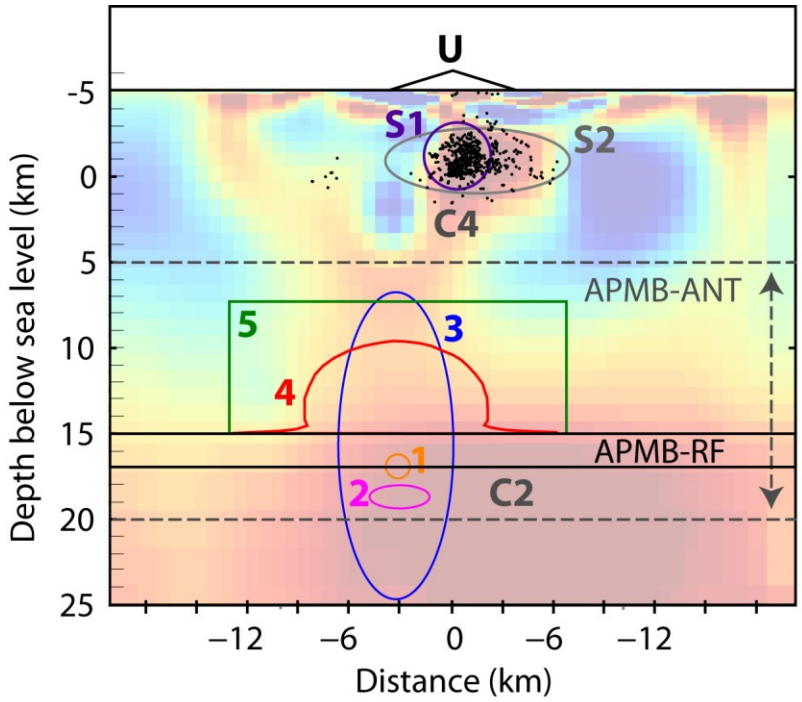

Figure 7.20: Several proposed geodynamic models overlain with the preferred 3-D resistivity model. C2 — The deep conductor interpreted as the APMB. C4 — The shallow conductor interpreted as a pre-eruptive magma body. 1 — Spherical inflation source (Pritchard and Simons, 2004). 2 — Horizontal ellipsoid source (Pritchard and Simons, 2004). 3 — Vertical ellipsoid source (Hickey et al., 2013). 4 — Diapir extending above APMB (Fialko and Pearse, 2012). 5 — Flat topped body above the APMB (Walter and Motagh, 2014). Depths to the Altiplano-Puna magma body from seismic receiver functions (APMB-RF; Zandt et al., 2003) correlate well with the depth inferred from the MT data. Ambient noise tomography (APMB-ANT; Ward et al., 2014) shows a broader range for the APMB, likely encompassing the small scale features above the APMB and smearing the results. U — relative location of Volcan Uturuncu. InSAR data reveals the inflation centre is located ~3 km West of the summit (Pritchard and Simons, 2004). Black dots are earthquake hypocenters from Jay et al., (2012). Earthquake locations correlate with the shallow conductor (C4) interpreted to be a pre-eruptive magma storage location, as predicted by Muir et al. (2014) from the geo-barometry of erupted dacites (S1) and Jay et al. (2012) from a low-velocity zone identified with ANT (S2).

7.8 Evidence for a Shallow Magma Chamber Below Volcan Uturuncu

Volcanic systems may be supplied by multiple magma chambers or melt reservoirs that are located at different depths in the crust or laterally offset at the same depth (see Annen et al., 2006). Geodetic data from Soufriere Hills Volcano, Montserrat, show magma is moving through vertical conduits from a deep supply source at the base of the crust (~20 km depth), to a sill-like mid-crustal reservoir (~12 km), and finally to a shallow chamber (~6 km) (Elsworth et al., 2008). Petrological studies and seismic studies at Krakatau, Indonesia, show similar results, with magma storage regions inferred at depths of ~5 km, ~10 km, and a deep storage region near the Moho at ~23 km depth (Dahren et al., 2012).

Below the APVC, InSAR data show a deep inflation source believed to be related to the APMB (e.g., Henderson and Pritchard, 2013; Fialko and Pearse, 2012), but the data do not contain information about a shallow magma body. The deformation signal of the shallow magma chamber could easily be hidden by the larger signal of the APMB (Sparks et al., 2008). The mineralogy observed in dacite samples from Volcan Uturuncu give evidence for the existence of a shallow magma chamber (de Silva and Gosnold, 2007). Petrological evidence for magma storage at shallow depths (4 - 10 km) has been seen at other volcanoes (e.g., Blundy and Cashman, 2005; Bachmann and Bergantz, 2008). Sparks et al. (2008) propose that dacite magmas derived from the APMB ascend periodically to form shallow magma bodies at depths of 4 - 8 km below surface throughout the APVC, and that these shallow magma bodies supply magma during eruptions. Furthermore, the authors suggest that the brittle-ductile transition zone is shallow below the APVC (5 km depth below surface, near sea-level) due to the thermal heating of the upper crust, which explains why the magma ascends and ponds at such shallow levels. Muir et al. (2014) identified a pre-eruptive magma storage location below Volcan Uturuncu at a depth of 2 - 6 km below surface from the geo-chemistry of erupted dacites, and similar shallow storage locations of silicic melts for other ignimbrites in the APVC

To date, the only geophysical evidence of a shallow magma chamber below Volcan Uturuncu has come from a small seismic ANT survey which imaged a low-velocity zone at 2 - 4 km depth

below surface (Jay et al., 2012) (see Section 7.6.4). The small low-velocity zone was also spatially correlated with earthquake hypocenters. In this study, both the 2D and 3D MT resistivity models show a shallow magma chamber at a depth of 3 - 7 km below surface, which correlates well with the position of the assumed shallow magma chamber, identified from previous petrological and seismic studies.

7.8.1 Volume of a Shallow Magma Chamber Below Volcan Uturuncu

The resistivity models produced in this study show a shallow magma chamber below Volcan Uturuncu (C4). In the 3-D inversion model, conductor C4 consists of a series of 2 or 3 dike-shaped conductors. The approximate dimensions for each of these conductors is: 6 km tall, 17 km long (East-West), and 5 km wide (North-South). This gives a volume of ~500 km^3 each, or 1000-1500 km^3 in total.

As was discussed in Section 2.4.1, the VEI scale is a logarithmic scale that measures eruption magnitude based (primarily) on the volume of ejecta erupted. A super-volcano is classified as having an ejected volume greater than 1000 km^3 in a single eruption (a VEI of 8), see Figure 2.5. The Tambora, Indonesia, eruption of April 1815 was the largest historical eruption with an estimated erupted ejecta of 100 km^3 (a VEI of 7) (Newhall and Self, 1982; Stothers, 1984). The Tambora eruption had a large global impact because it caused the mean temperature in the Northern Hemisphere to drop by as much as 0.7°C the following year (1816; known as "the year without a summer"), causing an agricultural disaster as crops failed and limited harvests led to widespread famine (Stothers, 1984).

The magma volume of the APMB is estimated to be ~60,000 km^3 (de Silva and Gosnold, 2007). Even if only 20% was eruptible (the fluid component of crystal-rich, mushy magma), this is more than enough to cause super-eruptions in the future, as has occurred across the APVC in the past 10 m.y., see Section 2.5. Assuming the intermediate depth conductors below Volcan Uturuncu are pre-eruptive magma storage chambers, the maximum volume of eruptible magma currently stored in the shallow crust below Volcan Uturuncu is 500-1500 km^3. This is enough to

cause an eruption with a VEI of 7.7-8.7, implying that Volcan Uturuncu may be a super-volcano. Volcan Uturuncu has had several eruptions with a VEI of 4-5 over the past 1 m.y., with the most recent pulse 0.27 Ma, and the largest pulse of activity from 0.6-0.5 Ma, which produced a cumulative ejecta volume of ~20 km^3 (Muir et al., 2015); see Section 2.5.2 and Figure 2.12. An eruption with a VEI of 4 (>0.1 km^3 of ejecta) is similar in size to the 2010 eruption of Eyjafjallajökull, Iceland, which shut down air-traffic for weeks, whereas an eruption with a VEI of 5 (>1 km^3 of ejecta) is similar in size to the 1980 eruption of Mt. St. Helens, USA.

It is possible that more super-eruptions will occur in the APVC from the APMB, as have occurred over the last 10 m.y., but when, or if, it will happen is unknown. Some researchers believe the APVC has entered a waning stage, possibly due to the deeper mantle source being shut off, and is expected to remain quiet for some time (e.g., Salisbury et al., 2010). Caricchi et al. (2014) showed that super-volcanoes can accumulate magma in the shallow crust for a 200,000-600,000 years before triggering a caldera-forming super-eruption. Volcan Uturuncu has the potential to create a super-eruption, and the ongoing inflation pattern, fumarolic activity near the summit, and active seismicity could be signs of future activity (Jay et al., 2012; Sparks et al., 2008). However, past single eruption events have not exceeded a VEI of 5, and Volcan Uturuncu has remained quiet since it last erupted 0.25 Ma.

7.9 Summary

The magnetotelluric data presented in Chapter 6 and interpreted in this chapter have provided images of the magma distribution beneath the APVC. The resistivity models show a deep, horizontally continuous conductive layer identified as the APMB, overlain with discrete zones of low resistivity that correspond to both past and present episodes of magmatism. In the upper crust, melt is confined to a set of dike-shaped zones, and aqueous fluids are required in addition to partial melt to explain the observed resistivity values. These shallow conductors may be shallow magma storage region below Volcan Uturuncu. The MT data give new constraints on the distribution of magma beneath Volcan Uturuncu and show that the APMB requires 15-45% andesitic melt. The top of the APMB appears to shallow beneath Volcan Uturuncu, with

potential pathways of low resistivity connecting the APMB to the surface below Volcan Uturuncu, and across the entire extent of the APMB. These represent both active magmatic systems and the hydrothermal alteration produced by past magmatic episodes. The resistivity structure of the entire east-west profile across the APMB shows the effects of both past and present magmatism.

A quantitative comparison with the seismic velocity model of Ward et al. (2014) shows a reasonable agreement between the geometry of zones of low velocity and low resistivity (i.e., the APMB and zones of partial melt). However, a difference in the depth to the top of the low-velocity zone and to the high-conductivity zone remains to be fully reconciled. One explanation is the resolution difference between the two geophysical imaging methods. The MT method detects small zones of melt ascending through the crust while the seismic method smears these into a continuous low-velocity zone. A second viable hypothesis is that the APMB is a layered magma body, with a silica-rich top layer or a water-rich lower layer. This would cause the MT method to see the top of a high-conductivity zone at a greater depth than the low-velocity zone seen by the seismic method.

Beneath the region of observed surface deformation (below Volcan Uturuncu), it can be seen that magma extends above the APMB and is inconsistent with some of the proposed inflation source geometries. Assuming a minimum melt fraction of 20% the APMB and the crust above it are estimated to have a maximum effective viscosity of 10^{14} - 10^{16} Pa·s. These values are in good agreement with the geodynamic model of Fialko and Pearse (2012) which proposed the diapir-like ascent of magma from the APMB towards the surface.

CHAPTER 8: SUMMARY AND CONCLUSIONS

8.1 Thesis Summary

The Andean subduction zone has developed since 45 Ma. (e.g., Cahill and Isacks, 1992; Capitanio et al., 2011). Uplift of the Altiplano-Puna plateau began later, about 25 Ma, and today it has an average elevation of more than 4000 m (Allmendinger et al., 1997). The crust of the Altiplano-Puna is very thick with an average of 65 km, and was formed by crustal shortening and magmatic addition (e.g., Isacks, 1988; Allmendinger et al., 1997; Beck et al., 1996). A steepening of the subducting slab 10 Ma caused an ignimbrite flare-up, creating the large ignimbrite complex of the APVC (Allmendinger et al., 1997; de Silva, 1989). Several of the eruptions caused by the ignimbrite flare-up had volumes of ejecta greater than 1,000 km^3, and so are classified as supervolcanoes (Salisbury et al., 2010). The large calderas observed at the surface and the geochemical analysis of the erupted ignimbrites give evidence for a large homogenous magma reservoir below the APVC at a depth of ~20 km below surface, with multiple shallow magma chambers located beneath individual calderas or volcanoes and which contains eruptible, evolved magma (e.g., de Silva and Gosnold, 2007; Sparks et al., 2008).

Geophysical studies have detected regions in the crust beneath the APVC with anomalous properties, including a low velocity zone (e.g., Chmielowski et al., 1999; Zandt et al., 2003), a zone of high seismic attenuation (e.g., Haberland et al., 2003), a high conductivity zone (e.g., Schwarz and Kruger, 1997; Brasse et al., 2002), anomalously high heat flow values (e.g., Henry and Pollack, 1988; Hamza et al., 2005), and a negative density anomaly (e.g., del Potro et al., 2013). Together, these anomalies give evidence for a major mid-crustal magma body, the Altiplano-Puna Magma Body (APMB), at a depth of 10-15 km below sea-level.

Geodetic data show a spatially broad (~75 km) and temporally continuous (decades long) deformation pattern centered on Volcan Uturuncu and coincident with the spatial extent of the APMB. This deformation pattern includes a central ring of uplift and an outer ring of subsidence

(Henderson and Pritchard, 2013). Geodynamic models explain the deformation pattern with an inflation source at depths of 15 - 20 km BSL (e.g., Pritchard and Simons, 2004). The geometry of the inflation source is not well constrained, but most estimates place it within the APMB. The question of the distribution of melt within the APMB and above it remains unconstrained, and more geophysical data are necessary to answer this question.

The MT method is a geophysical technique that uses temporal fluctuations of electric and magnetic fields measured at the Earth's surface in order to determine the spatial variations of the electrical resistivity within the Earth. The electrical resistivity is sensitive to the presence of fluids and magma and therefore the MT method is useful to identify magma bodies in the Earth because it maps subsurface electrical resistivity (e.g., Unsworth and Rondenay, 2012; Nover, 2005),

Broadband (300 Hz - 3,000 s) MT data were collected across the APVC in Bolivia and Northern Argentina from 2011-2013. Owing to the lack of cultural noise in the remote study area, the data are of high-quality. Three distinct types of apparent resistivity curves were identified from the MT data. Type 1 apparent resistivity curves were seen throughout most of the study area and showed a large, strong conductor at a period of 300 s (a depth of 15-20 km BSL) which was interpreted to be the APMB. Type 2 curves were seen locally beneath Volcan Uturuncu and showed a second prominent conductor at a period of 20 s (a depth near sea-level), and this was interpreted to be a shallow magma storage area. Type 3 curves were seen only near the edges of the study and were essentially flat, showing no prominent conductors, which indicates the absence of a deep conductor (i.e. the APMB) at the edges of the study area and helps define its spatial extent.

Dimensionality analysis from tensor decomposition, the alignment of the induction vectors, and phase tensor angles all indicated that the MT data could be fit with a 2-D resistivity model using a geo-electric strike direction of N30°E for the western region (Bolivia) and N0°E for the eastern region (Argentina). However significant 3-D effects (e.g., high Bahr Skew, high phase tensor skew) were observed at several stations, mostly near Volcan Uturuncu and Volcan Quetena. This

implies that the structure is at least partially 3-D near Volcan Uturuncu and gave motivation for a 3-D resistivity model around Uturuncu.

Both 2-D and 3-D resistivity models of the MT data were presented. The 2-D resistivity model along Profile 1 (r.m.s. misfit of 1.49; algorithm of Rodi and Mackie, 2001) shows the regional resistivity structure below the APVC. The 3-D resistivity model on a network around Volcan Uturuncu (S73, r.m.s. misfit of 0.95; algorithm of Siripunvaraporn et al., 2005) shows the local resistivity structure below volcano. These r.m.s. misfit values indicate an acceptable fit to the measured MT data. Many combinations of inversion parameters were investigated for both inversions. However, the main resistivity features were found to not depend on any specific choice of inversion parameters, indicating that the main resistivity features are required by the MT data. The model resolution was investigated with synthetic inversions, which showed that the main resistivity features are resolvable.

The resistivity models derived from the MT data show a deep, horizontally continuous conductive layer that was identified as the APMB at a depth of 10-20 km. Near sea-level a set of dike-shaped conductors are imaged beneath Volcan Uturuncu. These shallow conductors may represent a shallow magma storage region below Uturuncu. The MT data show that the APMB requires 15-45% andesitic melt. The top of the APMB appears to bulge upwards and shallows beneath Volcan Uturuncu, with potential pathways of low resistivity connecting the APMB to the surface below Volcan Uturuncu, and across the entire extent of the APMB. The shallow set of conductors below Volcan Uturuncu require aqueous fluids in addition to partial melt to explain the observed resistivity values, and therefore may also have a hydrothermal origin.

A quantitative comparison and correlation between the 3-D resistivity model and the seismic velocity model of Ward et al. (2014) shows a good agreement between the geometry of the zones of low velocity and low resistivity, which are each interpreted as being caused by the partial melts of the APMB. The depth to the top of the APMB as determined by the two geophysical methods is fairly consistent, however some small discrepancies exist. One explanation is the resolution difference between the two geophysical imaging methods. A second hypothesis is that the APMB is a layered magma body, with a silica-rich upper layer. This would cause the MT

method to image the top of a high-conductivity zone at a greater depth than the low-velocity zone seen by the seismic method. Forward modeling of MT responses and synthetic inversions show that this hypothesis is probable and can be resolved within error by MT data.

Volcan Uturuncu is surrounded by a ring of inflation. The resistivity models show that magma extends above the APMB towards the surface. This is inconsistent with some of the proposed inflation source geometries, while it is consistent with others. Fialko and Pearse (2012) proposed diapiric ascent of magma through the crust from the APMB and modelled the APMB with a viscosity of 10^{16} Pa·s. Using the relation of Pommier et al. (2013), composition values and temperatures provided by Sparks et al (2008), and the resistivities from the MT data, the viscosity of the pure melt in the APMB is estimated to be ~10^{6} Pa·s. Accounting for crystal fraction with the relations of Costa (2005) and Caricchi et al. (2007) the viscosity of 20% partial melt in the APMB and above it is calculated to be 10^{14}-10^{16} Pa·s. These viscosity values are consistent with the geodynamic model of Fialko and Pearse (2012) which proposed that a diapir forming at the surface of the APMB with a viscosity of 10^{16}-10^{18} Pa·s could explain the inflation source below Volcan Uturuncu and the ascent of magma towards the surface.

8.2 Conclusions

The MT data collected as part of this thesis represent the first large-scale, high-resolution, broadband MT study of the Altiplano-Puna plateau and the only MT study of Volcan Uturuncu to date. The goal of this thesis was to image the APMB below the APVC and the magmatic system beneath Volcan Uturuncu. A number of conclusions have come from this work and a short list is given below.

1. The depth to the top of APMB as determined from the 3-D electrical resistivity model derived from MT data is 14 +1/-3 km BSL (16-20 km below surface; for the 3 Ωm resistivity contour). The thickness of the APMB is not constrained by the MT data. However, the APMB has a very high conductance (~30,000 S) and if the APMB is assumed to have a minimum resistivity of 0.1-0.3 Ωm, this gives a minimum thickness of 3-10 km.

2. The existence of shallow (2-7 km below surface) magma storage region below Volcan Uturuncu, as inferred by petrological studies (Sparks et al., 2008; Muir et al., 2014) has been verified with MT resistivity models which show a conductor (~5 Ωm) at that location. A set of three parallel dyke-like bodies oriented approximately east-west and separated by ~10 km are imaged with the MT data.

3. The spatial extent of the APMB has been defined with the regional resistivity model of Profile 1. The western edge is near Laguna Colorado in Bolivia (longitude of ~67.7°W, ~55 km west of Uturuncu), and the eastern edge is near Mungayoc in North-Western Argentina (longitude of ~66.2°W, ~130 km east of Uturuncu), giving an east-west extent of ~170 km. MT data near Soniquera (latitude of ~21.9°S, ~50 km North of Uturuncu), within the deformation zone of Volcan Uturuncu, show only a weak conductor, implying this is the northern edge of the APMB. The southern edge of the APMB is not well constrained with the MT station coverage but is believed to extend to the Bolivia-Chile border (latitude of ~22.8°S, ~60 km south of Uturuncu).

4. The geometry of the upper surface of the APMB is undulating with an upwards bulge beneath Volcan Uturuncu where it is shallowest. Pathways of low resistivity connecting the APMB to the surface below Volcan Uturuncu and across the entire extent of the APMB are imaged with MT data.

5. The APMB requires 15-45% andesitic melt to explain the observed resistivity values. The shallow conductor below Volcan Uturuncu cannot be explained with dacitic melt alone, but requires the addition of saline aqueous fluids to explain the observed resistivity values, hinting at a possible hydrothermal origin.

6. Correlation of conductors and volcano-tectonic earthquakes below Volcan Uturuncu supports the interpretation of fluid or magma migration through the crust (e.g., as dike propagation) and the injection of new magma from a deeper source below.

7. Synthetic modeling shows that MT data can distinguish between a uniform and a layered magma body. A layered magma body which has a more resistive, silica-rich upper layer would cause the MT method to see the top of a high-conductivity zone (i.e., the APMB) at a greater depth than the low-velocity zone of seismic methods.

8. The viscosity of the APMB for 20% partial melt is calculated to be less than 10^{16} Pa·s. This viscosity is consistent with the geodynamic model of Fialko and Pearse (2012) which proposed that a diapir could be rising from the APMB.

8.3 Future Work

Several tasks have been identified for future work on this project, and a short list is included below.

1. A 3-D inversion with a finer grid and the inclusion of more MT stations is now possible with faster 3-D MT inversion algorithms, such as MODEM (Kelbert et al., 2014). MODEM also has the advantage that it can include topography. Preliminary models have been run with this algorithm, and show similar features to those presented in this thesis.

2. A detailed comparison of the resistivity models of the APVC and Uturuncu with those of the Puna and Lazufre from Unsworth et al. (Manuscript in preparation) will shed light on the differences between these two regions. The Lazufre volcanic region shows a similar (albeit smaller) pattern of deformation as Uturuncu.

3. A joint inversion of the seismic velocity data of Ward et al. (2014) and the MT data collected as part of this thesis remains to be done. As shown in this thesis, the data correlate well and show the same main features (i.e., the APMB), but have some minor differences, which remain to be resolved.

3. Collect more MT data at a few locations. (1) On the southern line (Profile 2) from Totoral to Loromayu to Vilama where the current MT stations stray from the profile direction so that a better comparison with Profile 1 can be made. (2) A new profile from Laguna Verde to Zapaleri in order to better define the southern extent of the APMB. (3) On the volcano edifice in the NE and the WNW quadrants to better define the shallow conductors below Volcan Uturuncu. (4) A denser grid of MT station around Volcan Quetena to better understand its link to Volcan Uturuncu.

WORKS CITED

Aizawa, K., Ogawa, Y., Mishina, M., Takahashi, K., Nagaoka, S., Takagi, N., Sakanaka, S., Miura, T., 2009, Structural controls on the 1998 volcanic unrest at Iwate volcano: Relationship between a shallow, electrically resistive body and the possible ascent route of magmatic flui, Journal of Volcanology and Geothermal Research, v. 187, p. 131–139.

Allen, J.H., 1982, Some Commonly Used Magnetic Activity Indices: Their Derivation, Meaning, and Use, in Proceedings of a Workshop on Satellite Drag, March 18 1982, Boulder, Colorado, p 114-134.

Allmendinger, R.W., and Gubbels, T., 1996, Pure and simple shear plateau uplift, Altiplano - Puna, Argentina and Bolivia, Tectonophysics, v. 259, p. 1-13.

Allmendinger, R.W., Jordan, T.E., Kay, S.M., Isacks, B.L., 1997, The evolution of the Altiplano-Puna plateau of the Central Andes, Annual Review of Earth and Planetary Sciences, v. 25, p. 139-174.

Allmendinger, R.W., Smalley, R., Bevis, M., Caprio, H., Books, B., 2005, Bending the Bolivian orocline in real time, Geology, v. 33, p. 905-908.

ANCORP working group, 2003, Seismic imaging of a convergent continental margin and plateau in the Central Andes (Andean Continental Research Project 1996 – ANCORP'96), Journal of Geophysical Research, v. 108, p. 2328.

Annen, C., Blundy, J.D., Sparks, R.S.J., 2006, The genesis of intermediate and silicic magmas in deep crustal hot zones, Journal of Petrology, v. 47, p. 505–539.

Aranovich, L.Y., Newton, R.C., Manning, C.E., 2013, Brine-assisted anatexis: Experimental melting in the system haplogranite–H2O–NaCl–KCl at deep-crustal conditions, Earth and Planetary Science Letters, v. 374, p. 111–120.

Archie, G.E., 1942, The electrical resistivity log as an aid in determining some reservoir characteristics, Transactions of the American Institute of Mining and Metallurgical Engineers, v. 146, p. 54-62.

Arriagada, C., Roperch, P., Mpodozis, C., Cobbold, P.R., 2008, Paleogene building of the Bolivian Orocline: Tectonic restoration of the central Andes in 2-D map view, Tectonics, v. 27.

Babeyko, A.Y., Sobolev, S.V., Trumbull, R.B., Oncken, O., Lavier, L.L., 2002, Numerical models of crustal scale convection and partial melting beneath the Altiplano-Puna plateau, Earth and Planetary Science Letters, v. 199, p. 373-388.

Bachmann, O., and Bergantz, G.W., 2004, On the origin of crystal-poor rhyolites: extracted from batholithic crystal mushes, Journal of Petrology, v. 45, p. 1565-1582.

Bachmann O., Miller C.F., de Silva, S.L., 2007, The volcanic-plutonic connection as a stage for understanding crustal magmatism, Journal of Volcanology and Geothermal Research, v. 167, p. 1– 23.

Bachmann, O., and Bergantz, G., 2008, The magma reservoirs that feed supereruptions, Elements, v. 4, p. 17-21.

Bahr, K., 1988, Interpretation of the magnetotelluric impedance tensor: regional induction and local telluric distortion, Journal of Geophysics, v. 62, p. 119-127.

Bahr, K., 1991, Geological noise in magnetotelluric data: a classification of distortion types, Physics of the Earth and Planetary Interiors, v. 66, p. 24-38.

Balch, R.S., Hartse, H.E., Sanford, A.R., Lin, K., 1997, A new map of the geographic extent of the Socorro mid-crustal magma body, Bulletin of the Seismological Society of America, v. 87, p. 174-182.

Bartels, J., Heck, N.H., Johnston, H.F., 1939, The three-hour range index measuring geomagnetic activity, Journal of Geophysical Research, v. 44, p. 411–454.

Bass, J.D., 1995, Elasticity of minerals, glasses, and melts, in Ahrens, T.J., ed., *Mineral Physics and Crystallography: A Handbook of Physical Constants*, American Geophysical Union, Washington, DC, p. 45–63.

Battaglia, M., Roberts, C., Segall, P., 1999, Magma intrusion beneath Long Valley caldera confirmed by temporal changes in gravity, Science, v. 285, p. 2119-2122.

Beck, S. L., and Zandt, G., 2002, The nature of orogenic crust in the central Andes, Journal of Geophysical Research, v. 107, p. 1-6.

Beck, S., Zandt, G., Myers, S.C., Wallace, T.C., Silver, P.G., Drake, L., 1996, Crustal-thickness variations in the central Andes, Geology, v. 24, p. 407-410.

Beck, S.L., Zandt, G., Ward, K.M, Scire, A., 2014, Multiple styles and scales of lithospheric foundering beneath the Puna Plateau, central Andes, in DeCelles, P.G., et al., eds., *Geodynamics of a Cordilleran orogenic system: The Central Andes of Argentina and northern Chile*, Geological Society of America Memoir 212.

Bedrosian, P.A., Unsworth, M.J., Egbert, G.D., Thurber, C.H., 2004, Geophysical images of the creeping segment of the San Andreas fault: Implications for the role of crustal fluids in the earthquake process, Tectonophysics, v. 385, p. 137–158.

Bedrosian, P.A., Maercklin, N., Weckmann, U., Bartov, Y., Ryberg, T., Ritter, O., 2007, Lithology-derived structure classifi cation from the joint interpretation of magnetotelluric and seismic models, Geophysical Journal International, v. 170, p. 737–748.

Bertrand, E. A., Caldwell, T. G., Hill, G. J., Wallin, E. L., Bennie, S. L., Cozens, N., Onacha, S.A., Ryan, G.A., Walter, C, Zaino, A., Wameyo, P., 2012, Magnetotelluric imaging of upper-crustal convection plumes beneath the Taupo Volcanic Zone, New Zealand, Geophysical Research Letters, v. 39.

Bibby, H.M., Risk, G.F., Caldwell, T.G., Bennie, S.L., 2005, Misinterpretation of Electrical Resistivity Data in Geothermal Prospecting: a Case Study from the Taupo Volcanic Zone, in Geological and Nuclear Sciences, World Geothermal Congress, Antalya, Turkey, p. 1-8.

Bibby, H. M., Caldwell, T. G., Brown, C., 2005b, Determinable and non-determinable parameters of galvanic distortion in magnetotellurics, Geophysical Journal International, v. 163, p. 915–930.

Blundy, J., and Cashman, K., 2005, Rapid decompression-driven crystallization recorded by melt inclusions from Mount St. Helens volcano, Geology, v. 33, p. 793-796.

Boehl, J.E., Bostick F.X., Smith H.W., 1977, An application of the Hilbert transform to the magnetotelluric method, National Science Foundation Report, University of Texas, Austin, p. 1-98.

Booker, J., 2014, The Magnetotelluric Phase Tensor: A Critical Review, Surveys in Geophysics, v. 35, p. 7-40.

Botcharnikov, R.E., Behrens, H., Holtz, F., 2006, Solubility and speciation of C–O–H fluid in andesitic melt at T=1100−1300°C and P=200 and 500 MPa. Chemical Geology, v. 229, p. 125–143.

Bottinga, Y., and Weill, D.F., 1970, Densities of liquid silicate systems calculated from partial molar volumes of oxide components, American Journal of Science, v. 269, p. 169-182.

Brasse, H., and Eydam, D., 2008, Electrical conductivity beneath the Bolivian Orocline and its relation to subduction processes at the South American continental margin, Journal of Geophysical Research, v. 113.

Brasse, H., Lezaeta, P., Rath, V., Schwalenberg, K., Soyer, W., Haak, V., 2002, The Bolivian Altiplano Conductivity Anomaly, Journal of Geophysical Research, v. 107.

Brown, M., 2013, Granite: From genesis to emplacement, GSA Bulletin, v. 125, p. 1–79.

Cagniard, L., 1953, Basic theory of the magnetotelluric method of geophysical prospecting, Geophysics, v. 18, p. 605-635.

Cahill, T., and Isacks, B.L., 1992, Seismicity and shape of the subducted Nazca Plate, Journal of Geophysical Research, v. 97, p. 17503-17529.

Caldwell, T.G., Bibby, H.M., Brown, C., 2004, The magnetotelluric phase tensor, Geophysical Journal International, v. 158, p. 457–469.

Canavan, R.R., Carrapa, B., Clementz, M.T., Quade, J., DeCelles, P., Schoenbohm, L.M., 2014, Early Cenozoic uplift of the Puna Plateau, central Andes, based on stable isotope paleoaltimetry of hydrated volcanic glass, Geology, v. 42, p. 447–450.

Capitanio, F.A., Faccenna, C., Zlotnik, S., Stegman, D.R., 2011, Subduction dynamics and the origin of Andean orogeny and the Bolivian orocline, Nature, v. 480, p. 83-86.

Caricchi, L., Annen, C., Blundy, J., Simpson, G., Pinel, V., 2014, Frequency and magnitude of volcanic eruptions controlled by magma injection and buoyancy, Nature Geoscience, v. 7, p. 126-130.

Caricchi, L., Burlini, L., Ulmer, P., Gerya, T., Vassalli, M., Papale, P., 2007, Non-Newtonian rheology of crystal-bearing magmas and implications for magma ascent dynamics, Earth and Planetary Science Letters, v. 264, p. 402–419.

Chave, A. D., J. T. Smith, 1994, On Electric and Magnetic Galvanic Distortion Tensor Decompositions, Journal of Geophysical Research, v. 99, p. 4669-4682.

Chave, A.D., and Jones, A.G., eds., 2012, *The Magnetotelluric Method: Theory and Practice,* Cambridge University Press, Cambridge, 552 pp.

Chmielowski, J., Zandt, G., Haberland, C., 1999, The Central Andean Altiplano-Puna Magma Body, Geophysical Research Letters, v. 26, p. 783–786.

Chu, R., Helmberger, D.V., Sun, D., Jackson, J.M., Zhu, L., 2010, Mushy magma beneath Yellowstone, , Geophysical Research Letters, v. 37.

Clark, M.K., and Royden, L.H., 2000. Topographic ooze; building the eastern margin of Tibet by lower crustal flow, Geology, v. 28, p. 703–706.

Coira, B., Kay, S.M., Viramonte, J., 1993, Upper Cenozoic magmatic evolution of the Argentine Puna - A model for changing subduction geometry, International Geology Review, v. 35, p. 677-720.

Comeau, M.J., Unsworth, M.J., Ticona, F., Sunagua, M., 2015, Magnetotelluric images of magma distribution beneath Volcán Uturuncu, Bolivia: implications for magma dynamics, Geology, v. 43, p. 243–246.

Comeau, M.J., and Unsworth, M.J., 2015b, New constraints on magma distribution beneath Volcan Uturuncu, Bolivia, from magnetotelluric data, Geosphere, Manuscript submitted for publication.

Constable, S.C., Parker, R.L., Constable, C.G., 1987, Occam's inversion: A practical algorithm for generating smooth models from EM sounding data, Geophysics, v. 52, p. 289-300.

Cordani, U.G., D'Agrella-Filho, M.S., Brito Neves, B.B., Trindade, R.I.F., 2003, Tearing up Rodinia: the Neoproterozoic palaeogeography of South American cratonic fragments, Terra Nova, v. 15, p. 350-359.

Costa, A., 2005, Viscosity of high crystal content melts: Dependence on solid fraction, Geophysical Research Letters, v. 32.

Costa, A., Caricchi, L., Bagdassarov, N., 2009, A model for the rheology of particle-bearing suspensions and partially molten rocks, Geochemistry, Geophysics, Geosystems, v. 10.

Currie, C., Beaumont, C., Huismans, R., 2007, The fate of subducted sediments: A case for backarc intrusion and underplating, Geology, v. 35, p. 1111-1114.

Dahren, B., Troll, V., Andersson, U., Chadwick, J., Gardner, M., Jaxybulatov, K., Koulakov, I., 2012, Magma plumbing beneath Anak Krakatau volcano, Indonesia: evidence for multiple magma storage regions, Contributions to Mineralogy and Petrology, v. 163, p. 631–651.

de Silva, S.L., 1989, Altiplano-Puna volcanic complex of the Central Andes, Geology, v. 17, p. 1102–1106.

de Silva, S., and Francis, P.W., 1991, *Volcanoes of the Central Andes*, Springer, 216 pp.

de Silva, S.L., Zandt G., Trumbull R., Viramonte J., Salas G., Jimenez N., 2006, Large-scale silicic volcanism in the Central Andes—A tectonomagmatic phenomenon, in de Natale G., Troise C., Kilburn C., eds*., Mechanisms of activity and unrests at large calderas*, Geological Society of London Special Publication, v. 269, p. 47– 64.

de Silva S.L., and Gosnold W.A., 2007, Episodic construction of batholiths: Insights from the spatiotemporal development of an ignimbrite flare-up, Journal of Volcanology and Geothermal Research, v. 167, p. 320– 335.

DeCelles, P.G., Ducea, M.N., Kapp, P., Zandt, G., 2009, Cyclicity in Cordilleran orogenic systems, Nature Geoscience, v. 2, p. 251-257.

DeCelles, P.G., Zandt, G., Beck, S.L., Currie, C.A., Ducea, M.N., Kapp, P., Gehrels, G.E., Carrapa, B., Quade, J., Schoenbohm, L.M., 2015, Cyclical orogenic processes in the Cenozoic central Andes, Geological Society of America Memoirs, v. 212.

del Potro, R., Díez, M., Blundy, J., Camacho, A., Gottsmann, J., 2013, Diapiric ascent of silicic magma beneath the Bolivian Altiplano, Geophysical Research Letters, v. 40, p. 2044–2048.

del Potro, R., Diez, M., Muller, C., Perkins, J. P., Finnegan, N. J., Gottsmann, J., 2013b, Long-lived large-scale ground deformation caused by a buoyantly rising magma reservoir (abstract #V51E-2742), American Geophysical Union, Fall Meeting, San Francisco, CA.

Dingwell, D.B., 2006, Transport properties of magmas: Diffusion and rheology, Elements, v. 2, p. 281–286.

Dingwell, D.B., and Hess, K.U., 1998, Melt viscosities in the system Na–Fe–Si–O–F–Cl; Contrasting effects of F and Cl in alkaline melts, American Mineralogist, v. 83, p. 1016–1021.

Ducea M., 2001, The California Arc: Thick granitic batholiths, eclogitic residues, lithospheric-scale thrusting, and magmatic flare-ups, GSA Today, v. 11, p. 4– 10.

Ducea, M.N., Seclaman, A.C., Murray, K.E., Juanu D., Schoenbohm, L.M., 2013, Mantle-drip magmatism beneath the Altiplano-Puna plateau, central Andes, Geology, v. 41, p. 915-918.

Duffy, J.A., and Ingram, M.D., 1975, Optical basicity—IV: Influence of electronegativity on the Lewis basicity and solvent properties of molten oxyanion salts and glasses, Journal of Inorganic and Nuclear Chemistry, v. 37, p. 1203–1206.

Dvorak, J., and Dzurisin, D., 1997, Volcano geodesy: the search for magma reservoirs and the formation of eruptive vents, Reviews of Geophysics, v. 35, p. 343-384.

Dvorkin, J.P., 2008, Yet another Vs equation, Geophysics, v. 73.

Dzurisin, D., 2003, A comprehensive approach to monitoring volcano deformation as a window on the eruption cycle, Reviews of Geophysics, v. 41.

Egbert, G.D., and Booker, J.R., 1986, Robust estimation of geomagnetic transfer functions, Geophysical Journal of the Royal Astronomical Society, v. 87, p. 173-194.

Einstein, A., 1906, Eine neue Bestimmung der Molekuldimensionen (A New Determination of Molecular Dimensions), Annalen der Physik, v. 19, p. 289–306.

Elsworth, D., Mattioli, G., Taron, J., Voight, B., Herd R., 2008, Implications of Magma Transfer Between Multiple Reservoirs on Eruption Cycling, Science, v. 322.

Evans, J.R., 1982, Compressional wave velocity structure of the upper 350 km under the eastern Snake River Plain near Rexburg, Idaho, Journal of Geophysical Research, v. 87, p. 2654–2670.

Evans, R., 2012, Earth's electromagnetic environment, in Chave, D.C., and Jones, A.G., eds., *The Magnetotelluric Method, Theory and Practice*, Cambridge University Press, Cambridge, p. 50–121.

Farrell, J., Smith, R.B., Husen, S., Diehl, T., 2014, Tomography from 26 years of seismicity revealing that the spatial extent of the Yellowstone crustal magma reservoir extends well beyond the Yellowstone caldera, Geophysical Research Letters, v. 41, p. 3068–3073.

Feigl, K., Le Mevell, H., Tabrez, A., Cordova, L., Andersen, N., DeMets, C., Singer, B., 2014, Rapid uplift in Laguna del Maule volcanic field of the Andean Southern Volcanic zone (Chile) 2007–2012, Geophysics Journal International, v. 196, p. 885-901.

Fialko, Y., and Simons, M., 2001, Evidence for on-going inflation of the Socorro magma body, New Mexico, from interferometric synthetic aperture radar imaging, Geophysical Research Letters, v. 28, p. 3549–3552.

Fialko, Y., and Pearse, J., 2012, Sombrero Uplift Above the Altiplano-Puna Magma Body: Evidence of a Ballooning Mid-Crustal Diapir, Science, v. 338, p. 250–252.

Francis, P.W., and Hawkesworth, C.J., 1994, Late Cenozoic rates of magmatic activity in the central Andes and their relationship to continental crust formation and thickening, Journal of the Geological Society of London, v. 151, p. 845-854.

Gaillard, F., 2004, Laboratory measurements of electrical conductivity of hydrous and dry silicic melts under pressure, Earth and Planetary Science Letters, v. 218, p. 215–228.

Gamble, T.B., Goubau, W.M., Clarke, J., 1979, Magnetotellurics with a remote reference, Geophysics, v. 44, p. 53-68.

Garzione, C., Hoke, G., Libarkin, J., Withers, S., 2008, Rise of the Andes, Science, v. 320, p. 1304–1307.

Giese, P., and Schilling, F.R., 2000, Some consequences from the temperature-heat-paradox in the Altiplano (Central Andes), EOS Transactions of the American Geophysical Union, v. 81.

Gill, J. B., 1981, *Orogenic Andesites and Plate Tectonics*, Springer-Verlag, New York, 390 pp.

Giordano, D., Russell, J.K., Dingwell, D.B., 2008, Viscosity of magmatic liquids: A model, Earth and Planetary Science Letters, v. 271, p. 123–134.

Glover, P., Hole, M.J., Pous, J., 2000, A modified Archie's Law for two conducting phases, Earth and Planetary Science Letters, v. 180, p. 369-383.

Götze, H.J., and Kirchner, A., 1997, Interpretation of Gravity and Geoid in the Central Andes between 20° and 29°S, Journal of South American Earth Sciences, v. 10, p. 179–188.

Götze, H.J., and Krause, S., 2002, The Central Andean Gravity High, a relic of an old subduction complex?, Journal of South American Earth Sciences, v. 14, p. 799–811.

Goubau. W.M., Gamble., T.D., Clarke., J., 1979, Magnetotelluric data analysis: removal of bias, Geophysics, v. 43, p. 1157-1169.

Gregory-Wodzicki, K.M., 2000, Uplift history of the Central and Northern Andes: a review, GSA Bulletin, v. 112, p. 1091-1105.

Griffiths, D.J., 1999, *Introduction to Electrodynamics*, 3 rd Edition, Prentice Hall, New Jersey, 576 pp.

Groom, R., and Bailey, R., 1989, Decomposition of Magnetotelluric Impedance Tensors in the Presence of Local Three-Dimensional Galvanic Distortion, Journal of Geophysical Research, v. 94, p. 1913-1925.

Gutscher, M.A., Sparkman, W., Bijwaard, H., Engdahl, E.R., 2000, Geodynamics of flat subduction: Seismicity and tomographic constraints from the Andean margin, Tectonics, v. 19, p. 814-833.

Haberland, C., Rietbrock, A., Schurr, B., Brasse, H., 2003, Coincident anomalies of seismic attenuation and electrical resistivity beneath the southern Bolivian Altiplano plateau, Geophysical Research Letters, v. 30.

Hamza, V.M., and Munoz, M., 1996, Heat Flow map of South America, Geothermics, v. 25, p. 599-646.

Hamza, V., Silva, D., Gomes, A., Terceros, Z., 2005, Numerical and functional representation of regional heat flow in South America, Physics of the Earth and Planetary Interiors, v. 152, p. 223-256.

Haschke, M.R., Scheuber, E. Gunther, A., Reutter, K.J., 2002, Evolutionary cycles during the Andean orogeny: repeated slab breakoff and flat subduction?, Terra Nova, v. 14, p. 49-55.

Hashim, L., Gaillard, F., Champallier, R., Le Breton, N., Arbaret, L., Scaille, B., 2013, Experimental assessment of the relationships between electrical resistivity, crustal melting and strain localization beneath the Himalayan–Tibetan Belt, Earth and Planetary Science Letters, v. 373, p. 20-30.

Hashin, Z., and Shtrikman, S., 1962, A variational approach to the elastic behavior of multiphase minerals, Journal of the Mechanics and Physics of Solids, v. 11 , p. 127-140.

Heise, W., and Pous, J., 2001, Effects of anisotropy on the two-dimensional inversion procedure, Geophysical Journal International, v. 147, p. 610-621.

Heise, W., and Pous, J., 2003, Anomalous phases exceeding 90^{o} in magnetotellurics: anisotropic model studies and a field example, Geophysical Journal International, v. 155, p. 308-318.

Heise, W., Caldwell, T.G., Bibby, H.M., Brown, C., 2006, Anisotropy and phase splits in magnetotellurics, Physics of the Earth and Planetary Interiors, v. 158, p. 107-121.

Heit, B., Koulakov, G., Asch, G., Yuan, X., Kind, R., Alcocer-Rodriguez, I., Tawackoli, S., Wilke, H., 2008, More constraints to determine the seismic structure beneath the Central Andes at 21°S using teleseismic tomography analysis, Journal of South American Earth Sciences, v. 25, p. 22–36

Henderson, S.T., and Pritchard, M.E., 2013, Decadal volcanic deformation in the Central Andes Volcanic Zone revealed by InSAR time series, Geochemistry, Geophysics, Geosystems, v. 14, p. 1358-1374.

Henry, S., and Pollack, H., 1988, Terrestrial heat flow above the Andean Subduction Zone in Bolivia and Peru, Journal of Geophysical Research, v. 93, p. 15153–15162.

Hermance, J.F., 1979, The electrical conductivity of materials containing partial melt: a simple model from Archie's Law, Geophysical Research Letters, v. 6, p. 613-616.

Hermance, J.F., and Neumann, G.A., 1990, The Rio Gradne Rift, New electromagnetic constraints on the Socorro magma body, Physics of the Earth and Planetary Interiors, v. 66, p. 101-117.

Hickey, J., Gottsmann, J., del Potro, R., 2013, The large-scale surface uplift in the Altiplano-Puna region of Bolivia: A parametric study of source characteristics and crustal rheology using finite element analysis, Geochemistry, Geophysics, Geosystems, v. 14, p. 540-555.

Hildreth, W., 1981, Gradients in silicic magma chambers: implications for lithospheric magmatism, Journal of Geophysical Research, v. 86, p. 10153–10192.

Hildreth, W., and Moorbath, S., 1988, Crustal contributions to arc magmatism in the Andes of central Chile, Contributions to Mineralogy and Petrology, v. 98, p. 455– 48.

Hill, D.P., and Prejean, S., 2005, Magmatic unrest beneath Mammoth Mountain, California, Journal of Volcanology and Geothermal Research, v. 146, p. 257-283.

Hill, G.J., Caldwell, T.G., Heise, W., Chertkoff, D.G., Bibby, H.M., Burgess, M.K., Cull, J.P., Cas, R.A.F., 2009, Distribution of melt beneath Mount St Helens and Mount Adams inferred from magnetotelluric data, Nature Geoscience, v. 2, p. 785-789.

Huang, H., Lin, F., Schmandt, B., Farrell, J., Smith, R., Tsai, V.C., 2015, The Yellowstone magmatic system from the mantle plume to the upper crust, Science, v. 348, p. 773-776.

Humphreys, E., Hessler, E., Dueker, K., Farmer, G., Erslev, E., Atwater, T., 2003, How Laramide-Age Hydration of North American Lithosphere by the Farallon Slab Controlled Subsequent Activity in the Western United States, International Geology Review, v. 45, p. 575–595.

Ingham, M. R., Bibby, H. M., Heise, W., Jones, K. A., Cairns, P., Dravitzki, S., Bennie, S. L., Caldwell, T. G., Ogawa, Y., 2009, A magnetotelluric study of Mount Ruapehu volcano, New Zealand. Geophysical Journal International, v. 179, p. 887–904.

Isacks, B.L., 1988, Uplift of the Central Andean Plateau and Bending of the Bolivian Orocline, Journal of Geophysical Research, v. 93, p 3211.

Isherwood, W.F., 1976, Gravity and magnetic studies of The Geysers- Clear Lake geothermal region, California, in Proceedings of the Second United Nations Symposium on the Development and Use of Geothermal Resources, v. 2, p. 1065-1073.

Iyer, H.M., 1984, Geophysical Evidence for the Locations, Shapes and Sizes, and Internal Structures of Magma Chambers beneath Regions of Quaternary Volcanism, Philosophical Transactions of the Royal Society of London A, v.310, p. 473-510.

Jay, J.A., Pritchard, M.E., West, M.E., Christensen, D.H., Haney, M., Minaya, E., Sunagua, M., McNutt, S.R., Zabala, M., 2012, Shallow seismicity, triggered seismicity, and ambient noise tomography at the long-dormant Uturuncu volcano, Bolivia, Bulletin of Volcanology, v. 74, p. 817–837.

Jiracek, G.R., Rodi, W.L., Vanyan, L.L., 1987, Implications of magnetotelluric modeling on the deep crustal environment in the Rio Grande rift, Physics of the Earth and Planetary Interiors, v. 45, p. 179-192.

Jiracek, G.R., 1990, Near-surface and topographic distortions in electromagnetic induction, Surveys in Geophysics, v. 11, p. 163-203.

Jones, F. W., and Price, A.T., 1970, The perturbations of alternating geomagnetic fields by conductivity anomalies, Geophysical Journal of the Royal Astronomical Society, v. 20, p. 317-334.

Jones, A., 1988, Static shift of MT data and it's removal in a sedimentary basin environment, Geophysics, v. 53, p. 967-978.

Jones, A.G., and Groom, R.W., 1993, Strike-angle determination from the magnetotelluric impedance tensor in the presence of noise and local distortion: rotate at your peril!, Journal of Geophysical Research, v. 113, p. 524-534.

Kauahikaua, J., Hildenbrand, T., Webring, M., 2000, Deep magmatic structures of Hawaiian volcanoes, imaged by three-dimensional gravity models, Geology, v. 28, p. 883–886.

Kay, S. M., Coira, B., Viramonte J., 1994, Young mafic back arc volcanic-rocks as indicators of continental lithospheric delamination beneath the Argentine Puna Plateau, Central andes, Journal of Geophysical Research, v. 99, p 24323.

Kay, S.M., and Mpodozis, C., 2001, Central Andean ore deposits linked to evolving shallow subduction systems and thickening crust, GSA Today, v. 11, p. 4-9.

Kay, S.M., Coira, B.L., Caffe, P.J., Chen, C.H., 2010, Regional chemical diversity, crustal and mantle sources and evolution of central Andean Puna plateau ignimbrites, Journal of Volcanology and Geothermal Resources, v. 198, p. 81–111.

Kelbert, A., Meqbel. N., Egbert, G.D., Tandon, K., 2014, ModEM: A modular system for inversion of electromagnetic geophysical data, Computers and Geosciences, v. 66, p. 40-53.

King, P.L., and Holloway, J.R., 2002, CO2 solubility and speciation in intermediate (andesitic) melts: the role of H2O and composition, Geochimica et Cosmochimica Acta, v. 66, p. 1627–1640.

Lahr, J.C., Chouet, B.C., Stephens, C.D., Power, J.A., Page, R.A., 1994, Earthquake classification, location, and error analysis in a volcanic environment: Implications for the magmatic system of the 1989–1990 eruptions at Redoubt volcano, Alaska, Journal of Volcanology and Geothermal Research, v. 62, p. 137–152.

Lamb, S., and Davis, P., 2003, Cenozoic climate change as a possible cause for the rise of the Andes, Nature, v. 425, p. 792-797.

Langston, C.A., 1977, The effect of planar dipping structure on source and receiver responses for constant ray parameter, Bulletin of the Seismological Society of America., v. 67, p. 1029-1050.

Larsen, S.R., Reilinger, R., Brown, L., 1986, Evidence of ongoing crustal deformation related to magmatic activity near Socorro, New Mexico, Journal of Geophysical Research, v. 91, p. 6283–6293.

Laumonier, M., Gaillard, F., Sifre, D., 2014, The effect of pressure and water concentration on the electrical conductivity of dacitic melts: Implication for magnetotelluric imaging in subduction areas, Chemical Geology, v. 385.

Ledo, J., and Jones, A.G., 2005, Upper mantle temperature determined from combining mineral composition, electrical conductivity laboratory studies and magnetotelluric field observations: Application to the intermontane belt, Northern Canadian Cordillera, Earth and Planetary Science Letters, v. 236, p. 258-268.

Lehman, J. A., Smith, R.B., Schilly, M.M., 1982, Upper crustal structure of the Yellowstone caldera from seismic delay time analyses and gravity correlations, Journal of Geophysical Research, v. 87, p.2713-2730.

Leidig, M., and Zandt, G., 2003, Modeling of highly anisotropic crust and application to the Altiplano-Puna volcanic complex of the central Andes, Journal of Geophysical Research, v. 108.

Lezaeta, P., 2002, Confidence limit of the magnetotelluric phase sensitive skew, Earth Planets Space, v. 54. p. 451-457.

Longsdale, P., 2005, Creation of the Cocos and Nazca plates by fission of the Farallon plate, Tectonophysics, v. 404, p. 237-264.

Lowrie, W., 2004, *Fundamentals of Geophysics*, Cambridge University Press, Cambridge, 381 pp.

Lowry, R., 2015, *VassarStats: Web Site for Statistical Computation (Concepts and Applications of Inferential Statistics)*, Vassar College, New York, accessed online September 10, 2015, http://vassarstats.net.

Madden, T., and Nelson, P., 1964, A defence of Cagniard's magnetotelluric method, Project NR-371-401, Geophysical Lab, Massachusetts Institute of Technology, p. 41.

Mai, K., 2006, The Altiplano (Central Andes) High Conductivity Zone: Interpretation and Modeling of Magnetotelluric Data, Technical University Berlin, Diploma thesis.

Malfait, J., Seifert, R., Petitgirard, S., Perrillat, J., Mezouar, M., Ota, T., Nakamura, E., Lerch, P., Sanchez-Valle, C., 2014, Supervolcano eruptions driven by melt buoyancy in large silicic magma chambers, Nature Geoscience, v. 7, p. 122–125.

Mardia, K.V., 1972, *Statistics of Directional Data*, Academic Press, New York, 357 pp.

Mardia, K.V., and Jupp, P.E., 2000, *Directional Statistics (2nd edition)*, John Wiley and Sons Ltd., New York.

Mason, B.G., Pyle, D.M., Oppenheimer, C., 2004, The size and frequency of the largest explosive eruptions on Earth, Bullentin of Volcanology, v. 66, p 735-748.

Mavko, G.M., 1980, Velocity and attenuation in partially molten rocks, Journal of Geophysical Research, v. 85, p. 5173-5189.

Maxwell, J.C., 1873, *A treatise on electricity and magnetism,* Dover Publication Inc., New York, 452 pp.

McFarlin, H.L., Christensen, D.H., Thompson, G., McNutt, S.R., Ryan, J.C., Ward, K.M., Zandt, G., West, M.E., 2014, Receiver Function Analyses of Uturuncu Volcano, Bolivia and Lastarria/Cordon Del Azufre Volcanoes, Chile (abstract #V31E-4792), American Geophysical Union, Fall Meeting, San Francisco, CA.

McGlashan, N., Brown, L., Kay, S., 2008, Crustal thickness in the central Andes from teleseismically recorded depth phase precursors, Journal of Geophysical Research, v. 175, p. 1013-1022.

McNeice, G.M., and Jones, A.G., 2001, Multisite, multifrequency tensor decomposition of magnetotelluric data, Geophysics, v. 66, p. 158-173.

McQuarrie, N., 2002, Initial plate geometry, shortening variations, and evolution of the Bolivian orocline, Geology, v. 30, p. 867-870.

Moorkamp, M., Jones, A.G., Eaton, D.W., 2007, Joint inversion of teleseismic receiver functions and magnetotelluric data using a genetic algorithm: are seismic velocities and electrical conductivities compatible?, Geophysical Research Letters, v. 34.

Muir, D.D., Blundy, J.D., Rust, A.C., Hickey, J., 2014, Experimental constraints on dacite pre-eruptive magma storage conditions beneath Uturuncu volcano, Journal of Petrology, v. 55, p. 749–767.

Muir, D.D., Barfod, D.N., Blundy, J.D., Rust, A.C., Sparks, R.S.J, Clarke, K.M., 2015, The temporal record of magmatism at Cerro Uturuncu, Bolivian Altiplano, in Caricchi, L., and Blundy, J.D., eds., *Chemical, Physical and Temporal Evolution of Magmatic System,* Geological Society, London, Special Publications, v. 422.

Newhall, C.G., and Self, S., 1982, The volcanic explosivity index (VEI) an estimate of explosive magnitude for historical volcanism, Journal of Geophysical Research, v. 87, p. 1231–1238.

Newman, G.A., Wannamaker, P.H., Hohmann, G.W., 1985, On the detectability of crustal magma chambers using the magnetotelluric method, Geophysics, v. 50, p. 1136-1143.

Newman, S., and Lowenstern, J.B., 2002, VolatileCalc: a silicate melt–H2O–CO2 solution model written in Visual Basic for Excel, Computers and Geoscience, v. 28, p. 597–604.

Nover, G., 2005, Electrical properties of crustal and mantle rocks - A review of laboratory measurements and their explanation, Surveys in Geophysics, v. 26, p. 593-651.

Ogawa, Y., Mishina, M., Goto, T., Satoh, H., Oshiman, N., Kasaya, T., Takahashi, Y., Nishitani, T., Sakanaka, S., Uyeshima, M., Takahashi, Y., Honkura Y., Matsushima, M., 2001, Magnetotelluric imaging of fluids in intraplate earthquake zones, NE Japan back arc, Geophysical Research Letters, v. 28, p. 3741-3744.

Owens, T.J., Taylor, S.R., Zandt, G., 1987, Crustal structure at regional seismic test network stations determined from inversion of broadband teleseismic P waveforms, Bulletin of the Seismological Society of America, v. 77 , p. 631–662.

Park, S.K., and Torres-Verdin, C., 1988, A systematic approach to the interpretation of magnetotelluric data in volcanic environments with applications to the quest for magma in Long Valley, California, Journal of Geophysical Research, v. 93, p. 265-283.

Parker, E.N., 1958, Dynamics of the interplanetary gas and magnetic fields, Astrophysical Journal, v. 128, p. 664.

Parkinson, W.D., 1959, Directions of rapid geomagnetic fluctuations, Geophysical Journal of the Royal Astronomical Society, v. 2, p. 1-14.

Pearse, J., and Fialko, Y., 2010, Mechanics of active magmatic intraplating in the Rio Grande Rift near Socorro, New Mexico, Journal of Geophysical Research, v. 115.

Pearse, J., and Lundgren, P., 2013, Source model of deformation at Lazufre volcanic center, central Andes, constrained by InSAR time series, Geophysical Research Letters, v. 40, p. 1059-1064.

Peri, V.G., Barcelona, H., Pomposiello, C., Favetto, A., 2015, Magnetotelluric characterization through the Ambargasta-Sumampa Range: The connection between the northern and southern trace of the Río de La Plata Craton Pampean Terrane tectonic boundary, Journal of South American Earth Sciences, v. 59, p. 1-12.

Petford, N., 2003, Rheology of granitic magmas during ascent and emplacement, Annual Review of Earth and Planetary Science, v. 31, p. 399-427.

Petiau, G., 2000, Second generation of lead-lead chloride electrodes for geophysical applications, Pure and Applied Geophysics, v. 157, p. 357-382.

Pickett, G., 1963, Acoustic character logs and their applications in formation evaluation, Journal of Petroleum Technology, v. 15, p.650-667.

Pollack, H.N., et al., 1993, Heat Flow from the Earth's Interior: Analysis of the Global Data Set, Reviews of Geophysics, v.3, p. 273.

Pommier, A., and Le-Trong, E., 2011, “SIGMELTS”: A web portal for electrical conductivity calculations in geosciences, Computers and Geosciences, v. 37, p. 1450–1459.

Pommier, A., Evans, R., Key, K., Tyburczy, J., Mackwell, S., Elsenbeck, J., 2013, Prediction of silicate melt viscosity from electrical conductivity: A model and its geophysical implications, Geochemistry, Geophysics, Geosystems, v. 14.

Pommier, A., 2014, Interpretation of Magnetotelluric Results Using Laboratory Measurements, Surveys in Geophysics, v. 35, p. 41-84.

Pommier, A., 2014b, Geophysical assessment of migration and storage conditions of fluids in subduction zones, Earths, Planets and Space, v. 66.

Prezzi, C.B., Götze, H.J., Schmidt, S., 2009, 3D density model of the Central Andes, Physics of the Earth and Planetary Interiors, v. 177, p. 217–234.

Pritchard, M.E., and Simons, M., 2002, A satellite geodetic survey of large-scale deformation of volcanic centres in the central Andes, Nature, v. 418, p. 167–171.

Pritchard, M.E., and Simons, M., 2004, An InSAR-based survey of volcanic deformation in the Central Andes, Geochemistry, Geophysics, Geosystems, v. 5.

Pritchard, M.E., and Simons, M., 2004b, An InSAR-based survey of volcanic deformation in the southern Andes, Geophysical Research Letters, v. 31, p. 4-11.

Pritchard, M.E., 2006, InSAR, a tool for measuring Earth's surface deformation, Physics Today, p. 68-69.

Pysklywec, R.N., 2006, Surface erosion control on the evolution of the deep lithosphere, Geology, v. 34, p. 225–228.

Quade, J., Dettinger, M.P., Carrapa, B., DeCelles, P., Murray, K.E., Huntington, K.W., Cartwright, A., Canavan, R.R., Gehrels, G., Clementz, M., 2015, The growth of the central Andes, 22°S–26°S, The Geological Society of America, Memoir 212.

Ramos, V.A., 1988, The tectonics of the Central Andes; 30° to 33° S latitude, Geological Society of America Special Paper, v. 218, p. 31-54.

Ramos, V.A., 1999, Plate tectonic setting of the Andean Cordillera, Episodes, v. 22, p. 183-190.

Ramos, V.A., and Folguera, A., 2009, Andean flat-slab subduction through time, in Murphy, J.B., Keppie, J.D., Hynes, A.J., eds., *Ancient Orogens and Modern Analogues*, Geological Society, London, Special Publications, v. 327, p. 31–54.

Ramos, V.A., Cristallini, E.O., Perez, D.J., 2002, The Pampean flat-slab of the Central Andes, Journal of South American Earth Sciences, v. 15, p. 59-78.

Richards, J.P., 2011, Magmatic to hydrothermal metal fluxes in convergent and collided margins, Ore Geology Reviews, v. 40, p. 1–26.

Richter, C.F., 1935, An instrumental earthquake magnitude scale, Bulletin of the Seismological Society of America, v. 25, p. 1–32.

Riddick, S., and Schmidt, D.A., 2011, Time-dependent changes in volcanic inflation rate near Three Sisters, Oregon, revealed by InSAR, Geochemistry, Geophysics, Geosystems, v. 12.

Rietbrock, A., 2001, P wave attenuation structure in the fault area of the 1995 Kobe earthquake, Journal of Geophysical Research, v. 106, p. 4141-4154.

Rippe D., and Unsworth, M.J., 2010, Quantifying crustal flow in Tibet with magnetotelluric data, Physics of the Earth and Planetary Interiors, v. 179, p. 107-121.

Rodi, W., and Mackie, R.L., 2001, Nonlinear conjugate gradients algorithm for 2-D magnetotelluric inversion, Geophysics, v. 66, p. 174–187.

Roman, D., Cashman, K., 2006, The origin of volcano-tectonic earthquake swarms, Geology, v. 34, p. 457-460.

Roux, E., Moorkamp, M., Jones, A.G., Bischoff, M., Endrun, B., Lebedev, S., Meier, T., 2011, Joint inversion of long-period magnetotelluric data and surface-wave dispersion curves for anisotropic structure: Application to data from Central Germany, Geophysical Research Letters, v. 38.

Royden, L.H., Burchfiel, B.C., can der Hilst, R.D., 2008, The Geological Evolution of the Tibetan Plateau, Science, v. 321, p. 1054-1058.

Ruch, J., Anderssohn, J., Walter, T.R., Motagh, M., 2008, Caldera-scale inflation of the Lazufre volcanic area, South America: Evidence from InSAR, Journal of Volcanology and Geothermal Research, v. 174, p. 337-344.

Ruch, J., Manconi, A., Zeni, G., Solaro, G., Pepe, A., Shirzaei, M., Walter, T.R., Lanari, R., 2009, Stress transfer in the Lazufre Volcanic area, Central Andes, Geophysical Research Letters, v. 36.

Ryder, I., Parsons, B., Wright, T., Funning, G.J., 2007, Post-seismic motion following the 1997 Manyi (Tibet) earthquake: InSAR observations and modelling, Geophysical Journal International, v. 169, p. 1009-1027.

Sabra, K.G., Gerstoft, P., Roux, P., Kuperman, W.A., Fehler, M.C., 2005, Extracting time-domain Greens function estimates from ambient seismic noise, Geophysical Research Letters, v. 32.

Salisbury, M.J., Jicha, B.R., de Silva, S.L., Singer, B.S., Jimenez, N.C., Ort, M.H., 2011, 40Ar/39Ar chronostratigraphy of Altiplano-Puna volcanic complex ignimbrites reveals the development of a major magmatic province, Geological Society of America Bulletin, v. 123, p. 821-840.

Sanford, A.R., Mott, R.P., Shuleski, P.J., Rinehart, E.J., Caravella, F.J., Ward, R.M., Wallace, T.C., 1977, Geophysical evidence for a magma body in the vicinity of Socorro, New Mexico, in Heacock, J.G., ed., *The Earth's crust: Its nature and physical properties*, American Geophysical Union Geophysical Monograph, v. 20, p. 385–404.

Savino, J.M., Rodi, W.L., Jordan, T.H., Goff, R.C., Lambert, D.G., 1979, Joint Inversion of Geophysical Data as a Geothermal Exploration Tool: Applications to Yellowstone Park and the Imperial Valley, Geothermal Resources Council Transactions, v. 3, p. 625-628.

Schilling, F.R., Partzsch, G. M., Brasse, H., Schwarz, G., 1997, Partial melting below the magmatic arc in the central Andes deduced from geoelectromagnetic field experiments and laboratory data, Physics of the Earth and Planetary Interiors, v. 103, p. 17-31.

Schilling, F.R., Trumbull, R.B., Brasse, H., 2006, Partial Melting in the Central Andean Crust: A review of Geophysical, Petrophysical, and Petrologic Evidence, in Oncken, O., et al., eds., *The Andes: active subduction orogeny (Frontiers in Earth Sciences Volume 1),* Springer-Verlag, Berlin, p. 459–474.

Schlue, J., Aster, R., Meyer, R., 1996, A lower-crustal extension to a mid-crustal magma body in the Rio Grande rift, New Mexico, Journal of Geophysical Research, v. 101, p. 25,283-25,291.

Schmitt, D.R., 2015, Geophysical Properties of the Near Surface Earth: Seismic Properties, in Schubert, G., ed., *Treatise on Geophysics (Second Edition)*, Oxford Press, Oxford, p. 43-87.

Schmitz M., 1994, A balanced model of the southern Central Andes, Tectonics, v. 13, p. 484-492.

Schurr, B., 2000, Seismic structure of the Central Andean subduction zone from local earthquake data, GeoForschungsZentrum Potsdam Scientifc Technical Report STR01/01

Schurr, B., Asch, G., Rietrbrock, A., Trumbull, R., Haberland, C., 2003, Complex patterns of fluid and melt transport in the Central Andean subduction zone revealed by attenuation tomography, Earth and Planetary Scientific Letters, v. 215, p. 105-119.

Schutt, D.L., Dueker, K., Yuan, H., 2008, Crust and upper mantle velocity structure of the Yellowstone hot spot and surroundings, Journal of Geophysical Research, v. 113.

Schwarz, G., and Kruger, D., 1997, Resistivity cross section through the southern Central Andes as inferred from magnetotelluric and geomagnetic depth soundings, Journal of Geophysical Research, v. 102, p. 11957-11978.

Schwarz, G., Chong, D.G., Krüger, D., Martinez, M., Massow ,W., Rath, V., Viramonte, J., 1994, Crustal high conductivity zones in the southern Central Andes, in Reutter, K.J., Scheuber, E., Wigger, P., eds., *Tectonics of the Southern Central Andes*, Springer, Berlin, p. 49–67.

Shapiro, N.M., Campillo, M., Stehly, L., Ritzwoller, M.H., 2005, High-resolution surface-wave tomography from ambient seismic noise, Science, v. 307, p. 1615-1618.

Shearer, P.M., 2009, *Introduction to Seismology, Second Edition*, Cambridge University Press, Cambridge.

Sheetz, K.E., and Schlue, J.W., 1992, Inferences for the Socorro magma body from teleseismic receiver functions, Geophysical Research Letters, v. 19, p. 1867-1870

Sheffells, B.M., 1990, Lower bound on the amount of crustal shortening in the central Bolivian Andes, Geology, v. 18, p. 812-815.

Simpson, F., and Bahr, K., 2005, *Practical Magnetotellurics*, Cambridge University Press, Cambridge.

Sims, W.E., Bostick, F.X., Smith, H.W., 1971, The Estimation of Magnetotelluric Impedance Tensor Elements from Measured Data, Geophysics, v. 36, p. 938-942.

Siniscalchi, A., Tripaldi, S., Neri, M., Balasco, M., Romano, G., Ruch, J., Schiavone, D., 2012, Flank instability structure of Mt. Etna inferred by a magnetotelluric survey, Journal of Geophysical Research, v. 117.

Siripunvaraporn, W., Egbert, G.D., Lenbury, Y., Uyeshima, M., 2005, Three dimensional magnetotelluric inversion: Data subspace method, Physics of the Earth and Planetary Interiors, v. 150, p. 3–14.

Skinner, S., and Clayton, R., 2013, The lack of correlation between flat slabs and bathymetric impactors in South America Earth and Planetary Science Letters, v. 371.

Soyer, W., and Brasse, H., 2001, A magneto-variation array study in the Central Andes of N Chile and SW Bolivia, Geophysical Research Letters, v. 28.

Sparks, R.S.J., Folkes, C.B., Humphreys, M.C.S., Barfod, D.N., Clavero, J., Sunagua, M.C., McNutt, S.R., and Pritchard, M.E., 2008, Uturuncu volcano, Bolivia: Volcanic unrest due to mid-crustal magma intrusion, American Journal of Science, v. 308, p.727-769.

Springer, M., 1999, Interpretation of heat-flow density in the Central Andes, Tectonophysics, v. 306, p. 377–395.

Springer, M., and Förster, A., 1998, Heat-flow density across the Central Andean subduction zone, Tectonophysics, v. 291, p. 123–139.

Stankova, J., Bilek, S.L., Rowe, C.A., Aster, R.C., 2008, Characteristics of the October 2005 microearthquake swarm and reactivation of similar event seismic swarms over decadal time periods near Socorro, New Mexico, Bulletin of the Seismological Society of America, v. 98, p. 93–105.

Steeples, D.W., and Iyer, H.M., 1976, Low-velocity zone heat conduction models for Long Valley caldera, Journal of Geophysical Research, v. 81, p. 769-784.

Stern, R., 2002, Subduction Zones, Reviews of Geophysics, v. 40, p. 1-38.

Stothers, R.B., 1984, The Great Tambora Eruption in 1815 and Its Aftermath, Science, v. 224, p. 1191–1198.

Swift, C.M., 1967, A magnetotelluric investigation of an Electrical Conductivity Anomaly in the Southwestern United States, MIT, PhD thesis.

Takei, Y., 2000, Acoustic properties of partially molten media studied on a simple binary system with a controllable dihedral angle, Journal of Geophysical Research, v. 105, p.16,665-16,682.

ten Grotenhuis, S.M., Drury, M.R., Spiers, C.J., Peach, C.J., 2005, Melt distribution in olivine rocks based on electrical conductivity measurements, Journal of Geophysical Research, v. 110.

Thurber, C.H., 1993, Local earthquake tomography: velocities and Vp/Vs-theory, in Iyer, H.M. and Hirahara, K., eds., *Seismic Tomography: Theory and Practice*, Chapman and Hall, London, p. 563-583.

Tikhonov, A.N., 1950, Determination of the electrical characteristics of the deep strata of the Earth's crust, Dok. Akad. Nauk., USSR, v. 73, p. 295-297.

Tizzani, P., Battaglia, M., Zeni, G., Atzori, S., Berardino, P., Lanari, R., 2012, Uplift and magma intrusion at Long Valley caldera from InSAR and gravity measurements, Geology, v.37, p. 63-66.

Turkoglu, E., Unsworth, M. J., Çağlar, I., Tuncer, V., Avşar, U., 2008, Lithospheric structure of the Arabia-Eurasia collision zone in eastern Anatolia: Magnetotelluric evidence for widespread weakening by fluids?, Geology, v. 36, p. 619-622.

Unsworth, M.J., 2007, *Magnetotellurics*, in Gubbins D., and Herrero-Bervera, E., eds., Encyclopedia of Geomagnetism and Paleomagnetism, Springer, Berlin, p.670-673.

Unsworth, M.J., 2010, Magnetotelluric studies of active continent-continent collisions, Surveys in Geophysics, v. 31, p. 137-161.

Unsworth, M.J., and Rondenay, S., 2012, Mapping the distribution of fluids in the crust and lithospheric mantle utilizing geophysical methods, in Harlov, D.E., and Austrheim, H., eds., *Metasomatism and the Chemical Transformation of Rock, Lecture Notes in Earth System Sciences*, Springer Verlag, Berlin, p. 535-598.

Vasco, D.W., Puskas, C.M., Smith, R.B., Meertens, C.M., 2007, Crustal deformation and source models of the Yellowstone volcanic field from geodetic data, Journal of Geophysical Research, v. 112.

von Huene, R., and Scholl, D.W., 1991, Observations at convergent margins concerning sediment subduction and the growth of continental crust, Reviews of Geophysics, v. 29, p. 279–316.

von Huene, R., Corvalán, J., Flueh, E.R., Hinz, K., Korstgard, J., Ranero, C.R., Weinrebe, W., CONDOR Scientists, 1997, Tectonic control on the subducting Juan Fernandez Ridge on the Andean margin near Valparaiso, Chile, Tectonics, v. 16, p. 474–488.

Vozoff, V., 1990, Magnetotellurics: Principles and practice, Earth Planetary Science, v. 99, p. 441-471.

Wait, J.R., 1954, On the relation between Telluric Currents and the Earth's Magnetic Field, Geophysics, p. 281-289.

Walter, T.R., and Motagh, M., 2014, Deflation and inflation of a large magma body beneath Uturuncu volcano, Bolivia? Insights from InSAR data, surface lineaments and stress modelling, Geophysical Journal International, v. 198, p. 462–473.

Wang, H., Currie, C.A., DeCelles, P.G., 2015, Hinterland basin formation and gravitational instabilities in the central Andes: Constraints from gravity data and geodynamic models, GSA Memoirs, v. 212.

Wannamaker, P.E., Hohmann, G.W., and SanFilipo, W.A., 1984, Electromagnetic modeling of three-dimensional bodies in layered earths using integral equations, Geophysics, v. 49, p. 60-74.

Wannamaker, P.E., Wright, P.M., Zi-xing, Z., Xing-bin, L., Jing-xiang, Z., 1991, Magnetotelluric transect of Long Valley Caldera; resistivity cross-section, structural implications, and the limits of a 2-D analysis, Geophysics, v. 56, p. 926-940.

Wannamaker, P.E., 1999, Affordable magnetotellurics: Interpretation in natural environments, in Oristaglio, M., and Spies, B., eds., *Three-Dimensional Electromagnetics*, Geophysical Development Series, Society of Exploration Geophysicists, Tulsa, p. 349-374.

Wannamaker, P.E., Caldwell, T.G., Jiracek, G.R., Maris, V., Hill, G.J., Ogawa, Y., Bibby, H.M., Bennie, S.L., Heise, W., 2009, Fluid and deformation regime of an advancing subduction system at Marlborough, New Zealand, Nature , v. 460, p. 733-737.

Ward, K.M., Porter, R.C., Zandt, G., Beck, S.L., Wagner, L.S., Minaya, E., Tavera, H., 2013, Ambient noise tomography across the central Andes, Geophysical Journal International, v. 194, p. 1559–1573.

Ward, K., Zandt, G., Beck, S., Christensen, D.H., McFarlin, H., 2014, Seismic imaging of the magmatic underpinnings beneath the Altiplano-Puna volcanic complex from the joint inversion of surface wave dispersion and receiver functions, Earth and Planetary Science Letters, v. 404, p. 43–53.

Watanabe, T., and Kurita, K., 1993, The relationship between electrical conductivity and melt fraction in a partially molten simple system: Archie's Law behavior, Physics of the Earth and Planetary Interiors, v. 78, p. 9–17.

Waxman, M.H., and Smits, L.J.M., 1968, Electrical Conductivities in Oil-Bearing Shaly Sands, Society of Petroleum Engineers Journal, v. 243, p. 107-122.

Weaver, J.T., 1994, *Mathematical Methods for GeoElectromagnetic Induction*, Res. Stud. Press, Taunton, Mass.

Wei, W., Unsworth, M., Jones, A., Booker, J., Tan, H., Nelson, D., Chen, L., Li, S., Solon, K., Bedrosian, P., Jin, S., Deng, M., Ledo, J., Kay, D.,Roberts, B., 2001, Detection of Widespread Fluids in the tibetan Crust by Magnetotelluric Studies, Science, v. 292, p.716-718.

Weidelt, P., 1972, The inverse problem of geomagnetic induction, Journal of Geophysics, v. 38, p. 257-289.

Wessel, P., and Smith, W., 1991, Free Software helps Map and Display Data, Eos, Transactions, American Geophysical Union, v. 72, p. 441–446.

West, M., Kukarina, E., Koulakov, I., 2013, Structure of Uturuncu volcano from seismic tomography (abstract #V13B-2600), American Geophysical Union, Fall Meeting, San Francisco, CA.

White, L.T., Gibson, G.M., Lister, G.S., 2013, A reassessment of paleogeographic reconstructions of eastern Gondwana: Bringing geology back into the equation, Gondwana Research, v. 24, p. 984-998.

Wicks, C.W., Thatcher, W., Dzurisin, D., Svarc, J., 2006, Uplift, thermal unrest and magma intrusion at Yellowstone caldera, Science, v. 440, p. 72-75.

Wiese, H., 1962, Geomagnetische Tiefentellurik Teil II: Die Streichrichtung der Untergrund-strukturen des elektrischen Widerstandes, erschlossen aus geomagnetischen Variationen (Strike direction of underground structures of electric resistivity, inferred from geomagnetic variations), Pure and Applied Geophysics, v. 52, p. 83-103.

Wigger, P., 1994, Variation of the crustal structure of the southern central Andes deduced from seismic refraction investigations, in Reutter, K.J., Scheuber, E., Wigger, P., eds., *Tectonics of the Southern Central Andes,* Springer-Verlag, New York, p. 23–48.

Yuan X., Sobolev S.V., Kind R., 2002, Moho topography in the central Andes and its geodynamic implications, Earth and Planetary Science Letters, v. 199, p. 389–402.

Zandt, G., and Ammon, C., 1995, Continental Crustal composition constrained by measurements of crustal Poisson's ratio, Nature, v. 374, p. 152-154.

Zandt, G., Leidig, M., Chmielowski, J., Baumont, D., Yuan, X., 2003, Seismic detection and characterization of the Altiplano-Puna magma body, Central Andes, Pure and Applied Geophysics, v. 160, p. 1-19.

Zellmer, G.F., and Annen, C., 2008, An introduction to magma dynamics, Geological Society, London, Special Publications, v. 304, p. 1-13.

Zhang, G.H., and Chou, K.C., 2010, Simple method for estimating the electrical conductivity of oxide melts with optical basicity, Metallurgical and Materials Transactions B, v. 41, p. 131–136.

Zhdanov, M.S., and Keller, G.V., 1994, *The geoelectrical methods in geophysical exploration,* Elsevier, Amsterdam, 873 pp.

Zhdanov, M.S., Smith, R.B., Gribenko, A., Cuma, M., Green, M., 2011, Three-dimensional inversion of large-scale EarthScope magnetotelluric data based on the integral equation method: Geoelectrical imaging of the Yellowstone conductive mantle plume, Geophysical Research Letters, v. 38.

APPENDIX

A.1 List of Magnetotelluric Stations Used in Preferred 2-D Inversion Models

Magnetotelluric stations used for the 2-D inversion along Profile 1, Segment AB (Bolivia), are shown in Table A.1. Magnetotelluric stations used along Segment BC (NW Argentina), are shown in Table A.2.

VIR	1495N01_11b	1463O30_11	1465N07_12	1493O21_12
PEA	1493O24_12	1463N03_11b	1493N06_12	1465O31_13
1463O26_12	1463N01_11b	1465029_11b	1496N07_12	1493O31_13
1495N02_11b	1496O25_12	1495N11_11b	1493N13_11b	1494O30_13
1496O26_12	1463O31_11	1495O30_11b	1495N14_11b	1465O30_13
1493O26_12	1465O24_12	1493N11_11b	1465N05_12	1494O31_13
1463N02_11b	1465O31_11b	1465O30_11b	1496N05_12	1463O30_13
1493O25_12	1495N17_11b	1495N09_11b	1493N05_12	1463O31_13
1465N02_11b	1465N03_11b	1465N10_11b	1465O20_12	1463N01_13
1465O25_12	1495O31_11b	1463N09_11b	1496O20_12	1493N01_13
1465N01_11b	1495N03_11b	1465N09_11b	1493O20_12	1465N01_13
1463O25_12	1465N11_11b	1463N16_11b	1496O21_12	

Table A.1: Magnetotelluric stations used for the 2-D inversion along Profile 1, Segment AB (Bolivia).

1463N12_11b	1496O20_12	1494O31_13	1463N02_13	1465N17_13
1493N16_11b	1493O20_12	1463O30_13	1463N03_13	1465N05_13
1495N13_11b	1496O21_12	1463O31_13	1494N03_13	1463N05_13
1493N13_11b	1493O21_12	1463N01_13	1463N16_13	1465N18_13
1465N05_12	1465O31_13	1493N01_13	1465N16_13	1463N18_13
1496N05_12	1493O31_13	1465N01_13	1494N04_13	1494N18_13
1493N05_12	1494O30_13	1465N02_13	1463N17_13	
1465O20_12	1465O30_13	1494N02_13	1463N04_13	

Table A.2: Magnetotelluric stations used for the 2-D inversion along Profile 1, Segment BC (NW Argentina).

A.2 List of Magnetotelluric Stations Used in 3-D Inversion Models

A.2.1 Preferred 3-D Inversion S73

Magnetotelluric stations used for the 3-D inversion around Volcan Uturuncu, grid S73, are shown in Table A.3. Magnetotelluric stations used for grid S96 are shown in Table A.4.

1463N03_11b	1463N17_12	1465N11_12	1493N10_12	1495N12_11b
1463N04_12	1463O30_11	1465N14_12	1493N11_11b	1495N13_11b
1463N05_11b	1465O29_11b	1465N15_11b	1493N12_11b	1495N14_11b
1463N07_12	1465N04_11b	1465N15_12	1493N13_11b	1495O30_11b
1463N08_12	1465N04_12	1465N16_12	1493N14_11b	1496N05_12
1463N09_11b	1465N05_11b	1465N17_12	1493N16_11b	1496N07_12
1463N09_12	1465N05_12	1465N23_12	1493N16_12	1496N10_12
1463N10_11b	1465N06_11b	1465O18_12	1493N23_12	1496N14_12
1463N12_11b	1465N06_12	1465O19_12	1493O22_12	1496N16_12
1463N13_11b	1465N07_12	1465O22_12	1493O23_12	1496N23_12
1463N14_11b	1465N09_11b	1465O23_12	1495N04_11b	1496O19_12
1463N14_12	1465N09_12	1493N06_12	1495N05_11b	1496O22_12
1463N15_11b	1465N10_11b	1493N07_12	1495N06_11	1496O23_12
1463N16_11b	1465N10_12	1493N09_11b	1495N09_11b	
1463N16_12	1465N11_11b	1493N10_11b	1495N11_11b	

Table A.3: MT stations used for the 3-D inversion around Volcan Uturuncu, grid S73.

A.2.2 3-D Inversion S96

1495N14_11b	1465N16_12	1496N04_12	1463N14_11b	1493N14_11b
1463N04_12	1465N17_12	1496N05_12	1463N15_11b	1493N15_11b
1463N05_12	1465N18_12	1496N07_12	1463N16_11b	1493N16_11b
1463N07_12	1465N23_12	1496N08_12	1463N17_11b	1495N03_11b
1463N08_12	1465O18_12	1496N10_12	1463O30_11	1495N04_11b
1463N09_12	1465O19_12	1496N14_12	1465O29_11b	1495N05_11b
1463N14_12	1465O20_12	1496N16_12	1465N03_11b	1495N09_11b
1463N16_12	1465O22_12	1496N18_12	1465N04_11b	1495N11_11b
1463N17_12	1465O23_12	1496N23_12	1465N05_11b	1495N12_11b
1463N18_12	1465O28_12	1496O19_12	1465N06_11b	1495N13_11b
1463N23_12	1493N05_12	1496O20_12	1465N09_11b	1495N15_11b
1465N04_12	1493N06_12	1496O22_12	1465N10_11b	1495N16_11b
1465N05_12	1493N07_12	1496O23_12	1465N11_11b	1495N17_11b
1465N06_12	1493N10_12	1463N03_11b	1465N15_11b	1495O30_11b
1465N07_12	1493N16_12	1463N05_11b	1465N17_11b	1495O31_11b
1465N09_12	1493N17_12	1463N06_11b	1465O30_11b	1495N06_11
1465N10_12	1493N18_12	1463N09_11b	1493N09_11b	
1465N11_12	1493N23_12	1463N10_11b	1493N11_11b	
1465N14_12	1493O22_12	1463N12_11b	1493N12_11b	
1465N15_12	1493O23_12	1463N13_11b	1493N13_11b	

Table A.4: MT stations used for the 3-D inversion around Volcan Uturuncu, grid S96.

A.3 Preferred 3-D Resistivity Model Vertical Sections for Grid S73

The preferred 3-D resistivity inversion model for grid S73 is shown as an West-East vertical section along latitude 22.267°S in Figure A.1 and as a South-North vertical section along longitude 67.192°W in Figure A.2. Figure A.3 giveS an alternate 3-D perspective view.

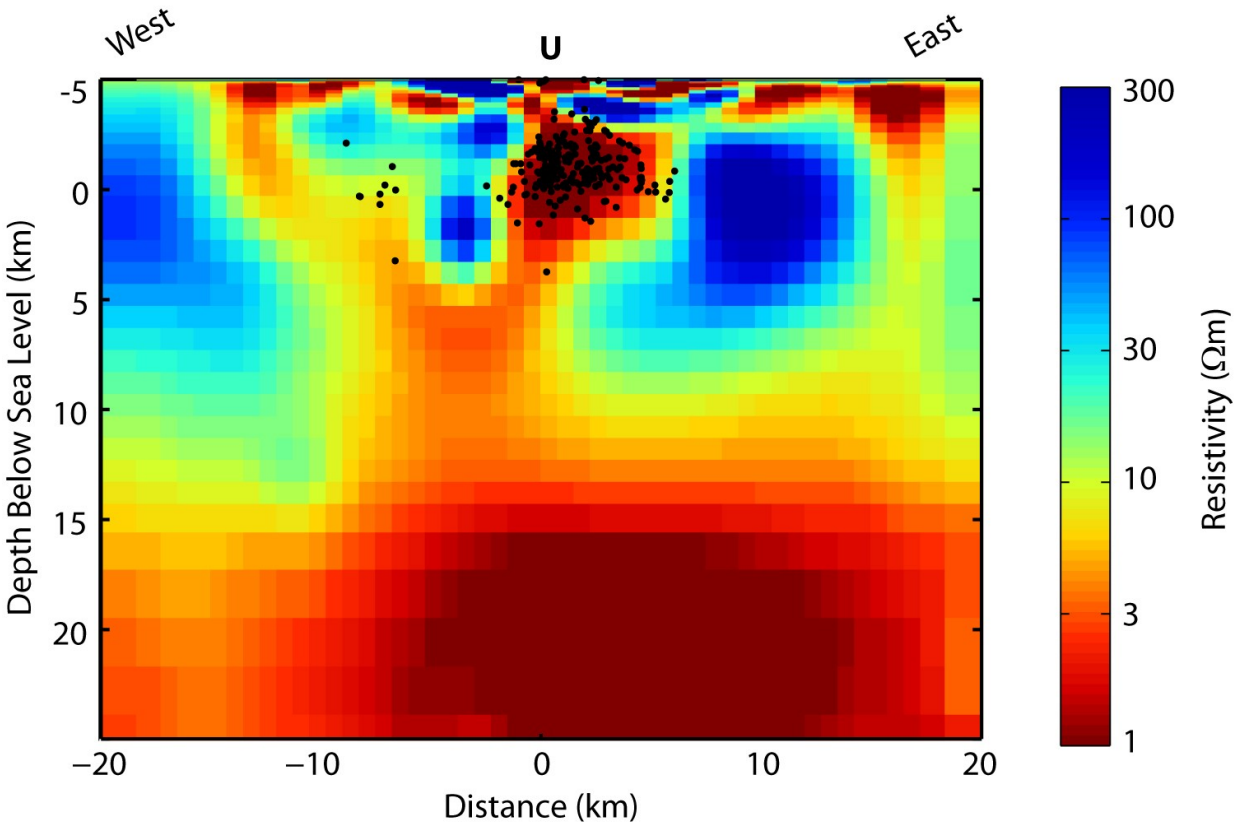

Figure A.1: Preferred 3-D resistivity model (S73). A vertical slice through the inversion model along latitude 22.267°S. Black dots are earthquake hypocenters from Jay et al. (2012). The symbol U marks the location of Volcan Uturuncu.

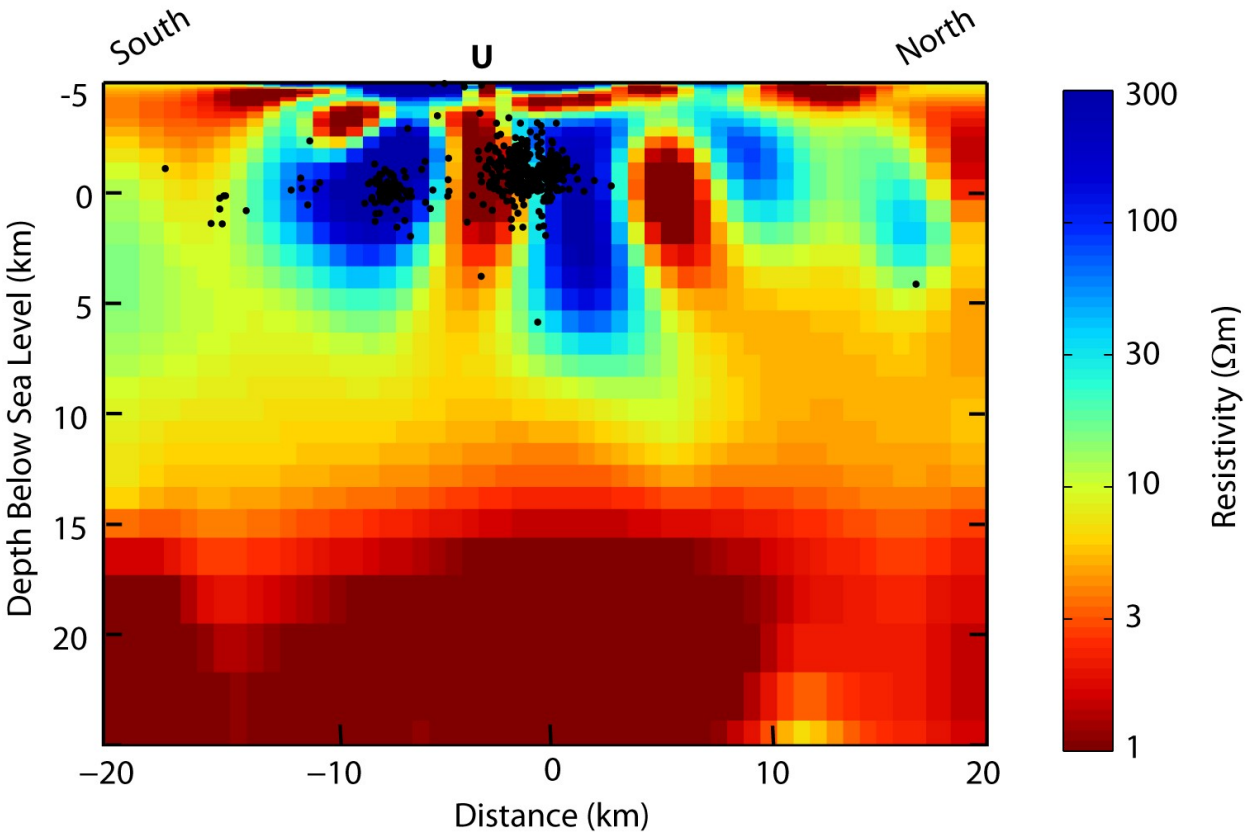

Figure A.2: Preferred 3-D resistivity model (S73). A vertical slice through the inversion model along longitude 67.192°W. Black dots are earthquake hypocenters from Jay et al. (2012). The symbol U marks the location of Volcan Uturuncu.

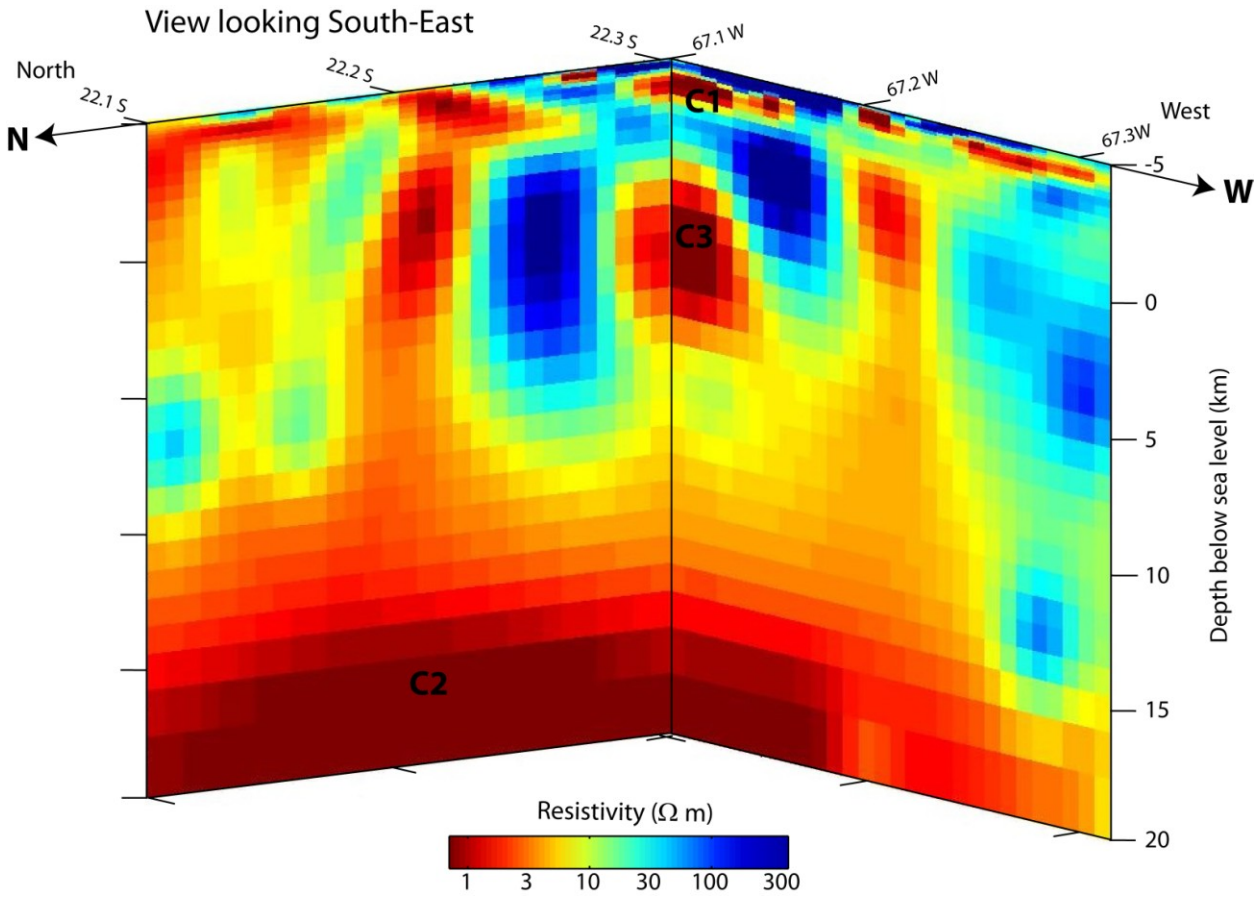

Figure A.3: An alternative view of the preferred 3-D MT resistivity inversion model (S73). The view is looking south-east, along two vertical slices which intersect at the location of Volcan Uturuncu.

A.4 SIGMELTS Resistivity Model

The SIGMELTS model of Pommier and LeTrong (2011) allows the computation of resistivity as a function of silica content, water content, pressure, temperature, and sodium content. Figure A.4 Panel A shows resistivity as a function of silica content, with the other variables fixed, and Panel B shows resistivity as a function of water content. The SIGMELTS model has regimes within which the equations are smooth and continuous. Crossing these regimes can cause discrepancies, for example going from 69.9% silica to 70% silica. Above ~9 wt% water content the equations saturate and level off, and no longer depend on silica content. The relation of Laumonier et al. (2014) gives the resistivity as a function of water content, pressure, and temperature for dacite (silica content of 63% - 68%). This relation is shown in Figure A.4 Panel B for comparison.

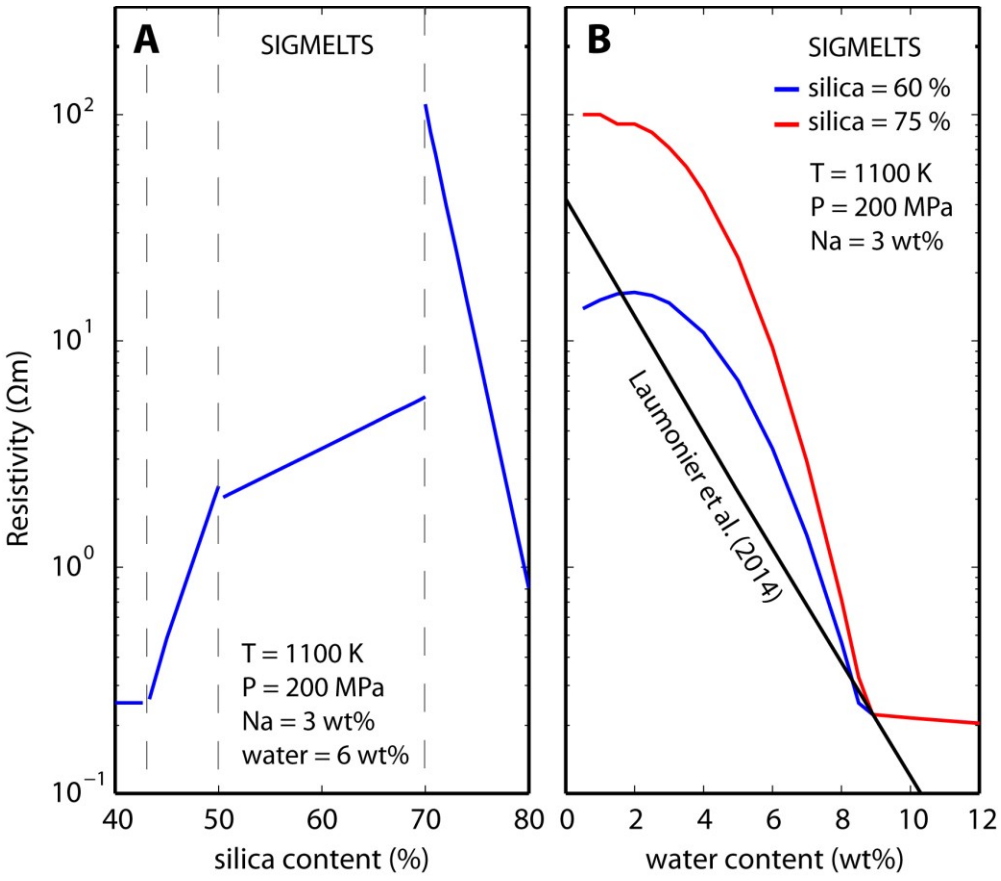

Figure A.4: Resistivity as a function of silica content (Panel A) and water content (Panel B) using the SIGMELTS model of Pommier and LeTrong (2011). Black line in Panel B shows the relation of Laumonier et al. (2014) for dacite (silica content of 63% - 68%).

A.5 3-D Resistivity Model S96 as Stacked Vertical Sections

The 3-D resistivity inversion model for grid S96 is shown as a series of stacked vertical sections looking northwards in Figure A.5 and westwards in Figure A.6.

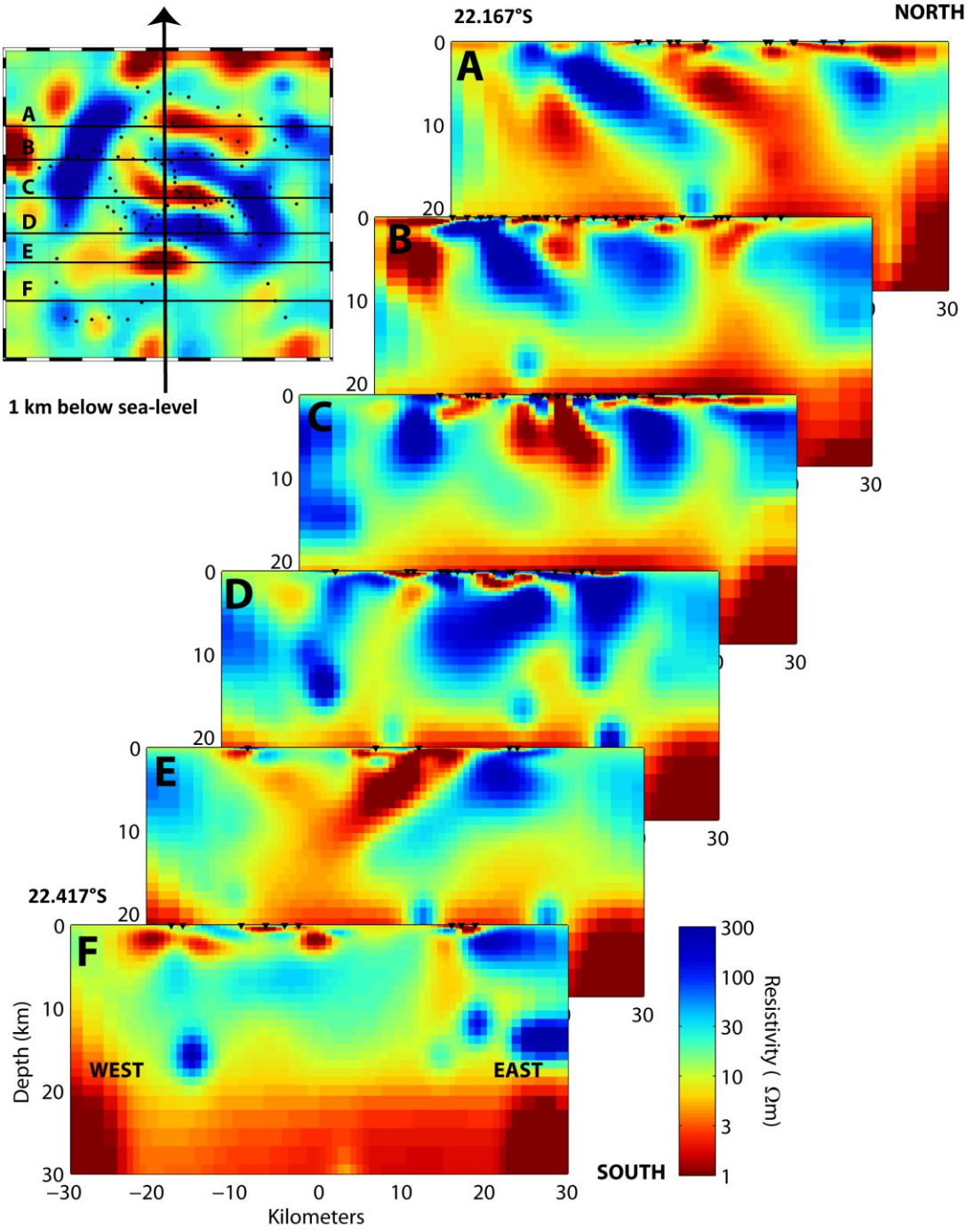

Figure A.5: Vertical sections of the 3-D resistivity model S96, shown looking northwards.

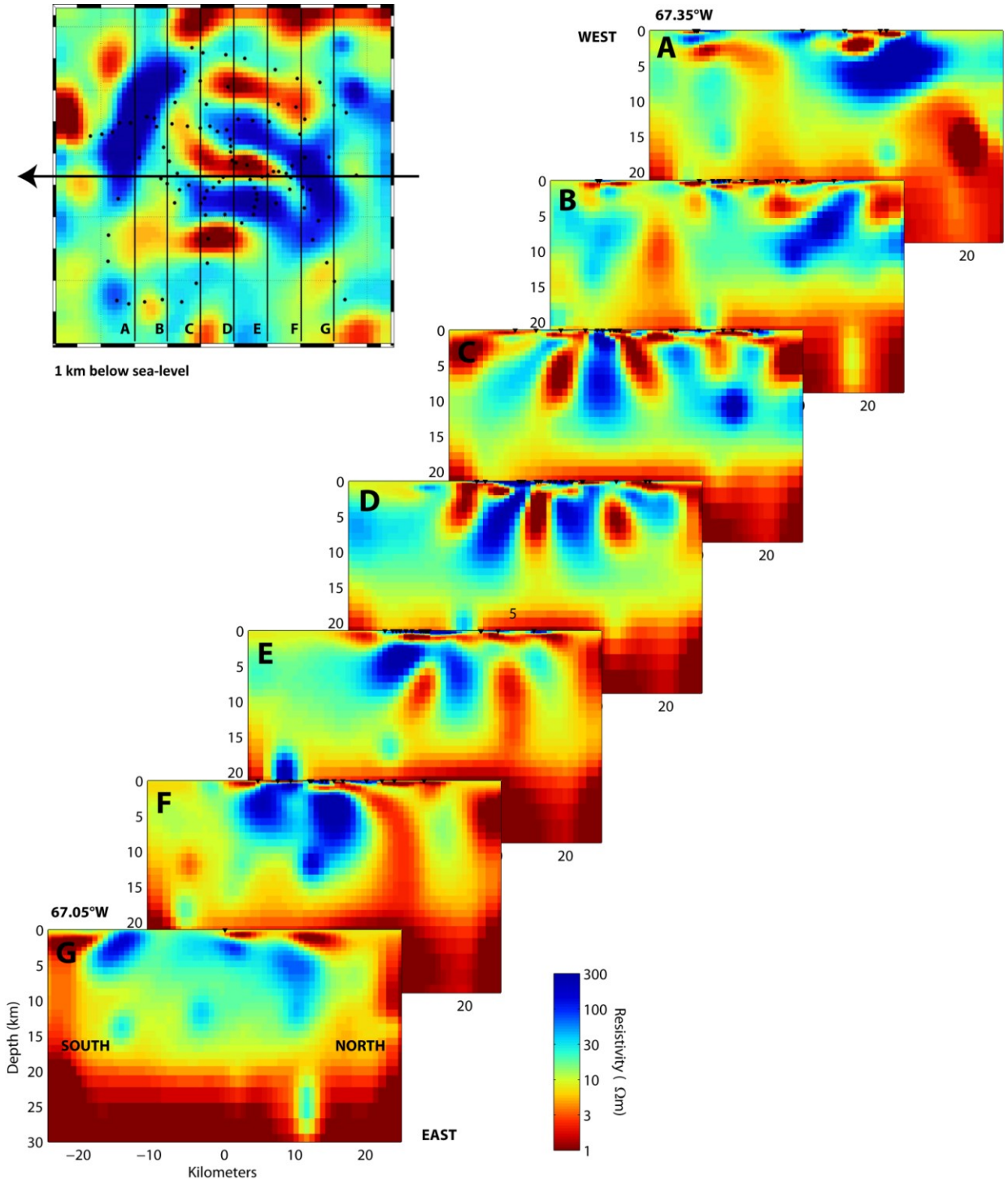

Figure A.6: Vertical sections of the 3-D resistivity model S96, shown looking westwards.

Appendix